
Site U1338¹

Expedition 320/321 Scientists²

Chapter contents

Background and objectives	1
Science summary	2
Operations	6
Lithostratigraphy	8
Biostratigraphy	11
Paleomagnetism	22
Geochemistry	23
Physical properties	26
Stratigraphic correlation and composite section	29
Downhole measurements	29
References	33
Figures	36
Tables	117

Background and objectives

In principle, the age-transect strategy of this expedition would not be complete without data from the Pliocene and Pleistocene. However, in addition to the logistical reasons of cruise length, near-equatorial records have already been recovered during Ocean Drilling Program (ODP) Legs 138 (Pisias, Mayer, Janecek, et al., 1995) and 202 (Mix, Tiedemann, Blum, et al., 2003). This earlier drilling provides information about the development of Northern Hemisphere glaciation. Our last site focuses instead on the interesting events during and just after a mid-Miocene maximum in sediment deposition (van Andel et al., 1975) and temperature (Zachos et al., 2001).

Integrated Ocean Drilling Program (IODP) Site U1338 (2°30.469'N, 117°58.178'W; 4200 m water depth; PEAT-8 site survey) (Fig. F1; Table T1) was sited to collect a 3–18 Ma segment of the Pacific Equatorial Age Transect (PEAT) equatorial megasplite. Site U1338 is on ~18 Ma crust just north of the Galapagos Fracture Zone, 324 nmi (600 km) southeast of Site U1337 (Fig. F1), in abyssal hill topography that strikes 350° (Fig. F1). The topography slopes down to the north-northwest from a regional high in the south. A seamount (3.7 km water depth) with a surrounding moat is found ~25 km north-northwest of Site U1338, at the downslope end of the survey area. Originally a site (proposed Site PEAT-8C) was chosen ~10 km from the seamount. However, alternate proposed Site PEAT-8D was selected and drilled uphill and further away from the seamount to avoid possible turbidites, as were found near seamounts at Sites U1331 and U1335.

Site U1338 is on a minor ridge along Line 1 of the PEAT-8 survey (Fig. F2) under 4200 m of water. In the survey area, sediment thickness ranges from ~400 ms two-way traveltime (TWT; ~320 m) at the top of the abyssal hills to a maximum of a little more than 550 ms TWT (~450 m) within basins. Estimated sediment thickness from the seismic reflection profile using an ODP Site 849 velocity-depth age model is 402 m at the Site U1338 location. The sediment pattern is typical “pelagic drape” and lies conformably on basement. Ridges at the seafloor reflect basement highs even though the sediment layer is about twice as thick as the original relief. Basement topography has been subdued somewhat by preferential infilling of the abyssal valleys. Pits often occur along the edge of the ridge lines away from the location of Site U1338 (Moore et al., 2007). Good examples of pits lie just west of Line 5

¹Expedition 320/321 Scientists, 2010. Site U1338. In Pälike, H., Lyle, M., Nishi, H., Raffi, I., Gamage, K., Klaus, A., and the Expedition 320/321 Scientists, *Proc. IODP, 320/321*: Tokyo (Integrated Ocean Drilling Program Management International, Inc.).
doi:10.2204/iodp.proc.320321.110.2010

²Expedition 320/321 Scientists' addresses



at 2°30'N in Figure F1. Moore et al. (2007) attributed these features to a variety of processes that fracture the sediments and establish conduits for warm fluid flow from the basement, and Moore et al. (2007) hypothesized that sediments are partly dissolved by the fluid flow.

Based on stage-pole reconstructions of Pacific plate motion, observations of basement age from previous drilling, and magnetic maps (Cande et al., 1989) we determined Site U1338 to be located on ~18 Ma basement. During the AMAT-03 site survey we collected magnetic anomaly data that can be correlated to additional collated observations (Barckhausen et al., 2005; Engels et al., 2007) and can confirm the anomaly location.

The target equatorial interval of Site U1338, the middle and late Miocene, exhibits large changes in global temperature and major changes in equatorial Pacific plankton communities and carbon cycle. Large changes in the glaciation state and frequency have recently been found in the middle Miocene (Holbourn et al., 2005; Abels et al., 2005; Holbourn et al., 2007) in the interval between 14 and 16 Ma. There is a wide latitude range of calcium carbonate (CaCO₃) deposition during the earliest Neogene, with a relatively sharp transition to a narrower CaCO₃ belt after 20 Ma (Lyle, 2003). CaCO₃ mass accumulation rates in the central equatorial Pacific recovered from the 18–19 Ma “famine” and in the period between 14 and 16 Ma reached a second maximum in carbonate deposition, which is also evident in the seismic stratigraphy of the equatorial sediment bulge (Mitchell et al., 2003). The middle/late Miocene boundary interval is also marked by a significant increase in carbonate dissolution in the eastern Pacific.

The early/middle Miocene boundary interval is also the warmest interval in the Neogene, but it does not appear to have highly elevated atmospheric pCO₂ levels associated with it. Pagani et al. (1999) estimated by alkenones that atmospheric pCO₂ was near modern levels (~250 ppm CO₂), whereas more recently Kurschner et al. (2008) estimated by leaf stomata that the atmospheric pCO₂ level at 15.5 Ma was as high as 650–700 ppm. New sedimentary records are needed to study temperatures and greenhouse gas levels during this important warm interval, as well as to understand the role of the equatorial Pacific in the global carbon cycle.

Site U1338 should have crossed the equatorial region between 10 and 11 Ma and been within the equatorial zone (±2° of the Equator) between 3 and 18 Ma using the Koppers (2001) fixed hotspot stage-poles for Pacific plate motion. Site U1338 should have

been at the Equator during the major late Miocene diatom mat interval at Site U1337 (see “Lithostratigraphy” in the “Site U1337” chapter) (Kemp and Barron, 1993) when Site U1337 was located ~1° north of the Equator. We expected higher deposition of diatoms and perhaps larger diatom mat intervals at Site U1338 than at Site U1337 because it was nearer to the Equator.

Site U1338 is also the easternmost PEAT site and is nearest to the Americas. It has always been within the southeast tradewind belt and should have the highest deposition of windblown dust of all the PEAT sites. Changes in aluminosilicate deposition should reflect changes in wind strength and dust source aridity over the Miocene, Pliocene, and Pleistocene. Finally, we used wireline logging and physical property studies to groundtruth seismic stratigraphy for the equatorial Pacific and to determine how well the seismic stratigraphy at Site U1338 conforms to the central equatorial Pacific seismic stratigraphy of Mayer et al. (1985) (see “Downhole logging”).

Science summary

Site U1338 (proposed Site PEAT-8D; 2°30.469'N, 117°58.178'W; 4200 mbsl) (Figure F1; Table T1) was sited to collect a 3–18 Ma segment of the PEAT equatorial megasplite and is located on ~18 Ma crust just north of the Galapagos Fracture Zone, 324 nmi (600 km) southeast of Site U1337 (Fig. F1). A seamount (3.7 km water depth) with surrounding moat is found ~25 km north-northwest of Site U1338 at the downslope end of the survey area. Originally a site was chosen ~10 km from the seamount (proposed Site PEAT-8C). However, the alternate proposed site was selected and drilled uphill and further away from the seamount to avoid possible turbidites, as were found near seamounts during drilling of Expedition 320 Sites U1331 and U1335. The recovered sediment column at Site U1338 represents a nearly complete and continuous lower Miocene to Holocene sedimentary section.

Operations

Four holes were cored at Site U1338. From Hole U1338A, advanced piston corer (APC) cores were taken from the seafloor to 221.2 m drilling depth below seafloor (DSF) (Cores 321-U1338A-1H through 24H) using nonmagnetic core barrels and the FlexIt core orientation tool installed. FlexIt and steel core barrels were used for Cores 321-U1338A-25H and 26H. In addition, five successful advanced piston corer temperature tool (APCT-3) temperature measurements were taken with Cores 321-U1338A-5H,

7H, 9H, 11H, and 13H. Extended core barrel (XCB) coring continued with Cores 321-U1338A-27X through 44X. A small piece of basement was recovered in the core catcher of Core 321-U1338A-44X.

From Hole U1338B, APC cores were taken from the seafloor to 188.1 m DSF (Cores 321-U1338B-1H through 20H) except for a short drilled interval of 2.5 m from 235.6 to 238.1 m DSF to adjust the core breaks. Nonmagnetic core barrels and the FlexIt core orientation tool were used through Core 321-U1338B-20H. FlexIt and steel core barrels continued through Core 321-U1338B-42H to 387.4 m DSF. Coring continued with three XCB cores (321-U1338B-43X through 45X) to 416.1 m DSF. Basement contact was recovered in Core 321-U1338B-45X. Three logging strings (triple combination [triple combo], Formation MicroScanner [FMS]-Sonic, and Versatile Sonic Imager [VSI]) were deployed in Hole U1338B.

Hole U1338C was cored to recover sections that were missing from Holes U1338A and U1338B. APC cores were taken from the seafloor to 189.8 m DSF (Cores 321-U1338C-1H through 21H) using nonmagnetic core barrels and the FlexIt core orientation tool. FlexIt and steel core barrels were used through Core 321-U1338C-44H to 396.9 m DSF. Coring continued through Core 321-U1338C-47H to a total depth of 414.4 m DSF, which, at the time, set a new all time depth record for the APC.

Hole U1338D was primarily planned to recover a few “instructional” cores to be used during Expedition 323. Three APC cores were cut to 23.9 m DSF.

Lithostratigraphy

At Site U1338, ~415 m of nannofossil ooze and chalk with varying concentrations of diatoms and radiolarians overlie the seafloor basalt and are divided into three lithologic units (Fig. F3). Pleistocene through middle Pliocene sediments of Unit I are characterized by multicolored (various hues of white, brown, green, and gray) nannofossil ooze, diatom nannofossil ooze, and radiolarian nannofossil ooze that alternate on a decimeter to meter scale. Light green and light gray nannofossil ooze with occasional darker intervals with abundant siliceous microfossils, notably diatoms, comprise the upper Miocene to middle Pliocene Unit II. Decimeter-, meter- and tens of meters-scale color alternations in Units I and II are associated with variations in lithology and physical properties. Some of these color changes, as well as common millimeter- and centimeter-scale color banding, are not associated with compositional changes and likely reflect variations in sediment redox state. White, pale yellow, light greenish gray, and very pale brown nannofossil oozes and chalks dominate Unit III of

the lower to upper Miocene, although slightly darker green and gray intervals with larger amounts of siliceous microfossils remain present. Seafloor basalt (Unit IV) was recovered at the base of the sedimentary section, overlain by lower Miocene sediments.

Biostratigraphy

All major microfossil groups have been found in the ~415 m thick succession of Holocene to lower Miocene sediment bulge recovered from Site U1338. Calcareous nannofossils at Site U1338 are in general moderately preserved, but there are some intervals in which the preservation is good or poor. Nannofossil Zones NN4 to NN21 are present, indicating an apparently complete sequence. Planktonic foraminifers vary from rare to abundant, with moderate to good preservation throughout most of the succession, but are absent or rare in a short interval in the upper Miocene. Planktonic foraminifer Zones PT1b (upper Pleistocene) to M2 (lower Miocene) are documented, with the exception of Zones PL4, M12, and M6. The radiolarian stratigraphy spans the interval from the uppermost part of Zones RN16–RN17 (upper Pleistocene) to the uppermost part of Zone RN3 (lower Miocene). Radiolarian assemblages show good to moderate preservation except in the lowermost portion (lower Miocene), which is barren of radiolarians. The high resolution diatom stratigraphy spans the interval from the *Fragilariopsis (Pseudoemotia) doliolus* Zone (upper Pleistocene) to the lowermost part of the *Craspedodiscus elegans* Zone (lower Miocene). The diatom assemblage is generally well to moderately preserved throughout the recovered section; however, there are several intervals in which valve preservation becomes moderate to poor. The nannofossil, foraminifer, radiolarian, and diatom datums and zonal schemes generally agree, with some inconsistencies (Fig. F3). Benthic foraminifers occur continuously throughout the succession recovered in Hole U1338A and show generally good preservation. The overall assemblage composition indicates lower bathyal to abyssal paleodepths.

Stratigraphic correlation

Stratigraphic correlation provided a complete spliced record to a depth of ~260 m core composite depth below seafloor (CCSF-A) (see “Core composite depth scale” in the “Methods” chapter). Several gaps were seen between 280 and 360 m CCSF-A. Comparison of gamma ray attenuation (GRA) density records with well logging density data suggests that no more than 1 m of section was lost in any of the gaps. Correlation between the holes became difficult again several times between 435 m CCSF-A and

basement at 460 m CCSF-A. The growth factor for the correlation was 1.11. The linear sedimentation rate decreases from ~29 m/m.y. in the Miocene to 13 m/m.y. in the Pliocene–Pleistocene.

Paleomagnetism

Paleomagnetic measurements were conducted on archive-half sections of 26 APC cores from Hole U1338A, 42 APC cores from Hole U1338B, and 47 APC cores from Hole U1338C. The FlexIt core orientation tool was deployed in conjunction with all APC cores except for the deepest three cores of Hole U1338C, and we conclude that the FlexIt orientation data are generally reliable. Natural remanent magnetization (NRM) measurements indicate moderate magnetization intensities (on the order of 10^{-3} A/m) for depth intervals 0–50, 280–225, and 295–395 m core depth below seafloor (CSF). Polarity reversal sequences of these intervals are provisionally correlated to Chrons C1n to C2Ar (0 to ~4 Ma), Chrons C4An to C5n (~9–11 Ma), and Chrons C5r to C5Br (~12–16 Ma) of the geomagnetic polarity timescale (GPTS), respectively (Fig. F3). Except for these intervals, remanent magnetic intensities after alternating-field (AF) demagnetization of 20 mT are reduced to values close to magnetometer noise level in the shipboard environment ($\sim 2 \times 10^{-5}$ A/m). Magnetization directions are dispersed and not interpretable there.

Physical properties

A complete physical property program was conducted on whole cores, split cores, and discrete samples. Whole-Round Multisensor Core Logger (WRMSL) (GRA bulk density, magnetic susceptibility, *P*-wave velocity, and electrical noncontact resistivity), thermal conductivity, and natural gamma radiation (NGR) measurements comprised the whole-core measurements. Compressional wave velocity measurements on split cores and moisture and density (MAD) analyses on discrete core samples were made at a frequency of one per undisturbed section. Compressional wave velocities were measured toward the bottom of sections. MAD analyses were located 10 cm downsection from carbonate analyses (see “[Geochemistry](#)”). Lastly, the Section Half Multisensor Logger (SHMSL) was used to measure spectral reflectance on archive-half sections. Physical property measurements on whole-round sections and samples from split cores display a variation strongly dependent on the relative abundance of biosiliceous and calcareous sediment components at Site U1338. As at Site U1337, intervals enriched in siliceous microfossils and clay generally display darker colors, lower grain density and bulk density, and higher porosity, magnetic susceptibility, and NGR. The variation of

velocity is more complex in that it is dependent on both the wet bulk density and the sediment rigidity. These parameters vary independently with the variation in abundance of biosiliceous and calcareous components. The physical properties at Site U1338 also display cyclicity on multiple scales, a decimeter to meter scale and a scale with a spacing on the order of tens of meters.

Lithologic Unit I at Site U1338 is characterized by low wet bulk density that decreases from 1.4 g/cm³ near the seafloor to 1.2 g/cm³ at the base of the unit as a result of an increasing abundance of radiolarians and diatoms with depth. The grain density in Units I and II displays a greater variability than is found deeper at the site as a result of the greater variability in the abundance of biosiliceous and calcareous components. The average grain density for Units I and II is relatively low, at 2.59 g/cm³. The NGR signal at Site U1338 is characterized by a near-seafloor peak that is somewhat lower than those recorded at the other PEAT drill sites but extends deeper and is marked by a double peak. Spectral reflectance measurements show that Unit I is characterized by lower *L** and higher *a** and *b** values in the upper 25 m of Unit I (Fig. F3). Below 25 m CSF, the sediment becomes lighter colored (*L** increases) and more bluish green (*a** and *b** decrease).

Unit II is characterized by increasing wet bulk density with depth to ~175 m CSF. Below this depth, an increase in the abundance of siliceous microfossils produces a broad density minimum. Magnetic susceptibility and NGR signals are low in Unit II to the depth at which the biosiliceous material increases in abundance. The interval of the broad density minimum is characterized by higher magnetic susceptibility values that are roughly equal to those in the upper 25 m of Unit I. Unit II is lighter colored than Unit I (higher *L**) and more blue (lower *b**).

Unit III at Site U1338 is characterized by a higher and more uniform carbonate content and, as a result, more uniform physical properties. Wet bulk density increases from ~1.5 g/cm³ at the top of Unit III to 1.7 g/cm³ at the base of the unit. Grain density varies over a narrower range in Unit III than it does in Units I and II and displays an average (2.64 g/cm³) nearer to that of calcite. Velocity, which through much of Units I and II is close to the velocity of water, displays a regular increase in Unit III, from ~1620 m/s at the top to ~1820 m/s near the base of the unit. Velocity gradient increases near the base of Unit III accompanying the transition from nannofossil ooze to chalk. Magnetic susceptibility is low from the boundary between Units II and III, at ~245 m CSF, to 300 m CSF. Below 300 m CSF, susceptibility again increases to values comparable to those in the

upper part of Unit I. NGR variability is lower in Unit III than in Unit II and remains uniformly low throughout the unit. Overall, Unit III is the lightest colored (highest L^* values) unit at Site U1338. The transition from greenish gray to pale yellow is marked at ~385 m CSF by a shift to higher values of both a^* and b^* .

Downhole logging

Three downhole logging tool strings were deployed in Hole U1338B: a modified triple combo (that did not include a neutron porosity measurement), an FMS-sonic combination, and a VSI seismic tool with a Scintillation Gamma Ray (SGT-N) sonde. The modified triple combo and FMS-sonic tool strings took downhole measurements of natural gamma ray radioactivity, bulk density, electrical resistivity, elastic wave velocity, and borehole resistivity images in the 125–413 m wireline log depth below seafloor (WSF) depth interval. The VSI seismic tool string measured seismic waveforms in a vertical seismic profile (VSP) experiment that covered the 189.5–414.5 m WSF depth interval. Measurement depths were adjusted to match across different logging runs, obtaining the wireline log matched depth below seafloor (WMSF) depth scale.

Downhole log measurements were used to define three logging units: Unit I (139–244 m WMSF) and Unit II (244–380 m WMSF) have average densities of ~1.45 and ~1.6 g/cm³, respectively, that do not show any trend with depth, whereas in Unit III (from 380 m WMSF) density increases with depth, reaching 1.7 g/cm³ at the base of the hole (Fig. F4). Resistivity and P -wave velocity follow a pattern similar to that of density throughout the logged interval, suggesting that the major control on these physical properties are variations in sediment porosity. Both resistivity and density measurements show a small-scale peak at 280 m WMSF. This peak at 280 m WMSF is clearly visible in the borehole resistivity images as a high-resistivity layer 16 cm thick, and it corresponds to a chert layer that has only been recovered as rubble in the cores. Natural gamma ray measurements are low throughout (~4 gAPI) but do show a pronounced high at the seafloor caused by a local increase in uranium concentration.

In the VSP experiment, the arrival time of a seismic pulse was measured from the sea surface at 14 stations. Together with the traveltime to the seafloor, the VSP measurements are the basis for a traveltime-depth conversion that allows seismic reflectors to be correlated to stratigraphic events. Downhole temperature measurements and thermal conductivities of

core samples were combined to estimate a geothermal gradient of 34.4°C/km and a heat flow of 33.6 mW/m² at Site U1338.

Geochemistry

A standard shipboard suite of geochemical analyses of pore water and organic and inorganic sediment properties was undertaken on samples from Site U1338. Alkalinity increases slightly downhole from ~2.7 mM at the sediment/water interface to peak slightly above 4 mM at 140 m CSF. A large dissolved manganese peak of 150 mM at 10 m CSF is captured by the high-resolution interstitial water sampling and is remarkably similar to that observed at Site U1337. These peaks are >10 times larger than the highest dissolved manganese concentrations encountered during Expedition 320. Lithium concentrations decrease from ~26 μM at the surface to a minimum of ~3 μM at ~250 m CSF before increasing sharply with depth to seawater values at the base of the section. The interstitial water strontium profile is a mirror image to that of lithium except the decrease from the peak of 400 μM at 200 m CSF is punctuated by a sharp drop of >100 μM between ~260 and 290 m CSF. The lithium and strontium profiles indicate seawater circulation in the basement as their values tend toward seawater values near the basement.

Calcium carbonate contents range between 26 and 88 wt% with substantial variability in the upper 273.31 m CCSF-A, corresponding to the alternation between calcite and opal production in the upper two lithologic units. Below 273.31 m CCSF-A (lithologic Unit III), calcium carbonate contents become relatively high and stable between 66 and 91 wt% compared with the upper part of the stratigraphic column (Fig. F3). In the upper ~230 m CCSF-A, total organic carbon (TOC) content is generally high and variable ranging between 0.09 and 0.46 wt%, whereas below ~230 m CCSF-A, TOC content is <0.09 wt%. Downhole TOC variability is most likely related to lithologic changes, with higher TOC being found in the more biosiliceous intervals.

Interstitial water and bulk sediment geochemistry reflect large variations in sediment composition resulting from shifts between carbonate and opal dominance. The large-scale redox state and diagenetic processes of the sediment column are related to overall changes in sediment composition. Interstitial water chemistry points to seawater circulation in the basement, although the basement itself appears to exert little influence on the geochemistry of the sediments and interstitial waters.

Highlights

Color changes, lithology, and redox state

Smear slide analyses and visual core descriptions show that many of the decimeter-, meter-, and tens of meters-scale color variations in lithologic Units I and II to some extent relate to changes in lithology (e.g., Fig. F3). We suspect, however, that some of these color variations, notably the transitions between pale green and pale yellow lithologies, are controlled by sediment redox state, similar to those recorded at Sites U1331–U1337 and earlier work in the equatorial Pacific Ocean (e.g., Lyle, 1983).

Magnetic susceptibility is moderately low in the light gray and light brown intervals in Unit I (Fig. F3). A significant decrease in magnetic susceptibility in Unit II suggests dissolution of magnetite resulting from intensified microbial Fe reduction. In the lower part of Unit III, a sharp downcore transition from green to yellow is not associated with any other lithologic change, does not occur at the same stratigraphic level between holes, and thus should not be considered as an equivalent time horizon. Pore water Fe concentrations reach 6 to 7 μM in the green interval, and Fe is absent below the transition to yellow and brown. Although some of this signal may be affected by seawater contamination during XCB drilling, all available information suggests that the lowermost color change represents a redox front.

Occurrence of diatom-rich layers

Lithologic Unit II at Site U1338 is mainly composed of nannofossil ooze with relatively high abundances of biosiliceous components, notably diatoms (Fig. F3). The relative abundance of diatoms is lower than that at Site U1337, and the record lacks laminated diatom ooze intervals (diatom mats) such as those observed at Site U1337. However, centimeter to sometimes 1–2 m thick diatom nannofossil ooze layers containing abundant specimens of *Thalassiothrix* spp. are occasionally interbedded with nannofossil ooze (e.g., ~126.2–127.1 and ~231.8–234.3 m CSF in Hole U1338A and ~127.3–128.0 and ~233.8–234.8 m CSF in Hole U1338C). Units II and III also contain significant amounts of pyrite, particularly in diatom-rich intervals in Unit II (e.g., Cores 321-U1338B-14H, 19H through 21H, 26H, 28H, 29H, and 32H through 41H). In addition, the middle part of Unit III contains thin intervals of abundant pyrite-filled siliceous microfossils (e.g., intervals 321-U1338B-33H-4, 58–66 cm, and 35H-5, 76–82 cm). These diatom-rich layers, pyrite nodule occurrences, and pyrite-rich siliceous microfossil layers in Units II and III are associated with high TOC content, suggesting a relation between the

abundance of diatoms in the sediments, sediment redox state, and the export or preservation of organic carbon.

Operations

Unless otherwise noted, times are local ship time, which was Pacific Standard Time (Universal Time Coordinated [UTC] – 7 h).

Transit to Site U1338

The transit to Site U1338 (proposed Site PEAT-8D) began at 1625 h on 2 June 2009, after recovering all thrusters/hydrophones and shifting control to cruise mode on the bridge. The transit was uneventful. In relatively mild seas and moderate wind the vessel averaged 10.5 kt for the 324 nmi transit. Thrusters and hydrophones were lowered and at 2320 h on 3 June, and control was switched from bridge cruise mode to dynamic positioning mode.

Site U1338

As at the previous site, the position reference was a combination of the Global Positioning System and an acoustic beacon on the seafloor. At 0005 h on 4 June, the same positioning beacon (FSI BAP-547, SN 1010, 15.0 kHz, 208 dB) used on the previous site was deployed. Four holes were drilled at this site using the APC/XCB coring systems. The last hole (U1338D) was limited to only three cores to be used in the labs for processing demonstrations during the upcoming expedition. Hole U1338B was wireline logged using the triple combo, FMS-sonic, and VSI tool strings. The APCT-3 was deployed in Holes U1338A and U1338C. Overall recovery for Site U1338, using both APC and XCB coring systems, was 97%. Basement was recovered in two of the four holes drilled at the site.

Hole U1338A

Rig floor operations commenced at 2330 h on 3 June. The top drive was picked up, and the drill string was spaced out, placing the bit at 4196.0 m drilling depth below rig floor (DRF) or 3.4 m above the “corrected” precision depth recorder depth of 4199.4 m DRF. The first APC barrel recovered was empty, so the bit was lowered an additional 5.0 m to 4201.0 m DRF and another attempt for mudline was made. This time the barrel obviously contacted the mudline; however, the small amount of core recovered was completely destroyed by the sloshing of the water column above. For the third attempt, the bit was repositioned an additional 3.0 m lower at 4204.0 m DRF. This time the barrel recovered 2.7 m of core,

and an official seafloor depth was established at 4210.8 m DRF. APC coring continued through Core 24H to 221.2 m DSF using nonmagnetic coring assemblies and the FlexIt core orientation system. Overpull forces of 100,000 lb and the need to drill over the APC barrel led to the use of steel core barrels beginning with Core 25H. APC coring was eventually ended with Core 26H at 240.2 m DSF. All barrels fully stroked; however, the last three cores (24H through 26H) required 100,000 lb overpull and drill-over to extract from the formation. Five successful APCT-3 measurements were obtained with Cores 5H, 7H, 9H, 11H, and 13H at 40.7, 59.7, 78.7, 97.7, and 116.7 m DSF, respectively. Average core recovery for the APC was 105%. XCB coring continued with Cores 27X through 44X, achieving an average recovery of 56%. A small piece of basement was recovered in the core catcher of Core 44X, to a total depth of 4620.8 m DRF for Hole U1338A (410.0 m DSF). XCB coring performance was highly variable, with some cores achieving near 100% recovery and others recovering <1% and sometimes zero. In the areas of little or no recovery there were diatom-rich intervals and/or porcellanite (baby chert) found in the surrounding cores. Just as in the earlier holes at Site U1337, these proved to be the troublesome areas for recovery and were targeted in later Holes U1338B and U1338C in an attempt to complete recovery for the section. Overall recovery for Hole U1338A, using both APC and XCB coring systems, was 84%. The drill string was pulled clear of the seafloor at 1900 h on 6 June, officially ending operations in Hole U1338A.

Hole U1338B

Operations in Hole U1338B officially began when the drill string cleared the seafloor at 1900 h on 6 June. The drilling line was slipped and cut while the ship was offset 20 m west of Hole U1338A. With the drill bit placed at 4208.0 m DRF to optimize the core gaps between holes, the APC was deployed and once again a water core was recovered. After checking the drill string tally it was discovered that the driller was off by a single joint of drill pipe. This single was added to the string, and with the bit positioned at the same depth, Hole U1338B was spudded at 2330 h on 6 June. Core recovery with APC Core 1H determined the seafloor depth as 4209.9 m DRF. Except for a short drilled interval of 2.5 m to adjust the core breaks, continuous APC coring continued through Core 20H to 188.1 m DSF using the FlexIt core orientation system and nonmagnetic coring assemblies. FlexIt and steel core barrels were then used as APC coring continued through Core 42H to 387.4 m DSF. At the time of drilling, Hole U1338B was the second

deepest APC hole in ODP and IODP history, surpassing the 378.0 m DSF depth achieved during Expedition 320 in Hole U1335B. APC extraction overpull reached 100,000 lb on 19 of the 42 cores taken, including the last 11 APC cores. Full stroke was achieved on all but two cores (30H and 31H) from 276.1 to 282.9 m DSF. Coincidentally, the shear pressure for these two cores was inconclusive, so this may have been the reason for the incomplete stroke. Drillover was required on 13 cores, including the last 10. Except for Cores 30H and 31H, shear pressures were consistent throughout the coring process at 2800 psi. Core liner issues were relatively mild. The Core 1H liner was broken, the liner for Core 13H was cracked at the bottom, and the liner of Core 42H was recovered split. Average core recovery for the APC was 104%. Coring continued with three XCB cores (43X through 45X) to 416.1 m DSF. Basement was recovered in Core 45X. Overall the XCB coring system recovered 58% of the interval penetrated. Recovery was problematic with the XCB, and the material that was recovered suffered significantly from the typical “biscuiting” effect. Total depth of Hole U1338B was 4626.0 m DRF (416.1 m DSF). Overall core recovery using both APC and XCB coring systems was 101%. In preparation for downhole logging, the hole was swept clean with 50 bbl of attapulgitic mud. A wiper trip revealed no ledges or bridges, and no fill was identified at total depth. The lockable float valve was locked open, the hole was displaced with heavy 10.5 ppg logging mud, and the end of pipe was placed at 84.7 m DSF. Rig-up for wireline logging began at 2145 h on 9 June. Three logging strings were deployed. The triple combo and the FMS-sonic tool reached total hole depth of 416.1 m WSF. The third and final logging string consisted of the VSI. This tool reached total hole depth and shooting stations were conducted at ~15 m stations. All VSP logging was done during daylight hours to conform with established IODP mammal watch protocols, including a preshooting mammal watch and soft start procedures for the air guns. Wireline logging in Hole U1338B was successfully concluded and all logging equipment was rigged down by 1615 h on 11 June. The drill string was pulled back until the bit cleared the seafloor at 1655 h on 11 June, officially ending operations in Hole U1338B.

Hole U1338C

Operations in Hole U1338C officially began when the drill string cleared the seafloor at 1655 h on 11 June. The ship was offset 20 m to the west of Hole U1338B. The drilling line was slipped and cut and the Rigwatch drawworks/block position encoder was recalibrated. The drill bit was placed at 4204 m DRF

(same as Hole U1338A) to optimize the core gaps with respect to Holes U1338A and U1338B. The APC was deployed, and, for the third time at this site, a water core was recovered. Because 2.7 m of core had been recovered in Hole U1338A with the bit at the same depth, it was suspected that vessel heave, induced by a large long-period swell from the south, had impacted bit depth by being on the high side of the swell when the core was taken. The drill string was lowered another 3 m, and the bit was repositioned at 4207.0 m DRF. Hole U1338C was spudded at 2135 h on 11 June. The 3.83 m of core recovery with APC Core 1H determined the seafloor depth at 4212.7 m DRF. APC coring continued through Core 21H to 189.8 m DSF using the FlexIt core orientation system and nonmagnetic coring assemblies. FlexIt and steel core barrels were then used as APC coring continued through Core 44H to 396.9 m DSF. Core 45H appeared to fully stroke, and drillover was required to extract it from the formation. Retrieval was delayed because a bent core barrel initially prevented the core barrel from being pulled back up the drill string. Repeated jarring with the wireline jars eventually sheared the overshot pin. The sinker bar string was recovered, and the FlexIt core orientation tool was removed. The sinker bar assembly was redeployed, and the core barrel was immediately recovered without any further incident. It was deemed prudent at this point to not use the FlexIt tool for the remainder of coring. Coring continued through Core 47H to a total depth of 414.4 m DSF, at the time setting a new depth record for the APC. This surpassed the standing record set on 7 August 1992 (ODP Leg 145) when the APC penetrated to a total depth of 398.3 m DSF in Hole 882A. APC extraction overpull reached 100,000 lb on Cores 22H through 47H. Drillover prior to removal from the formation was required for 22 cores and full stroke was achieved on all but 4 cores (31H and 45H through 47H). Shear pressures were consistent throughout the coring process at 2800 psi. Core liner issues were relatively mild with only two cores recovered with imploded liners (Cores 10H and 12H), although several barrels were bent during the coring process and several piston rods had to be adjusted and repinned because of overtorqued threads that caused misalignment of the rod grooves. Overall core recovery for the APC was 104%. The drill string was pulled clear of the seafloor at 2015 h on 14 June, officially ending operations in Hole U1338C.

Hole U1338D

Operations in Hole U1338D officially began when the drill string cleared the seafloor at 2015 h on 14 June. The ship was offset 20 m to the west of Hole U1338C. This hole was primarily planned to recover

a few “instructional” lab demonstration cores to be used during Expedition 323 scientist orientation. Hole U1338D was spudded at 2150 h on 14 June, and the 4.89 m recovered with Core 1H established a seafloor depth of 4212.6 m DSF. Three APC cores were cut to 23.9 m DSF. APC core recovery was 104%. Official APC/XCB coring totals for Site U1338 include 139 total cores, 1261.9 m penetrated, and 1220.41 m recovered, for 97% recovery. The coring tools were secured and the drill string was pulled clear of the seafloor at 0145 h on 15 June. The top drive was set back, the knobby joints were laid out, and the drill string was recovered. Once the drill collars were laid out and the rig floor was secured for transit, control was transferred from dynamic positioning mode to the bridge. The ship was placed in cruise mode at 1030 h on 15 June for the anticipated 7.6 day (1811 nmi) transit to San Diego, California.

Transit to San Diego

The vessel departed Site U1338 ~4.5 h ahead of the projected schedule on a northerly course. The 1811 nmi transit from Site U1338 to the San Diego pilot station required 7.3 days at an average speed of 10.5 kt. Expedition 321, the second and final segment of the PEAT program, was officially concluded at 1715 h on 22 June with the first line ashore Berth 10-7 at the Tenth Avenue Marine Terminal, San Diego Harbor.

Lithostratigraphy

Drilling at Site U1338 recovered a ~415 m thick section of pelagic sediments overlying seafloor basalt (Fig. F5; Table T2). The sedimentary sequence is divided into three major lithologic units (Fig. F5; Table T3). Unit I (~50 m CSF; middle Pliocene to Pleistocene) consists of an alternating sequence of multicolored (including various hues of white, brown, green, and gray) nannofossil ooze, diatom nannofossil ooze, and radiolarian nannofossil ooze. Unit II (~194 m thick; upper Miocene to middle Pliocene) is mainly composed of light green and light gray nannofossil ooze with varying amounts of diatoms and radiolarians. Unit III (~171 m thick; lower to upper Miocene) predominantly consists of white, pale yellow, light greenish gray, and very pale brown nannofossil ooze and chalk, with generally low but sometimes common abundances of siliceous microfossils. Unit IV is composed of lower Miocene aphanitic basalt.

Lithologic units and boundaries are defined by changes in lithology, physical properties, color reflectance, and CaCO₃ content. Lithologic differences, based on both visual core description and

smear slide observations, are primarily attributable to varying amounts of biogenic components (nannofossils, diatoms, and radiolarians) (Fig. F6; see “Site U1338 smear slides” in “Core descriptions”). Lithologic descriptions are based on sediments recovered in Hole U1338B and supplemented with observations from Holes U1338A and U1338C. Three cores were recovered from Hole U1338D and were saved for instructional purposes during upcoming expeditions. No measurements were made on these cores during Expedition 321.

See “Corrected core composite depth scale” in the “Methods” chapter for an explanation of the CCSF-B depth scale.

Unit I

Intervals: 321-U1338A-1H-1, 0 cm, through 6H-7, 65 cm; 321-U1338B-1H-1, 0 cm, through 6H-4, 51 cm; 321-U1338C-1H-1, 0 cm, through 6H-5, 55 cm

Depths: Hole U1338A = 0–50.35 m CSF (0–55.91 m CCSF-A; 0–50.37 m CCSF-B); Hole U1338B = 0–50.61 m CSF (0–55.76 m CCSF-A; 0–50.23 m CCSF-B); Hole U1338C = 0–48.35 m CSF (0–55.96 m CCSF-A; 0–50.42 m CCSF-B)

Age: middle Pliocene to Pleistocene

Lithology: nannofossil ooze, calcareous nannofossil ooze, nannofossil calcareous ooze, diatom nannofossil ooze, and radiolarian nannofossil ooze

The major lithologies in Unit I are nannofossil ooze, calcareous nannofossil ooze, nannofossil calcareous ooze, diatom nannofossil ooze, and radiolarian nannofossil ooze (Figs. F6, F7A). Calcite grains, which are generally <5 μm in size, are relatively abundant in this unit.

Visual core descriptions and smear slide observations indicate that Unit I generally exhibits decimeter- to meter-scale cyclic alternations in color and lithology. Lighter colored sediments, such as white (e.g., 10YR 8/1 and N 8/), pale hues of brown (e.g., 10YR 8/2, 10YR 6/3, and 10YR 5/4), grayish brown (2.5Y 5/2), and lighter hues of gray (e.g., 10Y 7/1 and 5Y 6/2), are richer in nannofossils. Darker colored sediments, such as darker hues of brown (e.g., 2.5Y 5/3 and 10YR 7/4), greenish gray (e.g., 10Y 5/1), and darker hues of gray (e.g., 5Y 7/2 and N 4/), contain more siliceous microfossils. Alternations in lithology covary with physical properties, including magnetic susceptibility and b^* reflectance, as well as CaCO_3 weight percent (Fig. F5). Unit I shows higher amplitude variability in magnetic susceptibility and higher b^* reflectance values than underlying units. Sediments are intensely bioturbated and mottled.

The transition to Unit II (Fig. F8) is defined by the last downcore occurrence of gray (e.g., 10Y 5/1 and N 4/) sediments and the base of the interval of highly variable magnetic susceptibility and coincides with a significant downhole decrease in b^* and an increase in L^* reflectance.

Unit II

Intervals: 321-U1338A-6H-7, 65 cm, through 27X-3, 74 cm; 321-U1338B-6H-4, 51 cm, through 26H-5, 44 cm; 321-U1338C-6H-5, 55 cm, through 27H-6, 12 cm

Depths: Hole U1338A = 50.35–243.94 m CSF (55.91–271.72 m CCSF-A; 50.37–244.79 m CCSF-B); Hole U1338B = 50.61–244.54 m CSF (55.76–271.47 m CCSF-A; 50.23–244.57 m CCSF-B); Hole U1338C = 48.35–244.92 m CSF (55.96–271.73 m CCSF-A; 50.42–244.80 m CCSF-B)

Age: late Miocene to middle Pliocene

Lithology: nannofossil ooze, diatom nannofossil ooze, nannofossil diatom ooze, and radiolarian diatom ooze

The major lithologies in Unit II are alternating nannofossil ooze, diatom nannofossil ooze, nannofossil diatom ooze, and radiolarian diatom ooze (Figs. F6, F7B, F7C). Although sediments in Unit II generally consist of nannofossils, in some intervals diatoms and radiolarians are more abundant sedimentary components (Figs. F5, F6).

Unit II exhibits meter- to tens of meters-scale alternations in color and lithology. Lighter colored sediment, such as white (e.g., 2.5Y 8/1 and N 8/) and lighter hues of gray (e.g., 10Y 8/1, 5PB 8/1, 5BG 8/1, and 5Y 7/2), contains a high abundance of nannofossils. Sediment in darker hues of gray and green (e.g., 10Y 5/1, 5PB 6/1, 5Y 5/2, 2.5Y 5/1, and N 4/) is richer in siliceous microfossils. This unit is also characterized by occasional diatom nannofossil ooze layers (generally several centimeters thick and in some intervals 1–2 m thick; e.g., intervals 321-U1338A-15H-1, 0–95 cm, and 26H-1, 109 cm, to 26H-3, 84 cm), which contain abundant specimens of the diatom *Thalassiothrix* spp. interbedded with nannofossil ooze. However, laminated diatom ooze intervals (diatom mats), such as those observed in equivalent time intervals at Site U1337, are absent. Pyrite nodules, mainly found as centimeter-sized burrow casts, occasionally occur in Unit II. Color banding (e.g., light greenish gray, light gray, and light bluish gray) of millimeter to centimeter scale is common in all lithologies in Unit II.

Magnetic susceptibility is low throughout Unit II, apart from the lowermost 35 m. GRA bulk density, L^*

reflectance, CaCO₃ content, and TOC content are highly variable throughout the section (Figs. F5, F9), reflecting meter- to tens of meters-scale alternations between nannofossil ooze and diatom nannofossil ooze. Intervals of relatively high TOC concentrations reflect diatom-rich layers and contain abundant pyrite (Fig. F9). Bioturbation is intense throughout.

The transition to Unit III is defined as the base of the interval in which siliceous microfossils are a major sedimentary component and is associated with a significant downhole increase in GRA density and CaCO₃ content (Figs. F5, F10).

Unit III

Intervals: 321-U1338A-27X-3, 74 cm, through 44X-CC, 40 cm; 321-U1338B-26H-5, 44 cm, through 45H-CC, 48 cm; 321-U1338C-27H-6, 12 cm, through 47H-CC, 35 cm (base of hole)

Depths: Hole U1338A = 243.94–408.37 m CSF (271.72–453.43 m CCSF-A; 244.79–408.50 m CCSF-B); Hole U1338B = 244.54–414.94 m CSF (271.47–459.78 m CCSF-A; 244.57–414.22 m CCSF-B); Hole U1338C = 244.92–414.41 m CSF (271.73–455.28 m CCSF-A; 244.80–410.16 m CCSF-B, base of hole)

Age: early to late Miocene

Lithology: nannofossil ooze, nannofossil chalk, calcareous nannofossil chalk, calcareous radiolarian nannofossil chalk, radiolarian nannofossil chalk, nannofossil calcareous chalk, and calcareous chalk

The major lithologies in Unit III are nannofossil ooze, nannofossil chalk, calcareous nannofossil chalk, calcareous radiolarian nannofossil chalk, radiolarian nannofossil chalk, nannofossil calcareous chalk, and calcareous chalk (Figs. F6, F7D, F7E). Meter-scale lithologic alternations covary with color changes throughout the section: nannofossil oozes are white (N 8/) or light greenish gray (e.g., 10G 7/1 and 10GY 8/1), whereas increased abundances of siliceous microfossils are slightly darker greenish gray (5G 8/1 to 5G 6/1) and bluish gray (5PB 8/1 to 5PB 4/1) (Fig. F6). A minor lithology of light gray (2.5Y 7/2) nannofossil diatom ooze with opaques, containing abundant pyrite-filled siliceous microfossils, occurs in interval 321-U1338B-33H-4, 58–66 cm, at 297.54–297.62 m CSF, and in interval 35H-5, 76–82 cm, at 318.32–318.38 m CSF (Fig. F11). Accessories include regular millimeter-sized pyrite and manganese oxide grains; the latter are particularly abundant in the lowermost part of Unit III. Interval 321-U1338B-45X-6, 1–13 cm, contains a ground drilling slurry of black (10YR 2/1) manganese oxides. The transition from ooze to chalk occurs

between Cores 321-U1338B-41H and 42H at ~377.9 m CSF and at roughly equivalent depths in Hole U1338C between Cores 321-U1338C-43H and 44H at ~386.4 m CSF. This transition occurs at a shallower depth in the cores recovered from Hole U1338A (between Cores 321-U1338A-33X and 34X at ~307.3 m CSF), probably related to sediment disturbance (biscuits) associated with XCB drilling.

Drilling breccia of chert was recovered in Core 321-U1338B-31H (282.1–282.91 m CSF) and interval 321-U1338C-32H-1, 0–6 cm (282.90–282.96 m CSF). The thickness of the original chert interval is undeterminable from the cores because of poor recovery, but downhole logging indicates it is ~16 cm thick (see “Downhole measurements”). The chert interval hampered core recovery across this interval in all holes, but from composite section analysis the unrecovered sediment section is estimated to be <1 m thick (see “Stratigraphic correlation and composite section”).

A downhole sharp transition from light greenish gray (5G 7/1) to pale yellow (2.5Y 8/3) nannofossil ooze occurs at 386.72 m CSF in Hole U1338B (interval 321-U1338B-42H-6, 127 cm), at 382.72 m CSF in Hole U1338A (interval 321-U1338A-41X-CC, 25 cm), and at 391.73 m CSF in Hole U1338C (interval 321-U1338C-44H-3, 130 cm) (Fig. F12). In the lowermost part of Unit III, another downhole sharp transition from pale yellow to very pale brown sediments occurs at 405.94 m CSF in Hole U1338A (interval 321-U1338A-44X-3, 20 cm) and at 412.68 m CSF in Hole U1338C (interval 321-U1338C-47H-2, 67 cm), below which nannofossil chalks are very pale brown (10YR 6/4 and 10YR 8/3) (Fig. F12). Bioturbation is intense throughout Unit III. The transition to Unit IV is defined at the base of the sediment column, overlying basement.

Unit IV

Intervals: 321-U1338A-44X-CC, 40 cm, through 44X-CC, 48 cm; 321-U1338B-45X-CC, 48 cm, through 45X-CC, 53 cm

Depths: Hole U1338A = 408.37–408.45 m CSF (453.43–453.51 m CCSF-A; 408.50–408.58 m CCSF-B); Hole U1338B = 414.94–414.99 m CSF (459.78–459.83 m CCSF-A; 414.22–414.27 m CCSF-B)

Age: early Miocene

Lithology: aphanitic basalt

Aphanitic basalt fragments were recovered at the base of Holes U1338A and U1338B. Unit III nannofossil chalk overlies the basalt. Coring in Hole U1338C ceased before reaching basement.

Discussion

Color changes, lithology, and redox state

Smear slide analyses and visual core descriptions show that many of the decimeter-, meter-, and tens of meters-scale color variations in Units I and II to some extent relate to changes in lithology (e.g., Fig. F9). We suspect, however, that some of these color variations, notably the transitions between pale green and pale yellow lithologies, are controlled by sediment redox state similar to those recorded at Sites U1331–U1337 and earlier work in the equatorial Pacific (e.g., Lyle, 1983).

Magnetic susceptibility is relatively low in the light gray and light brown intervals in Unit I and for most of Unit II. A significant decrease in the intensity of the magnetic signal in Unit II suggests dissolution of magnetite (see “[Paleomagnetism](#)”), resulting from intensified microbial Fe reduction. In the lower part of Unit III, a sharp downhole transition from green to yellow is not associated with any lithologic change and does not occur at the same stratigraphic level between holes (see “[Stratigraphic correlation and composite section](#)”), and thus should not be considered as an equivalent time horizon (Fig. F12). Whereas pore water Fe concentrations reach 6–7 $\mu\text{M/L}$ in the green interval, it is absent below the transition to yellow and brown (see “[Geochemistry](#)”). Although some of this signal may be affected by seawater contamination during XCB drilling in Hole U1338A, all available information suggests that the lowermost color change represents a redox front.

Occurrence of diatom-rich layers

Unit II at Site U1338 is mainly composed of nannofossil ooze with relatively high abundances of biosiliceous components, notably diatoms (Figs. F5, F6). The relative abundance of diatoms is lower than that at Site U1337, and the record lacks laminated diatom ooze intervals (diatom mats) such as those observed at Site U1337. However, 1 cm to sometimes 1–2 m thick intervals of diatom nannofossil ooze containing abundant specimens of the diatom *Thalassiothrix* spp. are occasionally interbedded with nannofossil ooze (e.g., ~126.2–127.1 and ~231.8–234.3 m CSF in Hole U1338A and ~127.3–128.0 and ~233.8–234.8 m CSF in Hole U1338C) (Fig. F9). Units II and III also contain significant amounts of pyrite, particularly in diatom-rich intervals in Unit II (e.g., Cores 321-U1338B-14H, 19H–21H, 26H, 28H, 29H, and 32H–41H). In addition, the middle part of Unit III contains thin intervals of abundant pyrite-filled siliceous microfossils (e.g., intervals 321-U1338B-33H-4, 58–66 cm, and 35H-5, 76–82 cm) (Fig. F11). These diatom-rich layers, pyrite nodule

occurrences, and pyrite-rich siliceous microfossil layers in Units II and III are associated with higher TOC content (Figs. F9, F11), suggesting a relation between the abundance of diatoms in the sediments, sediment redox state, and the production or preservation of organic carbon.

Summary

At Site U1338, ~415 m of nannofossil ooze and chalk with varying concentrations of diatoms and radiolarians overlie early Miocene seafloor basalt and are divided into three lithologic units. Unit I Pleistocene through middle Pliocene sediments are characterized by multicolored (various hues of white, brown, green, and gray) nannofossil ooze, diatom nannofossil ooze, and radiolarian nannofossil ooze that alternate on decimeter to meter scales. Light green and light gray nannofossil ooze with occasional darker intervals with abundant siliceous microfossils, notably diatoms, comprise the upper Miocene to middle Pliocene Unit II. Decimeter-, meter-, and tens of meters-scale color alternations in Units I and II are associated with variations in lithology and physical properties. Some of these color changes, as well as common millimeter- and centimeter-scale color banding, are not associated with compositional changes and likely reflect variations in sediment redox state. White, pale yellow, light greenish gray, and very pale brown nannofossil oozes and chinks dominate Unit III of the lower to upper Miocene, although slightly darker green and gray intervals with larger amounts of siliceous microfossils remain present. Lower Miocene seafloor basalt (Unit IV) was recovered at the base of the sedimentary section.

Biostratigraphy

At Site U1338, a ~415 m thick succession of Holocene to lower Miocene sediments was recovered. Calcareous nannofossils at Site U1338 are in general moderately preserved, but in some intervals the preservation is good or poor. Nannofossil Zones NN21 to NN4 are present, indicating an apparently complete sequence. Planktonic foraminifers vary from rare to abundant, with moderate to good preservation throughout most of the succession, but are absent or rare in the interval from Sample 321-U1338A-22H-5, 41–43 cm, to 24H-CC. Planktonic foraminifer Subzone PT1b (upper Pleistocene) to Zone M2 (lower Miocene) are documented, with the exception of Zones PL4, M12, and M6. Radiolarian stratigraphy spans the interval from the uppermost part of Zone RN16–RN17 (upper Pleistocene) to the uppermost part of Zone RN3 (lower Miocene). Radiolarian as-

semblages show good to moderate preservation except in the lowermost portion (lower Miocene), which is barren of radiolarians. High-resolution diatom stratigraphy spans the interval from the *Fragilariopsis (Pseudoeunotia) doliolus* Zone (upper Pleistocene) to the lowermost part of the *Craspedodiscus elegans* Zone (lower Miocene). The diatom assemblage is generally well to moderately preserved throughout the recovered section; however, there are several intervals in which valve preservation becomes moderate to poor. The nannofossil, foraminifer, radiolarian, and diatom datums and zonal schemes generally agree, with some minor inconsistencies. The integrated calcareous and siliceous microfossil biozonation is shown in Figure F13. An age-depth plot including biostratigraphic and paleomagnetic datums is shown in Figure F14. Benthic foraminifers occur continuously throughout the succession recovered in Hole U1338A and show generally good preservation. The overall assemblage composition indicates lower bathyal to abyssal paleodepths. Marked variations in downcore abundance and species distribution may reflect major changes in global climate linked to fluctuations in ice volume and reorganization of Pacific Ocean circulation during the Neogene.

Calcareous nannofossils

Calcareous nannofossil biostratigraphy indicates that a continuous sediment sequence was recovered at Site U1338. Zones NN20–NN21 through lower NN4 are recognized in all three holes cored (Table T4). Calcareous nannofossil biostratigraphic markers are often determined to ± 0.75 m in all three holes. The oldest biostratigraphic marker observed is the first occurrence of common *Sphenolithus heteromorphus* at 403.2 ± 0.4 m CSF in Hole U1338A, ~ 5 m above the sediment/basalt contact. Zones NN15 through NN13 are not differentiated. The Zone NN8/NN9 boundary is readily recognized by the first occurrence of *Discoaster hamatus*, but the base of Zone NN8 is poorly constrained because of discontinuous and exceptionally rare occurrences of members of the genus *Catinaster*. Similarly, the base of Zone NN5 is poorly constrained because of discontinuous and rare occurrences of *Helicosphaera ampliaptera*.

Calcareous nannofossils generally make up between 50% and 90% of the biogenic particles in the smear slides investigated. Exceptions include: (1) the uppermost 12–13 m of the sediment sequence where nannofossils are dominant ($>90\%$ of the fossils) and (2) a biosilica-rich interval around the middle/late Miocene boundary where nannofossils are less abundant and make up $\sim 10\%$ – 50% of the biogenic particles in several samples. Preservation follows abun-

dances, with good preservation in the uppermost 12–13 m where nannofossils dominate, moderate preservation in the majority of samples investigated, variable preservation in the interval with biosilica-rich sediments, and generally poor preservation in the chalks of Zone NN4. Members of the genus *Discoaster* vary markedly in terms of composition and abundance. Their preservation is often good in the more dissolved samples. Many of the morphotypes observed have been grouped under the *Discoaster variabilis* concept, although it is likely that several species are included in this group. Discoasters in upper Miocene sediments exhibit large morphologic variability and taxonomic diversity, which is only partially resolved at the species level here. Middle and lower Miocene discoasters are generally made indistinct by overgrowth of secondary calcite. Abundances of all calcareous nannofossil taxa and preservation of samples are summarized in range chart format from Hole U1338A, including a few samples from Hole U1338B, in Table T5.

Pleistocene sediments are recognized by a series of extinctions, from top to bottom: *Pseudoemiliania lacunosa*, *Reticulofenestra asanoi*, *Gephyrocapsa* spp. >5.5 μm , and *Calcidiscus macintyreii*. The Pleistocene assemblages are partly characterized by a complete dominance of small geophyrocapsids (<3 μm), for example in Samples 321-U1338A-2H-2, 24 cm, and 2H-5, 120 cm, outnumbering other taxa by at least an order of magnitude. The undifferentiated Zones NN20/NN21 are only recognized in Sample 321-U1338A-1H-CC.

Pliocene bioevents include the extinctions of *Discoaster brouweri* (top Zone NN18), *Discoaster pentaradiatus* (top Zone NN17), *Discoaster surculus* (top Zone NN16), *Sphenolithus abies*, and *Reticulofenestra pseudoumbilicus* (top Zone NN15). *D. pentaradiatus* and *D. surculus* disappear together in the 2 m sample distance used in the pertinent interval, thereby eliminating Zone NN17. The latter species has a more distinct last occurrence. *D. pentaradiatus* is continuously present only in a ~ 40 m long interval across the Miocene/Pliocene boundary and shows discontinuous occurrences in middle Pliocene and lower upper Miocene sediments. Some lower Pliocene samples (e.g., Sample 321-U1338A-7H-CC) contain quite large (>15 μm) specimens of *D. pentaradiatus*. The onset of abundant *Discoaster triradiatus* is observed in Section 321-U1338C-4H-1.

Sample 321-U1338A-7H-CC contains a nannolith that resembles transitional forms between the middle Miocene *Discoaster micros* and *Catinaster* spp. The lower Pliocene morphotypes in Core 321-U1338A-7H are likely indigenous, as neither *D. micros* nor *Catinaster* spp. occur in any corresponding abun-

dance in lower upper Miocene sediments, nor is there evidence of lower upper Miocene nannofossil reworking. *Discoaster altus* is also present in these lower Pliocene sediments. A lack of *R. pseudoumbilicus* is observed in a few samples at the Miocene/Pliocene boundary (upper interval of Core 321-U1338A-9H, lower interval of Core 8H). A longer interval in upper Miocene sediments also shows a paracme episode of this species (Sections 321-U1338A-16H-4 through 20H-3). The underlying reason(s) causing these two paracme intervals is probably similar.

Zone NN11 is 75 m thick in the interval between the extinction of *Discoaster quinqueramus* in Sample 321-U1338A-10H-3, 70 cm, and the appearance of *Discoaster berggrenii* in Sample 321-U1338A-18H-3, 65 cm, suggesting an average late Miocene sedimentation rate of 27.5 m/m.y. Assemblages in Zone NN11 are moderately preserved, with abundant nannofossils. Bioevents observed within this zone include the top and basal occurrence of *Nicklithus amplificus*, the top of the paracme interval of *R. pseudoumbilicus*, and the base of *Amaurolithus* spp. Members of the genus *Discoaster* are generally well preserved and richly represented in these upper Miocene sediments. Several different morphotypes are grouped in a broadly applied *D. variabilis* concept, implying that the taxonomic diversity of late Miocene discoasters is not fully resolved in this report.

Samples from the base of Core 321-U1338A-19H and the top of Core 20H have moderate to good preservation and are dominated by *Dictyococcites* spp. <3 µm and small *Sphenolithus* specimens. These assemblages have few discoasters and reticulofenestrads, common calcidiscids, and no dictyococcitids or reticulofenestrads >5 µm. The onset of the paracme interval of *R. pseudoumbilicus* occurs over <1.5 m in lower Core 321-U1338A-20H. The silica content increases downhole from Cores 321-U1338A-20H to 25H, but in general nannofossils are abundant and moderately preserved. In this lower upper Miocene interval, *Discoaster* diversity and abundance increases with several species of five- and six-rayed forms present, whereas the placolith assemblage composition and diversity remains constant. Zone NN9 is placed between Samples 321-U1338A-22H-4, 80 cm, and 25H-1, 80 cm, defined by the total range of *D. hamatus*. The stratigraphically highest occurrence of *Coccolithus miopelagicus* is observed from just below the base of *D. hamatus*, similar to that observed at Site U1337 (see “[Biostratigraphy](#)” in the “Site U1337” chapter for discussion). A few specimens of *Catinaster coalitus* are observed in Core 321-U1338A-25H, indicating an age not older than Zone NN8 for this core. Extensive searches for *Catinaster* spp. in corresponding cores from Holes U1338B and U1338C re-

inforced the initial findings from Hole U1338A, which were that members of this genus occur only sporadically in the occasional sample. This absence is likely not caused by selective calcite dissolution, judging from the abundant occurrences of other calcareous nannofossils such as discoasters, various placoliths, sphenoliths, and umbilicosphaerids. Catinasters occur abundantly in sediments of coeval age at ODP Site 926 in the western Atlantic Ocean (Backman and Raffi, 1997) at a time when Atlantic and Pacific Ocean surface waters were connected by the Central American seaway (Keigwin, 1978). The similar positions of Site 926 (3°43'N) and Site U1338 (2°30'N) with respect to latitude suggests that temperatures in the photic zone were similar at the two near-equatorial sites. Some other factor was involved that resulted in the ecological exclusion of catinasters from the calcareous nannoplankton assemblages at Site U1338. A clue is provided by the absence of diatoms at Site 926 and the high abundance of this group at Site U1338, which may suggest that catinasters occupied the same ecological niche as the prolific diatoms and simply were outcompeted.

The preservation in Cores 321-U1338A-26H and 27X varies from poor to good depending upon the amount of silica present. An assemblage in lower Core 321-U1338A-27X is characterized by abundant to dominant small placolith species and few discoasters. Core 321-U1338A-28X had only 2% recovery, and the top of common *Discoaster kugleri* occurs in the missing interval. In Hole U1338B, the top of common *D. kugleri* occurs between Samples 321-U1338B-27H-2, 80 cm, and 28H-1, 80 cm, but this datum cannot be resolved further in this hole because of severe core disturbance (flow-in) from interval 321-U1338B-27H-2, 100 cm, to Sample 321-U1338B-27H-CC (see “[Lithostratigraphy](#)”). The best constrained determination of the top of *D. kugleri* is from Hole U1338C, where it is placed to within ±0.26 m. The first appearance of common *D. kugleri* (Zone NN6/NN7 boundary) occurs at the base of Core 321-U1338A-29X, which corresponds to Core 321-U1338B-29H. The poor recovery in Cores 321-U1338A-30X (1%) and 31X (5%) implies that datums correlated to upper Zone NN6 are lost in the unrecovered intervals. These datums are, however, determined in Hole U1338B. The extinctions of *Cycliscardiolithus floridanus* and *Coronocyclus nitescens*, separated by only 80 k.y., both occur between Samples 321-U1338B-29H-2, 80 cm, and 29H-3, 80 cm. The top of *Calcidiscus premacintyreii* occurs ~3 m further downcore.

Sediment from Zone NN6 (Cores 321-U1338A-30X through 35X) contains abundant moderately preserved nannofossils, but pervasive overgrowth is

present throughout, making discoasters difficult to identify. The top of common *C. floridanus* is placed at the base of Core 321-U1338A-34X. Several changes in the *Triquetrorhabdulus* lineage occur in Zone NN6 (Fig. F15). The species present in Zones NN4 and NN5 are *Triquetrorhabdulus milowii* and *Orthorhabdus serratus*, the latter of which has a sporadic presence. The evolutionary appearance of *Triquetrorhabdulus rioi* is observed at the base of Zone NN6 (Sample 321-U1338A-34X-CC). This taxon has a continuous presence throughout Zone NN6 and has a frequent to common abundance. *Orthorhabdus serratus* has an elevated abundance throughout the samples from Zone NN6, whereas *T. milowii* gradually decreases in its occurrence toward the top of Zone NN6. The first common occurrence of *Triquetrorhabdulus rugosus* occurs in Sample 321-U1338B-29H-4, 80 cm. Below this sample *T. rugosus* is rare in Zone NN6. Both *T. rioi* and *T. rugosus* have a notable first common occurrence, which was also observed by Raffi et al. (1995), potentially making these events useful biostratigraphic datums.

The stratigraphically highest occurrence of *S. heteromorphus* occurs in Sample 321-U1338A-35X-CC, marking the Zone NN5/NN6 boundary. Cores 321-U1338A-35X through 37X all had minimal recovery (1%–3%). The assemblages observed in the core catchers tend to be diverse and overgrown. The extinction of *H. ampliaperta*, which defines the Zone NN4/NN5 boundary, is difficult to recognize because the marker is rare, with a handful of specimens observed in only four samples (Table T5). A single etched specimen of *H. ampliaperta*, which may possibly be reworked, is observed in Sample 321-U1338A-38X-CC. The top of common *D. deflandrei* and the base of *Discoaster petaliformis*, referred to as *Discoaster signus* in Bukry (1971), occur with a short overlap (<2.8 m). These two events are only 34 k.y. apart in the western equatorial Atlantic Ocean (Raffi et al., 2006). The base of Hole U1338A (Cores 321-U1338A-40X through 44X) contains carbonate-rich sediment with abundant nannofossils. The preservation in this interval is poor with extensive overgrowth. Despite the preservational state, nannofossil assemblages are diverse and contain multiple species of *Helicosphaera* and *Scyphosphaera*. The base of common *S. heteromorphus* is in Core 321-U1338A-44X, located 5 m above the sediment/basalt contact. At a sedimentation rate of 20 m/m.y., this makes the basement age 17.96 Ma (0.25 m.y. older than the base of common *S. heteromorphus*).

Radiolarians

High-resolution radiolarian biostratigraphy at Site U1338 was performed on core catchers and addi-

tional samples (mostly two per core) from Hole U1338A. Six samples from Cores 321-U1338B-27H through 30H were also used because the corresponding interval was not recovered in Hole U1338A.

The radiolarian stratigraphy at Site U1338 (Table T6) spans the interval from Zones RN16–RN17 (upper Pleistocene) to RN3 (lower Miocene) (Fig. F13). Below Sample 321-U1338A-44X-2, 44–46 cm (uppermost portion of Zone RN3), sediments are barren of radiolarians. Assemblages tend to show good to moderate preservation. Upper upper Miocene to lowermost Pleistocene sediments contain rare reworked radiolarian individuals from the early to middle Miocene. Abundances of all radiolarian taxa and preservation of samples are summarized in Tables T7 and T8.

The top of Hole U1338A corresponds to Zone RN16–RN17 (Pleistocene). The base of Zone RN16–RN17 is placed between Samples 321-U1338A-1H-CC and 2H-2, 67–69 cm, as indicated by the top of *Stylatractus universus*. The base of *Collosphaera tuberosa*, which indicates the boundary between Zones RN15 and RN14, also occurs in the same interval. The top of *Anthocyrtidium angulae* occurs between Samples 321-U1338A-2H-5, 110–112 cm, and 2H-CC, marking the base of Zone RN14.

The top of *Theocyrtidium vetulum* is between Samples 321-U1338A-2H-5, 110–112 cm, and 2H-CC. The last occurrence of *Lamprocyrtis heteroporos* and the first occurrences of *Theocyrtidium tracherium* and *A. angulae* are both distinguished between Samples 321-U1338A-3H-2, 67–69 cm, and 3H-5, 110–112 cm. The top of *Pterocanium prismaticum* occurs between Samples 321-U1338A-3H-5, 110–112 cm, and 3H-CC and defines the base of Zone RN13. The top of *Didymocyrtis avita* is recognized between Samples 321-U1338A-4H-4, 34–36 cm, and 4H-CC. The top of *Stichocorys peregrina* is observed between Samples 321-U1338A-4H-CC and 5H-2, 123–124 cm, marking the boundary between Zones RN12 and RN11. The base of *L. heteroporos* is distinguished between Samples 321-U1338A-5H-2, 123–124 cm, and 5H-4, 50–51 cm. The range of *Lamprocyrtis neoheteroporos* and top of *Anthocyrtidium pliocenica* are not determined because of their sporadic and discontinuous occurrence in Hole U1338A.

The top of *Phormostichoartus fistula* is recognized between Samples 321-U1338A-5H-4, 50–51 cm, and 5H-CC and defines the boundary between Subzones RN11b and RN11a. Both the top of *Spongaster pentas* and top of *Phormostichoartus doliolum* are observed between Samples 321-U1338A-6H-3, 131–133 cm, and 6H-5, 131–133 cm. The latter datum marks the top of Zone RN10. The base of *Amphirhopalum ypsilon* is observed between Samples 321-U1338A-6H-5,

131–133 cm, and 6H-CC. The top of *Spongaster tetras* is between Samples 321-U1338A-6H-CC and 7H-2, 47–49 cm.

The top of Zone RN9 is indicated by the base of *Didymocyrtis penultima*, which occurs between Samples 321-U1338A-6H-CC and 7H-2, 47–49 cm. The base of *Pterocanium prismaticum* is recognized between Samples 321-U1338A-7H-2, 47–49 cm, and 7H-4, 52–54 cm. The top of *Spongaster berminghami* is observed between Samples 321-U1338A-8H-CC and 9H-3, 14–16 cm. The lowermost occurrences of *Didymocyrtis avita* and *S. pentas* and the top of *Didymocyrtis antipenultima* are distinguished between Samples 321-U1338A-10H-6, 118–120 cm, and 10H-CC. The base of *Didymocyrtis tetrathalamus* is between Samples 321-U1338A-10H-CC and 11H-3, 110–112 cm. The top of *Stichocorys delmontensis* is observed between Samples 321-U1338A-11H-3, 110–112 cm, and 11H-5, 73–75 cm. The range of *Lychnodictyum anossa* is not clearly distinguished in Hole U1338A because of the sparse occurrence of this species.

The evolutionary transition from *S. delmontensis* to *S. peregrina*, which defines the boundary between Zones RN9 and RN8, occurs between Samples 321-U1338A-14H-CC and 15H-2, 48–50 cm. The base occurrence of *T. vetulum* is located between Samples 321-U1338A-15H-2, 48–50 cm, and 15H-4, 97–99 cm. The range of *Solenosphaera omnitubus* is not clearly distinguished in Hole U1338A because of its rare occurrence.

The top of *Diartus hughesi* is between Samples 321-U1338A-17H-CC and 18H-2, 68–70 cm. The boundary between Zones RN8 and RN7 is distinguished at this level. The top of *Didymocyrtis laticonus* also occurs between these two samples. The base of *D. penultima* and the top of *Botryostrobus miralestensis* are recorded between Samples 321-U1338A-20H-3, 13–15 cm, and 20H-5, 11–13 cm. The base of *S. berminghami* is between Samples 321-U1338A-20H-5, 11–13 cm, and 20H-CC.

The top of Zone RN6 is marked by the evolutionary transition of *Diartus pettersoni* to *D. hughesi* between Samples 321-U1338A-20H-5, 11–13 cm, and 20H-CC. The top of *Stichocorys wolffii* was not clearly observed in Site U1338 because of its sparse presence. The base of *D. hughesi* is recognized between Samples 321-U1338A-20H-CC and 21H-2, 42–44 cm. The base of *D. antipenultima* is observed between Samples 321-U1338A-22H-5, 53–55 cm, and 22H-CC. The top of *Cyrtocapsa japonica* is distinguished between Samples 321-U1338A-23H-5, 108–110 cm, and 23H-CC. The top events of both *Carpocanopsis cristata* and *Lithopera neotera* are observed between Samples 321-U1338A-24H-2, 42–44 cm, and 24H-5, 133–135 cm.

The top occurrences of *Cyrtocapsa cornuta*, *Cyrtocapsa tetrapera*, and *Lithopera renzae* are all located between Samples 321-U1338A-29X-4, 24–26 cm, and 29X-CC.

The base of *D. pettersoni* occurs between Samples 321-U1338A-31X-CC and 32X-2, 83–85 cm, indicating the top of Zone RN5. The base of *L. neotera* is located between Samples 321-U1338A-35X-CC and 36X-1, 29–31 cm. The top of *Calocycletta robusta* is between Samples 321-U1338A-35X-CC and 36X-1, 29–31. Top occurrences of *Acrocubus octopyle*, *Liriospyris parkerae*, and *Didymocyrtis mammifera* are between Samples 321-U1338A-36X-CC and 37X-1, 37–39 cm. Between Samples 321-U1338A-37X-CC and 38X-2, 35–37 cm, top occurrences of *Didymocyrtis violina*, *Calocycletta virginis*, and *Calocycletta costata* are observed. Top events of *Carpocanopsis bramlettei* and *Didymocyrtis tubaria* are distinguished between Samples 321-U1338A-39X-2, 75–78 cm, and 39X-5, 87–89 cm.

The Zone RN5/R4 boundary, defined by the evolutionary transition from *Dorcadospyris dentata* to *Dorcadospyris alata*, is recognized between Samples 321-U1338A-39X-CC and 40X-1, 103–105 cm. The top occurrence of *Liriospyris stauropora* is recognized between Samples 321-U1338A-40X-1, 103–105 cm, and 40X-3, 27–29 cm. The base of *L. parkerae* is distinguished between Samples 321-U1338A-41X-4, 22–24 cm, and 41X-CC. The top of *Carpocanopsios cingulata* is observed between Samples 321-U1338A-41X-CC and 42X-2, 46–48 cm. The base of *Acrocubus octopylus* is between Samples 321-U1338A-42X-4, 100–102 cm, and 42X-CC. The base of Zone RN4 is identified by the base of *C. costata*, recognized between Samples 321-U1338A-43X-2, 63–64 cm, and 43X-CC.

Diatoms

High-resolution biostratigraphy was performed on core catcher and additional samples from Hole U1338A. The diatom stratigraphy at Site U1338 spans the interval from the *Fragilariopsis doliolus* Zone (late Pleistocene) in Core 321-U1338A-1H (Sample 321-U1338A-1H-CC) to the lowermost part of the *Cestodiscus peplum* Zone (early Miocene) in the lower part of Core 321-U1338A-42X (Sample 321-U1338A-42X-CC) (Fig. F13; Tables T9, T10). Diatoms are, in general, moderately preserved in the upper 315 m CSF of Site U1338 (Samples 321-U1338A-1H-1, 98–100 cm, through 34X-6, 80 cm; Pleistocene to middle Miocene) and poorly preserved below 316 m CSF (Samples 321-U1338A-34X-CC through 42X-CC; middle Miocene) (Table T10). This decrease in preservation is not clearly associated with any particular lithologic observation, such as the occurrence of turbidites, nor is it associated with reworking of older

microfossils. The diverse diatom assemblage is composed of 110 species (Table T10) and, as already described for Site U1337, mainly consists of Neogene species typical of the low-latitude eastern equatorial Pacific Ocean, including *Actinocyclus ellipticus*, several species of *Azpeitia* and *Coscinodiscus*, *Nitzschia porteri*, *Fragilariopsis reinholdii*, a few varieties of *Thalassionema nitzschioides*, and several species of *Thalassiosira* and *Thalassiothrix* (Table T10).

The topmost Sample 321-U1338A-1H-1, 98–100 cm, is assigned to the Pleistocene *F. doliolus* Zone. Samples 321-U1338A-1H-CC through 2H-CC are within the diatom *F. reinholdii* Zone. The majority of the Pliocene section at Site U1338A is divided into the *Rhizosolenia praebergonii* and *Nitzschia jouseae* Zones (Fig. F13). The boundary between the *R. praebergonii* and *F. reinholdii* Zones is based on the base occurrence of *F. doliolus* and the top occurrence of *R. praebergonii*. The *R. praebergonii* Zone extends between Samples 321-U1338A-3H-1, 90 cm, and 6H-1, 40 cm. A secondary diatom event in this interval is the top occurrence of *N. jouseae* in Sample 321-U1338A-4H-CC. The *N. jouseae* Zone is tentatively defined as the stratigraphic interval from the top *Actinocyclus ellipticus* f. *lanceolata* in Sample 321-U1338A-7H-3, 55 cm, and the base occurrence of *N. jouseae* in Sample 321-U1338A-9H-CC. An additional stratigraphic event observed in this zone is the top occurrence of *Fragilariopsis cylindrica* (Sample 321-U1338A-9H-6, 110–111 cm).

The expanded Miocene section at Site U1338 is stratigraphically better constrained by diatoms than at Site U1337. The base occurrence of *N. jouseae* in Sample 321-U1338A-9H-CC defines the top boundary of the *Thalassiosira convexa* Zone. The lower boundary of the *T. convexa* Zone is tentatively assigned between Samples 321-U1338A-12H-4, 63–64 cm, and 12H-CC, below the top occurrence of *Thalassiosira praeconvexa*. The late Miocene *Nitzschia miocenica* Zone records the base occurrences of *T. convexa* in Sample 321-U1338A-14H-4, 38–39 cm, *T. praeconvexa* in Sample 321-U1338A-14H-CC, and *Nitzschia miocenica* in Sample 321-U1338A-17H-1, 95 cm.

Samples 321-U1338A-17H-4, 55 cm, through 19H-5, 70 cm, are placed in the *N. porteri* Zone. This zonal placement is based on the top occurrences of *Rossiella paleacea* in Sample 321-U1338A-17H-5, 55 cm, and *Thalassiosira yabei* in Sample 321-U1338A-19H-5, 70 cm. A secondary datum event in the *N. porteri* Zone is the top occurrence of *Thalassiosira burckliana* (Sample 321-U1338A-18H-3, 65 cm). The *N. porteri*/*T. yabei* Zone boundary occurs between Samples 321-U1338A-19H-5, 70 cm, and 19H-6, 70 cm, below the top of *T. yabei*. The lower boundary of the *T. yabei* Zone is tentatively assigned to the top

occurrence of *Actinocyclus moronensis* in Samples 321-U1338A-23H-CC and 29H-2, 3–31 cm. The base of *A. ellipticus* f. *lanceolata* defines the *A. moronensis* Zone. The base boundary of the *A. moronensis* Zone is tentatively allocated between Samples 321-U1338A-25-CC and 26H-2, 25–26 cm. As discussed for Site U1337, the problematic differentiation of the *A. moronensis* Zone suggests the low biostratigraphic potential of this diatom for the eastern equatorial Pacific Ocean (Baldauf and Iwai, 1995).

The *Craspedodiscus coscinodiscus* Zone represents the interval between Samples 321-U1338A-26H-2, 25–26 cm, and 30X-CC. Stratigraphic events in this zone are the base occurrences of *Hemidiscus cuneiformis* (Sample 321-U1338A-26H-CC) and *Thalassiosira brunii* (Sample 321-U1338A-27X-CC), as well as the top occurrences of *Cestodiscus pulchellus* (Sample 321-U1338A-29X-CC), and *N. porteri* (Sample 321-U1338A-30X-CC). The *Coscinodiscus gigas* var. *di-orama* Zone is placed in Core 321-U1338A-31X.

Samples 321-U1338A-32X-CC through 35X-2, 80 cm, are assigned to the *Coscinodiscus lewisianus* Zone. This zonal placement is based on the top of *C. lewisianus* in Sample 321-U1338A-31X-CC and the base of *Triceratium cinnamomeum* in Sample 321-U1338A-33X-3, 60–61 cm. Samples 321-U1338A-35X-CC through 42X-CC are assigned to the *C. peplum* Zone. Events occurring in the *C. peplum* Zone are base occurrences of *Thalassiosira tappanae* (Sample 321-U1338A-37X-CC) and *Actinocyclus ingens* (Sample 321-U1338A-40X-1, 122–123 cm). The lower boundary of the *C. peplum* Zone is tentatively assigned to the top occurrence of *Thalassionema fraga* in Sample 321-U1338A-42X-CC. Diatom abundance is predominantly low throughout the *C. peplum* Zone, and valve preservation is moderate to poor. Cores 321-U1338A-43X and 44X are barren.

Planktonic foraminifers

At Site U1338 planktonic foraminifer assemblages are characteristic of tropical-subtropical environments. Assemblages are highly variable and preservation is generally superior to Site U1337. Assemblages are diverse and many of the taxa that were absent in the previously drilled PEAT sites are recorded here.

A planktonic foraminifer biostratigraphy was generated at Site U1338 from Hole U1338A using core catchers and supplemented by additional samples (usually two per core). Six samples were examined from Hole U1338B between Samples 321-U1338B-27H-2, 57–59 cm, and 30H-2, 126–128 cm, to constrain species ranges during an interval of nonrecovery in Hole U1338A. The sedimentary succession at this site ranges from Subzone PT1b (Pleistocene) to Zone M2–M4 (lower Miocene) (Fig. F13; Table T11),

which agrees with the calcareous nannofossil, diatom, and radiolarian biostratigraphies except for some minor discrepancies (discussed below). The preservation of planktonic foraminifers varies from poor to very good, though fragmentation and infilling occurs in some samples. Planktonic foraminifer tests generally account for >80% of the total residue in each sample. Taxon-relative abundances and estimates of assemblage preservation are presented in range chart format (Table T12). A number of primary and secondary markers were absent in the Site U1338 samples or had insufficient abundances to provide robust stratigraphic control; these included *Globorotalia (Truncorotalia) truncatulinoides*, *Globorotalia (Hirsutella) cibaoensis*, *Turborotalita humilis*, *Globorotalia birnageae*, and *Catapsydrax dissimilis*.

The top of *Globigerinoides ruber* (pink) is between Samples 321-U1338A-1H-1, 89–91 cm, and 1H-CC, indicating that the top of Hole U1338A is Pleistocene Subzone PT1b and younger than 0.12 Ma. The division between Subzones PT1b and PT1a is indicated by the top of *Globorotalia (Truncorotalia) tosaensis* between Samples 321-U1338A-2H-2, 70–72 cm, and 2H-5, 115–117 cm. The top of *Globigerinoides obliquus* is well defined at Site U1338 and is consistently present from Samples 321-U1338A-3H-CC to 20H-2, 56–58 cm, with rare occurrences recorded in Sample 321-U1338A-34X-CC. The top of this species has been calibrated by Chaisson and Pearson (1997) to 1.30 Ma.

The Zone PT1/PL6 boundary is marked by the top of *Globigerinoides fistulosus* between Samples 321-U1338A-3H-2, 70–72 cm, and 3H-CC. The base of *G. fistulosus* is between Samples 321-U1338A-5H-2, 117–118 cm, and 5H-CC. The first appearance datum of this species has been correlated with the base of the Mammoth Subchron (Berggren et al., 1995), with a calibrated age of 3.33 Ma for the PEAT timescale. There are a number of secondary markers through Zone PL6. *Globigerinoides extremus* is present from Samples 321-U1338A-4H-CC to 16H-CC. The top of *Globorotalia pseudomiocenica* is between Samples 321-U1338A-4H-3, 56–58 cm, and 4H-5, 56–58 cm. As at Site U1337, *Globoturborotalita woodi* is rare and therefore we were unable to constrain the base of Zone PL6.

Globorotalia (Menardella) multicamerata was present to rare, and we find the top of this taxon between Samples 321-U1338A-4H-5, 56–58 cm, and 4H-CC. *Dentoglobigerina altispira* and *Sphaeroidinellopsis seminulina* vary in quantity from present to abundant. The top of both taxa are between Samples 321-U1338A-5H-2, 117–118 cm, and 5H-CC, so (as at Site U1337) we were unable to identify Zone PL4; further samples are required to constrain this zone. We find

the top of *Globorotalia (Hirsutella) margaritae* marking the Zone PL3/PL2 boundary between Samples 321-U1338A-6H-5, 118–120 cm, and 6H-CC. As at Site U1337 this event is hard to determine because the index species is rare.

The change in coiling direction of *Pulleniatina* spp. from sinistral to dextral occurs between Samples 321-U1338A-6H-5, 118–120 cm, and 6H-CC. The base of Zone PL2, as defined by the top of *Globoturborotalita nepenthes*, is between Samples 321-U1338A-7H-2, 52–54 cm, and 7H-4, 58–60 cm. *Globorotalia (Menardella) exilis* is rare, but the base is constrained between Samples 321-U1338A-7H-4, 58–60 cm, and 7H-CC. *Globorotalia (Hirsutella) cibaoensis* only occurs in two samples from Site U1338; therefore, we are unable to constrain the boundary between Subzones PL1b and PL1a.

Sphaeroidinella dehiscens s.l. occurs from the top of Hole U1338A, with the base of this species between Samples 321-U1338A-8H-2, 43–45 cm, and 8H-5, 106–108 cm. This event is significantly higher than the depth expected by the age-depth plot (Fig. F14). This was also observed at Site U1337 and is perhaps due to the low abundance of the primitive form *S. dehiscens* f. *immatura* (Banner and Blow, 1965) at the PEAT sites. Further studies are needed to determine the precise position of the base appearance in this region. *Globorotalia tumida* is abundant and commonly dominated the samples between the top of Hole U1338A and Sample 321-U1338A-10H-3, 47–49 cm. The base of *G. tumida*, marking the base of Zone PL1, is between Samples 321-U1338A-10H-3, 47–49 cm, and 10H-6, 108–110 cm. *Globoquadrina dehiscens* occurs from the base of Hole U1338A to Sample 321-U1338A-10H-CC. This event has been dated at 5.8 Ma (Berggren et al., 1995), and the recalibrated PEAT timescale age is 5.9 Ma. The base of *G. margaritae* is between Samples 321-U1338A-12H-CC and 13H-2, 105–107 cm; however, as noted above, this species was rare and the age-depth plot (Fig. F14) suggests that this event is depressed by ~10 m. This bioevent has been reported as diachronous from Chron C3An to the base of Chron C3r (Berggren et al., 1995). The age at the PEAT sites will be determined by further studies for documenting its diachroneity. The base of *Pulleniatina primalis* is between Samples 321-U1338A-11H-5, 65–67 cm, and 11H-CC. This event has been calibrated by Berggren et al. (1995) to 6.4 Ma, with a recalibrated PEAT timescale age of 6.6 Ma. This recalibrated age is generally concordant but somewhat older than that of the age-depth plot of the present site (Fig. F14).

The boundary between Zones PL1 and M14, as marked by the top of *Globorotalia linguaensis*, is between Samples 321-U1338A-13H-5, 44–46 cm, and

13H-CC. This species is rare, but the top horizon agrees with the integrated nannofossil, diatom, and radiolarian biostratigraphies at this site. The base of *Globorotalia plesiotumida*, marking the division between Subzones M13b and M13a, is between Samples 321-U1338A-21H-2, 39–41 cm, and 21H-5, 50–52 cm. This species is distinguished from its ancestral species, *Globorotalia merotumida*, by having a larger test, a larger increase in chamber-size growth, less convex in edge view on the spiral side, and a final chamber with width narrower than its height. These taxonomic features are clearly observed in specimens at the base horizon. However, the base datum observed at the present site is significantly older than that expected from the age-depth plot (Fig. F14). Further study is required to determine whether these specimens belong to a true evolutionary descendant or an ecologic phenotype of the ancestral species. The base of Zone M13, as indicated by the base of *Neogloboquadrina acostaensis*, is between Samples 321-U1338A-25H-3, 9–11 cm, and 25H-6, 5–7 cm. *Paragloborotalia mayeri* is abundant and the top of this species is recorded between Samples 321-U1338A-25H-3, 9–11 cm, and 24H-CC. However, we were unable to differentiate Zone M12, as we find the co-occurrence of *N. acostaensis* and *P. mayeri* in Sample 321-U1338A-25H-3, 9–11 cm. The absence of Zone M12 (Zone N15 of Blow, 1969) has also been reported in subtropical to temperate successions, namely at North Atlantic ODP Sites 563 and 608 (Berggren et al., 1995), and the Monte Gibliscemi section of Italy (Hilgen et al., 2000). At Site U1337, *N. acostaensis* is absent below Sample 321-U1337A-18H-3, 141–143 cm, and the top occurrence of *P. mayeri* could not be defined because of the barren interval from Samples 321-U1337A-18H-CC to 24X-CC. Lourens et al. (2004) proposed the base of regular occurrence of *N. acostaensis* with an astronomically tuned age of 9.83 Ma. At the present site, it is difficult to recognize the base of regular occurrence because of its sporadic occurrence and low abundance.

Globoturborotalita decoraperta was sporadically present, but the base of this species is between Samples 321-U1338A-27X-CC and 29X-2, 136–138 cm. The top of *Globigerinoides subquadratus* is also at this horizon. Both the base of *G. decoraperta* and the top of *G. subquadratus* are further constrained by analyses in Hole U1338B, where both events are found between Samples 321-U1338B-27H-2, 57–59 cm, and 28H-2, 120–122 cm. *G. nepenthes* has a sporadic occurrence, and the base of this species (base of Zone M11) is between Samples 321-U1338A-26H-2, 50–52 cm, and 26H-6, 130–132 cm (264.09 m CCSF-A), at a much younger level than expected. However, examination

of samples from Hole U1338B indicates that the base of *G. nepenthes* is between Samples 321-U1338B-27H-2, 57–59 cm, and 28H-2, 120–122 cm (282.42 m CCSF-A), and this occurrence is more consistent with the short duration of Zone M10/N13; therefore, we use this horizon in Figure F13.

Zone M8–M9/N12 is the total range zone of *Globorotalia (Fohsella) fohsi*. This species is present to abundant, with the top range between Samples 321-U1338A-29X-2, 136–138 cm, and 29X-4, 32–34 cm, and the base between Samples 321-U1338A-35X-2, 9–11 cm, and 35X-CC. The top of the *G. fohsi* group is supported by analyses from Hole U1338B, with the top between Samples 321-U1338B-28H-2, 120–122 cm, and 28H-6, 107–109 cm. In Sample 321-U1338A-29X-4, 32–34 cm, we find specimens of *G. fohsi* that are of consistent morphology but diminished in size. This may suggest a dwarfing of *G. fohsi* in the upper part of its range. Size reduction has also been recognized in other species of planktonic foraminifers prior to their extinction (Wade and Olsson, 2009). Within Zone N12, the base of *Gr. (Fohsella) fohsi robusta* is between Samples 321-U1338A-34X-2, 78–80 cm, and 34X-4, 91–93 cm, marking the base of Subzone M9b. The top of *Globorotalia praescitula* is between Samples 321-U1338A-33X-5, 47–49 cm, and 33X-CC. However, the top occurrence is marked by only one specimen and is significantly discontinuous from the lower occurrence. Moreover, the biohorizon is ~20 m higher than that indicated by the age-depth plot of the present site (Fig. F14). There is room for argument whether any bias such as reworking has impacted this datum.

Globorotalia (Fohsella) "praefohsi" is rare. The base of this species, marking the boundary between Zones N10 and N11, is between Samples 321-U1338A-36X-1, 36–38 cm, and 36X-CC. The base of *Globorotalia (Fohsella) peripheroacuta*, and therefore the base of Zone M7/N10, is between Samples 321-U1338A-36X-CC and 37X-1, 43–45 cm. The top of *Globigerinatella insueta* is between Samples 321-U1338A-38X-5, 109–111 cm, and 38X-CC. We are unable to constrain the top of *Clavatorella bermudezi* because of the rarity of this species; however, the base of this taxon can be found between Samples 321-U1338A-37X-CC and 38X-2, 35–37 cm.

The base of *Orbulina universa* is between Samples 321-U1338A-35X-2, 9–11 cm, and 35X-CC. This species is rare at this site in the lower part of its range, and the base occurrence is much higher than anticipated (Zone M8–M9/N12). We are therefore unable to constrain the base of Zone M6/N9. The division between Subzones M5a and M5b is constrained by the base of *Praeorbulina glomerosa* between Samples 321-U1338A-40X-CC and 41X-2, 66–68 cm. This in-

terval is also associated with the change in *Paragloborotalia* from random to exclusively sinistrally coiled, which is between Samples 321-U1338A-40X-1, 115–117 cm, and 41X-2, 66–68 cm (see “**Biostratigraphy**” in the “Site U1337” chapter for discussion). The Zone M4/M5 boundary is marked by the base of *Praeorbulina sicana* between Samples 321-U1338A-42X-4, 114–116 cm, and 42X-CC.

The base of *G. insueta* is between Samples 321-U1338A-43X-CC and 44X-2, 55–57 cm. We are unable to constrain the top of Zone M3 because of the absence of *Catapsydrax dissimilis*. We find abundant to rare occurrences of *Catapsydrax unicavus* from the base of the hole to Sample 321-U1338A-29X-4, 32–34 cm (Zone M7/N10). As at Site U1337, we find the top occurrence of *Globoquadrina binaiensis* (sensu stricto) in an unusually high stratigraphic position. This taxon is present from the base of the hole to Sample 321-U1338A-43X-2, 18–20 cm, above the base of *G. insueta*. We are therefore unable to differentiate Zones M2 and M3. The extended range of this form requires further investigation. Specimens of *Globoquadrina* cf. *binaiensis* (see “**Biostratigraphy**” in the “Site U1337” chapter for discussion) are also documented from the base of the hole to Sample 321-U1338A-38X-2, 35–37 cm (Subzone M5b).

Microperforate taxa (*Globigerinita*, *Globigerinatella*, *Mutabella*, and *Tenuitella*) are far more abundant at Site U1338 than at preceding sites. The diversity of this group is particularly high in the interval from Sample 321-U1338A-42X-4, 114–116 cm, to 29X-2, 136–138 cm (Subzone M5a to Zone M10). Stable isotopic evidence suggests that these taxa occupied the mixed layer (Pearson et al., 2001; Majewski, 2003). Our *Tenuitella* range into Subzone M5b, with a single specimen also recorded from Zone M8–M9/N12, indicating a younger stratigraphic position than previously suggested by Huber et al. (2006) but consistent with Site U1337 and the southern Indian Ocean (ODP Site 744; Majewski, 2003). Between Samples 321-U1338A-42X-4, 114–116 cm, and 29X-2, 136–138 cm, we find variable microperforate globular forms with numerous (often swollen) second generation bullae. Some of these forms may be consistent with *Globigerinatella* spp. documented from the western tropical Pacific Ocean (ODP Leg 144; Pearson, 1995). Detailed scanning electron microscope analyses are required to determine the full variability in these forms and their relationship to *G. insueta*.

Within the dentoglobigerinids, we commonly find distinct forms with a flattened umbilical face and incised sutures, referred to here as *Dentoglobigerina* sp. These forms range from Samples 321-U1338A-41X-CC to 29X-4, 32–34 cm (Subzone M5a to Zone M10/

N13) and are abundant in Sample 321-U1338A-39X-2, 72–74 cm. Many of these forms may have previously been considered as *Dentoglobigerina larmei*, but further postcruise studies are required to assess the full range of diversity in dentoglobigerinids.

We find distinctive changes in the assemblage composition throughout from the Miocene to Pleistocene (Fig. F16). From the base of Hole U1338A to Sample 321-U1338A-27X-4, 6–8 cm (244.77 CSF; Zone M11) the samples are dominated by species belonging to genera *Globoquadrina* and *Dentoglobigerina*. *Globoquadrina venezuelana* is present from the base of the hole to Sample 321-U1338A-7H-CC and commonly dominates the assemblages. *D. larmei* and forms referred to as *Dentoglobigerina tripartita* are a common component of the assemblage from the base of the hole to Zone M11 and often possess bullae. As at Site U1337, the decrease in globoquadrinids and dentoglobigerinids is associated with an increase in the genus *Globigerinoides*. *Globigerinoides* are much more diverse and abundant at this site and species include *Globigerinoides conglobatus*, *Globigerinoides extremus*, *Globigerinoides fistulosus*, *Globigerinoides immaturus*, *Globigerinoides mitra*, *Globigerinoides obliquus*, *Globigerinoides quadrilobatus*, *G. ruber*, *G. ruber* (pink), *Globigerinoides sacculifer*, *Globigerinoides subquadratus*, and *Globigerinoides trilobus*. *G. conglobatus* is present from Sample 321-U1338A-11H-CC to the top of the hole. Rare to abundant *G. immaturus* are found between Samples 321-U1338A-33X-CC and 6H-3, 118–120 cm. *G. obliquus* is present from Sample 321-U1338A-34X-CC but becomes a much more abundant component of the assemblages from Sample 321-U1338A-19H-2, 70–71 cm, to the top of its range in Sample 321-U1338A-3H-CC.

Keeled *Globorotalia* become a frequent component of the assemblages from Sample 321-U1338A-33X-CC (Zone M8–M9/N12) and become dominant from Sample 321-U1338A-11H-3, 100–102 cm (Zone M14), to the top of the hole (Fig. F16). *Globorotalia (Menardella) menardii* is abundant from Sample 321-U1338A-22H-2, 51–53 cm, to the top of the hole, with abundant *G. tumida* from Sample 321-U1338A-10H-3, 47–49 cm, to the top of the hole. *Globigerina bulloides* is present from the base to the top of the hole. Paragloborotaliids are a distinctive component of the assemblages from the base of the hole until the extinction of *P. mayeri* (Sample 321-U1338A-25H-3, 9–11 cm). In the upper part of their range (Samples 321-U1338A-32X-4, 67–69 cm, to 25H-6, 5–7 cm), *Paragloborotalia siakensis* increase their number of chambers in the final whorl from six to seven.

The interval with rare or barren planktonic foraminifers associated with the “carbonate crash” (Lyle et al.,

1995; Farrell et al., 1995) ranges from Samples 321-U1338A-22H-5, 41–43 cm, to 24H-CC. This interval is of shorter duration at Site U1338 and restricted to Subzone M13a (Fig. F13), whereas at Site U1337 the interval extends from Zone M11 to Subzone M13a (Fig. F13).

Benthic foraminifers

Benthic foraminifers occur continuously throughout the ~415 m thick Pleistocene to lower Miocene succession recovered at Site U1338, although abundances vary significantly. The early Miocene to Pleistocene assemblages predominantly consist of calcareous taxa with rare agglutinated forms, and the overall composition of assemblages indicates lower bathyal to abyssal paleodepths throughout the Neogene. Prominent variations in the downcore distribution of benthic foraminifers may reflect global climate fluctuations associated with fundamental changes in high-latitude ice volume and Pacific Ocean circulation (Fig. F17). Long-term trends can be correlated across sites drilled during the PEAT expeditions (Sites U1334, U1335, U1337, and U1338), and postcruise studies will provide an opportunity to investigate temporal and spatial variations across the equatorial Pacific Ocean and to unravel links with global climatic and oceanographic events during the Neogene.

Benthic foraminifers were examined in core catcher samples from Hole U1338A, supplemented by samples from Hole U1338A sections (two per core) after cores were split. Mudline samples recovered in Holes U1338A–U1338D were also investigated. Large samples with an average volume of ~50 cm³ were processed from all core catchers to obtain quantitative estimates of benthic foraminifer distribution patterns downcore. Smaller 10 cm³ samples were additionally investigated from core sections to provide realistic estimates of species availability for shore-based geochemical and paleontological studies, although these small samples do not yield statistically significant numbers of specimens. In contrast to Site U1337, the carbonate content of the sediment is generally higher and does not fluctuate so markedly, as prominent intercalations of diatom mats and carbonate-rich layers do not occur throughout the upper Miocene at Site U1338 (see “Geochemistry”). Therefore, sample selection was not biased toward carbonate-rich intervals, and core samples are overall more representative of lithologic variability at Site U1338 than at Site U1337.

To assess assemblage composition and variability downhole, all specimens from the >250 µm fraction were picked from core catcher and core samples and mounted onto slides prior to identification and

counting. The distribution of benthic foraminifers was additionally checked in the 150–250 µm fraction to ensure that assemblages in the >250 µm fraction were representative and that small species such as phytodetritus feeders were not overlooked. A total of 88 benthic foraminifer taxa were identified. Census counts from core catcher and core section samples are presented in Table T13. Figure F17 summarizes the downcore distribution of the more common benthic foraminifer taxa in core catcher samples from Hole U1337A. Common taxa include *Astrononion echolsi*, *Cibicidoides mundulus*, *Cibicidoides grimsdalei*, *Cibicidoides robertsonianus*, *Cibicidoides wuellerstorfi*, *Eggerella bradyi*, *Fissurina* spp., *Globocassidulina subglobosa*, *Gyroidinoides soldanii*, *Laticarinina pauperata*, *Oridorsalis umbonatus*, *Pyrgo murrhina*, *Pyrgo serrata*, *Pullenia bulloides*, *Quinqueloculina* spp., and *Siphonodosaria abyssorum*. Preservation is good overall, but deteriorates slightly in several levels (Cores 321-U1337A-18H through 21H, ~160–190 m CSF, and 26H through 27X, ~239–242 m CSF, and Sections 321-U1337A-35X-2, 37X-1, and 39X-5, ~318.5, ~336.4, ~361.7 m CSF, respectively). Well-preserved fish teeth and ostracodes are intermittently present throughout the succession.

Mudline samples from Holes U1338A–U1338D were gently washed in order to preserve fragile agglutinated specimens with extremely low fossilization potential. All mudline samples examined reveal a moderate degree of dissolution in the planktonic foraminifer assemblage, in particular among globorotalids. The mudline sample from Hole U1338A contains mainly radiolarians with some poorly preserved planktonic foraminifers and rare agglutinated tubular benthic foraminifers. Benthic foraminifers in mudline samples from Holes U1338B–U1338D are generally well preserved, consisting predominantly of agglutinated forms. Rare calcareous taxa include *Astrononion echolsi*, *Cibicidoides pachyderma*, *C. wuellerstorfi*, *Fissurina formosa*, *Fursenkoina bradyi*, *G. subglobosa*, *G. soldanii*, *L. pauperata*, *Melonis pompilioides*, *Melonis sphaeroides*, *Pyrgo* spp., and *Quinqueloculina* spp. Agglutinated taxa are mainly tubular forms with organic cement, such as the branching species *Rhizammina algaeformis*, which typically agglutinates a variety of planktonic foraminifer tests. Also present are the coarsely agglutinated *Reophax dentaliniformis*, *Lagenammina diffugiformis*, and *Psammosphaera* sp. and finely agglutinated *Buzasina glaeata*, *Hyperammina elongate*, and the calcareous agglutinated species *E. bradyi*. The sample from Hole U1338B contains exceptionally well preserved large specimens of *Astrorhizza arenaria* not found in other mudline samples. The sample from Hole U1338D contains two well-preserved tests of the planktonic species *Beella digitata*, which rarely fossilizes. Highly fragile agglu-

tinated assemblages typical of lower bathyal to abyssal depths occur in all mudline samples but are best preserved in Holes U1338B–U1338D, suggesting sediment recovery close to the sediment/water interface.

The Pleistocene to Pliocene assemblage within the biosiliceous-rich interval in the upper part of Hole U1338A (Cores 321-U1338A-1H through 8H; 2.68–69.65 m CSF) contains relatively low numbers of benthic foraminifers, representing only >1% of the total planktonic and benthic foraminifer assemblages. Variations in the abundance of organic flux-sensitive taxa such as *G. subglobosa*, *O. umbonatus*, *P. murrhina*, and *P. serrata* suggest that changes in equatorial Pacific Ocean surface productivity occurred throughout the Pleistocene to Pliocene, possibly associated with glacial–interglacial climate fluctuations. Sample 321-U1338A-6H-CC (50.70 m CSF), within an interval of lower CaCO₃ values (see “[Geochemistry](#)”), is characterized by high numbers of infaunal taxa (25%) including *Siphodinosaria abyssorum* and *Siphodinosaria* spp., which suggests that episodic decreases in bottom water ventilation occurred during the Pliocene. However, the low resolution of our shipboard data set prevents detection of variability that may occur on orbital to suborbital timescales.

Benthic foraminifer abundance increases and the benthic/planktonic ratio oscillates markedly during the latest Miocene (Cores 321-U1338A-10H through 13H; 97.05–126.80 m CSF). Sample 321-U1338A-14H-CC (126.80 m CSF), within a diatom-rich interval, is effectively barren of foraminifers. A prominent increase in miliolids is noted in Sample 321-U1338A-11H-CC (97.05 m CSF), where this group represents 37% of the total assemblage. The late Miocene assemblage in Cores 321-U1338A-14H through 21H (126.80–192.95 m CSF) generally shows high abundance and diversity, including high numbers of epifaunal or near-surface dwellers including *A. echolsi*, *C. mundulus*, *C. wuellerstorfi*, *G. soldanii*, *G. subglobosa*, *L. pauperata*, *O. umbonatus*, *P. murrhina*, *P. serrata*, and *Quinqueloculina* spp. The lowest occurrence of *Osangularia plummerae* in Hole U1338A occurs within this interval (Sample 321-U1338A-20X-5, 56–58 cm; 180.26 m CSF). Fluctuations in assemblage composition and benthic/planktonic ratio are evident, hinting at major changes in upper and deep ocean structure, which cannot be captured by our low-resolution data set. This interval coincides with improved carbonate preservation at the seafloor following an extended period of low carbonate deposition, widely recorded at ~9–11 Ma throughout the eastern Pacific Ocean and often referred to as the carbonate crash (Lyle et al., 1995; Farrell et al., 1995).

This transition to higher carbonate deposition marks a fundamental change in Pacific Ocean circulation and productivity regime, possibly associated with changing rates of deep water production and/or Northern Hemisphere ice development (Zachos et al., 2008).

Core catcher Samples 321-U1338A-22X-CC through 27X-CC (202.58–247.60 m CSF) are either barren or contain low numbers of planktonic foraminifers and are generally characterized by an impoverished benthic foraminifer assemblage. Sample 321-U1338A-23X-CC (212.16 m CSF), within a diatom-rich section, is effectively barren of benthic foraminifers. This interval corresponds to the early late Miocene carbonate crash and was also recorded in Site U1337. Interestingly, this prominent dissolution event appears less intense at Site U1338 than at Site U1337, as shown by higher numbers of planktonic and benthic foraminifers and higher carbonate content throughout (see “[Geochemistry](#)”) at Site U1338. This may be due to the fact that the site was located on younger oceanic crust and was closer to the Equator during this time window.

The middle to early Miocene assemblage in Cores 321-U1338A-29X through 41X (268.33–382.72 m CSF) is overall diverse and abundant, particularly within Cores 34X and 42X (316.10–391.07 m CSF). However, some fluctuations in abundance and composition are evident, which may reflect cyclic changes in surface productivity and circulation but cannot be ascertained because of the low resolution of our samples. The assemblage is characterized by epifaunal species such as *C. mundulus*, *C. wuellerstorfi*, and *L. pauperata* and by mobile, shallow infaunal dwellers living close to the sediment/water interface, such as *Cibicidoides bradyi*, *C. grimsdalei*, *C. robertsonianus*, *G. soldanii*, *G. subglobosa*, *O. umbonatus*, and *Pyrgo* spp. The benthic/planktonic ratio remains relatively low (~1%–20%) but rises intermittently within this interval, suggesting transient variations in carbonate preservation linked to changes in the CCD. Enhanced carbonate preservation at the seafloor during this interval is supported by overall high CaCO₃ values (see “[Geochemistry](#)”). This interval appears to coincide with the prolonged period of increased CaCO₃ deposition, widely identified at ~13–16 Ma in the eastern equatorial Pacific Ocean (Lyle, 2003). Interestingly, most of this interval corresponds to the episode of major global cooling at ~13–15 Ma, when ice sheets expanded in Antarctica toward the end of the “Monterey carbon isotope excursion” (Lewis et al., 2007). A substantial improvement in deepwater ventilation and deepening of the calcium carbonate compensation depth was also recorded at ODP Site 1237 in the southeast-

ern subtropical Pacific Ocean following middle Miocene ice growth (Holbourn et al., 2005; 2007).

The abundance and diversity of the early Miocene assemblage in Cores 321-U1338A-42X through 44X (391.07–408.34 m CSF) are generally lower, but marked variations in assemblage composition occur, indicating probable changes in water mass characteristics which are beyond the resolution of our sample set. For instance, Sample 321-U1338A-43X-2, 18–20 cm (394.88 CSF), is characterized by high numbers of infaunal taxa (>40%), including *S. abyssorum* and *Siphonodosaria* spp., and exhibits a high benthic/planktonic ratio (30%), which suggests somewhat reduced bottom water ventilation. In contrast, some of the other lower Miocene samples contain higher numbers of epifaunal taxa and have much lower benthic/planktonic ratios (1%–7%). This interval, where benthic foraminifer distribution remains highly variable, corresponds to a period of global warmth during the early part of the Monterey carbon isotope excursion, often referred to as the mid-Miocene climatic optimum. Sample 321-U1338A-44X-CC (408.34 CSF), which is close to the basaltic basement, contains heavily recrystallized benthic foraminifers.

Paleomagnetism

Using the pass-through magnetometer, we measured the natural remanent magnetization (NRM) of archive-half sections of 26 APC cores from Hole U1338A, 42 APC cores from Hole U1338B, and 47 APC cores from Hole U1338C. Discrete samples (total = 234) were collected at one per section (for the first six sections) from all APC cores of Hole U1338A and from Cores 321-U1338B-27H through 42H in an interval not covered by APC coring in Hole U1338A. Of these cubic (7 cm³) discrete samples, the NRM of 130 samples was measured prior to demagnetization and then after demagnetization at peak fields of 10 and 20 mT using the pass-through magnetometer.

The primary objective of shipboard measurements is to determine the magnetostratigraphy, thereby providing chronostratigraphic constraints. To accomplish this, the procedure in Hole U1338A was to measure the NRM of each section at 2.5 cm intervals before demagnetization and after demagnetization at peak AFs) of 10 and 20 mT. In Holes U1338B and U1338C, the NRM of each core section was measured prior to demagnetization and after a single 20 mT demagnetization step. The curtailed treatment for Holes U1338B and U1338C was necessary to maintain laboratory core flow. No XCB core sections from Site U1338 were measured based on experience at

Site U1337, where XCB cores, even those visibly undisturbed, do not yield useful paleomagnetic data. During processing of the paleomagnetic data at Site U1338, we removed measurements within 7.5 cm of section ends to avoid section-end effects. Data from visibly disturbed intervals (see “[Lithostratigraphy](#)”) were also removed.

At Site U1338, as at Site U1337, the FlexIt core orientation tool was deployed and its data were applied throughout the APC sections. For operation of the FlexIt tool, see “[Paleomagnetism](#)” in the “[Methods](#)” chapter and “[Paleomagnetism](#)” in the “[Site U1337](#)” chapter. The FlexIt tool was deployed in conjunction with all APC cores at Site U1338 except for Cores 321-U1338C-45H through 47H, the final three cores in Hole U1338C. The decision not to deploy the FlexIt tool for these cores was based on the possibility of damage to the FlexIt tool from overpull/jerking required to recover the preceding core (321-U1338C-44H). A malfunction of the FlexIt tool occurred for seven cores at the base of Hole U1338B (Cores 321-U1338B-36H through 42H), where FlexIt data were not recorded because of inexplicable tool failure immediately after its redeployment after charging and data download. The FlexIt tool was typically run for 6–8 h continuously (6–7 cores), although battery life of each unit should allow it to run for up to 24 h. Data loss in Hole U1338B led to the tool being replaced and recharged more frequently (after each 4–5 cores) for Hole U1338C. The orientation angle determined from the FlexIt software (by M. Hastedt) is listed in [Table T14](#).

The remanence inclination is close to zero, as expected for a site close to the paleoequator, making inclination not diagnostic of polarity. In the absence of FlexIt core orientation data, the 180° alternations in declination may be mapped downhole and correlated to the GPTS as described in “[Paleomagnetism](#)” in the “[Site U1331](#)” chapter, although this was proved to be impractical at this site.

Results

Paleomagnetic data for Holes U1338A–U1338C are presented in [Figures F18](#), [F19](#), and [F20](#), together with whole-core magnetic susceptibility data measured on the WRMSL. Magnetization directions are dispersed and not interpretable in a large part of the Site U1338 sections because of low remanent magnetization intensities (10⁻⁵–10⁻⁴ A/m) that approach the noise level of the magnetometer. Three intervals, however, feature magnetization intensities close to or above 10⁻³ A/m where the remanence directions can be adequately resolved. These intervals are 0–50, 180–225, and 295–395 m CSF. In these intervals, the recovery in magnetization intensity is accompanied

by increased susceptibility (Figs. F18, F19, F20), although the susceptibility increase is generally muted relative to the remanence intensity change. There is satisfactory agreement between directions and intensity of remanent magnetization after AF demagnetization at peak fields of 20 mT for archive-half sections and discrete samples taken from working halves in the 0–50 (Fig. F18A) and 180–225 (Fig. F18B) m CSF intervals. This agreement indicates that the radial-inward drilling-induced remanence occasionally reported from ODP/IODP cores is not present in these intervals. In the 295–395 m CSF interval, on the other hand, small but systematic differences occur in declinations (Fig. F19C), which indicate the drilling-induced magnetization remains even after demagnetization. In this interval, we also recognize some differences in remanence intensity, with discrete samples tending to have lower magnetization intensities than archive-half sections. This suggests that the rims of cores have been overprinted more strongly than their centers.

At depths where there was a likelihood that core barrels would need to be drilled over for recovery, cores were collected using a steel core barrel in order not to damage the more expensive nonmagnetic barrels. The utilization of steel (as opposed to nonmagnetic) core barrels began with Cores 321-U1338A-25H, 321-U1338B-21H, and 321-U1338C-22H. Core 321-U1338A-25H may have been affected by enhanced magnetic overprint associated with the steel core barrel (Fig. F18B), whereas Core 321-U1338C-22H (Fig. F20B) was not markedly affected. Remanence intensity tends to be highest near the top of some cores and gradually decreases toward the base (Figs. F19A, F20B). Inclinations, although highly scattered, occasionally show a tendency for uphole increase within each core (e.g., Cores 321-U1338B-20H, 34H, and below) (Fig. F19B, F19C). This indicates that the upper parts of the cores are more strongly affected by steep drill string-related magnetizations, possibly indicating that the secondary magnetizations are a function not only of the magnetic field strength within the drill string but also by the level of drilling disturbance that is generally enhanced toward the core tops.

Magnetostratigraphy

Our correlation of polarity zones with the GPTS is based on polarity zone pattern fit to the GPTS, being cognizant of the biostratigraphic constraints. Interpreted reversal depths are provided in Table T15, and polarity interpretations are shown in Figure F21. All declinations are based on FlexIt orientation information apart from those cores for which the FlexIt data

were lost (Cores 321-U1338B-36H through 42H) or where the FlexIt tool was not deployed (Cores 321-U1338C-45H through 47H). For Cores 321-U1338B-36H through 42H (321.1–387.4 m CSF; 354.1–430.9 m CCSF-A), the cores were “oriented” by applying a uniform rotation to each core that is consistent with the FlexIt oriented data for the same interval from Hole U1338C. The polarity interpretation is based on the declination record after demagnetization at peak fields of 20 mT (Fig. F21). Without multiple holes and robust correlation among holes, using digital image scans and WRMSL data (see “[Stratigraphic correlation and composite section](#)”), a polarity interpretation at this site would be difficult or impossible. As it is, scattered data from one hole are often compensated by less scattered data from another hole, allowing the polarity stratigraphy to be pieced together. The polarity interpretation (Fig. F21), based on a combination of polarity zone pattern fit to the GPTS and biostratigraphic constraints, should be considered tentative and provisional in some intervals, although it is consistent with site biostratigraphy, such as the top of *D. hamatus* (9.69 Ma) at 221.8 m CCSF-A and the top of *S. heteromorphus* (13.53 Ma) at 362.5 m CCSF-A (see “[Biostratigraphy](#)”). Our conclusion from this site is that the FlexIt orientation data is generally reliable. Sedimentation rates based on the polarity interpretation indicate increasing sedimentation rates downcore from ~14 m/m.y. at the top to ~30 m/m.y. at the base of the section (Fig. F22). It appears from this figure that the depth intervals of unresolved magnetic polarity with reduced remanent intensity are associated with increased sedimentation rates, implying that increased burial of organic matter and enhanced sedimentation rates may have promoted reductive dissolution of magnetite, although these intervals accompany no remarkable increase in total organic carbon content (see “[Geochemistry](#)”).

Geochemistry

Shipboard geochemical analyses of interstitial water and bulk sediment samples reflect large variations in sediment composition resulting from shifts in carbonate versus opal production. The large-scale redox state and diagenetic processes of the sediment column are related to overall changes in sediment composition. The interstitial water chemistry points to seawater circulation in the basement, whereas reactions with the basement itself appear to exert little influence on the geochemistry of sediments and interstitial waters.

Sediment gases sampling and analysis

A total of 39 headspace gas samples were taken from Hole U1338A at a frequency of one sample per core as part of the routine environmental protection and safety monitoring program. The concentration of methane (C_1) in the samples was <1.7 ppmv, and no hydrocarbon gases higher than C_1 were detected.

Interstitial water sampling and chemistry

A total of 118 interstitial water samples were collected from Holes U1338A and U1338B, 43 using the whole-round squeezing method and 75 by Rhizon sampling (Table T16). Whole-round squeezing was conducted throughout Hole U1338A and in two locations in Hole U1338B to cover poorly recovered intervals. Samples from the two holes were taken to constitute a single depth profile using the core composite depth below seafloor (CCSF-A) scale. Rhizon sampling was conducted at a resolution of four samples per core in the upper 100 m of Hole U1338A immediately after core sections were cut and transferred to the racks in the core laboratory. Rhizon samplers were inserted into the middle of the whole core through holes predrilled in the end cap at the bottom of sections. A diatom-rich interval (Section 321-U1338B-14H-5) was targeted for high-resolution Rhizon sampling (every 10 cm) in Hole U1338B, after being identified in the first hole. Following WRMSL physical property measurements to pin-point the location of the low-density diatom-rich interval, Rhizon samplers were inserted through holes drilled in the core liner at an angle of 55° to ensure only the center of the core was sampled. Chemical constituents were determined according to procedures outlined in “Geochemistry” in the “Methods” chapter. Analyses of squeezed and Rhizon-sampled waters were conducted during the same analytical sessions, and the data from adjacent Rhizon and squeezed samples agree within the measurement uncertainties in virtually all instances (Table T16; Fig. F23).

Chloride ion concentration (not corrected for Br contribution) varies slightly with depth and is generally within 555 to 565 mM (Fig. F23). Chloride values increase from ~ 559 to >565 mM in the upper 30 m of the section, potentially reflecting the more saline bottom waters of the Last Glacial Maximum (e.g., Adkins and Schrag, 2003). However, the precision of the potassium chromate indicator technique is poor compared to the small variation in chloride, and a potentiometric titration technique (Adkins and Schrag, 2003) would be required to reveal more detail. Alkalinity increases slightly downhole from ~ 2.7 mM at the sediment/water

interface to peak slightly above 4 mM at 140 m CSF. Below this depth alkalinity values remain stable at ~ 4 mM then decrease toward 3 mM at the base of the section. Seawater contamination of the XCB-sampled waters may be responsible for the apparent decrease, as the APC-cored samples from Hole U1338B both have high values. Sulfate concentrations decrease from 28 mM at the top of the section to a minimum of ~ 23 mM at ~ 130 m CSF before increasing with depth to ~ 26 mM near basement.

A very large dissolved manganese peak of $150 \mu\text{M}$ at 10 m CSF is captured by the high-resolution interstitial water sampling and is remarkably similar to that observed at Site U1337. These peaks are >3 times greater than the highest dissolved manganese concentrations encountered during Expedition 320. Below this peak, manganese values drop to low values of $\sim 2 \mu\text{M}$ around 150 m CSF before a much smaller second peak of $\sim 13 \mu\text{M}$, which is centered around 220 m CSF. Below 300 m CSF, dissolved manganese is low but always detectable. Dissolved Fe displays three distinctive peaks downcore centered around 40, 215, and 300 m CSF. Interestingly these dissolved Fe peaks of $\sim 5 \mu\text{M}$ broadly correspond to zones of good magnetic remanance (see “Paleomagnetism”). These large variations in dissolved Mn and Fe reflect changes in redox chemistry that also manifest as changes in sediment color. For example, below ~ 385 m CSF a sharp transition from pale green to yellow sediments occurs (see “Lithostratigraphy”) where the dissolved Fe concentration is below detection. Such tandem changes in sediment color and interstitial water chemistry are well documented for the uppermost sediments where the iron hosted in smectites is reduced (Lyle, 1983). To find such a redox front in a reversed position, extending from the basement upward, suggests seawater has circulated through the basement at some time.

The silicic acid (dissolved silicate) content of the interstitial waters is substantially greater than that of bottom waters (e.g., Peng et al., 1993) and increases with depth from $\sim 700 \mu\text{M}$ in the uppermost sediments to peak at $\sim 1200 \mu\text{M}$ at ~ 120 m CSF. Below this interval, silicic acid concentrations are high and generally stable between 1100 and $1200 \mu\text{M}$. This strong enrichment in silicic acid almost certainly originates from the dissolution and diagenesis of biogenic silica. High-resolution Rhizon sampling (every 10 cm) of a diatom-rich interval in Hole U1338B reveals generally high silicic acid contents throughout but slightly higher concentrations in the diatom mat interval itself (Fig. F24). More precise shore-based measurements are required, but the initial data suggest active dissolution of the diatom opal in this interval.

Ca concentrations display very little variation downcore with values increasing from a seawater value (~10.5 mM) to two maxima of 12 mM at ~300 and ~390 m CSF. Mg and K concentrations scatter around seawater values. As the alteration of basaltic basement exchanges K and Mg for Ca (e.g., Gieskes, 1981), the lack of strong gradients in these elements suggests the basement is no longer reactive at this site.

Li concentrations decrease from ~26 μM at the surface to a minimum of ~3 μM around 250 m CSF before increasing sharply with depth to seawater values at the base of the section. The interstitial water Sr profile is a mirror image to that of Li except the decrease from the peak of 400 μM at 200 m CSF is punctuated by a sharp drop of >100 μM between ~260 and 290 m CSF. Li and Sr profiles indicate seawater circulation in the basement, as their values tend toward seawater values near the basement. The source of Sr to the pore waters is most likely the dissolution and recrystallization of biogenic calcite (e.g., Baker et al., 1982). High-resolution (every 10 cm) Rhizon sampling reveals elevated Sr concentrations in a diatom-rich interval of Hole U1338B (Fig. F24), suggesting a link between opal and biogenic carbonate diagenesis.

The dissolved Ba concentration is low in all samples, as expected given the high dissolved sulfate concentrations throughout the sediments. B concentrations in the interstitial waters generally range between 440 and 380 μM .

Bulk sediment geochemistry

Major and minor elements

At Site U1338, bulk sediment samples at a frequency of one per core were analyzed for Si, Al, Fe, Mn, Mg, Ca, Na, K, Ti, P, Ba, Cu, Cr, Sc, Sr, V, Y, and Zr (Table T17).

The Al, Mg, Fe, and Ba contents of the bulk sediment all display a similar downcore pattern with two distinctive peaks centered around ~50 and ~225 m CCSF-A (Fig. F25). Mg and Fe also increase toward the base of the section, and Fe peaks broadly correspond to the dissolved Fe peaks observed in interstitial waters. The Ca and silicon oxide contents of the bulk sediment mirror each other precisely (Fig. F25), demonstrating the important role of opal versus biogenic calcite production or preservation in determining the composition of the sediments at this site. Generally the silicon oxide content is higher and more variable above 270 m CCSF-A and vice versa for the calcium (carbonate) content.

Carbonate leachates from Sites U1336–U1338

The trace element composition of the bulk carbonate fraction was determined for selected samples from Sites U1336–U1338 (Table T18; Fig. F26). Carbonate was selectively dissolved in 1 M acetic acid adjusted to pH 5 with sodium acetate (Tessier et al., 1979; Lyle et al., 1984; Kryc et al., 2003) following a wash in pure water buffered to pH 10 with ammonium hydroxide. Further details and evaluation of this methodology are given in “Geochemistry” in the “Methods” chapter.

The Mg/Ca ratio of the bulk carbonate generally ranges between 2 and 6 mM/M, with Site U1336 samples exhibiting the lowest values and Site U1337 samples the highest. Mn/Ca ratios are generally high, ranging between 2 and 6 mM/M at Sites U1337 and U1338. The Mn/Ca ratio of the bulk carbonates measured for Site U1336 are all below 2 mM/M, which may be related to the much lower dissolved Mn content of interstitial waters at Site U1336 compared to Sites U1337 and U1338. The Sr/Ca ratio of Site U1337 and U1338 bulk carbonates varies between 2 and 3 mM/M, which is consistent with Sr/Ca ratios measured on modern coccolith samples (e.g., Stoll et al., 2002). The Sr/Ca ratio of the bulk carbonates from Site U1336 is generally lower than that at Sites U1337 and U1338, ranging between 1 and 2 mM/M. This lower Sr/Ca ratio possibly reflects a higher degree of carbonate recrystallization at Site U1336 compared to Sites U1337 and U1338. The Fe content of the bulk carbonate leachates was below detection in most samples from Sites U1337 and U1338 but was detectable in all samples measured from below 100 m CSF at Site U1336. The Li content of the bulk carbonates investigated was below detection (<4.8 μM) for all samples. This finding negates the possibility of carbonates providing the large sedimentary Li sink inferred from the interstitial water profiles.

Sedimentary inorganic and organic carbon

Calcium carbonate and inorganic carbon concentrations were determined on 245 and 62 sediment samples from Holes U1338A and U1338B, respectively (Table T19; Fig. F27). Hole U1338B samples were used to fill the stratigraphic gaps in Hole U1338A sampling because of the low recovery and core disturbance associated with XCB coring below Core 321-U1338A-27X. Calcium carbonate concentrations range between 26 and 88 wt% with substantial variability in the upper 273.31 m CCSF-A, corresponding to the alternation between calcite and opal in the upper two lithologic units (see “Lithostratigra-

phy"). Below 273.31 m CCSF-A (lithologic Unit III), calcium carbonate contents become generally high and stable between 66 and 91 wt% compared with the upper part of the stratigraphic column, with the exception of distinctive decreases at 295.66–297.00, 327.95–350.96, and 390.95–424.42 m CCSF-A.

TOC was determined for 60 sediment samples from Holes U1338A and U1338B (Table T19; Fig. F27). In the upper ~230 m CCSF-A, TOC content is generally high and variable, between 0.09 and 0.46 wt%, whereas below ~230 m CCSF-A TOC content is <0.09 wt%. Downhole TOC variability is most likely related to lithologic changes with higher TOC being found in the more biosiliceous intervals. To test this, TOC measurements were performed on two samples targeted specifically for their high biosiliceous content from 327.95 and 350.96 m CCSF-A. The results reveal high TOC values of 0.50 and 0.20 wt% and indicate that higher TOC values are found in the biosiliceous-rich intervals.

Physical properties

Physical properties at Site U1338 were measured on whole cores, split cores, and discrete samples. WRMSL measurements (GRA bulk density, magnetic susceptibility, and *P*-wave velocity) (Fig. F28A–F28C), thermal conductivity, and NGR measurements (Fig. F28D) comprised the whole-core measurements. Compressional wave velocity measurements on split cores and MAD analyses on discrete core samples were made at a frequency of one per undisturbed section in Hole U1338A and Cores 321-U1338B-27H through 31H, 34H through 38H, 40H, and 41H. The SHMSL was used to measure spectral reflectance on all archive-half sections.

Density and porosity

Two methods were used to determine bulk sediment properties at Site U1338, GRA for bulk density of whole-round sections (Fig. F28B) and MAD analyses for wet bulk density, dry bulk density, grain density, water content, and porosity of discrete samples (Fig. F29; Table T20). MAD and GRA bulk densities display excellent agreement at Site U1338 (Fig. F29B). Cross-plots of wet bulk density and dry bulk density versus interpolated GRA bulk density (Fig. F30) show that MAD and GRA density data are well correlated for both APC- and XCB-cored intervals.

Variation in wet bulk density reflects the variation in biosiliceous and calcareous components at Site U1338. As at Site U1337, a direct relationship exists between carbonate content and wet bulk density (Fig. F31). Wet bulk density in lithologic Unit I

ranges from 1.19 to 1.46 g/cm³ and averages 1.29 g/cm³. Overall density decreases with depth in Unit I from ~1.4 g/cm³ near the seafloor to 1.2 g/cm³ at the base of Unit I (~50 m CSF) as the abundance of radiolarians and diatoms increases in the nannofossil ooze (see "Lithostratigraphy"). Within this depth interval density variation is characterized by small-scale fluctuations of ~0.10 to 0.20 g/cm³ with roughly 1 m spacing. The small fluctuations are superimposed on a larger scale variation with a 10 to 20 m spacing. Below the density minimum that marks the boundary between Units I and II, density increases with depth from ~1.3 g/cm³ at 50 m CSF to 1.5 g/cm³ at 175 m CSF. The interval from 175 m CSF to the boundary between Units II and III (243.94 m CSF in Hole U1338A) is characterized by a broad density low that accompanies an increase in radiolarians and diatoms in the sediment (see "Lithostratigraphy"). In this interval, wet bulk density averages 1.40 g/cm³. From the top of Unit III to the base of the sediment section, bulk density increases more regularly as the sediment becomes a more uniform nannofossil ooze and eventually chalk. Carbonate contents are uniformly high in this interval (see "Geochemistry"). Wet bulk density increases from ~1.5 g/cm³ at the top of Unit III to 1.7 g/cm³ near the base of Hole U1338A. One sample from immediately above the basement (Sample 321-U1338A-44X-3, 129–131 cm) has a density of 1.89 g/cm³. Within Unit III the variation of wet bulk density is less compared to the other units at the site, with roughly meter-scale fluctuations of 0.1 g/cm³ superimposed on 0.1–0.2 g/cm³ fluctuations with a spacing of ~10 m.

Variations in grain density at Site U1338 also reflect the relative abundances of biosiliceous and calcareous components in the sediment. In Hole U1338A, from near the seafloor to 175 m CSF, grain density averages 2.59 g/cm³ and varies within a 0.15 to 0.20 g/cm³ wide band (Fig. F29C). The lowest grain densities occur in the interval between 175 m CSF and the base of Unit II. In this interval grain density ranges from 2.29 to 2.66 g/cm³ and averages 2.55 g/cm³. Grain density is higher and more uniform in Unit III, averaging 2.64 g/cm³ and generally varying within a 0.10 g/cm³ wide band. Grain density at the base of the sediment section in Hole U1338A is 2.75 g/cm³.

Porosity and water content vary inversely with wet bulk density (Fig. F29A). Porosity near the surface at Site U1338 is 80%. At the base of Unit I in Hole U1338A, porosity is 88%. In the upper part of Unit II, porosity decreases with depth with the same cyclical pattern as that displayed by wet bulk density. Porosity is at a minimum (69%) at 175 m CSF in Hole

U1338A. Below this depth and extending to the base of Unit II, porosity is higher, averaging 76%. Porosity decreases more uniformly in Unit III, going from ~70% near the top of the unit to 56% near the base of the unit. Sample 321-U1338A-44X-3, 129–131 cm, at 407.10 m CSF in Hole U1338A, has a porosity of 50%.

Magnetic susceptibility

Whole-core magnetic susceptibility values are closely correlated with lithology at Site U1338 (Fig. F28B). Susceptibility in lithologic Unit I shows high-amplitude variations from 0 to 24×10^{-5} SI. Higher susceptibility intervals are associated with dark-colored, siliceous microfossil-rich sediments that have lower bulk density. The profiles of magnetic susceptibility and GRA bulk density display an inverse relationship in Unit I that coincides with changes in sediment color (Fig. F32). At the boundary between Units I and II, susceptibility decreases from 5×10^{-5} SI to near zero and remains low for the upper part of the Unit II (~50–178 m CSF). Susceptibility in the interval from 178 to 214 m CSF fluctuates with variation ranging from 4×10^{-5} to 10×10^{-5} SI. Higher susceptibility values are associated with diatom-rich intervals that display lower GRA bulk density, similar to Unit I. In the lowermost part of Unit II, from 214 to 245 m CSF, the susceptibility record shows 2 to ~4 m-scale fluctuations from 0 to 15×10^{-5} SI that do not correspond to changes in GRA bulk density. Across the boundary between Units II and III, susceptibility drops steadily to roughly zero. Below 295 m CSF, susceptibility increases from 0 to $\sim 4 \times 10^{-5}$ SI, with frequent susceptibility peaks of 5×10^{-5} to 10×10^{-5} SI that are associated with siliceous microfossil-rich intervals (see “Lithostratigraphy”). An increase in susceptibility and high susceptibility peaks, from $\sim 5 \times 10^{-5}$ to $\sim 24 \times 10^{-5}$ SI, are present below 395 m CSF and extend to the base of Unit III.

Compressional wave velocity

P-wave logger (PWL) measurements from whole-round sections and discrete velocity measurements made on split cores follow similar trends for Site U1338. Velocity fluctuates around 1500 m/s for lithologic Units I and II. In Unit III, velocities begin to increase with depth, relating to increased compaction (Fig. F33). A similar increase in velocity is observed in the borehole data (see “Downhole measurements”).

The velocity of water obtained from the PWL was consistently low, ~1423 m/s, for the quality assurance/quality control liner. Therefore, it was decided to add a constant shift of 67 m/s to the measured ve-

locity so that the water velocity equaled 1490 m/s at room temperature (20°C). The velocity of water was also measured with the *P*-wave gantry at regular intervals of 12 h, and it was observed that the velocity measured along the *x*-axis was higher (~1500 m/s) with a variability of ~10 m/s. Therefore, a shift was applied to the measured velocity along the *x*-axis based on the observed water velocity, such that the water velocity remained constant (1490 m/s) for all the cores. No correction was required for the velocities measured along the *y*- and *z*-axis. After applying proper corrections, discrete velocity measurements are in good agreement with the PWL results (Table T21; Fig. F33). The velocity along the *x*-axis is lower than that of the PWL in the biosiliceous-rich interval around 180 to 240 m CSF (see “Lithostratigraphy”). This difference is attributed to the fracturing induced during the contact probe measurement. Minor differences between whole-core and split-core measurements possibly reflect the presence of water in the space between the core liner and sediment in the whole cores and the slight compaction of the sediment in the contact probe technique. No reliable *y*- or *z*-axis measurements were obtained below ~140 m CSF, as the sediment was hard and easily fractured with insertion of the probes. Beginning with Core 321-U1338A-37X (337 m CSF), discrete samples removed from the core were used to measure the velocity along the *x*-axis. Liner correction was not applied to these measurements.

In Unit I, velocity increases linearly with depth from 1515 to 1545 m/s as a result of the increase in abundance of siliceous microfossils. Velocities fluctuate between 1495 and 1540 m/s in Unit I and between 1500 and 1520 m/s in Unit II. In Unit III, a linear increase in velocity from 1520 m/s to 1570 m/s occurs between 290 and 380 m CSF. At ~380 m CSF in Unit III, split core velocities begin to increase rapidly with depth from 1610 to ~1820 m/s at the base of Unit III.

The cross-plot of GRA bulk density with PWL velocity suggests that velocity is negatively correlated with bulk density in Unit I (Fig. F34) because of the increase in abundance of siliceous microfossils and a generally higher velocity for intervals rich in radiolarians (Busch et al., 2006). For constant porosity, an increase in abundance of biosiliceous material results in the decrease in bulk density and increase in *P*-wave velocity. In Unit II, bulk density decreases as a result of the increase in abundance of biosiliceous components; however, velocity remains constant because of the increase in porosity. In Unit III, which is predominantly nannofossil ooze, density and velocity are positively correlated.

Comparison between PWL velocity and borehole log velocity is excellent, if PWL velocities are offset (Fig.

F35). A slight shift in the depth scale is observed as the depth of PWL velocity is recorded in CSF, and the depth of the logs is in the WMSF domain. It should be noted that PWL and log velocities are plotted in different scales, as PWL measures the velocity at standard pressure and temperature conditions, whereas the log measures the velocity at in situ condition. The excellent agreement between PWL- and log-derived velocities suggests that the transformation of laboratory-measured velocity to in situ velocity is approximately linear.

Natural gamma radiation

NGR was measured on cores from all holes drilled at Site U1338. The highest counts per second (cps) are present in the upper 5 m of the sediment column, with values of ~45 cps near the seafloor (Fig. **F28D**). Below 5 m CSF, the NGR signal is characterized by small variations centered around 4 cps. This pattern extends through lithologic Units I and II and represents the varying abundance of biosiliceous and calcareous components. Silica-rich intervals are generally characterized by darker color, presumably higher organic contents, and higher NGR. However, a consistent relationship between organic carbon and NGR values does not exist (Fig. **F36**). In Unit III, variations in the NGR signal are centered around 2 cps, reflecting the higher and more uniform carbonate content of the unit (see “**Lithostratigraphy**”). In the lower part of Unit III, a small NGR peak of 4 cps at ~385 m CSF coincides with the color change from greenish gray to pale yellow. At the base of Unit III, several small spikes in the NGR signal are associated with manganese oxide fragments present in the sediment.

The peak in NGR near the seafloor is a common feature at all Expedition 320/321 drill sites. Although prominent at Site U1338, the NGR peak is the lowest of the NGR peaks recorded during Expedition 320/321. The Site U1338 NGR record also is unusual in that a pair of peaks is present within 2 m of the seafloor. A series of closely spaced samples for carbon analysis were taken in the upper 2.4 m in Hole U1338A. The analyses show that several peaks in TOC are present in the upper 2 m of the sediment column; however, these peaks do not strictly coincide with the NGR peaks (Fig. **F37**). The NGR peaks near the seafloor do coincide with lower GRA bulk density, higher magnetic susceptibility, low carbonate concentration, and dark sediment color (Fig. **F37**). The explanation of the origin of the near-surface NGR peaks remains a subject for further study.

Thermal conductivity

Thermal conductivity was measured on the third section of each core from Hole U1338A that contained at least three sections and the first or second section from all other Hole U1338A cores (Table **T22**). Thermal conductivity increases gradually with depth at Site U1338 from 0.92 W/(m·K) at 2.25 m CSF to 1.24 W/(m·K) at 405.10 m CSF (Fig. **F38**). This trend in conductivity is nearly uniform throughout the section in Hole U1338A. Conductivity in the upper part of the hole, above ~185 m CSF, displays slightly larger amplitude variations than in the lower part of the hole. Thermal conductivity at Site U1338 is inversely correlated to porosity (Fig. **F39**). Lower conductivity occurs with higher porosity as increased interstitial spacing attenuates the applied current from the probe.

Reflectance spectroscopy

Spectral reflectance was measured on the split archive-half sections from all holes at Site U1338 using the SHMSL. The three light reflectance parameters (L^* , a^* , and b^*) display a lithology-dependent variation that does not strictly follow the lithologic units identified for the site (Fig. **F40**). Unit I overall is characterized by darker, browner colors, those with low L^* and higher a^* and b^* values. At ~25 m CSF, a^* and b^* decrease sharply as the sediment color changes to one dominated more by blue (low b^*) and green (low a^*). The sediment also becomes slightly darker (lower L^*) at this depth. At the boundary between Unit I and II, b^* decreases as blue colors become more dominant, a^* remains relatively unchanged, and L^* increases as the sediment lightens in color. From the top of Unit II (~50 m CSF) to ~192 m CSF, b^* displays high-amplitude variations with a wavelength of ~50 cm. Values of a^* display a variation similar in wavelength to that of b^* , but lower in amplitude. The luminance record displays similar length cycles superimposed on a larger scale, a roughly 20 m wavelength variation. This variation in L^* is apparent to ~300 m CSF, below which L^* becomes more uniform. Below ~192 m CSF, the amplitude of the variation in b^* and a^* decreases, and the 20 m-scale color cycles become more apparent in these parameters. Between ~328 and 386 m CSF, the sediment color progressively becomes more yellow (higher b^*) and more green (lower a^*). Luminance remains relatively unchanged in this interval. The transition from greenish gray to pale yellow occurs at 386 m CSF and is marked by sharp increases in both a^* and b^* . The first appearance of brown-colored chalk, at the top of Core 321-U1338C-44H, is marked by a decrease in a^* , b^* , and L^* .

Stratigraphic correlation and composite section

Special Task Multisensor Logger data were collected at 5 cm intervals from Holes U1338B and U1338C and compared to the Whole-Round Multisensor Track (WRMST) data obtained at 2.5 cm resolution from Hole U1338A. In this way drilling was monitored in holes after Hole U1338A in real time to maximize the opportunity for the recovery and construction of a stratigraphically complete composite section. Cores from Holes U1338B and U1338C were measured on the WRMST for final correlation. After the cores were split and described, a composite section and spliced sequence were constructed.

Magnetic susceptibility, NGR, GRA bulk density, L^* , and scanned images all contributed to correlation between holes at Site U1338. GRA and magnetic susceptibility are illustrated in Figures F41 and F42. Features between all records are well aligned to ~280 m CCSF-A. Ship heave of several meters during coring in Hole U1338C resulted in relatively more core disturbance in the softer sediments recovered from that hole than from other holes, and the splice was subsequently made primarily from Holes U1338A and U1338B in the upper 260 m CCSF-A (to Core 321-U1338A-27H). The remainder of the splice alternated between Holes U1338B and U1338C. Offsets and composite depths are listed in Table T23.

At the base of Core 321-U1338C-28H, overlap was lost because of poor recovery in corresponding cores from Holes U1338A and U1338B. Another gap occurred at the base of Core 321-U1338C-31H, the level of the “baby chert.” Several other ties were made on the basis of short overlaps between 280 and 360 m CCSF-A. Images of cores from all three holes as well as a spliced image are presented in Figure F43. Ties below 360 m CCSF-A were generally good to 430 m CCSF-A, whereupon poor core condition and low variability in the data used for correlation left little to do but finish out the splice with the lower four cores from Hole U1338C. Splice tie points are listed in Table T24.

A growth factor of 1.11 is calculated by linear regression of CSF versus CCSF-A for all Site U1338 cores, indicating an 11% increase in CCSF-A relative to CSF depth (Fig. F44). We used this value to calculate the CCSF-B scale presented in Table T23 to aid in the calculation of sedimentation and mass accumulation rates.

Sedimentation rates

All principal biostratigraphic datums and a set of 22 tentatively interpreted paleomagnetic reversals (re-

stricted to the APC-cored sections) (Table T25; see also “[Biostratigraphy](#)” and “[Paleomagnetism](#)”) were used in establishing age control (Fig. F14). The linear sedimentation rate at Site U1338 decreases from 28.7 m/m.y. in the Miocene to 12.7 m/m.y. during the Pliocene–Pleistocene (Fig. F14).

Downhole measurements

Logging operations

Downhole logging of Hole U1338B started after APC/XCB coring to a total depth of 416.1 m DSF ended on 9 June 2009 at 1400 h (all times are U.S. Pacific Daylight Savings Time; UTC – 7 h). While drilling the last three cores, the hole was checked for fill at the bottom and no fill was detected. In preparation for logging, the hole was flushed with a ~50 bbl sweep of sepiolite/attapulgitic mud (~9 ppg) followed by a wiper trip up to 80 m DSF and down to the bottom. No tight spots were encountered during the reaming, and no fill was noted at the bottom. A go-devil was then pumped through the drill string to open and lock the lockable flapper valve located above the bit. Finally, the hole was displaced with barite/attapulgitic mud (~10 ppg) and the bit was raised to the final logging depth of 84.7 m DSF.

We deployed three downhole tool strings in Hole U1338B: a modified triple combo that did not include a neutron porosity measurement, a FMS-sonic combination, and a VSI tool with a SGT-N sonde. For tool and measurement acronyms, see “[Downhole measurements](#)” in the “[Methods](#)” chapter.

The modified triple combo was lowered into the hole at 2337 h on 9 June. The tool string reached the bottom of the hole at 4621 m wireline log depth below rig floor (WRF) and started logging uphole at 0301 h on 10 June (Fig. F45). This logging pass was stopped at 0310 h when the flying head of the wireline heave compensator (WHC) took a series of sudden large oscillations. These oscillations were caused by flaws of the control algorithm of the WHC and are potentially dangerous for the tool integrity if tension on the cable drops and the tool string hangs on caliper arms. We interrupted this first logging attempt, restarted heave compensation, and went back to the bottom of the hole (4622 m WRF) to start another logging pass at 0339 h.

This main triple combo logging pass proceeded without incident until the base of the tool string was reached at ~4340 m WRF. At this point, the wireline cable tension measured at the surface and at the head of the tool increased by 1500–2000 lb, indicating that the tool string was stuck in a borehole restriction (Fig. F45). We kept pulling up carefully, and

after a couple of attempts the tool string was freed with its base at ~4325 m WRF. As the log data acquired below the obstruction were of high quality, we decided that the risk of passing again through the restriction outweighed the benefit of an additional complete logging pass. Therefore, we reentered the drill pipe, logging the seafloor from a peak in the gamma ray at 4207 m WRF. The triple combo tool string reached the drill floor and was rigged down at 0848 h.

During the ascent of the triple combo tool string, options to continue logging Hole U1338B safely were discussed with the operations superintendent and the Co-Chief Scientist on watch. The final decision was to lower the base of the drill pipe below the base of the obstruction. Before rigging up the FMS-sonic tool string, the base of the pipe was deepened to 4351 m DRF (141 m DSF).

The second wireline tool string deployed in Hole U1338B was the FMS-sonic, which was rigged up and started its descent at 1100 h (Fig. F46). The tool string reached the bottom of the hole and started a first logging pass from 4626 m WRF at 1624 h. The first pass ended with the base of the tool string at 4394 m WRF (1716 h), and, after some testing the efficiency of heave compensation with the tool string midway in the open hole interval, the tool string was lowered again to the bottom of the hole to start a second logging pass from 4628 m WRF at 1925 h. The tool string reentered the drill pipe without incident, and the second pass ended when the seafloor was detected at 4209 m WRF. The FMS-sonic tool string was recovered and rig-down completed at 0220 h on 11 June.

The third and final tool string was deployed in Hole U1338B to shoot a VSP and consisted of the VSI tool plus a SGT-N tool for correlation. The Site U1338 VSP was shot during the daylight hours of 11 June so that a watch for the presence of marine mammals could be maintained following IODP procedure. While the VSI/SGT-N combination was being lowered in the hole, the marine mammal watch started at 0645 h and the air guns began ramping up the shooting a half-hour later. The first VSI station was taken at 1008 h immediately above the base of the hole (4623 m WRF). We took as many as five shot records at each station for stacking and moved uphole by 15 m between stations. We acquired 14 successful VSP stations up to 4398 m WRF; a shallower station was attempted, but the VSI tool could not be coupled to the borehole wall because of an enlarged hole and soft formation. At 1308 h we decided to end VSP operations and started logging with the SGT-N, detecting the seafloor at 4207.5 m WRF. Rig-down was completed at 1615 h.

Downhole log data quality

Figures F47 and F48 show a summary of the downhole log data acquired in Hole U1338B. These data were processed to convert to depth below seafloor and to match depths between different logging runs. The resulting depth scale is WMSF (see “Downhole measurements” in the “Methods” chapter).

The overall quality of the logging data can be assessed from the repeatability of measurements acquired in different passes, by the consistency of different measurements (e.g., density and resistivity), and by comparing downhole log data to core measurements. A key factor that influences downhole log data quality is the size and irregularity of the borehole, especially for measurements that require good contact with the borehole wall (e.g., the density measured by the Hostile Environment Litho-Density Sonde (HLDS) and the resistivity images obtained by the FMS tool). The “hole diameter” track in Figure F47 is measured by a caliper arm on the Hostile Environment Natural Gamma Ray Sonde (HNGS) and shows a hole at least 14 inches in diameter (bit diameter = 11.4375 inches), with values locally near the maximum caliper range (~18 inches). Despite the occasionally large hole, the HLDS density data are high quality, as shown by their close correlation with MAD core measurements on discrete core samples and with the electrical resistivity logs, which are relatively insensitive to hole size. As noted earlier, because of a hole obstruction we could only run one complete pass of the triple combo tool string in Hole U1338B, so we cannot compare passes to assess the repeatability of density and resistivity measurements.

Resistivities obtained by the spherically focused resistivity (SFLU) electrode measurement were lower than those obtained in induction measurements (e.g., medium induction phasor-processed resistivity in Fig. F47), probably because of current loss at the electrodes. The higher induction resistivities are closer to values typically measured in deep-sea sediments, and we applied a simple empirical correction to the SFLU data by multiplying them by a constant factor of 1.16. This correction brings the overall measured resistivity values in close agreement.

We measured *P*-wave velocities with the Dipole Sonic Imager (DSI) using two different transmitting frequencies in the two passes of the FMS-sonic tool string. Occasionally, the waveform processing algorithm that determines the *P*-wave velocity picks the borehole fluid velocity. The *P*-wave velocity log in Figure F47 is a combination of the two passes obtained by choosing the higher value of *P*-wave velocity determined at each depth, which corresponds to the velocity of the formation. Above 210 m WMSF,

the sonic log measured low formation velocities of 1550–1600 m/s, near those of the fluid circulating in the hole (~1500 m/s). Core measurements (see “[Physical properties](#)”) and results of the VSP experiment (see below) also indicate velocities near or just above 1500 m/s in the top 210 m of the hole.

Figure [F48](#) compares spectral gamma ray logs acquired by the HNGS in the triple combo and FMS-sonic tool strings. The gamma ray measurement is highly attenuated when the tool is inside the bottom-hole assembly and the drill pipe (above 83 m WMSF for the triple combo and above 139 m WMSF for the FMS-sonic tool string), and data in this interval should only be used qualitatively. The total gamma ray log is very similar in the two passes illustrated in Figure [F48](#); in the spectral data, some features are repeatable (e.g., the U peak at the seafloor), while others are less so (e.g., the Th peak at ~150 m WMSF). Spectral gamma ray features that are not repeatable in different passes may not be reliable.

In Hole U1338B, we also acquired FMS electrical resistivity images. The quality of these measurements depends on close contact between the measuring pads on the tool and the borehole wall. FMS borehole images are good quality between ~190 m WMSF and the base of the logged interval, where they reproduce sediment layers in detail.

Logging units

Downhole log measurements of bulk density, electrical resistivity, and *P*-wave velocity in Hole U1338B correlate very well (Fig. [F47](#)). The likely reason is that variations in sediment composition result in variations of porosity, and changes in porosity affect similarly bulk density, resistivity, and *P*-wave velocity. High porosities obviously result in low bulk densities. Also, resistivity variations in water-saturated sediments are controlled by variations in pore water content, which is the component of bulk sediment that conducts electricity. Finally, laboratory measurements and rock-physics models show that *P*-wave velocities in sediments decrease with increasing porosity. Details on these fundamental relationships between porosity and logged properties are given by Hearst and Nelson (1985) and Ellis and Singer (2007).

Downhole logs of gamma ray radioactivity (Fig. [F48](#)) are controlled by the sediment content of naturally occurring radioactive elements (K, U, and Th) and do not closely depend on porosity. The most significant feature in the gamma ray logs is the peak in U content at the seafloor. The seafloor peak is notably large, as it is attenuated because the tool is measuring through the drill pipe (see above) and it agrees

with natural gamma ray counts made on the cores immediately below the seafloor (see “[Physical properties](#)”). Gamma ray data at Site U1337 also showed a clear U peak at 240 m WMSF over a ~40 cm thick chert layer; this chert layer was also seen at Site U1338 in the same stratigraphic position, but no corresponding U peak is apparent in the downhole gamma ray data (Fig. [F48](#)). The reason could be that the chert layer at Site U1338 is only ~16 cm thick, as shown by the FMS resistivity images (see below). The vertical resolution of the HNGS measurements is ~50 cm (see “[Downhole measurements](#)” in the “[Methods](#)” chapter).

We divided the logged section into three units on the basis of the overall variation of density, resistivity, and *P*-wave velocity. Logging Unit 1 (from the top of the logged interval to 244 m WMSF) has low densities and resistivities that are variable but show no trend with depth. The transition between logging Units 1 and 2 is marked by a distinct increase in logged densities and resistivities and corresponds to the transition between lithologic Units II and III (see “[Lithostratigraphy](#)”). While density and resistivity do not show a clear trend with depth in logging Units 1 and 2, Unit 3 (from 380 m WMSF to the base of the logged interval) displays an increase with depth of density and resistivity. This increase is probably caused by lithification of the pelagic carbonate oozes in lithologic Unit III (see “[Lithostratigraphy](#)”). Logging Unit 3 is only ~30 m thick in Hole U1338B, but it can be clearly identified by correlating the density and resistivity curves at Sites U1337 and U1338, which are very similar.

Core-log correlation

Figure [F49](#) shows a notable interval in the FMS images with more conductive layers (darker color in the images) alternating with more resistive layers (lighter color). When compared to other downhole logging data from this site, these conductive bands correlate with lower values of resistivity and bulk density measured by the modified triple combo tool string (Fig. [F49C](#), [F49D](#)). Here we make a first attempt to correlate the spliced core images to the continuous downhole log data. The Site U1338 core image splice (see “[Stratigraphic correlation and composite section](#)”) has been uniformly reduced in length by 11% to account for core expansion on recovery, and we concentrated on the interval spanned by Cores 25H, 26H, 27H, and 28H. On closer inspection, the more conductive bands in the statically normalized FMS images match well with darker, more silica rich units in the core, and the more resistive bands match with the more carbonate rich intervals. Five main conductive bands are observed in this depth interval (230–

252 m WSF), highlighted by gray boxes in Figure F49. In these carbonate-rich sediments the logged density and resistivity are primarily influenced by changes in porosity (carbonate-rich sediments being less porous and silica-rich sediments more porous). The presence of these alternating units likely relates to changes in climatic and paleoceanographic conditions, as shown by the cyclicity in carbonate deposition.

At Site U1337 the process of coring the four holes was made more challenging by the presence of a ~40 cm thick chert layer. At Site U1338 evidence of a chert layer was seen in Hole U1338A and was confirmed by the logging data in Hole U1338B. The downhole logging data, particularly the FMS images, clearly identify the chert layer as a very resistive unit ~16 cm thick (Fig. F50, chert highlighted by a gray box); less than half the thickness of the chert unit seen at Site U1337. The high-resolution density measurements also highlight the location of the chert unit as a relatively dense layer. However, because of the very thin nature of the unit, it is probably not fully resolved and its density may be underestimated. The SFLU high, which correlated well with the chert unit imaged in Hole U1337A, is offset below the chert in Hole U1338B. The reason behind this will require further processing of the logging data and will be followed up postexpedition. Additionally, the gamma ray peak (a U peak) that was observed at the chert in the downhole logging data at Site U1337 is not seen here. As noted earlier, the chert layer is too thin to be resolved by the HNGS. Similarly, the thin chert layer at Site U1338 is associated with a silica-rich sediment layer immediately above it, seen in the FMS images as a dark colored, conductive band, and a lower resistivity and density value. This silica-rich layer is clearly visible in the core image splice (see “[Stratigraphic correlation and composite section](#)”), which has been uniformly reduced in length by 11%, as a distinctly darker sediment interval.

Vertical seismic profile

Figure F51A shows the stacked waveforms measured at 14 stations (190.6–415.7 m WSF) by the vertical direction geophone in the VSI. The waveforms are noticeably noisier than in the other VSP taken in Hole U1337A. The waveforms show clear first arrivals, but they do not display the basement reflection observed in the Hole U1337A VSP.

Table T26 lists the values of the measured and corrected one-way arrival times in the Hole U1338B VSP. Measured traveltimes are the differences between the arrival of the acoustic pulse at a hydrophone located immediately below the air gun source

and the arrival at the borehole receiver. Corrected traveltimes are traveltimes from the sea surface to the borehole receiver and account for the depth of the air guns (7 m below sea level) and the depth of the hydrophone below the air guns (2 m). More details on the VSP measurement procedure are in “[Downhole measurements](#)” in the “[Methods](#)” chapter.

Figure F51B shows the relationship between depth below seafloor in Hole U1338B and the TWT, which is the traveltime to reflectors in surface seismic sections. To construct this relationship, we start from the TWT from sea level to the seafloor (5.5862 s), computed from the uncorrected seafloor depth measured by the ship’s echo sounder (4189.6 m). The difference between this time and the arrival time to the shallowest receiver in the VSP gives an average *P*-wave velocity of 1500 m/s between the seafloor and 214.1 m WSF. At first approximation, the traveltime-depth relationship in Figure F51B assumes this constant velocity in the interval 0–190.6 m WSF. The dependence of the arrival times on depth in the VSP receiver array can be fit very closely by a second-degree polynomial

$$t(z) = 5.5796 + (1.5037 \times 10^{-3})z - (6.8064 \times 10^{-7})z^2,$$

where *t* is TWT (s) and *z* is depth below seafloor (190.6 ≤ *z* ≤ 415.7 m WSF). The maximum residual on this fit is 1.7 ms and the root-mean-square residual is 0.94 ms.

The variation of *P*-wave velocity in the depth interval spanned by the VSP receiver array can be obtained from the derivative of the time-depth relationship above, which gives

$$V(z) = [(0.75186 \times 10^{-3}) - (6.8064 \times 10^{-7})z]^{-1},$$

where *V* is *P*-wave velocity (m/s) and *z* is depth (190.6 ≤ *z* ≤ 415.7 m WSF). This relationship is compared to the velocities measured by acoustic logging with the DSI in Figure F47. The acoustic logging measurements contain small-scale details in the velocity structure that cannot be resolved by the VSP arrival time data. Whereas Site U1337 velocities from the VSP and from acoustic logging showed a similar trend in depth, at Site U1338 overall VSP velocities are somewhat higher than those measured by acoustic logging. The reason for this difference is not clear, and resolving it will require further processing of the VSP and acoustic logging data.

The traveltime-depth relationship allows for correlating stratigraphic events at Site U1338 to reflections in the surface seismic data. In Figure F52 we correlate the downhole logging results in Hole U1338B to seis-

mic reflection Line 1 of the AMAT-03 site survey in the proposed Site PEAT-8 area, which crosses the location of Site U1338 at Shotpoint 35658. To make an accurate correlation, the TWTs in the seismic reflection line were shifted so that the seafloor reflection time (originally estimated at 5.63 s) matched the more accurate TWT to the seafloor measured by the *JOIDES Resolution* echo sounder (5.5862 s; see above).

Reflections in the seismic line correspond to fluctuations in bulk density and velocity; for example, an increase in density at 130 m WMSF matches a reflection event at ~5.76 s TWT. The seismic reflection record at Site U1338 does not show a sequence of reflectors as rich and well resolved as that observed at Site U1337. Nonetheless, the preliminary well to seismic correlation of Figure F52 can be the starting point in assembling an up to date, age-calibrated interpretation of the seismic stratigraphy and of the Neogene sedimentation history in the equatorial Pacific (e.g., Mayer et al., 1985; Mitchell et al., 2003).

Heat flow

Downhole temperature measurements at Site U1338 consisted of seven APCT-3 measurements in Holes U1338A and U1338C (Table T27). Measured temperatures ranged from 3.33°C at 40.7 m DSF to 12.69°C at 316.4 m DSF and closely fit a linear geothermal gradient of 34.4°C/km (Fig. F53). The temperature at the seafloor was 1.65°C, based on the average of the measurements at the mudline in the seven temperature profiles. Thermal conductivity under in situ conditions was estimated from the laboratory-determined thermal conductivity using the method of Hyndman et al. (1974). The estimated in situ thermal conductivities in Figure F53 are as much as 2.3% below the measured laboratory values.

A simple estimate of the heat flow can be obtained from the product of the geothermal gradient times the average in situ thermal conductivity (0.97 W/m°C), which gives a value of 33.4 mW/m². However, thermal conductivity increases with depth, hence a more accurate heat flow value can be obtained from the slope of the temperature measurements plotted versus thermal resistance, as in the Bullard method (see Pribnow et al., 2000). The variation of thermal conductivity with depth was estimated by fitting a linear trend, and thermal resistance was calculated as the integral in depth of the inverse thermal conductivity (Pribnow et al., 2000). The fit between temperature and thermal resistance gives a slightly higher heat flow of 33.6 mW/m², which is similar to values of nearby sites in the global heat flow database (Pollock et al., 1993).

References

- Abels, H.A., Hilgen, F.J., Krijgsman, W., Kruk, R.W., Raffi, I., Turco, E., and Zachariasse, W.J., 2005. Long-period orbital control on middle Miocene global cooling: integrated stratigraphy and astronomical tuning of the Blue Clay Formation on Malta. *Paleoceanography*, 20(4):PA4012. doi:10.1029/2004PA001129
- Adkins, J.F., and Schrag, D.P., 2003. Reconstructing Last Glacial Maximum bottom water salinities from deep-sea sediment pore fluid profiles. *Earth Planet Sci. Lett.*, 216:109–123. doi:10.1016/S0012-821X(03)00502-8
- Backman, J., and Raffi, I., 1997. Calibration of Miocene nannofossil events to orbitally tuned cyclostratigraphies from Ceara Rise. In Shackleton, N.J., Curry, W.B., Richter, C., and Bralower, T.J. (Eds.), *Proc. ODP, Sci. Results*, 154: College Station, TX (Ocean Drilling Program), 83–99. doi:10.2973/odp.proc.sr.154.101.1997
- Baker, P.A., Gieskes, J.M., and Elderfield, H., 1982. Diagenesis of carbonates in deep-sea sediments—evidence from Sr²⁺/Ca²⁺ ratios and interstitial dissolved Sr²⁺ data. *J. Sediment. Petrol.*, 52:71–82.
- Baldauf, J.G., and Iwai, M., 1995. Neogene diatom biostratigraphy for the eastern equatorial Pacific Ocean, Leg 138. In Pisias, N.G., Mayer, L.A., Janecek, T.R., Palmer-Julson, A., and van Andel, T.H. (Eds.), *Proc. ODP, Sci. Results*, 138: College Station, TX (Ocean Drilling Program), 105–128. doi:10.2973/odp.proc.sr.138.107.1995
- Banner, F.T., and Blow, W.H., 1965. Progress in the planktonic foraminiferal biostratigraphy of the Neogene. *Nature (London, U. K.)*, 208:1164–1166. doi:10.1038/2081164a0
- Barckhausen, U., Engels, M., Cande, S., Ranero, C.R., and Weinrebe, W., 2005. New insights into the Farallon plate break-up. *Eos, Trans. Am. Geophys. Union*, 86(52)(Suppl.):GP33B-07. (Abstract)
- Barron, J.A., and Baldauf, J.G., 1989. Tertiary cooling steps and paleoproductivity as reflected by diatoms and biogenic siliceous sediments. In Berger, W.H., Smetacek, V.S., and Wefer, G. (Eds.), *Productivity of the Ocean: Present and Past*: Berlin (Springer), 341–354.
- Berggren, W.A., Kent, D.V., Swisher, C.C., III, and Aubry, M.-P., 1995. A revised Cenozoic geochronology and chronostratigraphy. In Berggren, W.A., Kent, D.V., Aubry, M.-P., and Hardenbol, J. (Eds.), *Geochronology, Time Scales and Global Stratigraphic Correlation*. Spec. Publ.—SEPM (Soc. Sediment. Geol.), 54:129–212.
- Blow, W.H., 1969. Late middle Eocene to Recent planktonic foraminiferal biostratigraphy. In Brönnimann, P., and Renz, H.H. (Eds.), *Proc. First Int. Conf. Planktonic Microfossils, Geneva, 1967*: Leiden (E.J. Brill), 1:199–422.
- Bukry, D., 1971. *Discoaster* evolutionary trends. *Micropaleontology*, 17(1):43–52. doi:10.2307/1485036
- Busch, W.H., Vanden Berg, M.D., and Masau, P.E., 2006. Velocity and density of Paleogene equatorial sediments: variation with sediment composition. In Wilson, P.A., Lyle, M., and Firth, J.V. (Eds.), *Proc. ODP, Sci. Results*,

- 199: College Station, TX (Ocean Drilling Program), 1–31. doi:10.2973/odp.proc.sr.199.226.2006
- Cande, S.C., LaBrecque, J.L., Larson, R.L., Pitmann, W.C., III, Golovchenko, X., and Haxby, W.F., 1989. *Magnetic Lineations of the World's Ocean Basins*. AAPG Map Ser., 13.
- Chaisson, W.P., and Pearson, P.N., 1997. Planktonic foraminifer biostratigraphy at Site 925: middle Miocene–Pleistocene. In Shackleton, N.J., Curry, W.B., Richter, C., and Bralower, T.J. (Eds.), *Proc. ODP, Sci. Results*, 154: College Station, TX (Ocean Drilling Program), 3–31. doi:10.2973/odp.proc.sr.154.104.1997
- Ellis, D.V., and Singer, J.M., 2007. *Well Logging for Earth Scientists*, 2nd edition: Dordrecht, The Netherlands (Springer).
- Engels, M., Barckhausen, U., and Gee, J.S., 2007. A new towed marine vector magnetometer: methods and results from a Central Pacific cruise. *Geophys. J. Int.*, 172(1): 115–129. doi:10.1111/j.1365-246X.2007.03601.x
- Farrell, J.W., Raffi, I., Janecek, T.R., Murray, D.W., Levitan, M., Dadey, K.A., Emeis, K.-C., Lyle, M., Flores, J.-A., and Hovan, S., 1995. Late Neogene sedimentation patterns in the eastern equatorial Pacific Ocean. In Pisias, N.G., Mayer, L.A., Janecek, T.R., Palmer-Julson, A., and van Andel, T.H. (Eds.), *Proc. ODP, Sci. Results*, 138: College Station, TX (Ocean Drilling Program), 717–756. doi:10.2973/odp.proc.sr.138.143.1995
- Gieskes, J.M., 1981. Deep-sea drilling interstitial water studies: implications for chemical alteration of the oceanic crust, Layers I and II. In Warme, J.E., Douglas, R.G., and Winterer, E.L. (Eds.), *The Deep Sea Drilling Project: A Decade of Progress*. Spec. Publ.—Soc. Econ. Paleontol. Mineral., 32:149–167.
- Hearst, J.R., and Nelson, P.H., 1985. *Well Logging for Physical Properties*: New York (McGraw-Hill).
- Hilgen, F.J., Krijgsman, W., Raffi, I., Turco, E., and Zachariasse, W.J., 2000. Integrated stratigraphy and astronomical calibration of the Serravallian/Tortonion boundary section at Monte Gibliscemi (Sicily, Italy). *Mar. Micropaleontol.*, 38(3–4):181–211. doi:10.1016/S0377-8398(00)00008-6
- Holbourn, A., Kuhnt, W., Schulz, M., and Erlenkeuser, H., 2005. Impacts of orbital forcing and atmospheric carbon dioxide on Miocene ice-sheet expansion. *Nature (London, U. K.)*, 438(7067):483–487. doi:10.1038/nature04123
- Holbourn, A., Kuhnt, W., Schulz, M., Flores, J.-A., and Andersen, N., 2007. Orbitally-paced climate evolution during the middle Miocene “Monterey” carbon-isotope excursion. *Earth Planet. Sci. Lett.*, 261(3–4):534–550. doi:10.1016/j.epsl.2007.07.026
- Huber, B.T., Olsson, R.K., and Pearson, P.N., 2006. Taxonomy, biostratigraphy and phylogeny of Eocene microporiferate planktonic foraminifera (*Jenkinsina*, *Cassigerinelloita*, *Chiloguembelina*, *Streptochilus*, *Zeauvergerina*, *Tenuitella*, and *Cassigerinella*) and problematica (*Dipsidripella*). In Pearson, P.N., Olsson, R.K., Huber, B.T., Hemleben, C., and Berggren, W.A. (Eds.), *Atlas of Eocene Planktonic Foraminifera*, Cushman Foundation Special Publication, 41:461–508.
- Hyndman, R.D., Erickson, A.J., and Von Herzen, R.P., 1974. Geothermal measurements on DSDP Leg 26. In Davies, T.A., Luyendyk, B.P., et al., *Init. Repts. DSDP*, 26: Washington, DC (U.S. Govt. Printing Office), 451–463. doi:10.2973/dsdp.proc.26.113.1974
- Keigwin, L.D., Jr., 1978. Pliocene closing of the Isthmus of Panama, based on biostratigraphic evidence from nearby Pacific Ocean and Caribbean Sea cores. *Geology*, 6(10):630–634. doi:10.1130/0091-7613(1978)6<630:PCOTIO>2.0.CO;2
- Kemp, A.E.S., and Baldauf, J.G., 1993. Vast Neogene laminated diatom mat deposits from the eastern equatorial Pacific Ocean. *Nature (London, U. K.)*, 362(6416):141–144. doi:10.1038/362141a0
- Koppers, A.A.P., Phipps Morgan, J., Morgan, J.W., and Staudigel, H., 2001. Testing the fixed hotspot hypothesis using ⁴⁰Ar/³⁹Ar age progressions along seamount trails. *Earth Planet. Sci. Lett.*, 185(3–4):237–252. doi:10.1016/S0012-821X(00)00387-3
- Kryc, K.A., Murray, R.W., and Murray, D.W., 2003. Elemental fractionation of Si, Al, Ti, Fe, Ca, Mn, P, and Ba in five marine sedimentary reference materials: results from sequential extractions. *Anal. Chim. Acta*, 487(1):117–128. doi:10.1016/S0003-2670(03)00492-6
- Kurschner, W.M., Kvacek, Z., and Dilcher, D.L., 2008. The impact of Miocene atmospheric carbon dioxide fluctuations on climate and the evolution of terrestrial ecosystems. *Proc. Natl. Acad. Sci. U. S. A.*, 105(2):449–453. doi:10.1073/pnas.0708588105
- Lewis, A.R., Marchant, D.R., Ashworth, A.C., Hemming S.R., and Machlus M.L., 2007. Major middle Miocene global climate change: evidence from East Antarctica and the Transantarctic Mountains. *GSA Bull.*, 119:1449–1461.
- Lourens, L.J., Hilgen, F.J., Laskar, J., Shackleton, N.J., and Wilson, D., 2004. The Neogene period. In Gradstein, F.M., Ogg, J., et al. (Eds.), *A Geologic Time Scale 2004*: Cambridge (Cambridge Univ. Press), 409–440.
- Lyle, M., 1983. The brown-green color transition in marine sediments: a marker of the Fe(III)-Fe(II) redox boundary. *Limnol. Oceanogr.*, 28:1026–1033.
- Lyle, M., 2003. Neogene carbonate burial in the Pacific Ocean. *Paleoceanography*, 18(3):1059. doi:10.1029/2002PA000777
- Lyle, M., Dadey, K.A., and Farrell, J.W., 1995. The late Miocene (11–8 Ma) eastern Pacific carbonate crash: evidence for reorganization of deep-water circulation by the closure of the Panama gateway. In Pisias, N.G., Mayer, L.A., Janecek, T.R., Palmer-Julson, A., and van Andel, T.H. (Eds.), *Proc. ODP, Sci. Results*, 138: College Station, TX (Ocean Drilling Program), 821–838. doi:10.2973/odp.proc.sr.138.157.1995
- Lyle, M., Heath, G.R., and Robbins, J.M., 1984. Transport and release of transition elements during early diagenesis: sequential leaching of sediments from MANOP Sites M and H. Part I. pH 5 acetic acid leach. *Geochim. Cosmochim. Acta*, 48(9):1705–1715. doi:10.1016/0016-7037(84)90026-7

- Majewski, W., 2003. Water-depth distribution of Miocene planktonic foraminifera from ODP Site 744, southern Indian Ocean. *J. Foraminiferal Res.*, 33(2):144–154. doi:10.2113/0330144
- Mayer, L.A., Shipley, T.H., Theyer, F., Wilkens, R.H., and Winterer, E.L., 1985. Seismic modeling and paleoceanography at Deep Sea Drilling Project Site 574. In Mayer, L., Theyer, F., Thomas, E., et al., *Init. Repts. DSDP*, 85: Washington, DC (U.S. Govt. Printing Office), 947–970. doi:10.2973/dsdp.proc.85.132.1985
- Mitchell, N.C., Lyle, M.W., Knappenberger, M.B., and Liberty, L.M., 2003. Lower Miocene to present stratigraphy of the equatorial Pacific sediment bulge and carbonate dissolution anomalies. *Paleoceanography*, 18(2):1038. doi:10.1029/2002PA000828
- Mix, A.C., Tiedemann, R., Blum, P., et al., 2003. *Proc. ODP, Init. Repts.*, 202: College Station, TX (Ocean Drilling Program). doi:10.2973/odp.proc.ir.202.2003
- Moore, T.C., Jr., Mitchell, N.C., Lyle, M., Backman, J., and Pälike, H., 2007. Hydrothermal pits in the biogenic sediments of the equatorial Pacific Ocean. *Geochem., Geophys., Geosys.*, 8(3):Q03015. doi:10.1029/2006GC001501
- Pagani, M., Arthur, M.A., and Freeman, K.H., 1999. Miocene evolution of atmospheric carbon dioxide. *Paleoceanography*, 14(3):273–292. doi:10.1029/1999PA900006
- Pearson, P.N., 1995. Planktonic foraminifer biostratigraphy and the development of pelagic caps on guyots in the Marshall Islands group. In Haggerty, J.A., Premoli Silva, I., Rack, F., and McNutt, M.K. (Eds.), *Proc. ODP, Sci. Results*, 144: College Station, TX (Ocean Drilling Program), 21–59. doi:10.2973/odp.proc.sr.144.013.1995
- Pearson, P.N., Norris, R.D., and Empson, A.J., 2001. *Mutabellia mirabilis* gen. et sp. Nov., a Miocene microporiferate planktonic foraminifer with an extreme level of intraspecific variability. *J. Foraminiferal Res.*, 31(2):120–132. doi:10.2113/0310120
- Peng, T.-H., Maier-Reimer, E., and Broecker, W.S. 1993. Distribution of ^{32}Si in the world ocean: model compared to observation. *Global Biogeochem. Cycles*, 7(2):463–474. doi:10.1029/93GB00686
- Pisias, N.G., Mayer, L.A., Janecek, T.R., Palmer-Julson, A., and van Andel, T.H. (Eds.), 1995. *Proc. ODP, Sci Results*, 138: College Station, TX (Ocean Drilling Program). doi:10.2973/odp.proc.sr.138.1995
- Pollack, H.N., Hurter, S.J., and Johnson, J.R., 1993. Heat flow from the earth's interior: analysis of the global data set. *Rev. Geophys.*, 31(3):267–280. doi:10.1029/93RG01249
- Pribnow, D.F.C., Kinoshita, M., and Stein, C.A., 2000. *Thermal Data Collection and Heat Flow Recalculations for ODP Legs 101–180*: Hanover, Germany (Inst. Joint Geosci. Res., Inst. Geowiss. Gemeinschaftsauf. [GGA]). <http://www-odp.tamu.edu/publications/heatflow/ODPReprt.pdf>
- Raffi, I., Backman, J., Fornaciari, E., Pälike, H., Rio, D., Lourens, L., and Hilgen, F., 2006. A review of calcareous nannofossil astrobiochronology encompassing the past 25 million years. *Quat. Sci. Rev.*, 25(23–24):3113–3137. doi:10.1016/j.quascirev.2006.07.007
- Raffi, I., Rio, D., d'Atri, A., Fornaciari, E., and Rocchetti, S., 1995. Quantitative distribution patterns and biomagnetostratigraphy of middle and late Miocene calcareous nannofossils from equatorial Indian and Pacific oceans (Leg 115, 130, and 138). In Pisias, N.G., Mayer, L.A., Janecek, T.R., Palmer-Julson, A., and van Andel, T.H. (Eds.), *Proc. ODP, Sci. Results*, 138: College Station, TX (Ocean Drilling Program), 479–502. doi:10.2973/odp.proc.sr.138.125.1995
- Stoll, H.M., Rosenthal, Y., and Falkowski, P., 2002. Climate proxies from Sr/Ca of coccolith calcite: calibrations from continuous culture of *Emiliania huxleyi*. *Geochim. Cosmochim. Acta*, 66(6):927–936. doi:10.1016/S0016-7037(01)00836-5
- Tessier, A., Campbell, P.G.C., and Bisson, M., 1979. Sequential extraction procedure for the speciation of particulate trace metals. *Anal. Chem.*, 51(7): 844–851. doi:10.1021/ac50043a017
- van Andel, T.H., Heath, G.R., and Moore, T.C., Jr., 1975. *Cenozoic History and Paleoceanography of the Central Equatorial Pacific Ocean: A Regional Synthesis of Deep Sea Drilling Project Data*. Mem.—Geol. Soc. Am., 143.
- Wade, B.S., and Olsson, R.K., 2009. Investigation of pre-extinction dwarfing in Cenozoic planktonic foraminifera. In Twitchett, R., and Wade, B.S. (Eds.), *Extinction, Dwarfing and the Lilliput Effect*. Palaeogeogr., Palaeoclimatol., Palaeoecol. Spec. Publ. doi:10.1016/j.palaeo.2009.08.026
- Zachos, J., Pagani, M., Sloan, L., Thomas, E., and Billups, K., 2001. Trends, rhythms, and aberrations in global climate 65 Ma to present. *Science*, 292(5517):686–693. doi:10.1126/science.1059412
- Zachos, J.C., Dickens, G.R., and Zeebe, R.E., 2008. An early Cenozoic perspective on greenhouse warming and carbon-cycle dynamics. *Nature (London, U. K.)*, 451(7176):279–283. doi:10.1038/nature06588

Publication: 30 October 2010
MS 320321-110

Figure F1. A. Site U1338 and PEAT program drill sites. F.Z. = fracture zone. B. Swath bathymetry from AMAT-03 site survey, Site U1338 region.

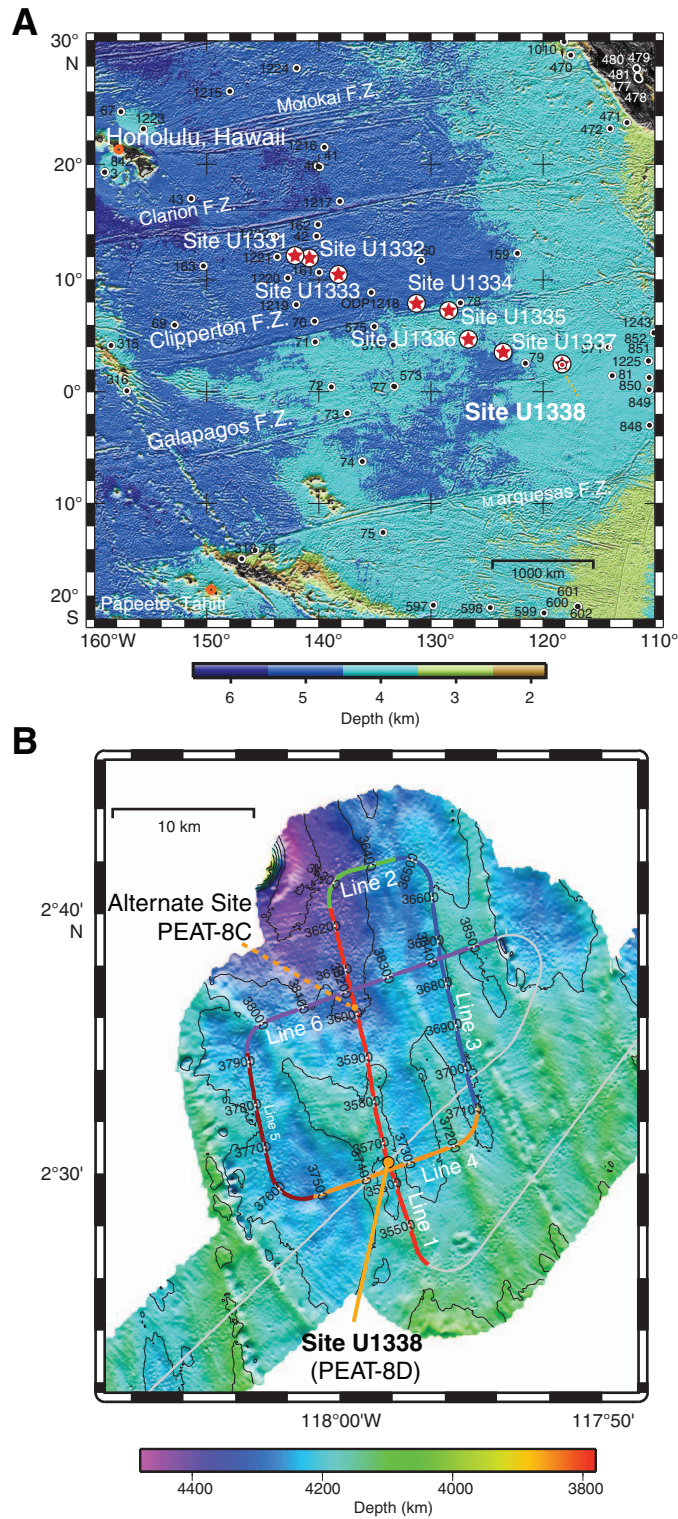




Figure F2. Seismic reflection Line 1 from AMAT-03 PEAT-8 survey. Data are 4-channel stacked and migrated, using a 250 inch³ generator-injector seismic source.

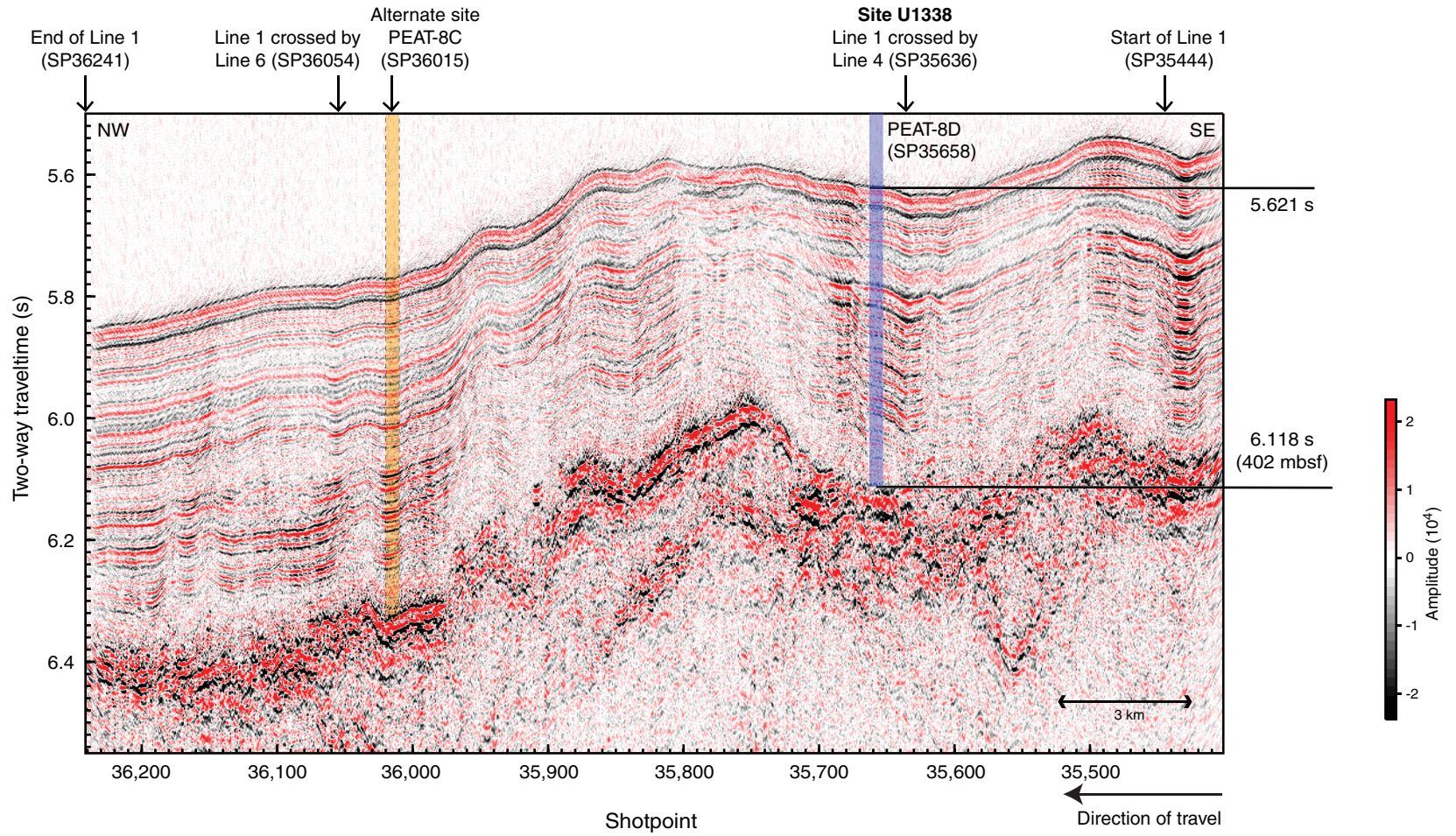


Figure F3. Site U1338 summary. Biostratigraphic zones and CaCO₃ contents mainly based on Hole U1338A. Light green circles = CaCO₃ contents from Hole U1338B. Core depth below seafloor for CaCO₃ samples from Hole U1338A were converted to core depth below seafloor from Hole U1338B. Magnetostratigraphy represents a spliced record from all holes and is plotted relative to corrected core composite depth below seafloor.

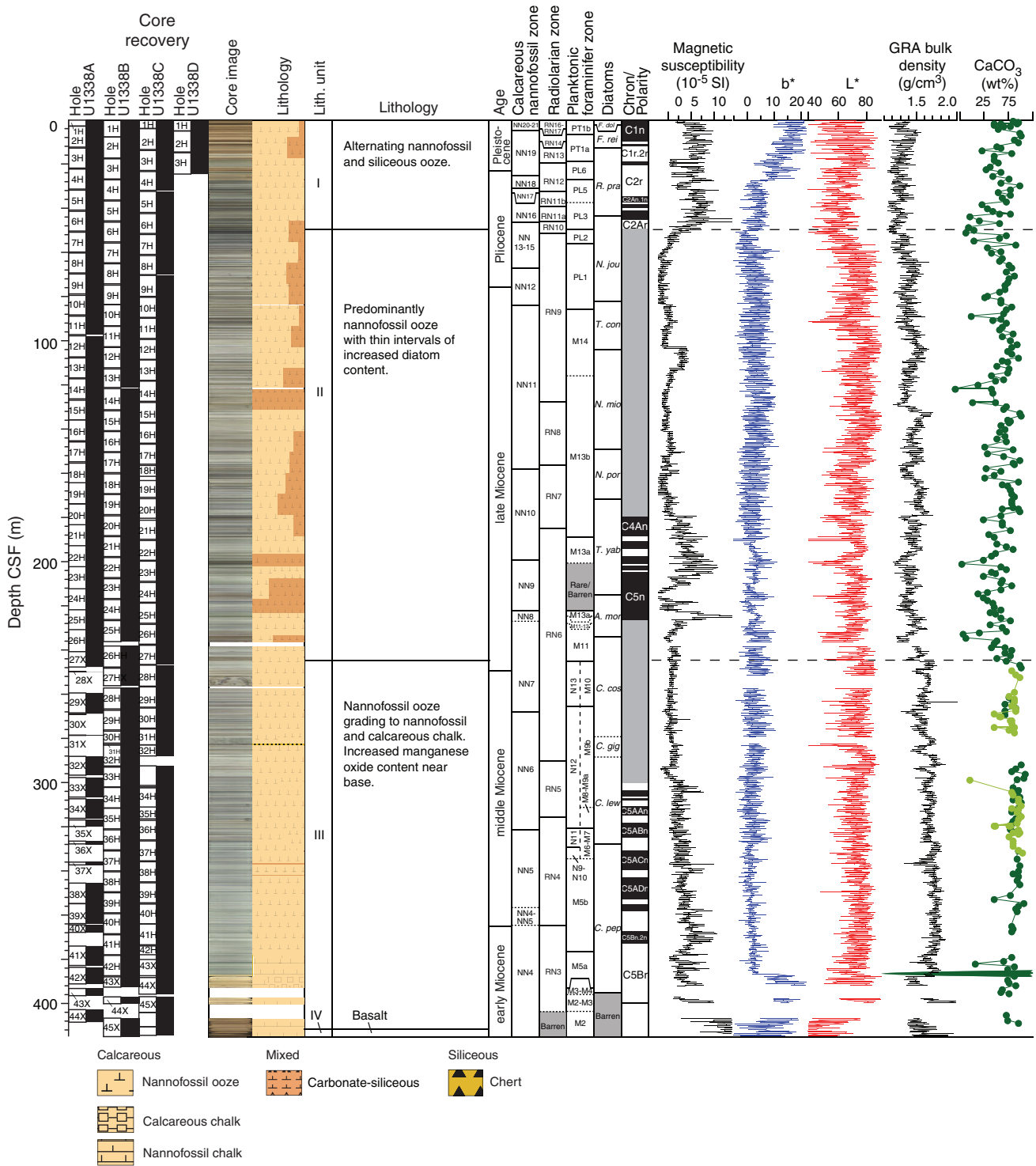


Figure F4. Downhole log measurement summary, Hole U1338B. TC = triple combo, MAD = moisture and density, IMPH = medium induction phasor-processed resistivity, SFLU = spherically focused resistivity, VSP = vertical seismic profile.

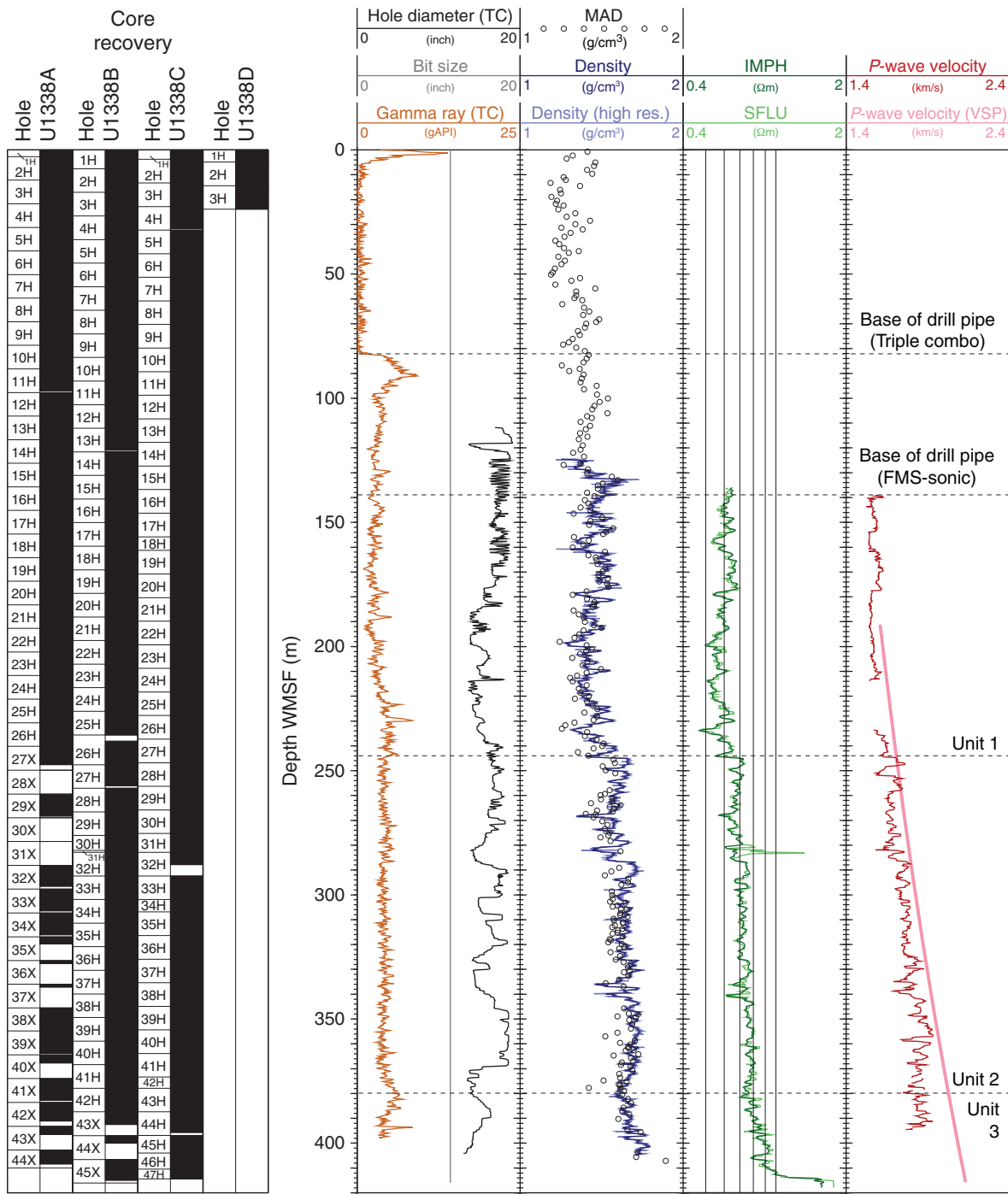


Figure F5. Lithostratigraphy summary, Site U1338. Biostratigraphic zones mainly based on Hole U1338A. CaCO₃ contents: dark green circles = Hole U1338A, light green circles = Hole U1338B. Other measurements are for Hole U1338B. CSF depths for CaCO₃ samples from Hole U1338A were converted to the CSF depths of Hole U1338B using the adjustments from Table U1338-I-1. Magnetostratigraphy represents a spliced record from all holes and is plotted relative to CCSF-B depth. See “**Biostratigraphy**” for clarification of zones. GRA = gamma ray attenuation; L*, b* = reflectance values of sediment as defined in the LAB color model.

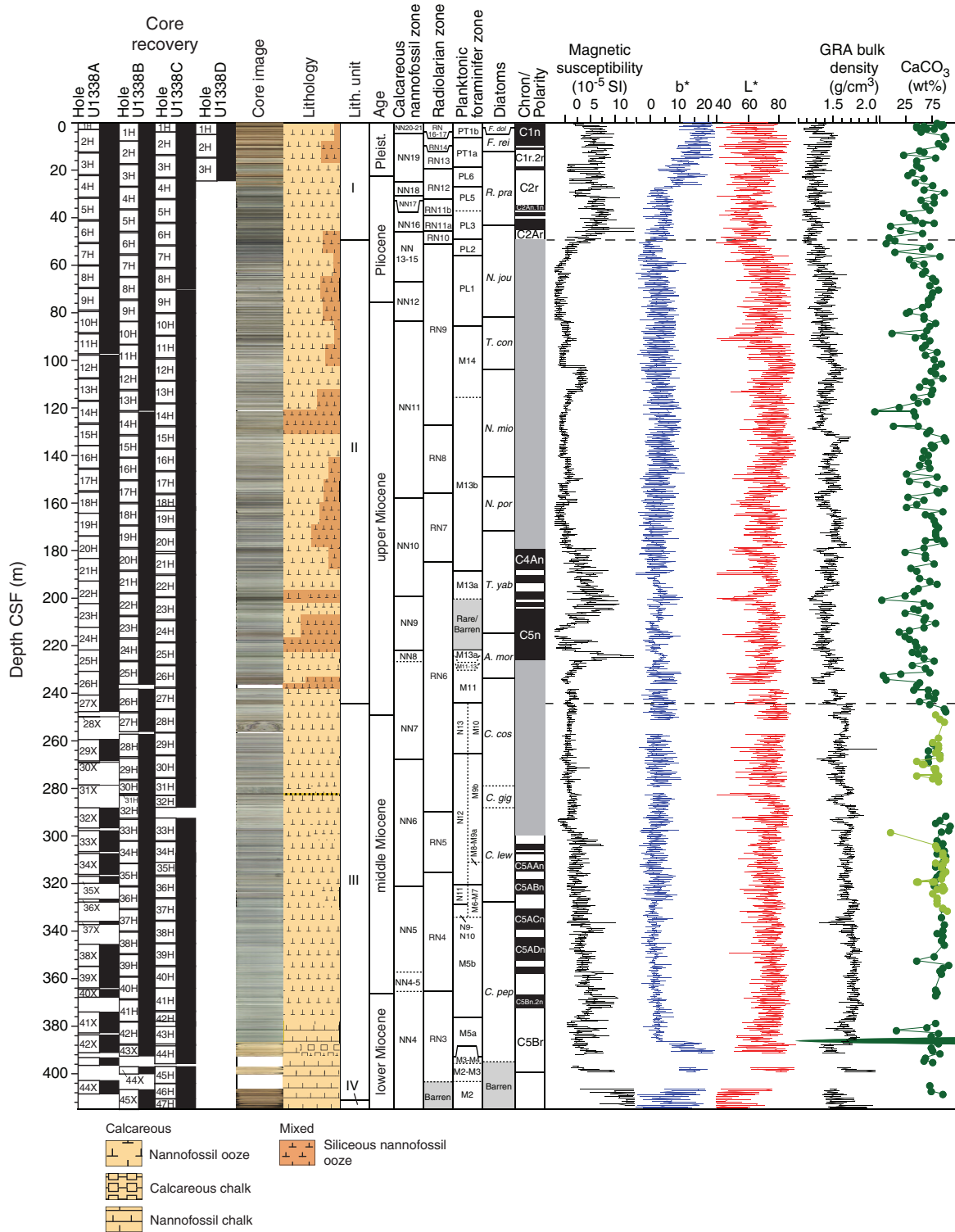


Figure F6. Smear slide results, Site U1338.

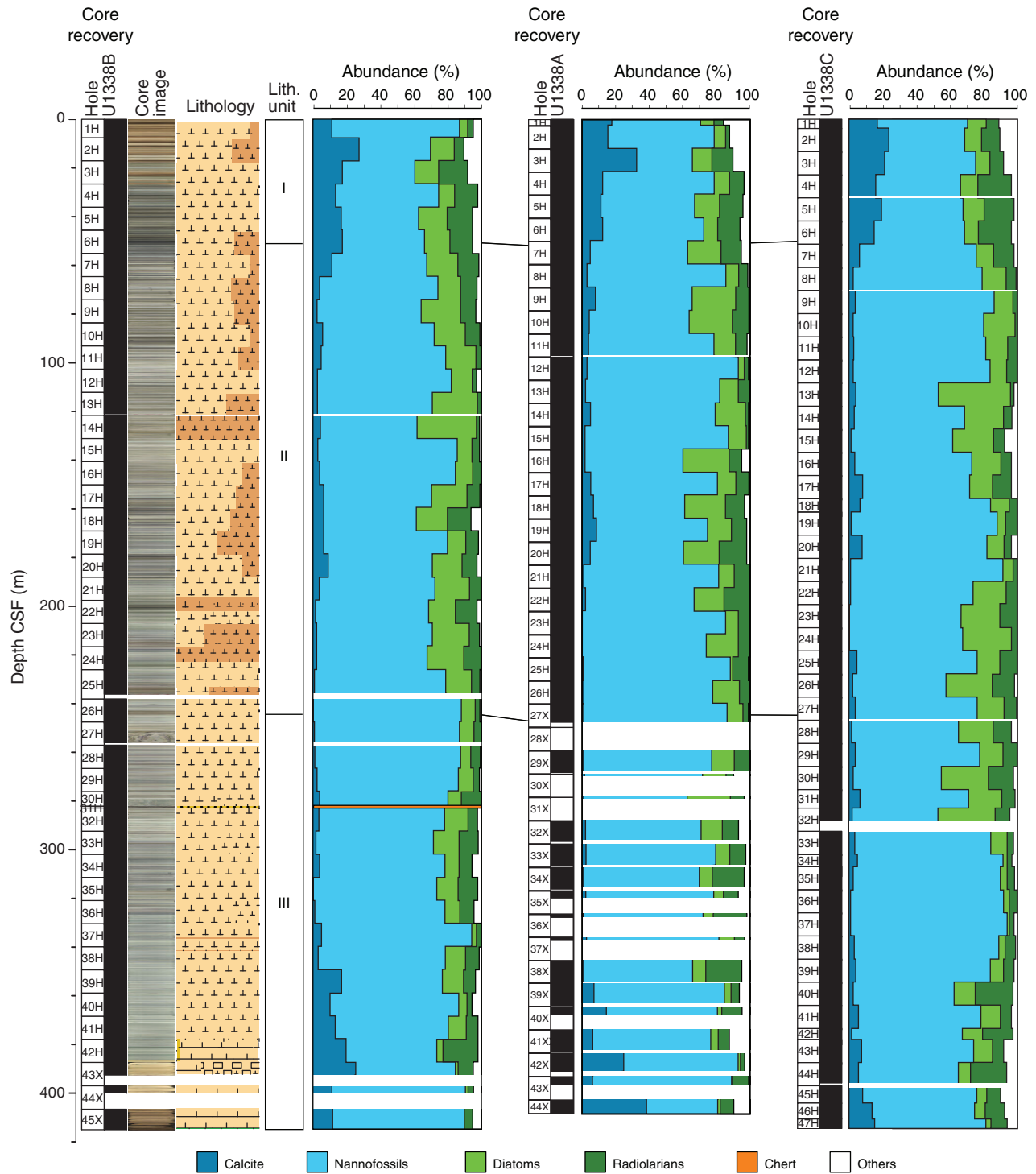


Figure F7. Photographs of smear slides indicating dominant lithologies of Units I–III. Right images = plane-polarized light, left images = cross-polarized light. **A.** Nannofossil ooze with calcites and radiolarians, Unit I (Sample 321-U1338B-4H-4, 110 cm). **B.** Diatom nannofossil ooze, Unit II (Sample 321-U1338B-17H-5, 81 cm). **C.** Nannofossil ooze with radiolarians and diatoms, Unit II (Sample 321-U1338B-19H-4, 110 cm). (**Continued on next page.**)

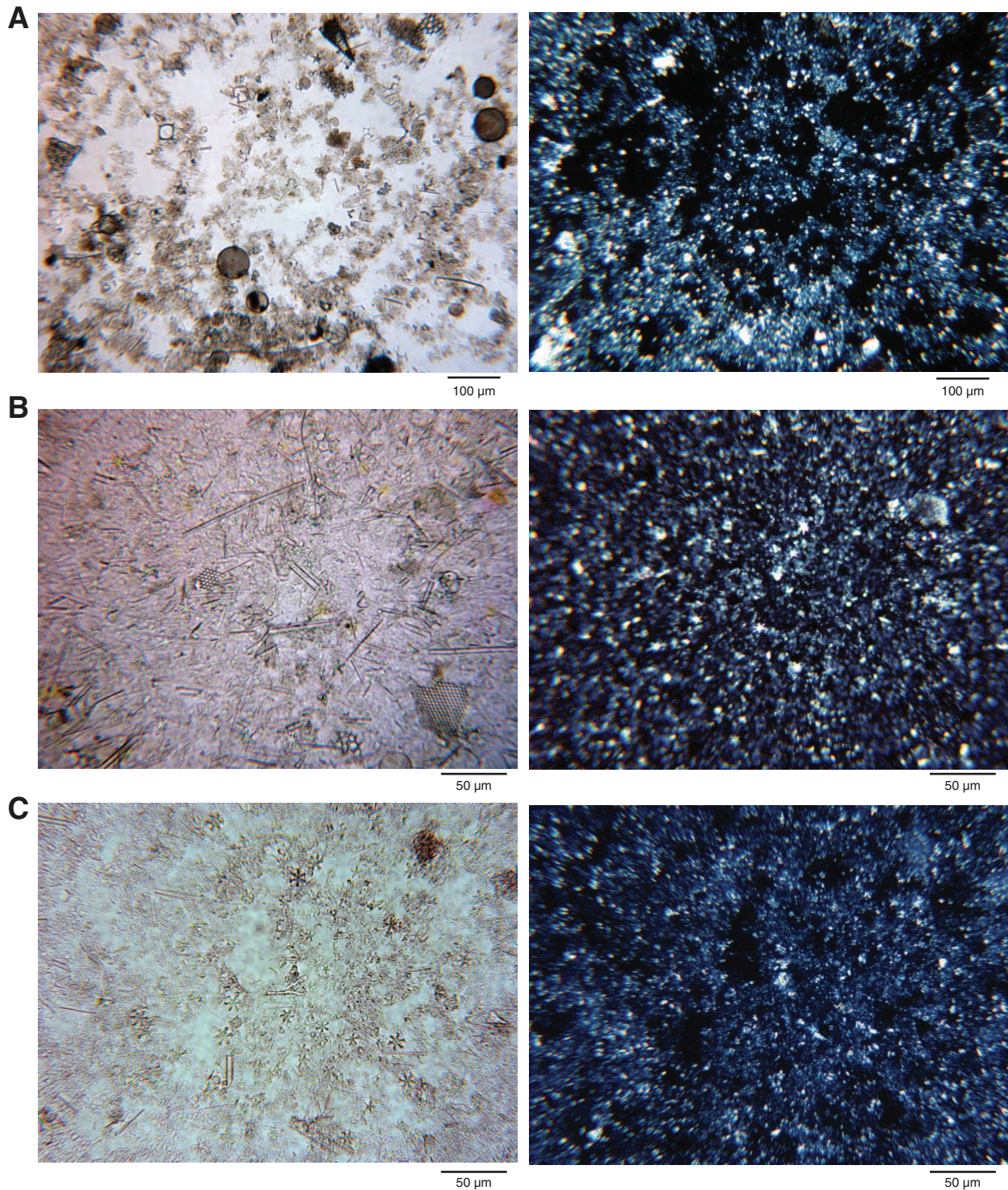


Figure F7 (continued). D. Nannofossil ooze, Unit III (Sample 321-U1338B-32H-3, 114 cm). E. Nannofossil chalk, Unit III (321-U1338B-44X-CC, 35 cm).

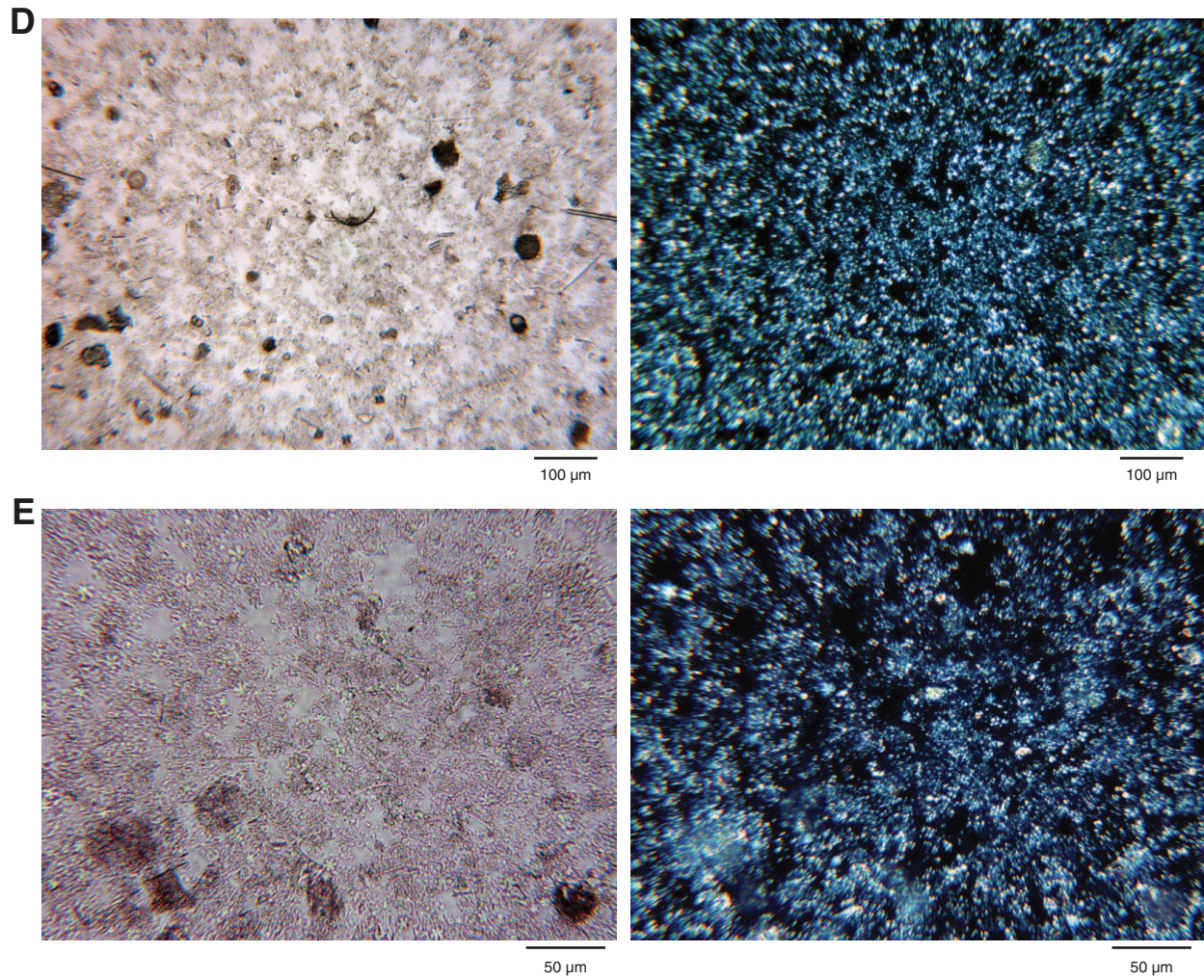


Figure F8. Lithologic Unit I-II transition (Cores 321-U1338B-6H and 7H). GRA = gamma ray attenuation, L^* , a^* , b^* = reflectance values of sediment as defined in the LAB color model.

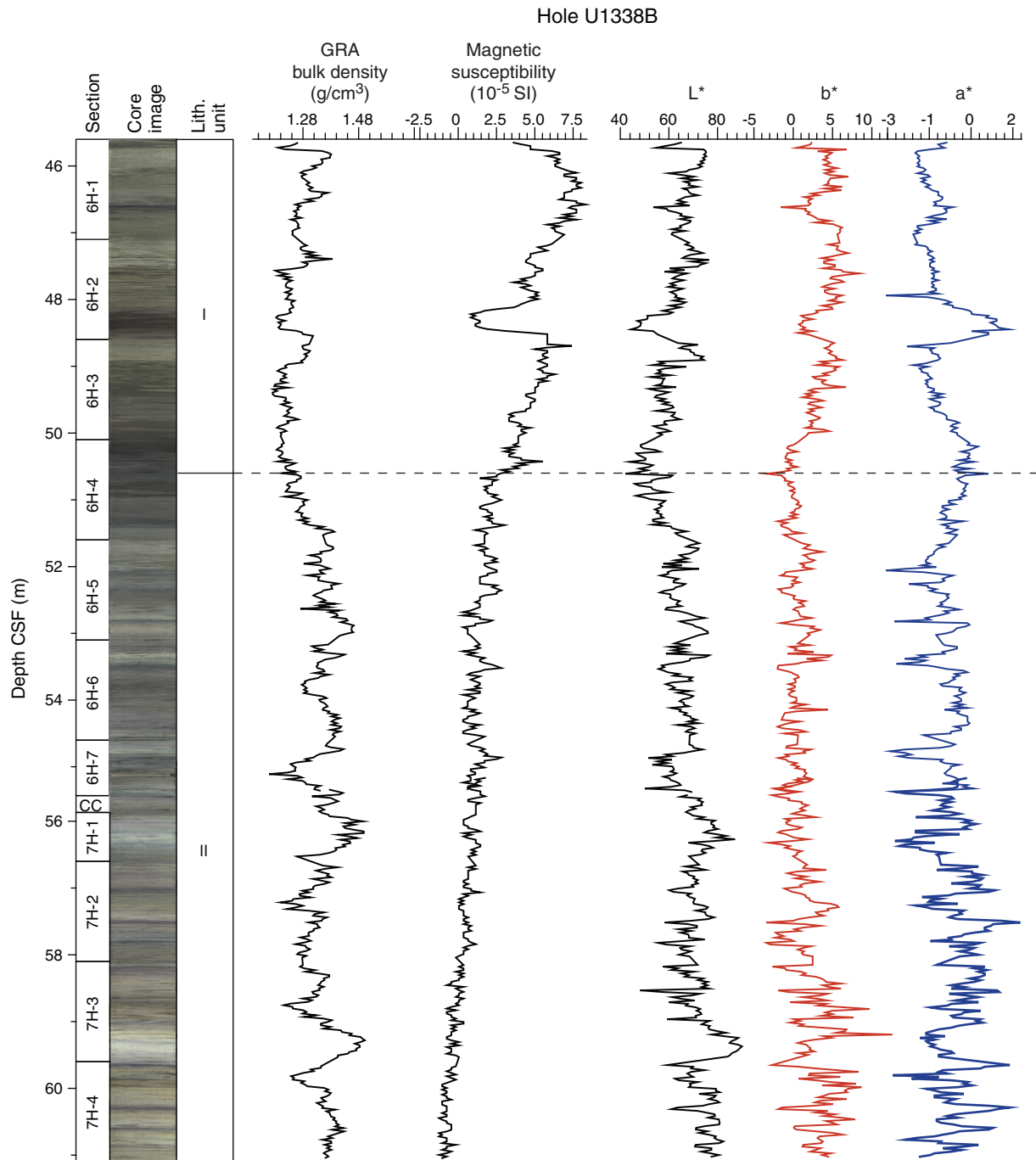


Figure F9. Intervals characteristic of lithologic Unit II (Cores 321-U1338A-13H through 24H). GRA = gamma ray attenuation, TOC = total organic carbon, L* = reflectance value of sediment as defined in the LAB color model.

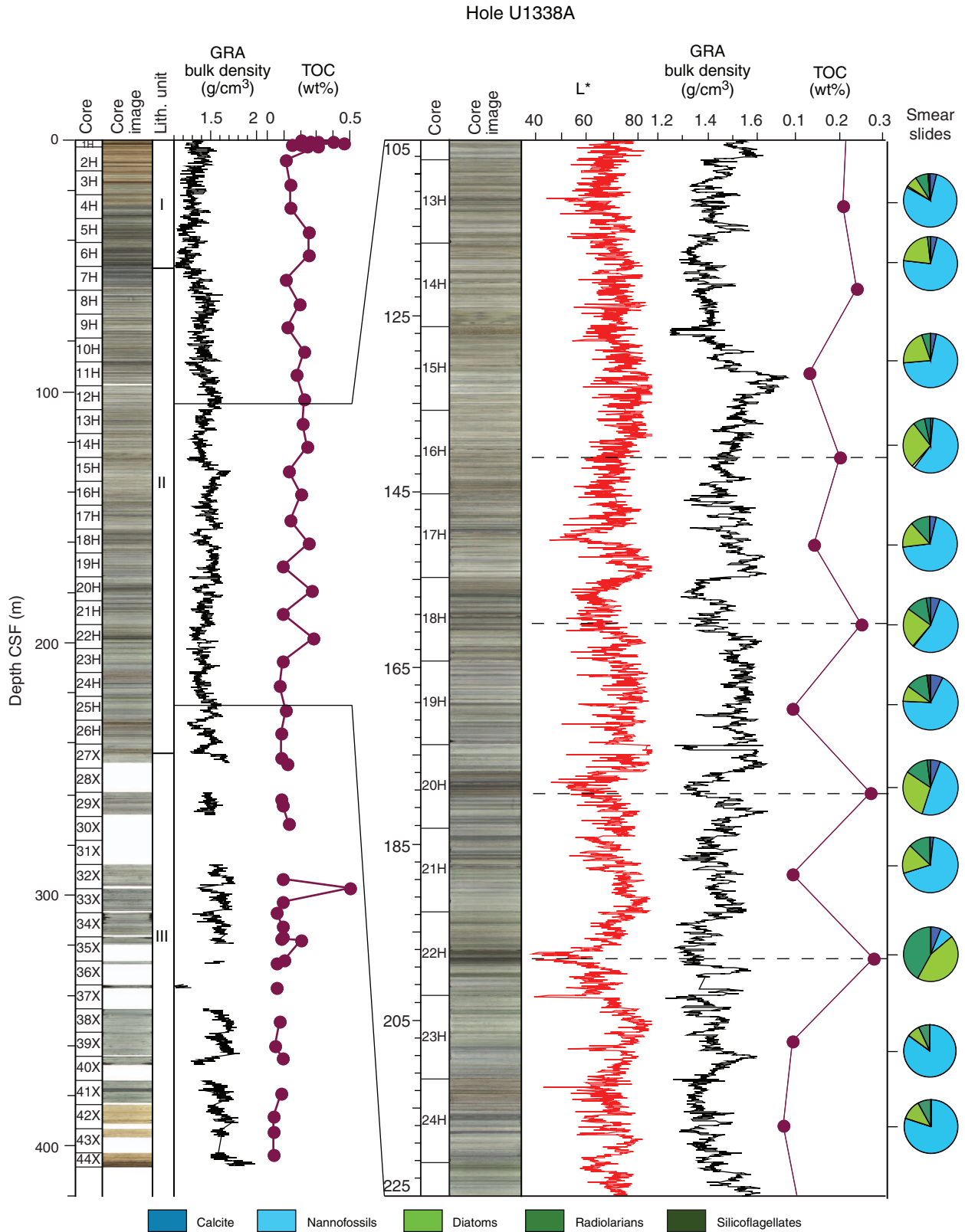


Figure F10. Lithologic Unit II–Unit III transition (Cores 321-U1338B-26H and 27H). GRA = gamma ray attenuation, L*, a*, b* = reflectance values of sediment as defined in the LAB color model.

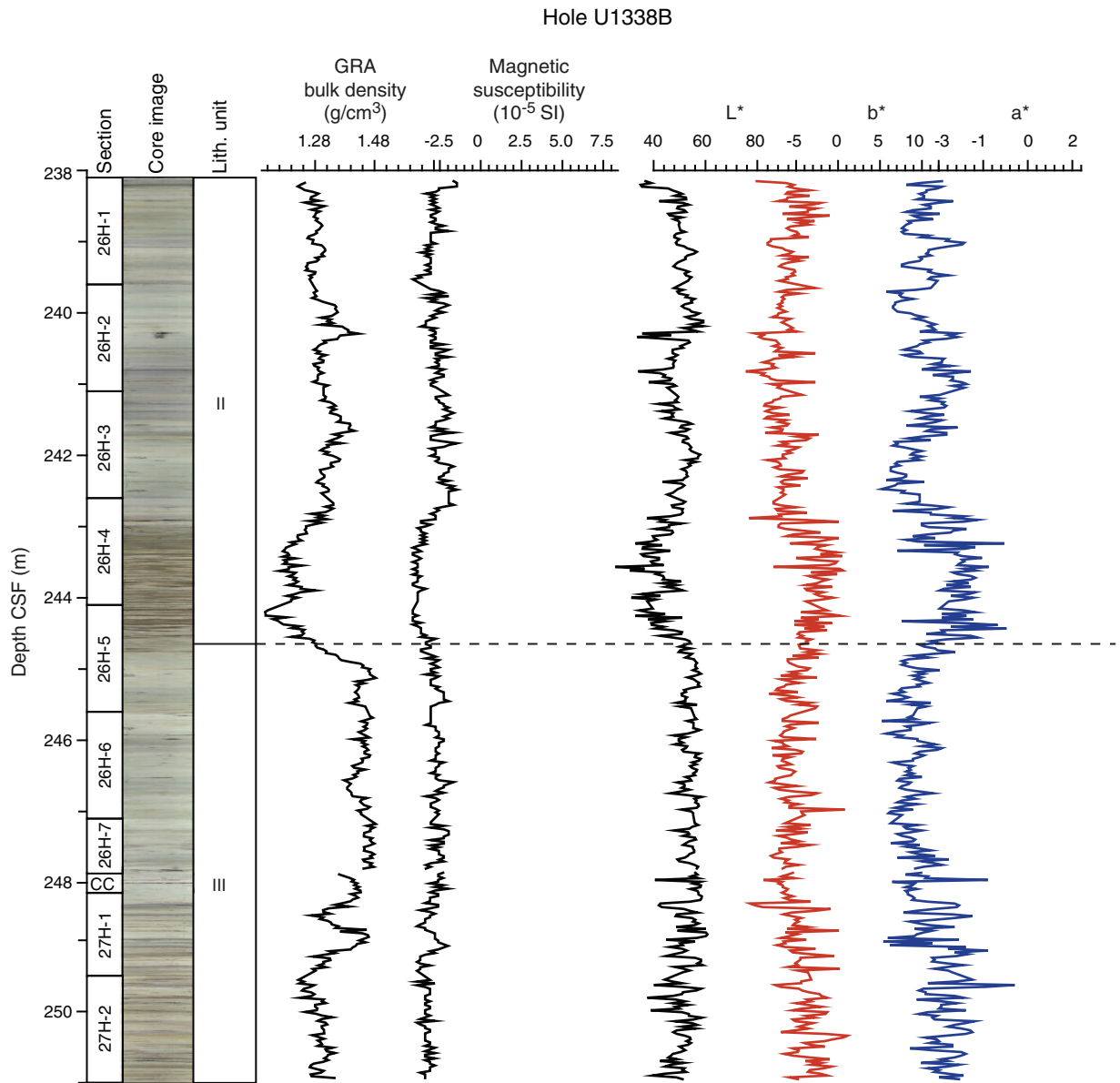


Figure F11. Line scan images and transmitted light microscope photograph (plane-polarized light, 250×) of a smear slide from a pyritized siliceous microfossil layer.

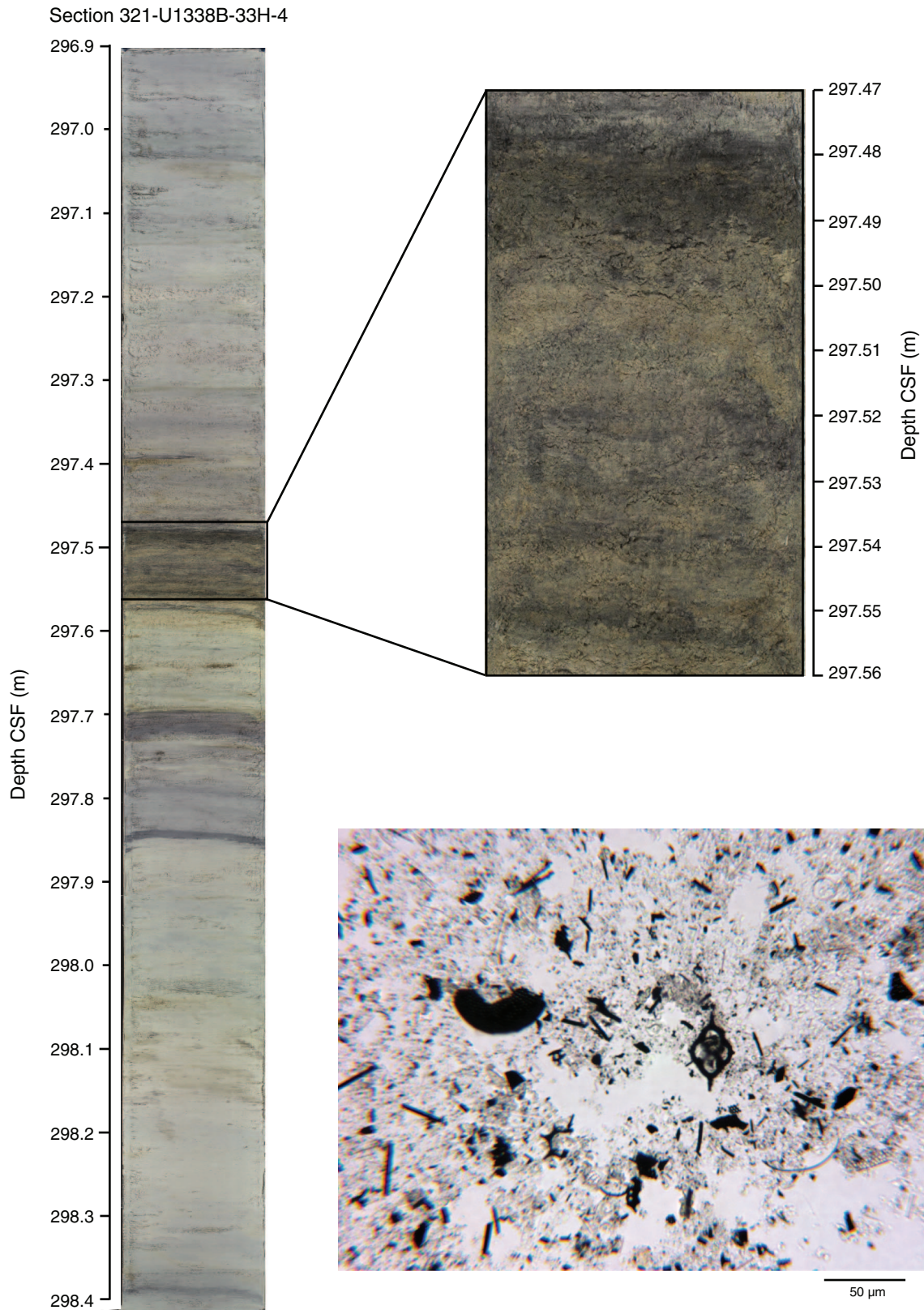


Figure F12. Green to yellow to brown transitions in the lowermost part of Unit III (Cores 321-U1338C-43H through 47H). b^* = reflectance value of sediment as defined in the LAB color model.

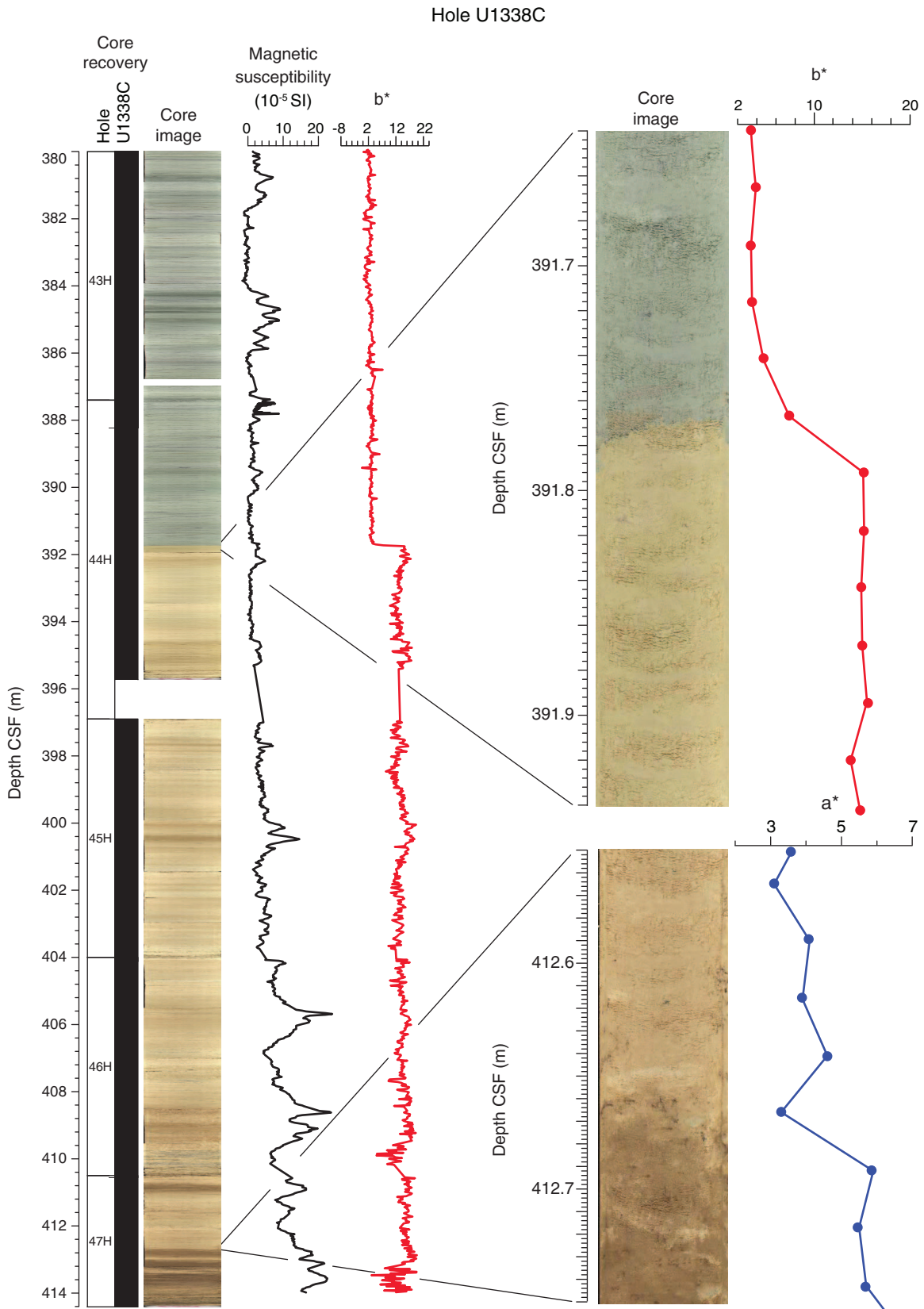


Figure F13. Integrated calcareous and siliceous microfossil biozonation, Site U1338.

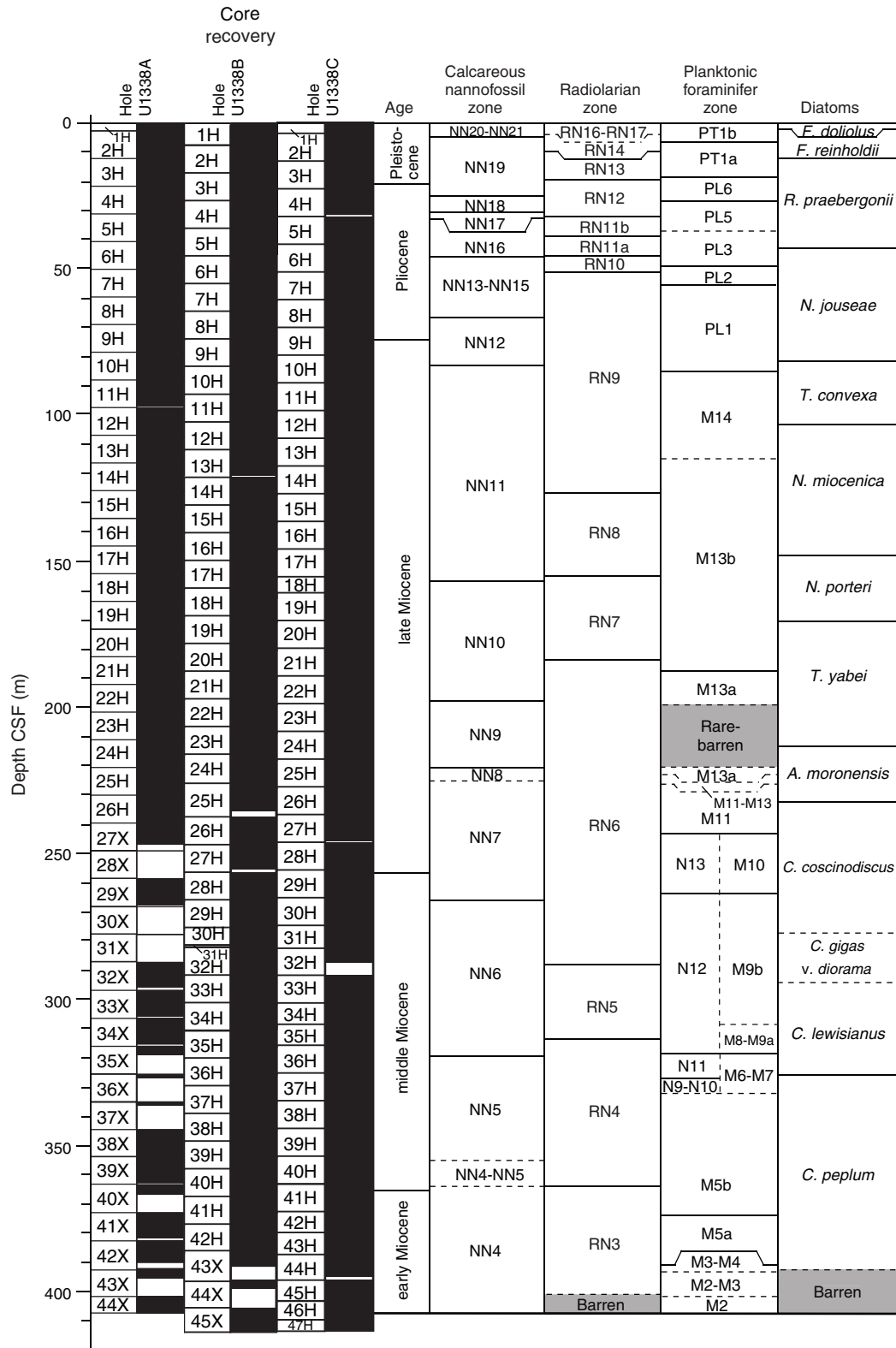


Figure F14. Linear sedimentation rates and chronostratigraphic markers, Site U1338.

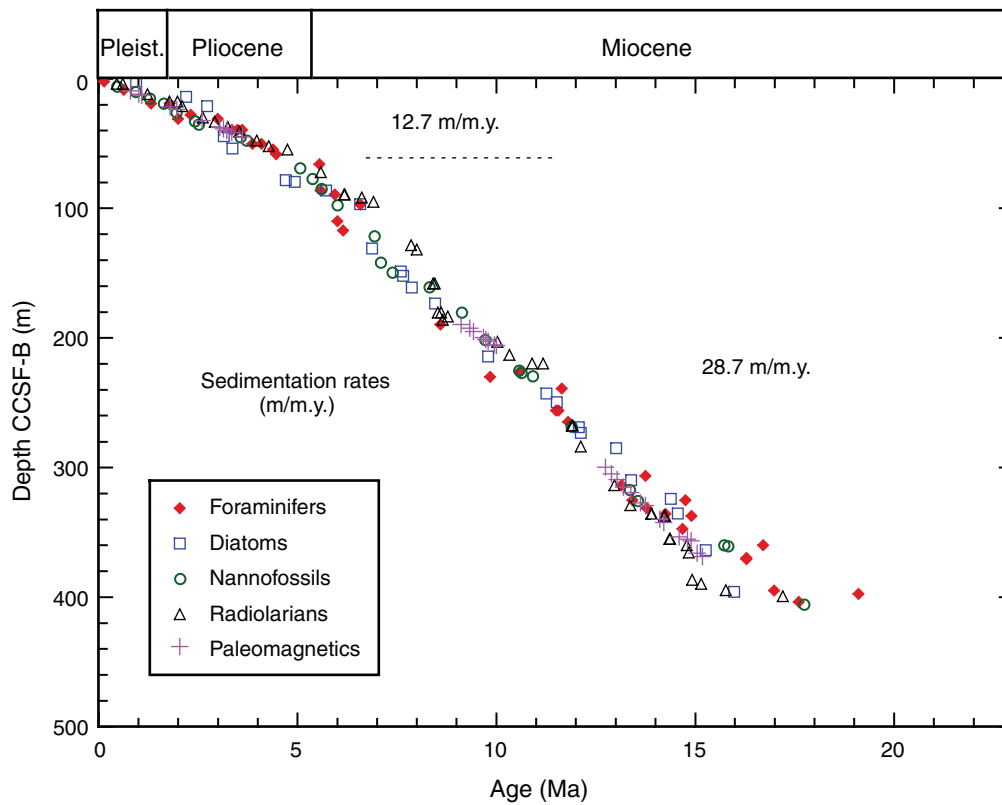


Figure F15. Qualitative abundances for the *Triquetrorhabdulus* lineage as reported from range chart samples. Abundance: 3 = common, 2 = frequent, 1 = rare, 0 = absent.

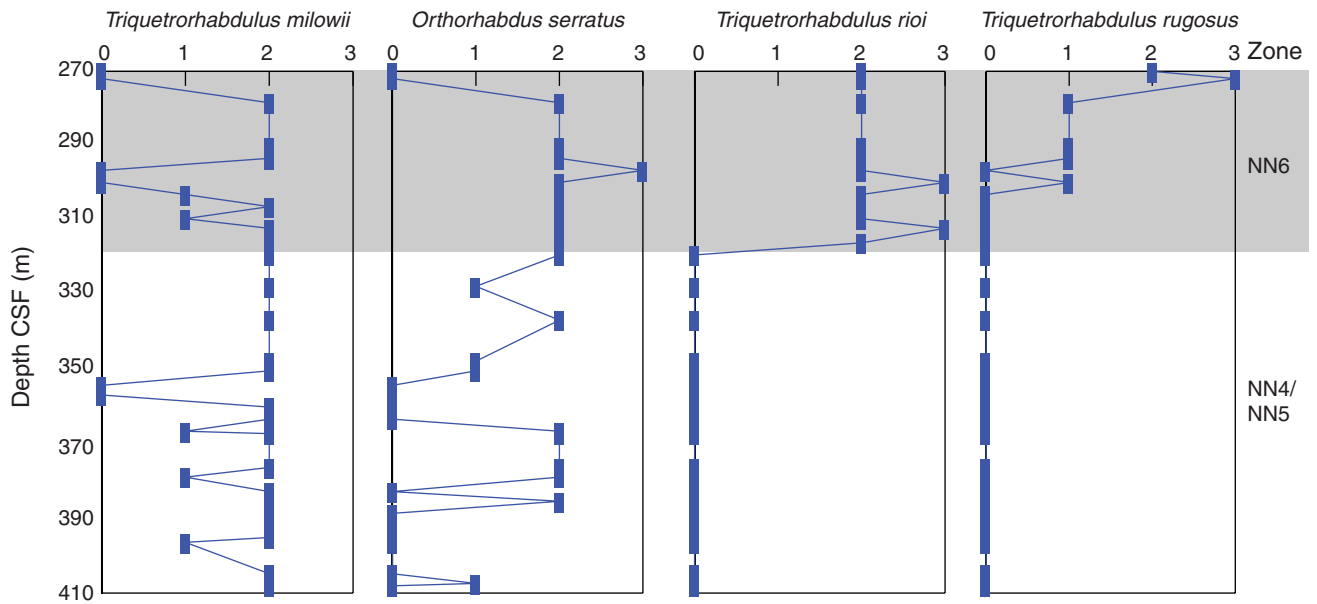


Figure F16. Planktonic foraminifer abundance and assemblage changes, Site U1338. Red line = three-point moving average.

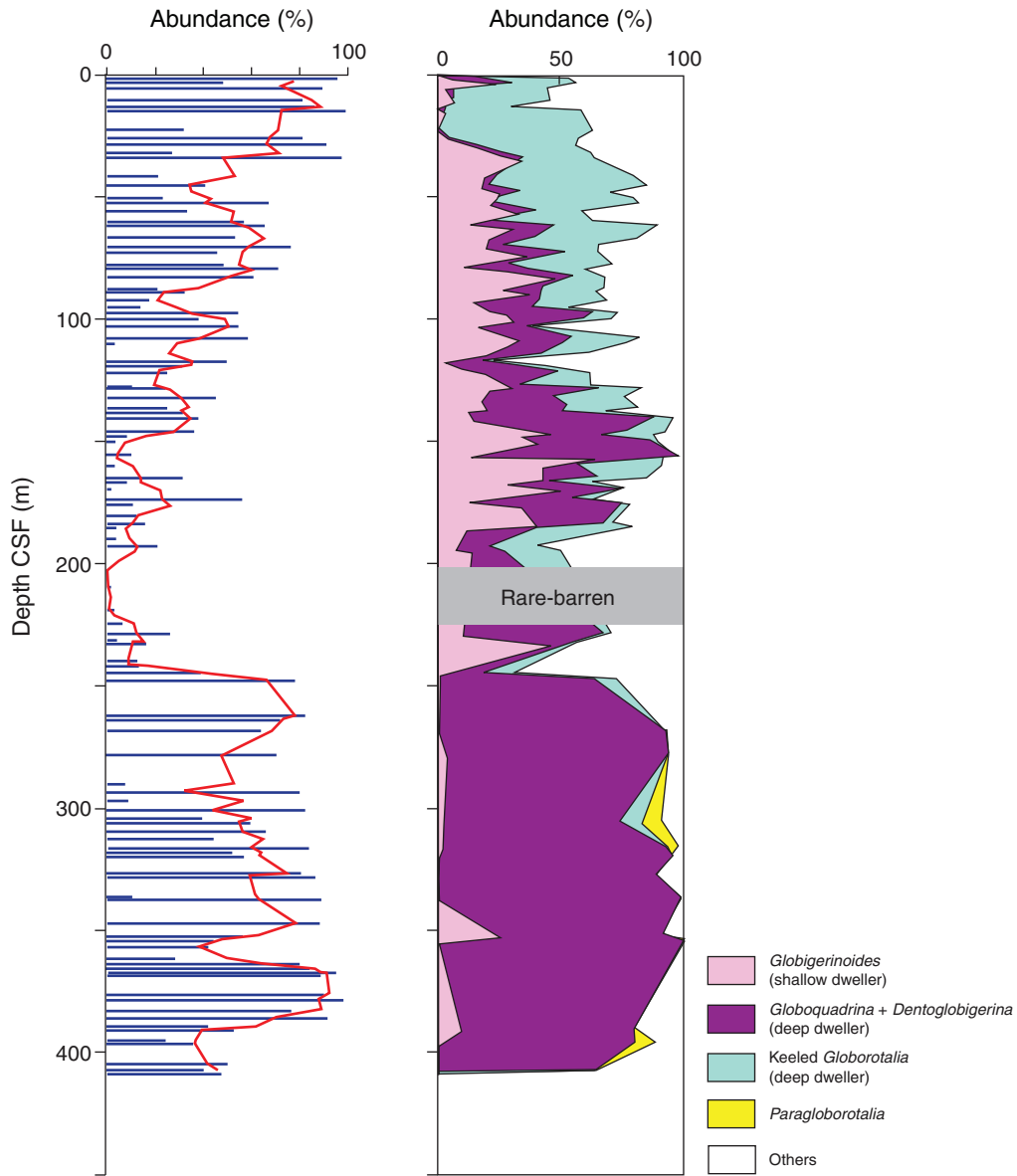


Figure F17. Distribution of common benthic foraminifer taxa in core catcher samples, Hole U1338A. Marked variations in downcore abundance and species distribution reflect major changes in global climate during the Neogene. CCD = carbonate compensation depth, BF = benthic foraminifer.

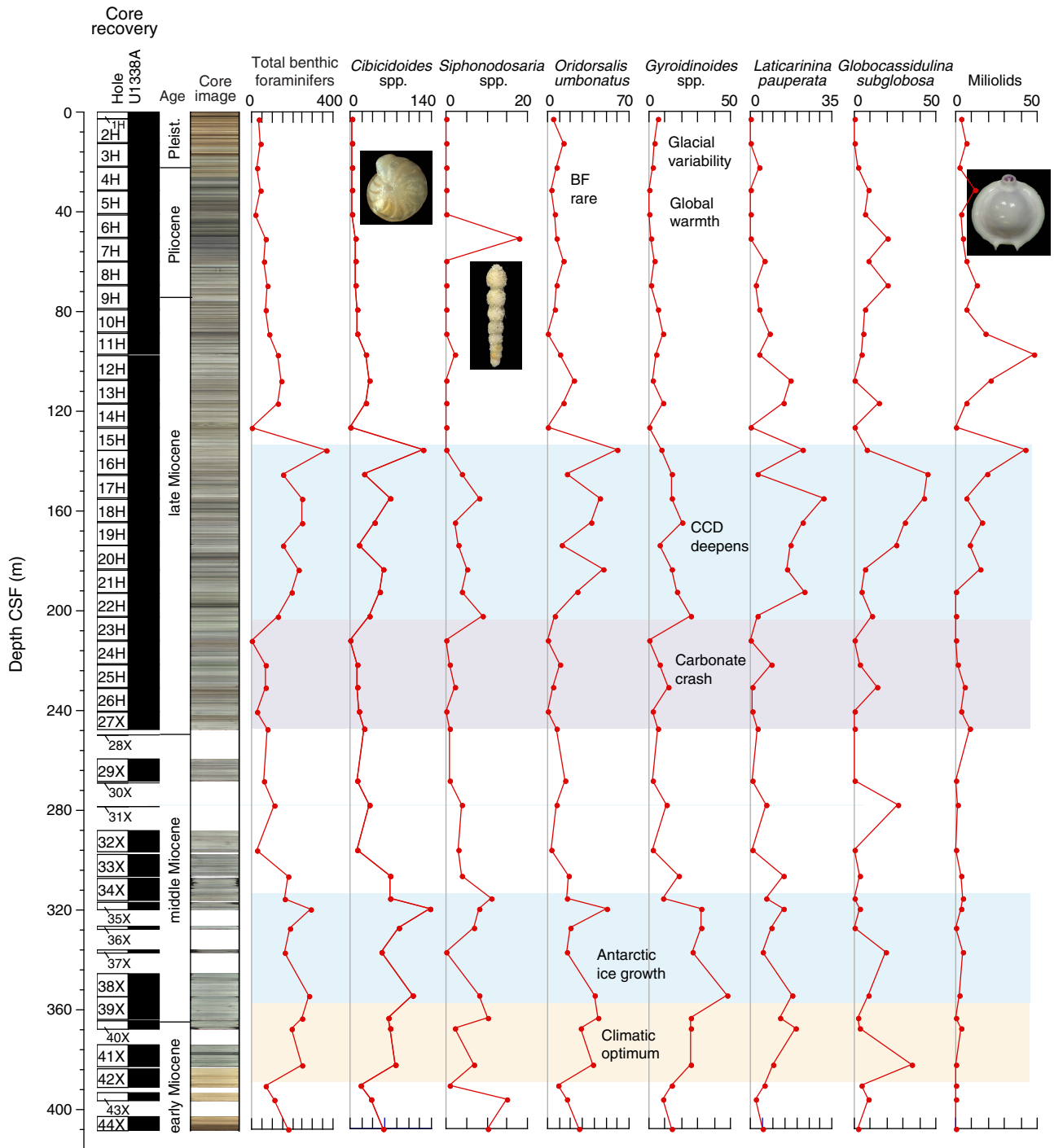


Figure F18. Magnetic susceptibility and paleomagnetic summary, Hole U1338A. Declinations are raw data before FlexIt tool orientation. Gray lines = measurements before demagnetization, red lines = measurements after 20 mT alternating-field demagnetization step, green line = magnetic susceptibility, blue squares = discrete sample data. A. 0–120 m CSF. (**Continued on next page.**)

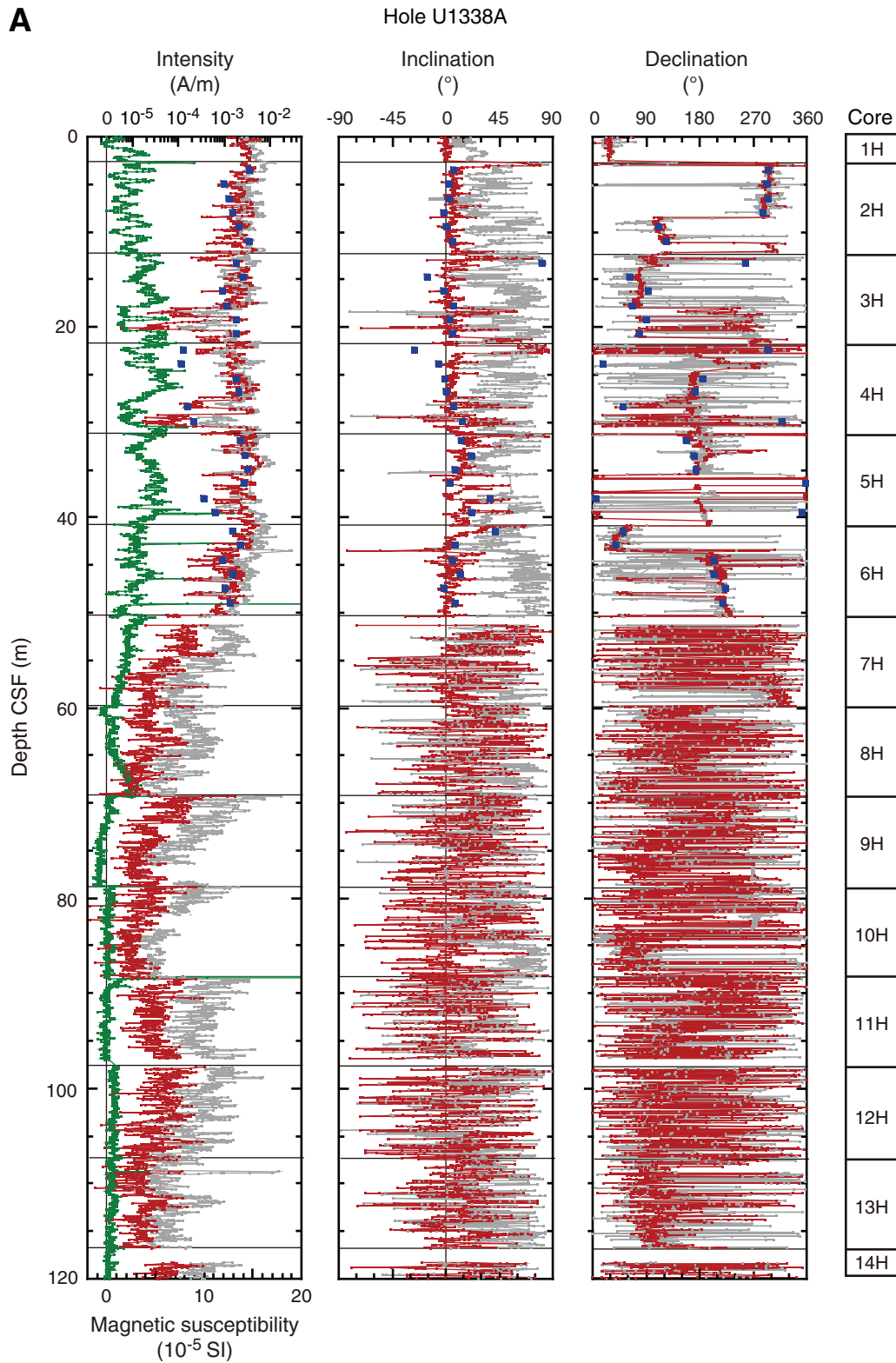


Figure F18 (continued). B. 120–240 m CSF.

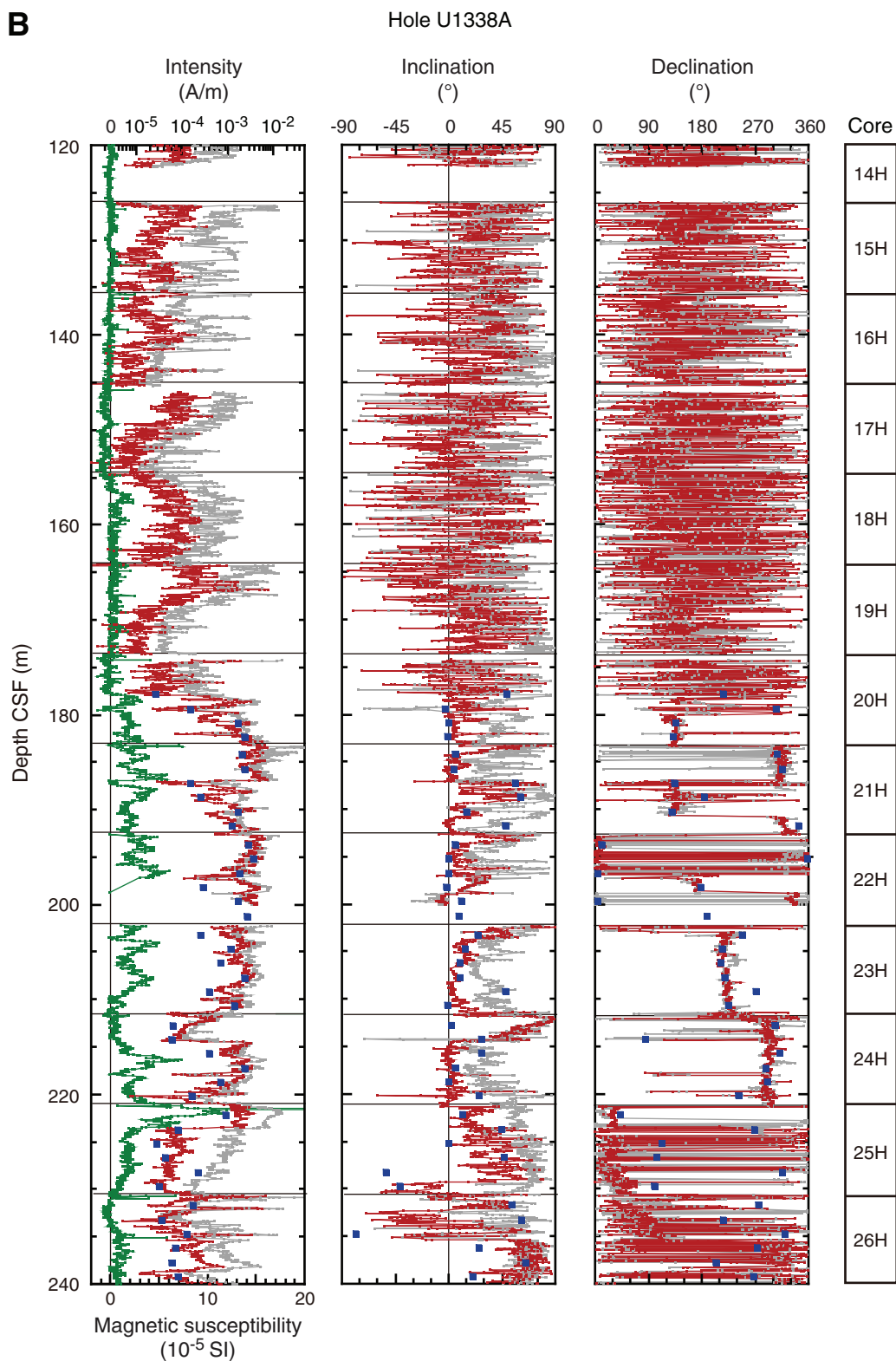


Figure F19. Magnetic susceptibility and paleomagnetic summary, Hole U1338B. Declinations are raw data before FlexIt tool orientation. Gray lines = measurements before demagnetization, red lines = measurements after 20 mT alternating-field demagnetization step, green line = magnetic susceptibility. A. 0–130 m CSF. (Continued on next two pages.)

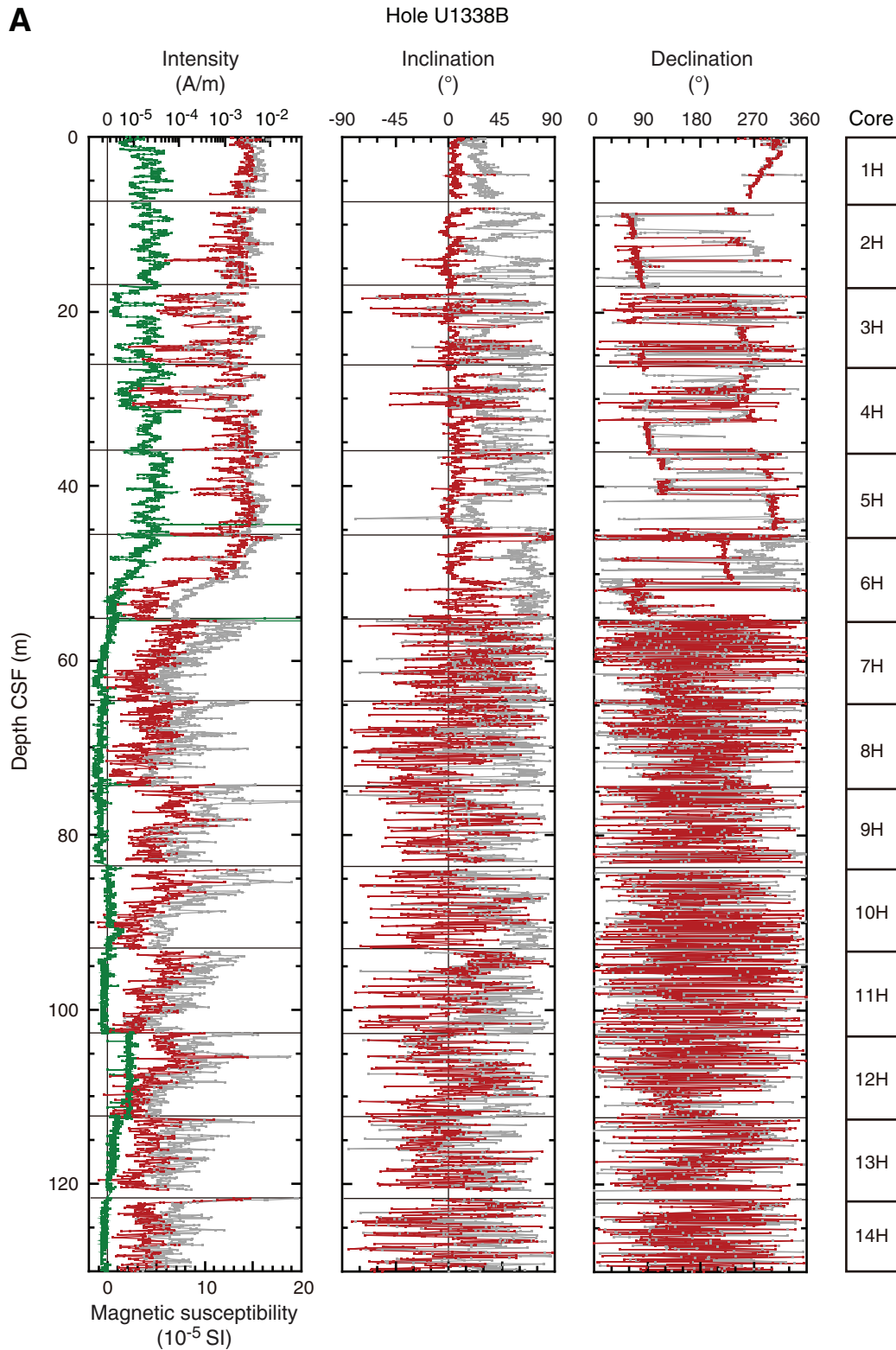


Figure F19 (continued). B. 130–260 m CSF. (Continued on next page.)

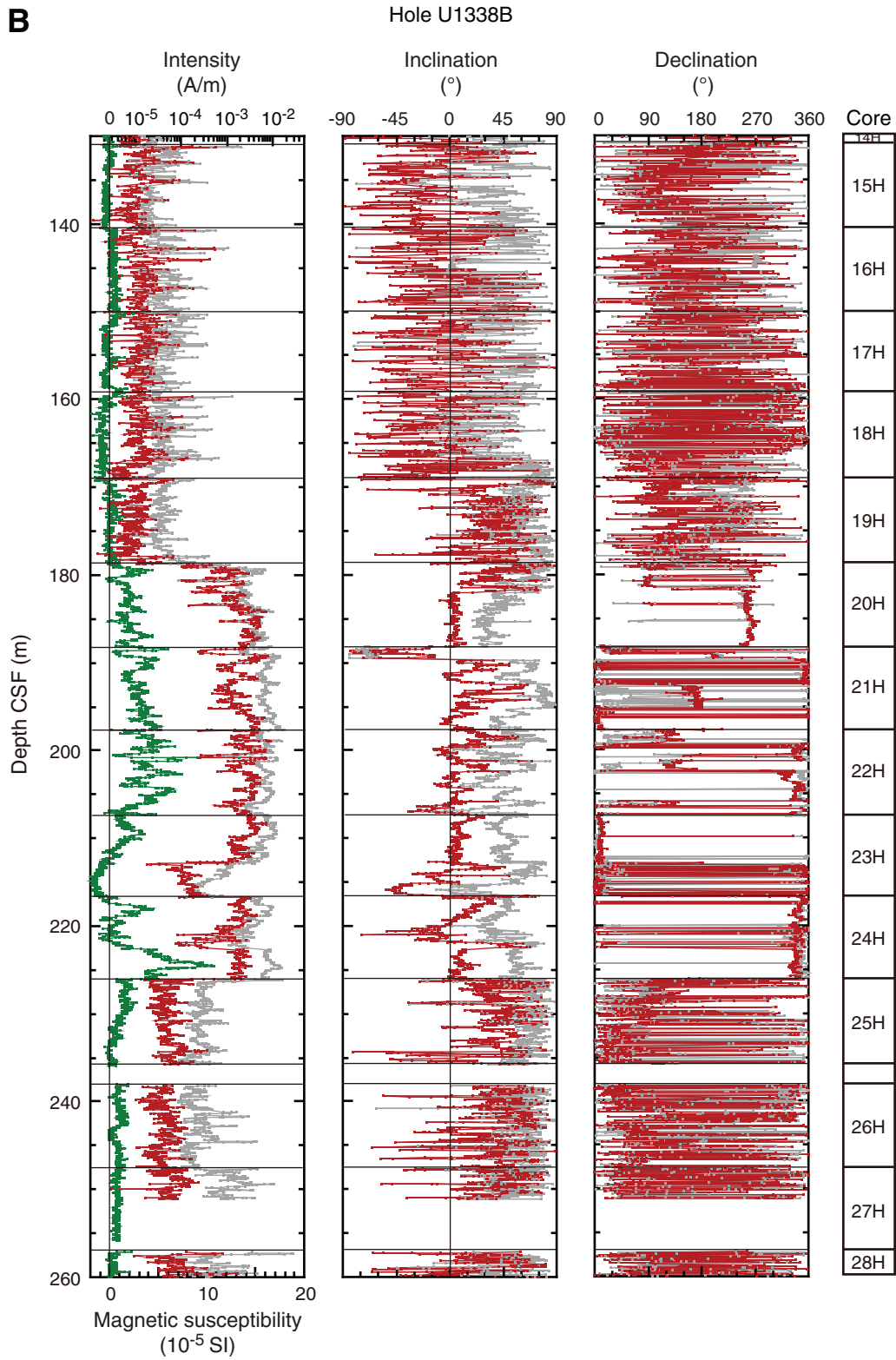


Figure F19 (continued). C. 260–390 m CSF.

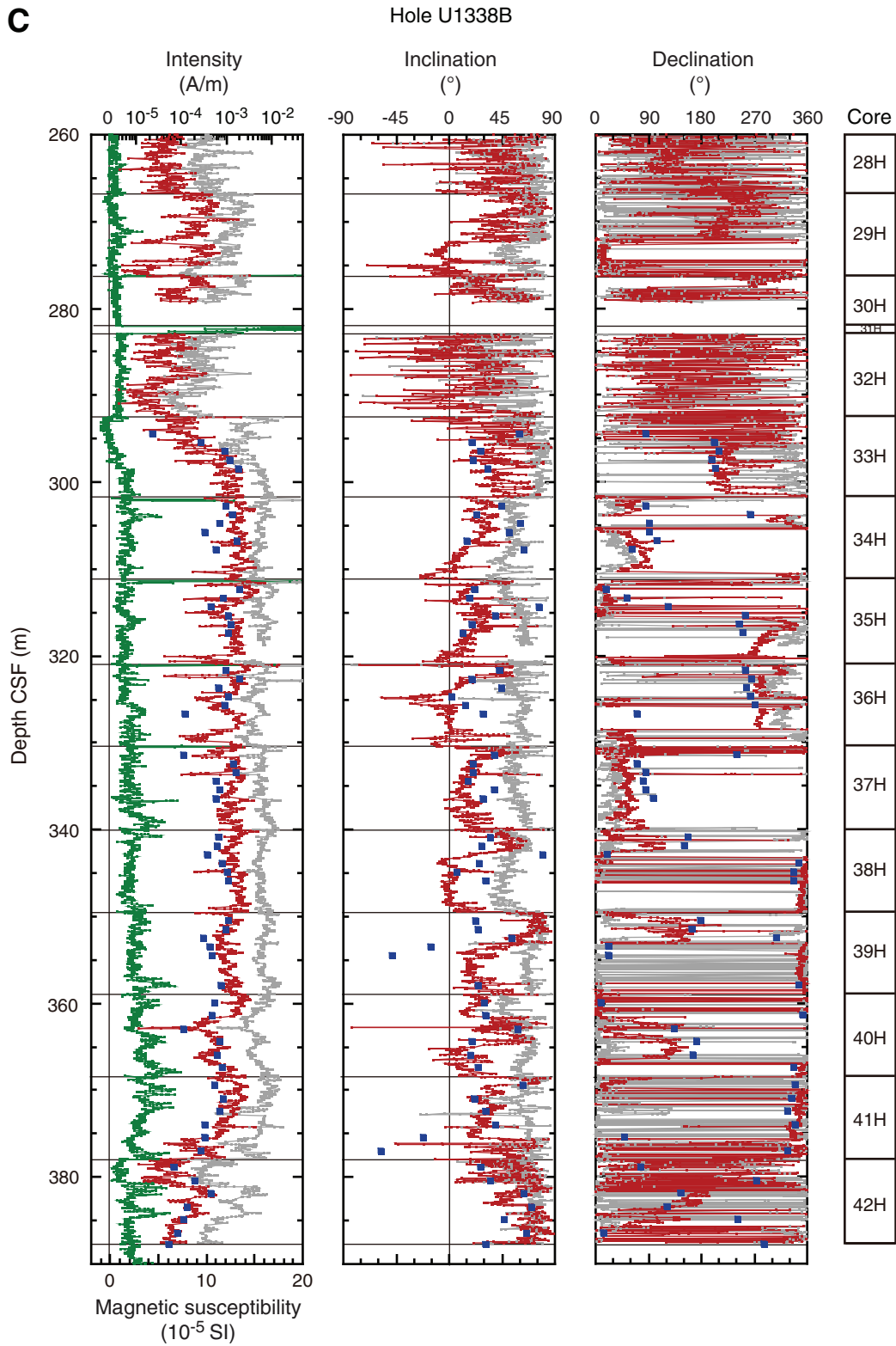


Figure F20. Magnetic susceptibility and paleomagnetic summary, Hole U1338C. Declinations are raw data before FlexIt tool orientation. Gray lines = measurements before demagnetization, red lines = measurements after 20 mT alternating-field demagnetization step, green line = magnetic susceptibility. A. 0–140 m CSF. (**Continued on next two pages.**)

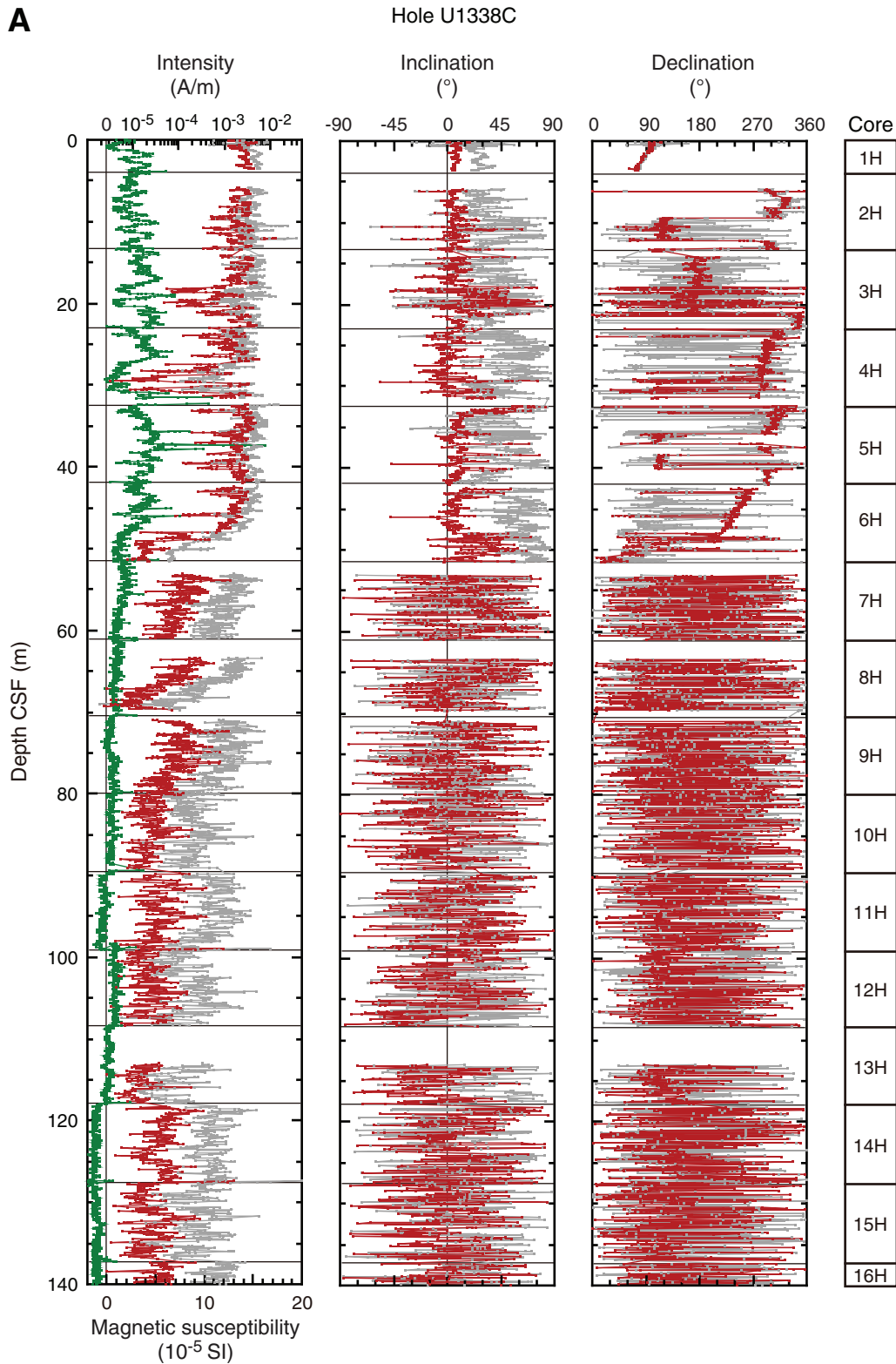


Figure F20 (continued). B. 140–280 m CSF. (Continued on next page.)

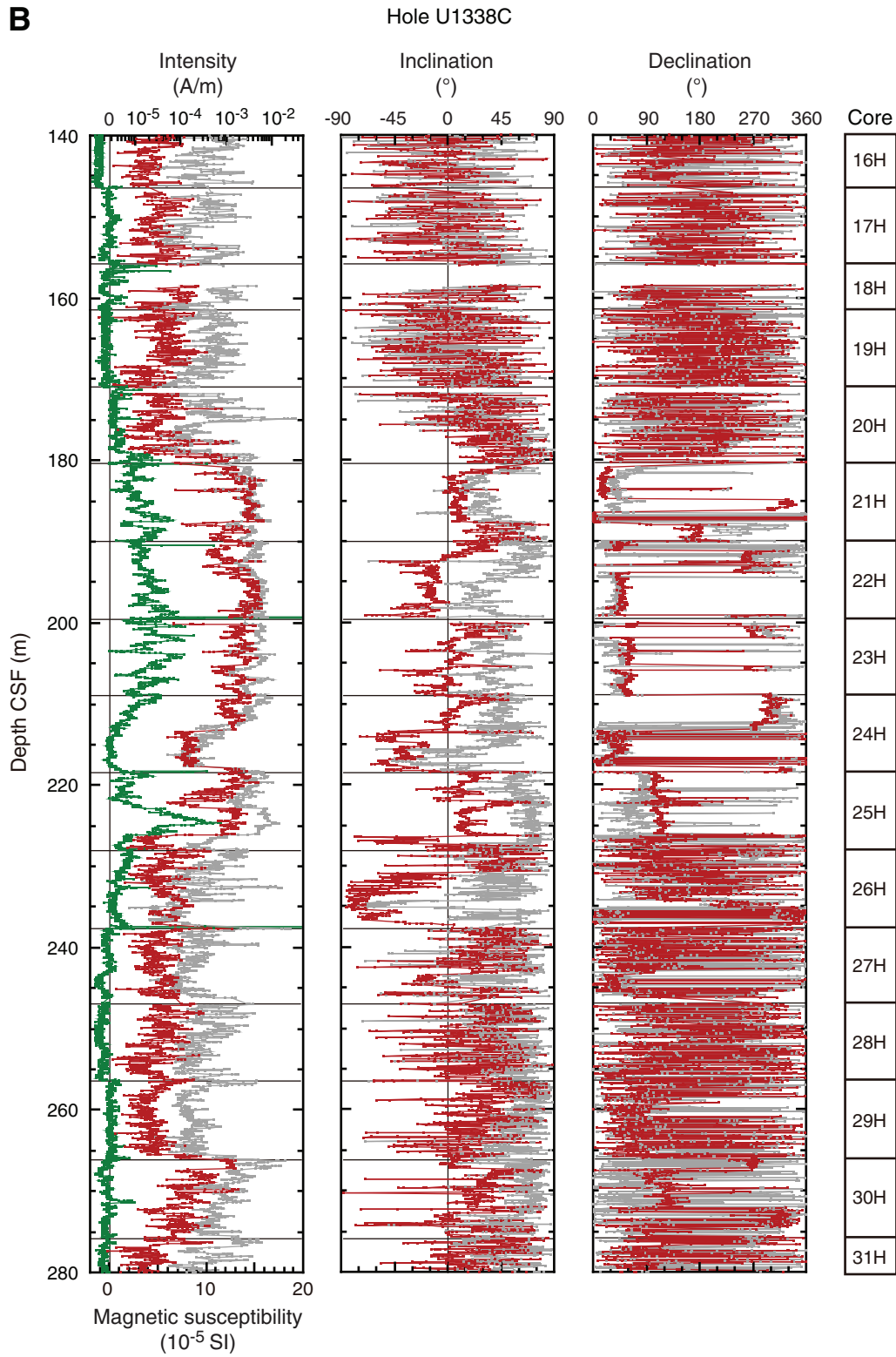


Figure F20 (continued). C. 280–420 m CSF.

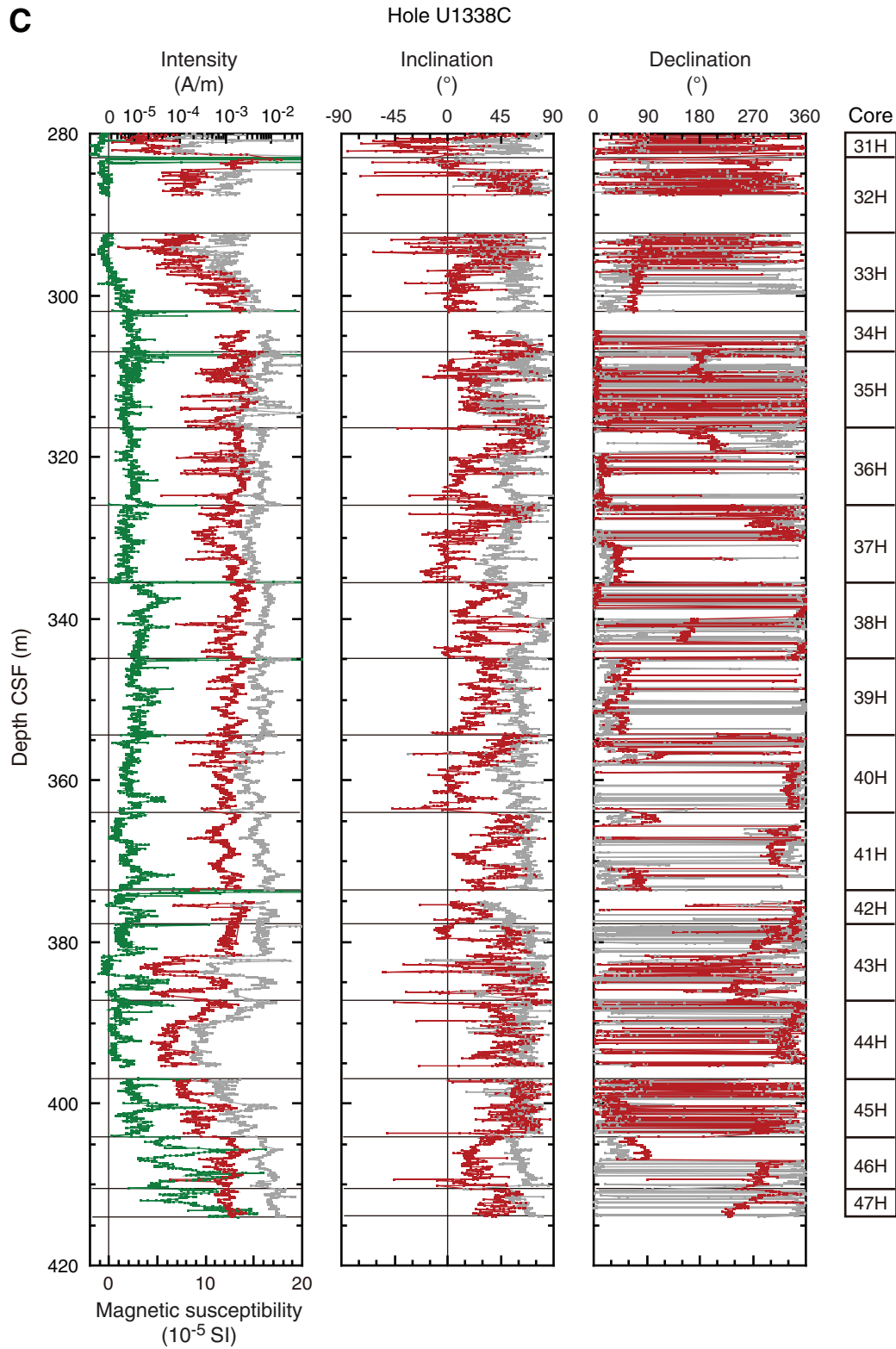


Figure F21. Declination of magnetic remanence after applying orientation using the FlexIt tool and 20 mT peak alternating-field demagnetization, Site U1338. Depths were determined independent of polarity record. See Table T15. GPTS = geomagnetic polarity timescale. A. 0–60 m CCSF-A. (Continued on next two pages.)

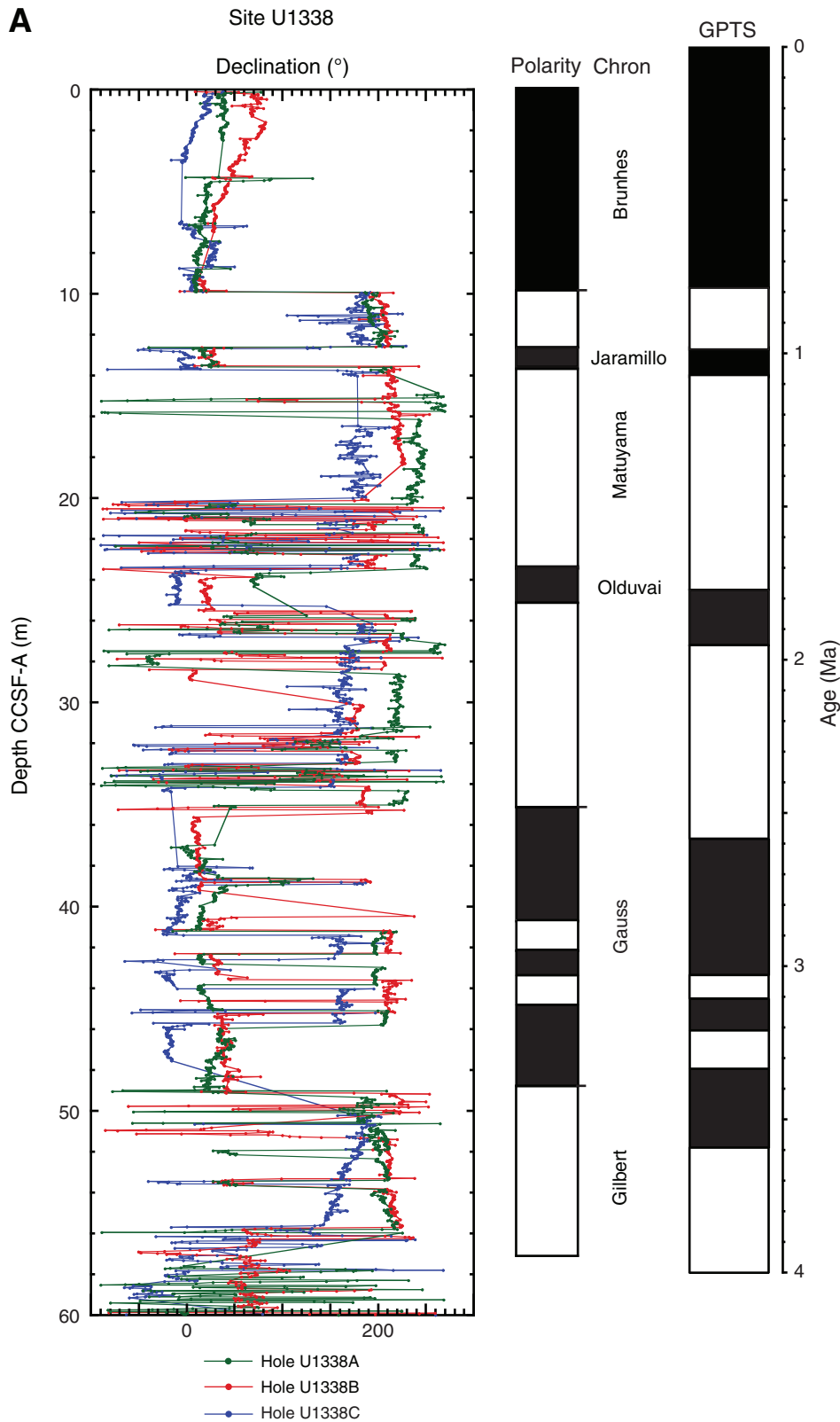


Figure F21 (continued). B. 190–260 m CCSF-A. (Continued on next page.)

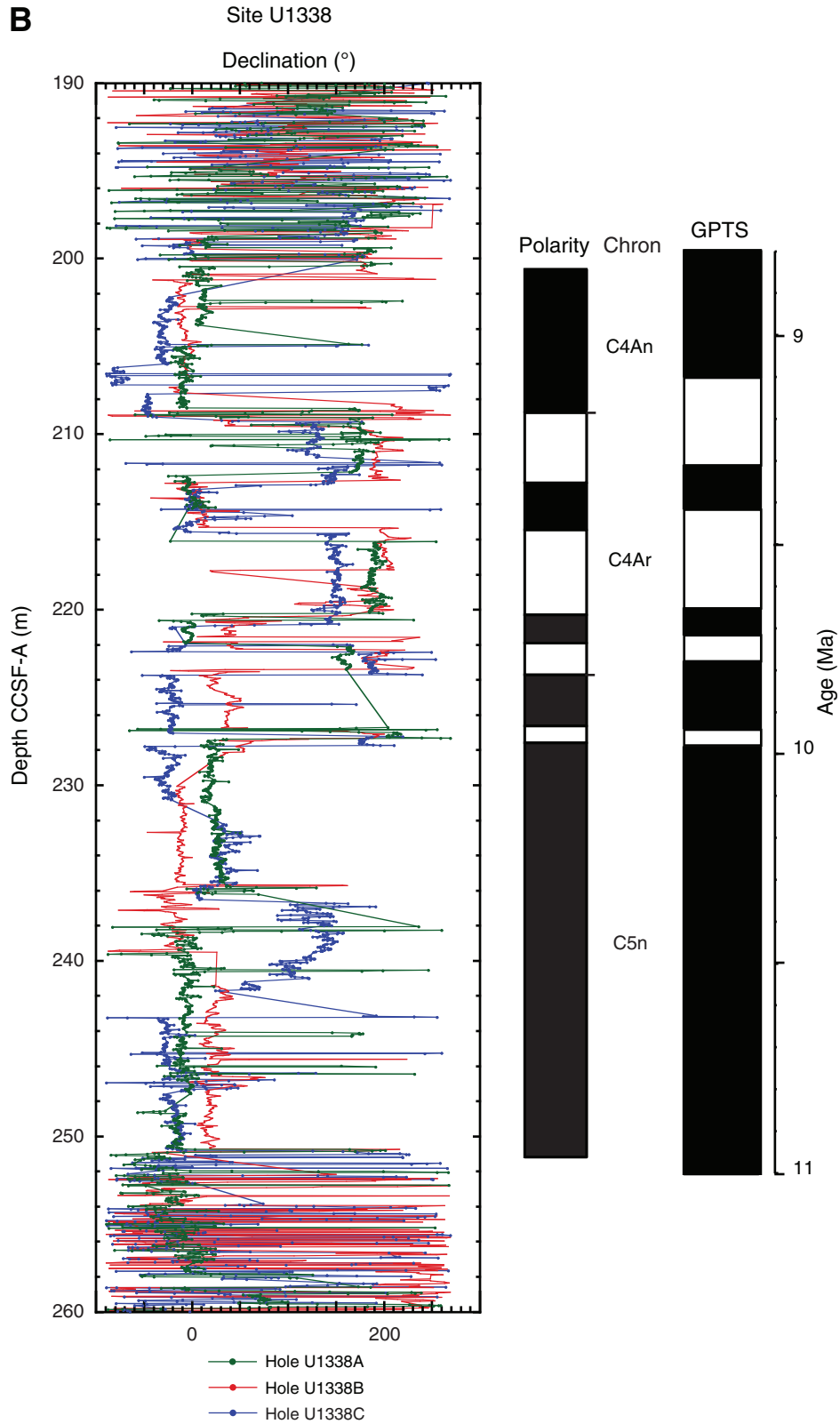


Figure F21 (continued). C. 320–460 m CCSF-A.

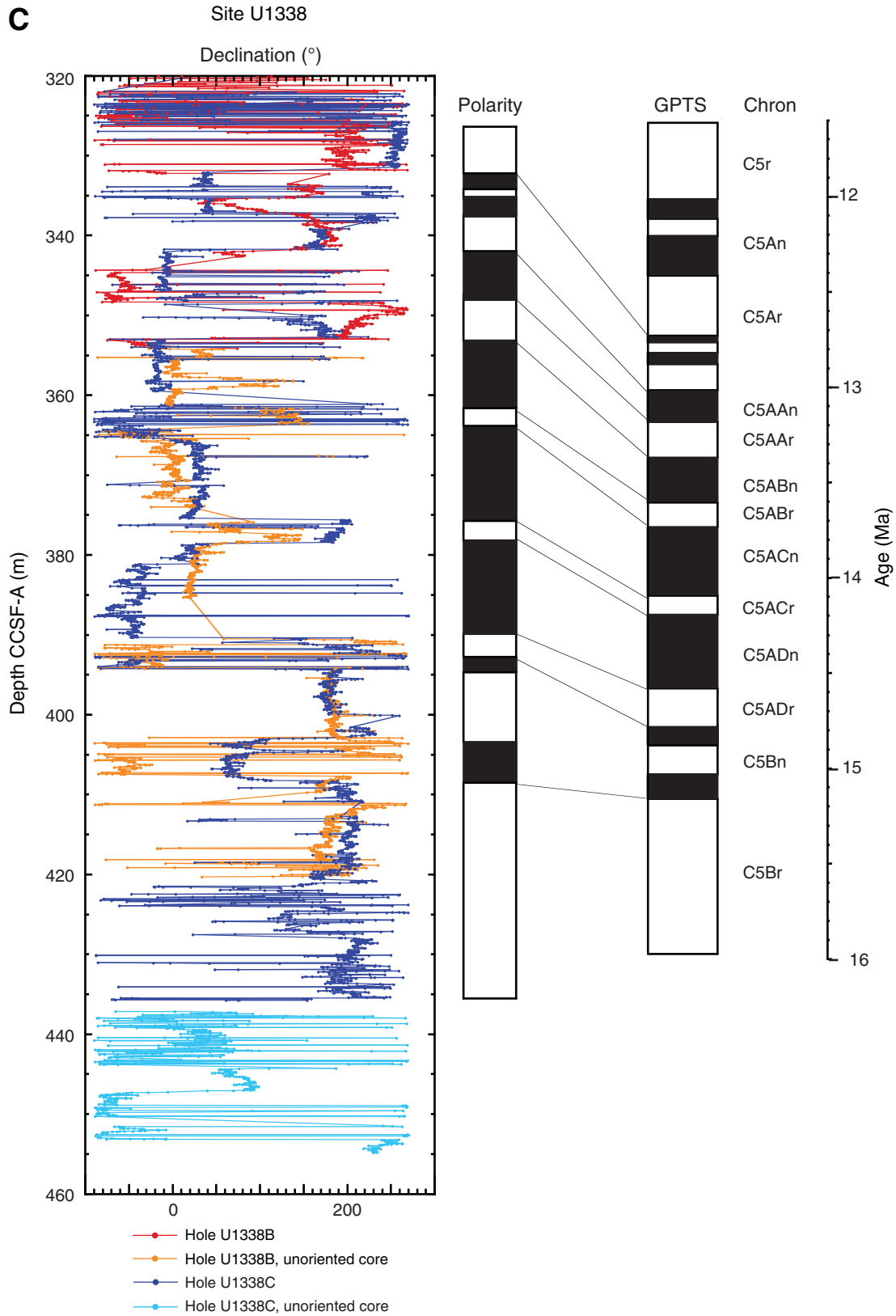


Figure F22. Depth-age plot based on polarity interpretation indicating mean sedimentation rates in the three intervals where polarity zones can be interpreted, Site U1338.

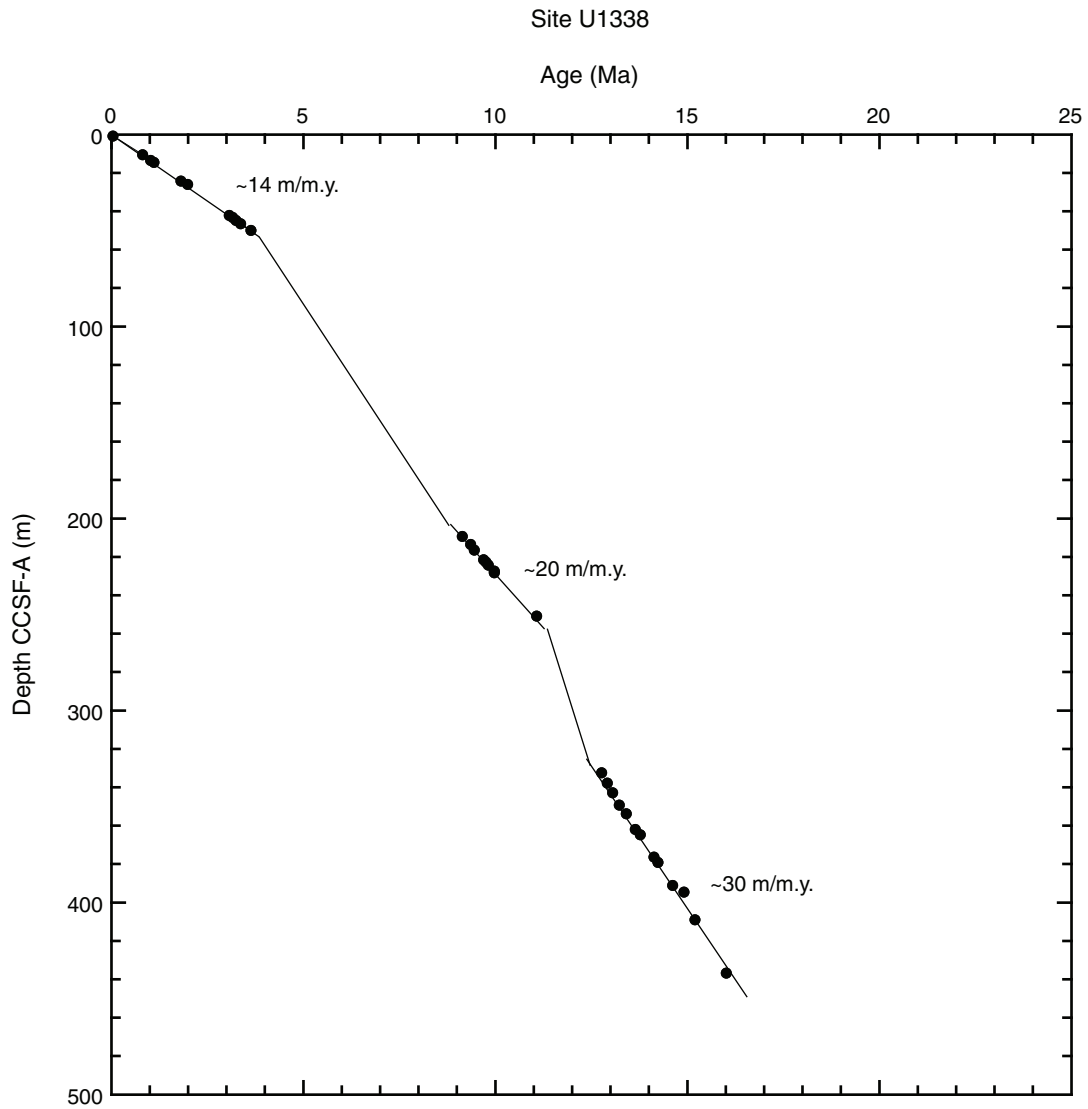


Figure F23. Interstitial water chemistry, Holes U1338A and U1338B. Blue open squares = Hole U1338A Rhizon samples, green open squares = Hole U1338B Rhizon samples, solid circles = squeezed samples for Hole U1338A, red triangles = squeezed samples for Hole U1338B. See “Geochemistry” in the “Methods” chapter for uncertainty estimates. Values below detection limit (see Table T16) plotted as zero.

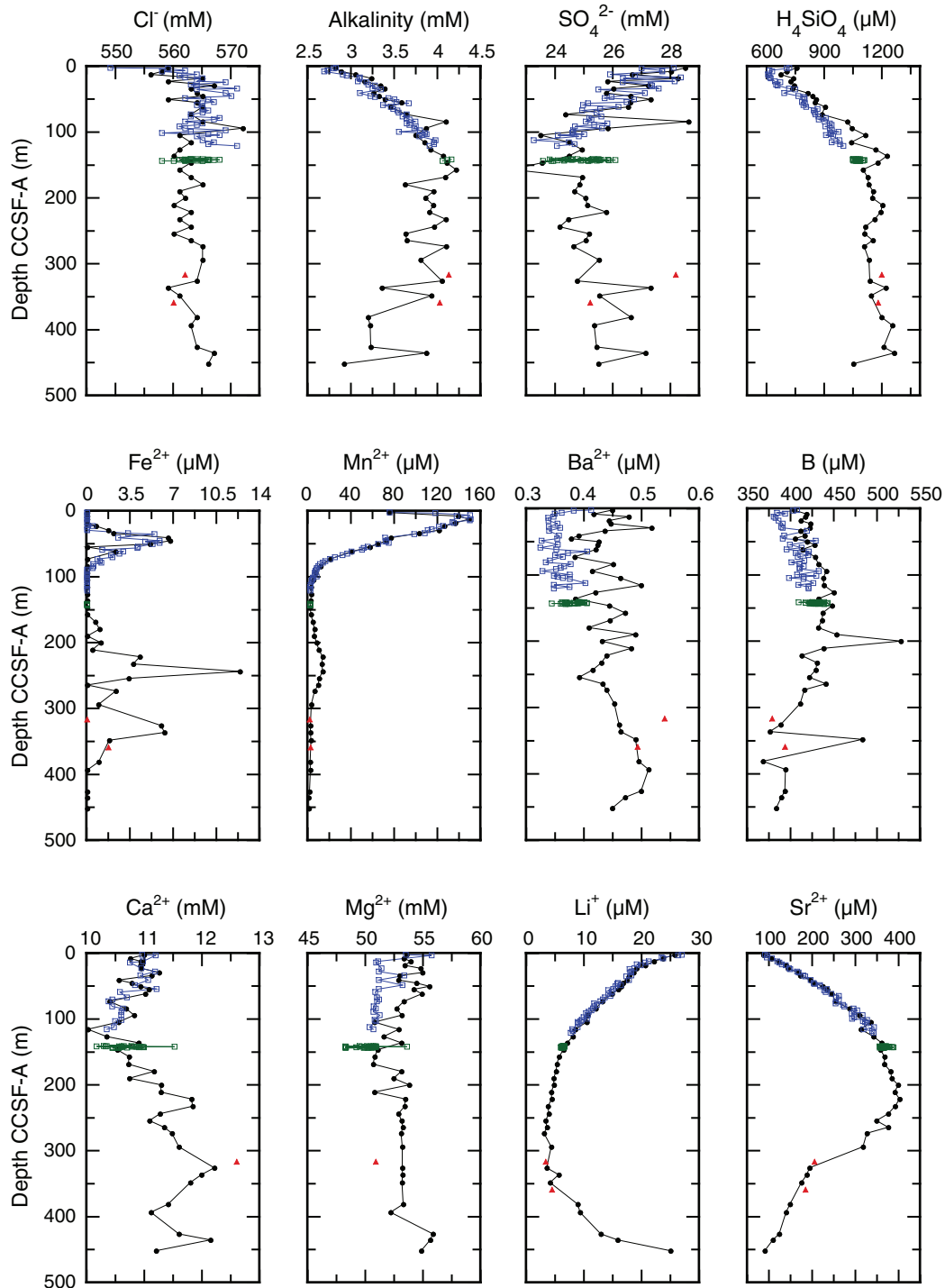


Figure F24. Strontium and silicic acid contents of high-resolution (every 10 cm) Rhizon interstitial water sampling across diatom-rich interval, Core 321-U1338-14H. Error bars (1σ) estimated by repeated measurement of some samples.

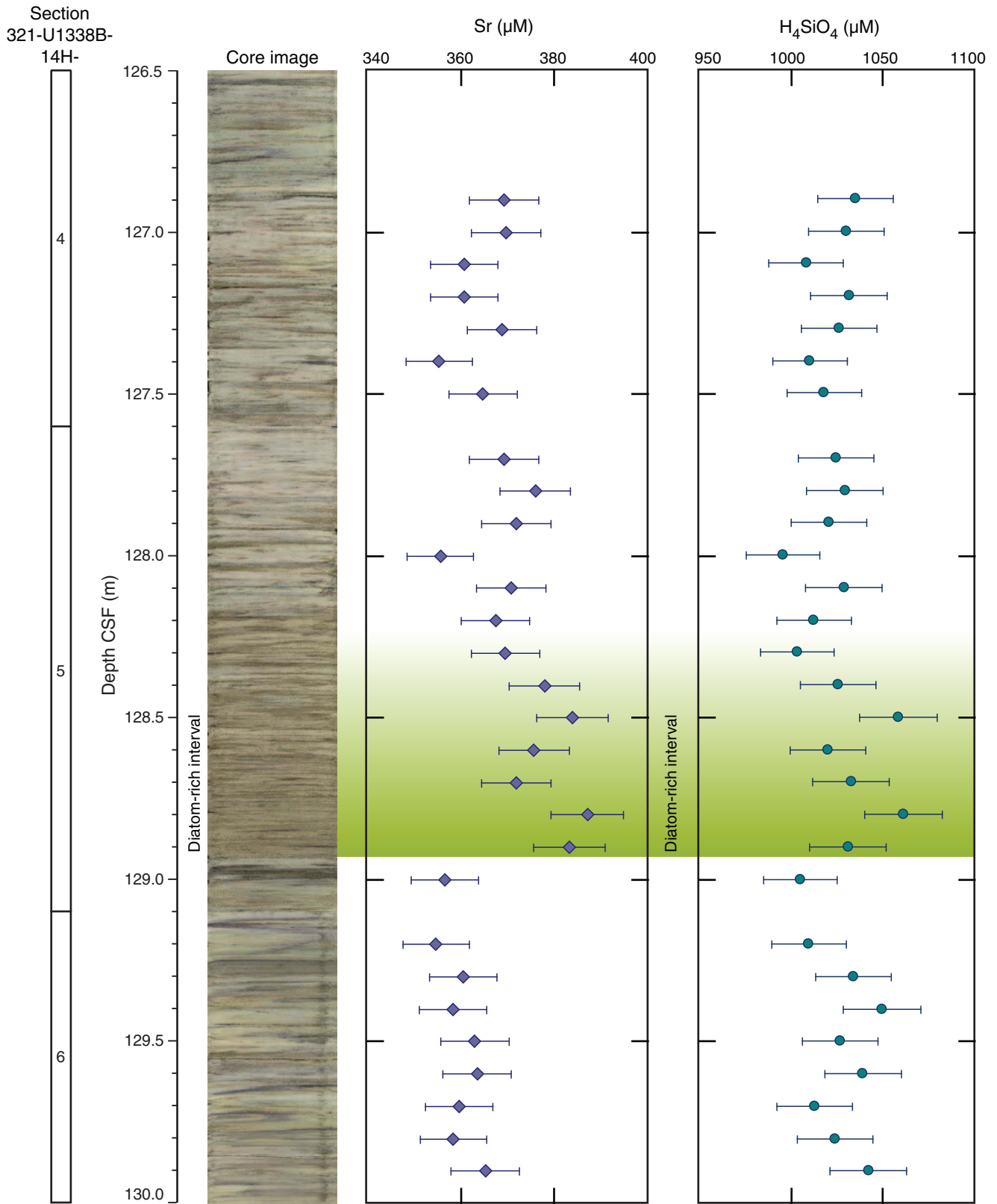


Figure F25. Selected bulk sediment geochemistry, Hole U1338A.

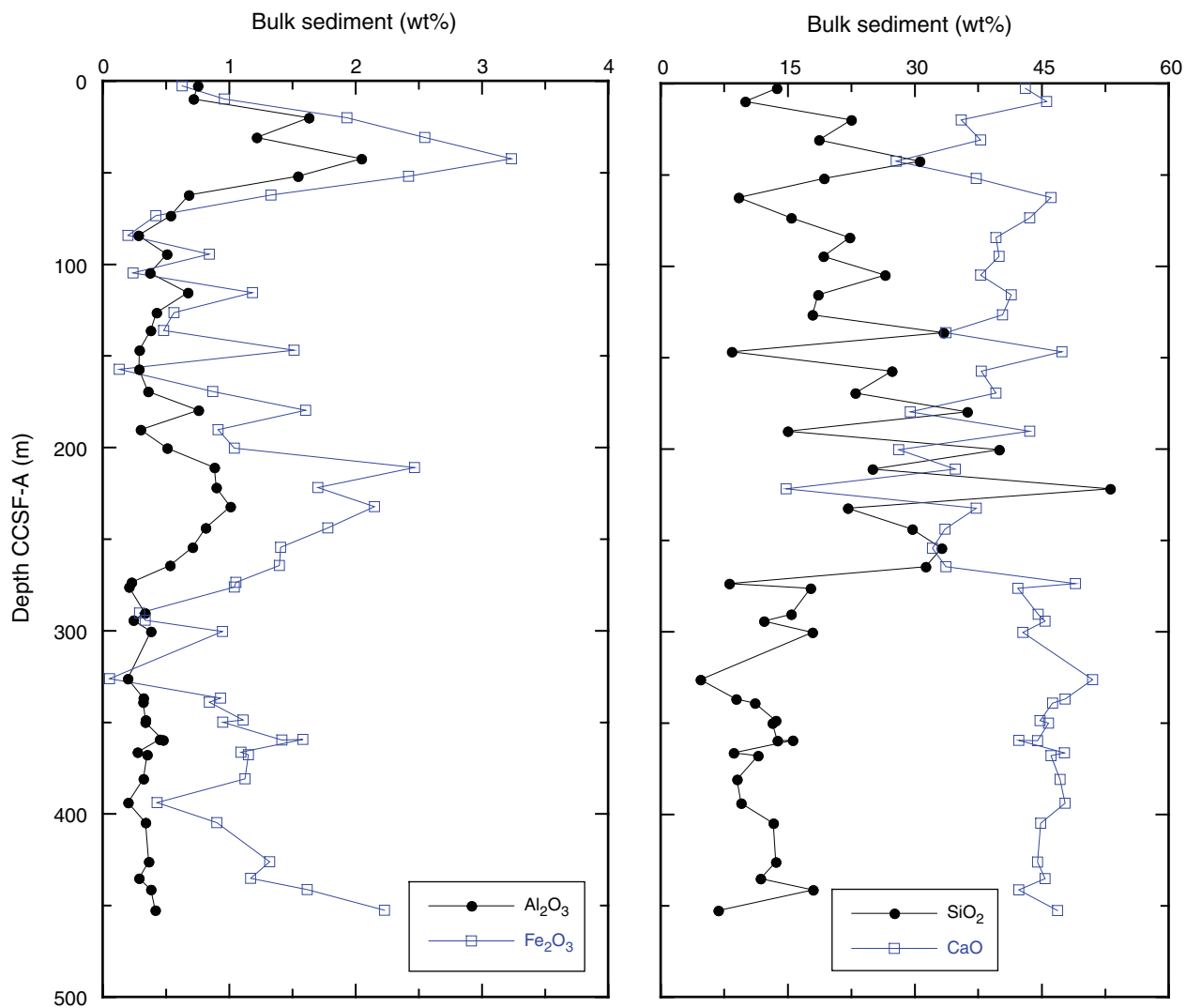


Figure F26. Mg/Ca, Mn/Ca, and Sr/Ca ratios for bulk carbonate leachates of selected samples, Sites U1336, U1337, and U1338. Error bars (1σ) are generally smaller than the symbols and were estimated from repeat measurements of the NIST 1c limestone standard for Mg/Ca/ and Mn/Ca ratios.

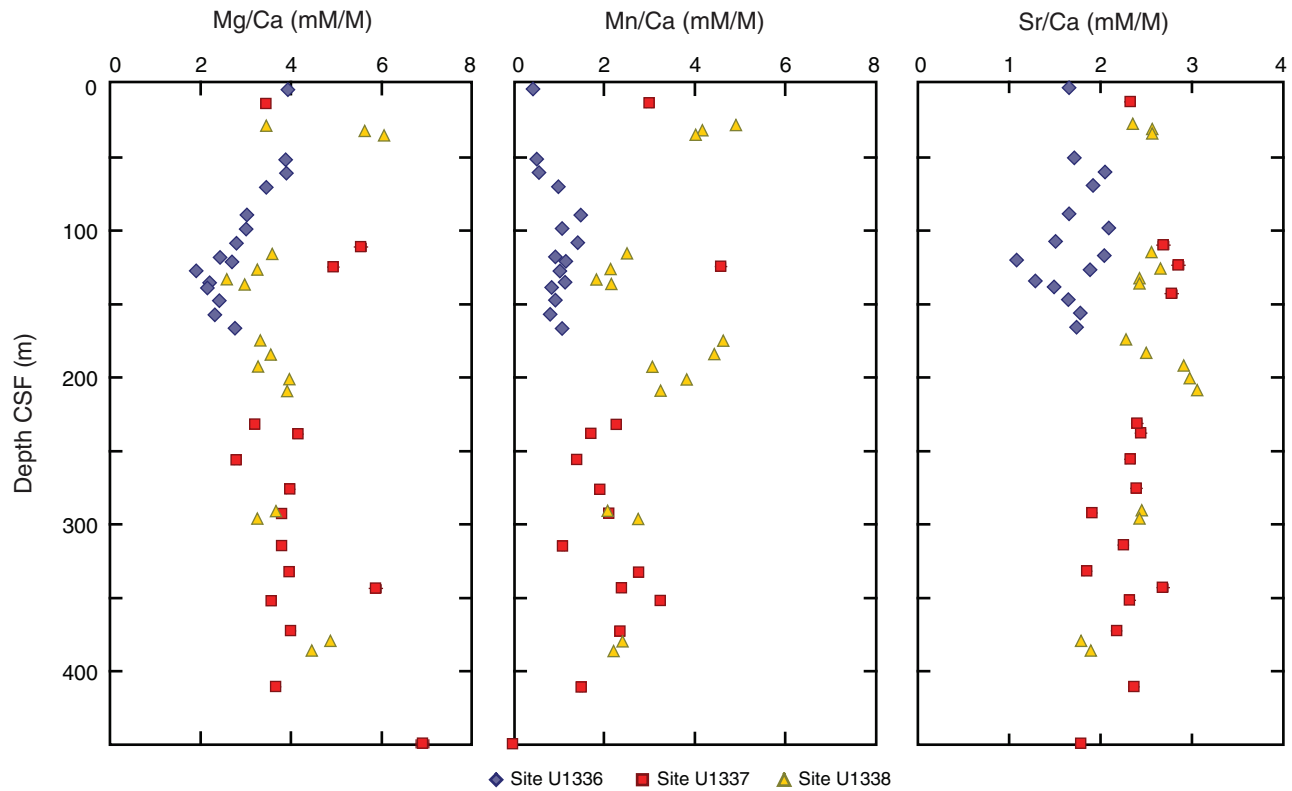


Figure F27. Sediment calcium carbonate (CaCO_3) and total organic carbon (TOC) concentrations, Holes U1338A and U1338B.

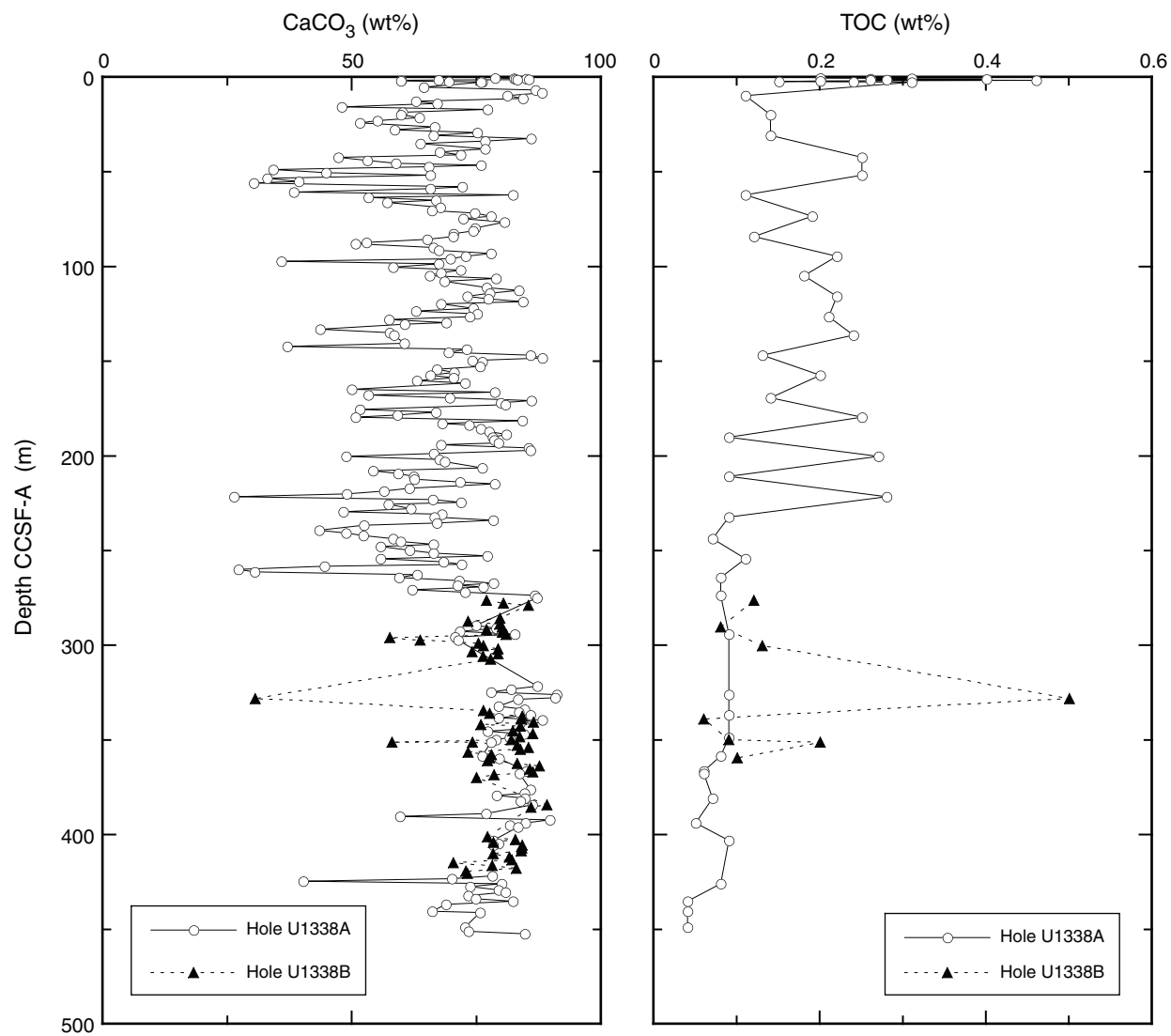


Figure F28. Whole-round measurements, Hole U1338C. A. Bulk density. B. Magnetic susceptibility. C. *P*-wave velocity. D. Natural gamma radiation. Note scale change at 16 cps.

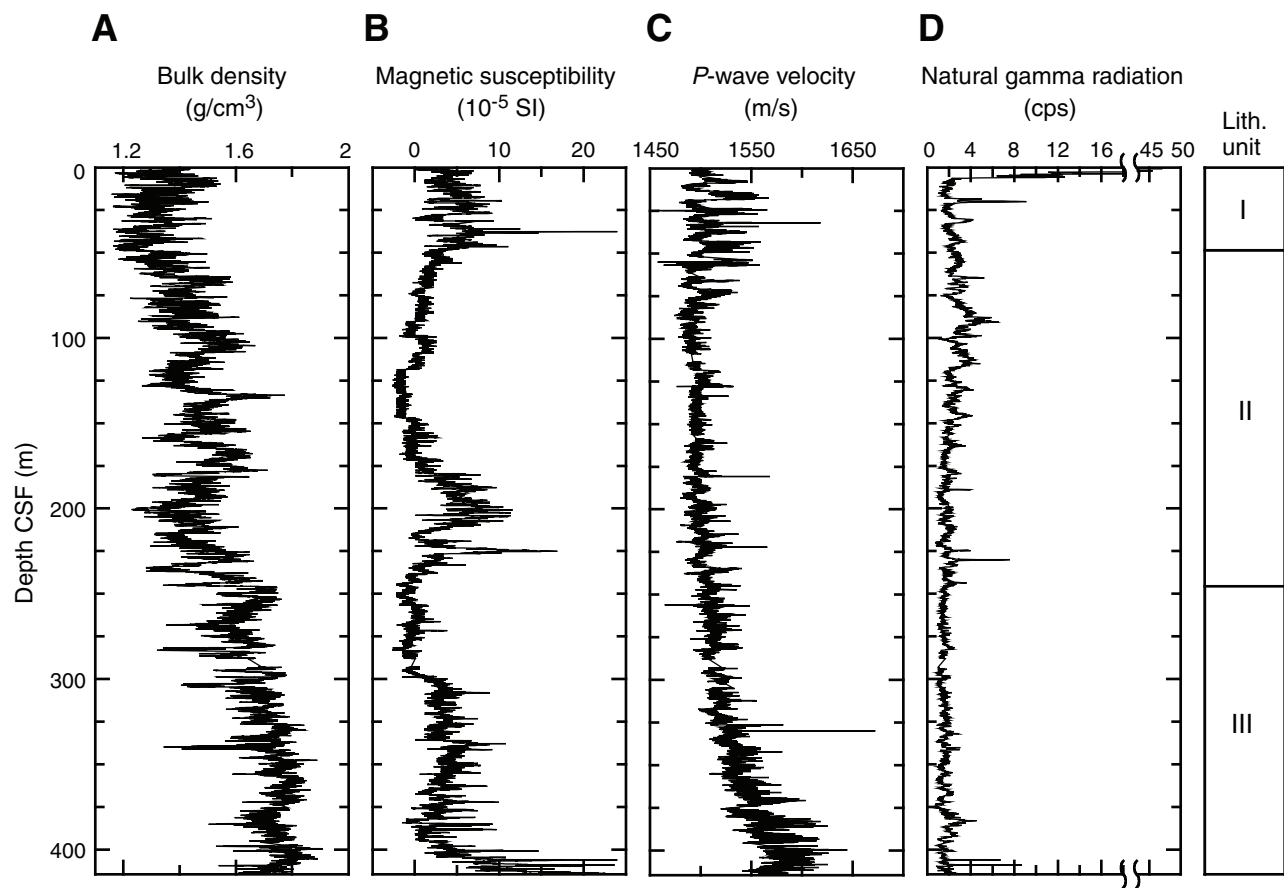


Figure F29. MAD measurements, Holes U1338A (black) and U1338B (red). **A.** Porosity (solid circles) and water content (open circles). **B.** Discrete sample wet bulk density and GRA bulk density (gray line). **C.** Grain density.

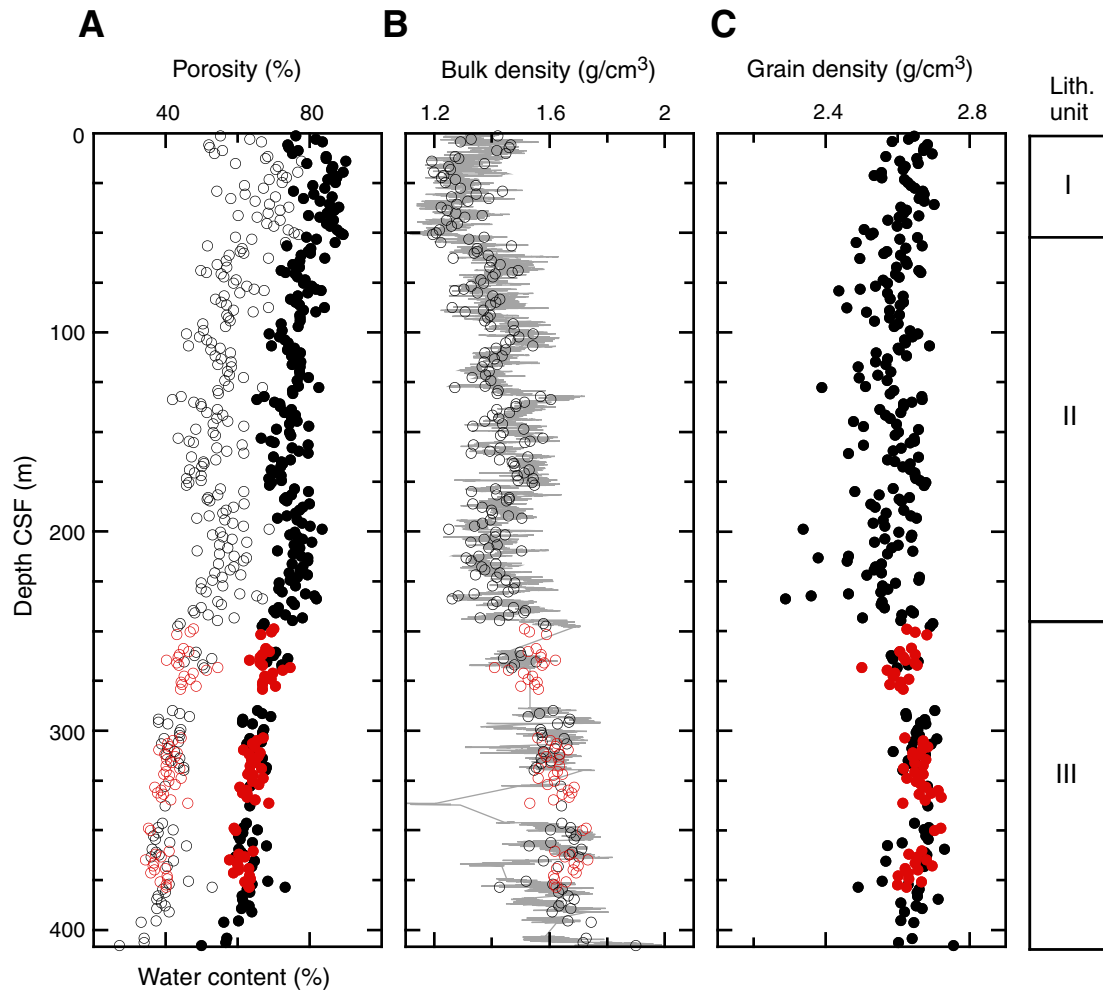


Figure F30. (A) Wet and (B) dry bulk density from MAD analysis of discrete samples plotted with gamma ray attenuation (GRA) bulk density interpolated with a 20 cm wide Gaussian window. Data are from Holes U1338A (black) and U1338B (red) for APC-cored intervals (solid circles) and XCB-cored intervals (open circles).

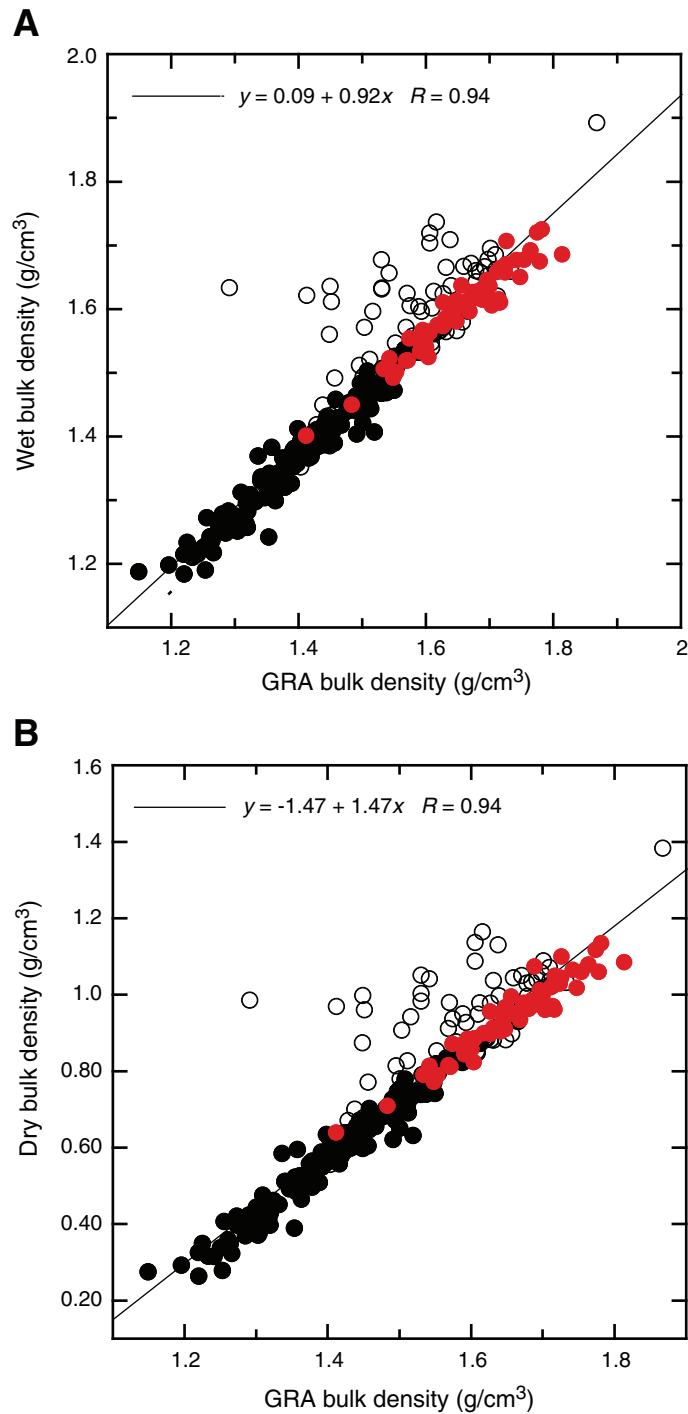


Figure F31. Wet bulk density vs. CaCO_3 . Note depth dependence of wet bulk density in addition to its variation with weight percent CaCO_3 .

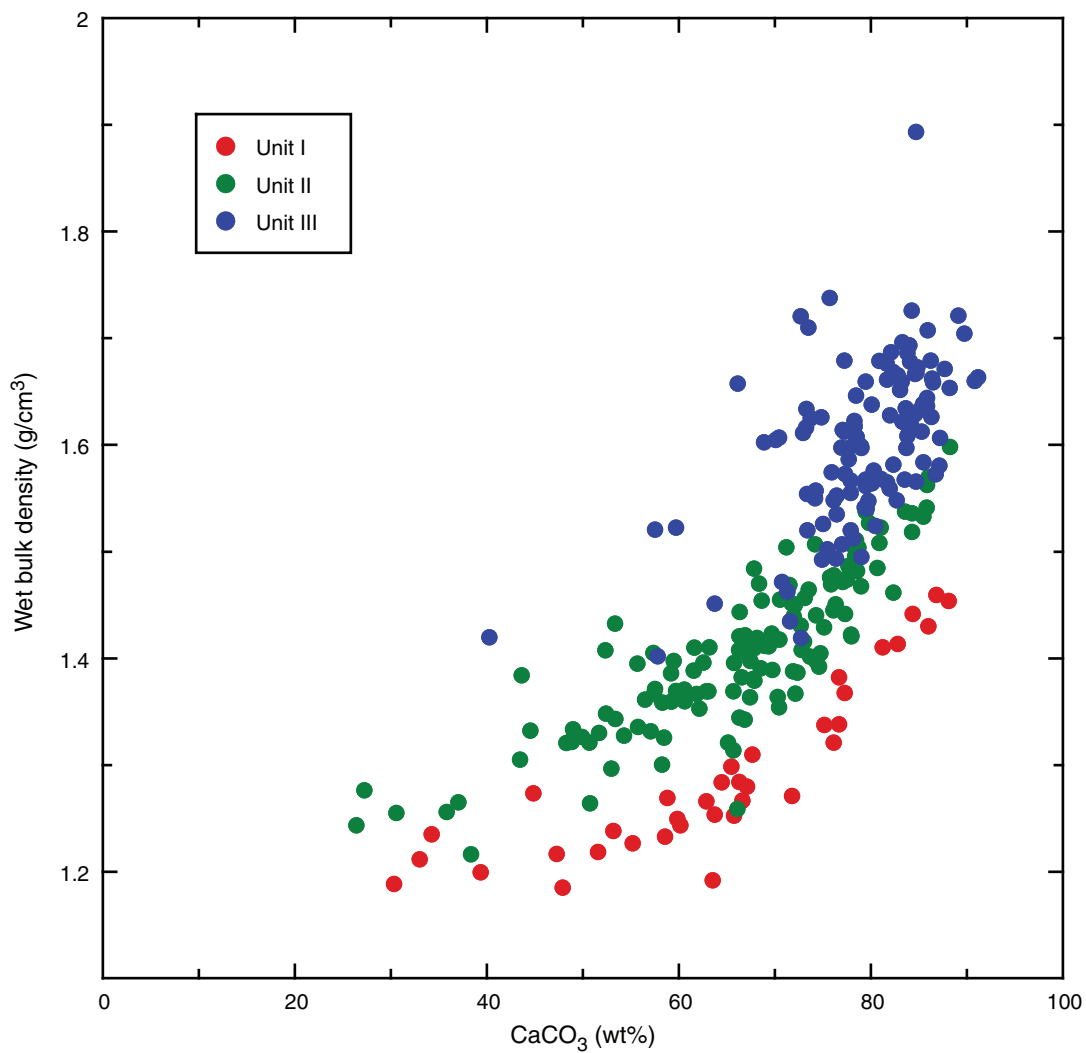


Figure F32. Magnetic susceptibility (black), gamma ray attenuation (GRA) bulk density (red), and digital core image for 0–50 m CSF, Hole U1338C.

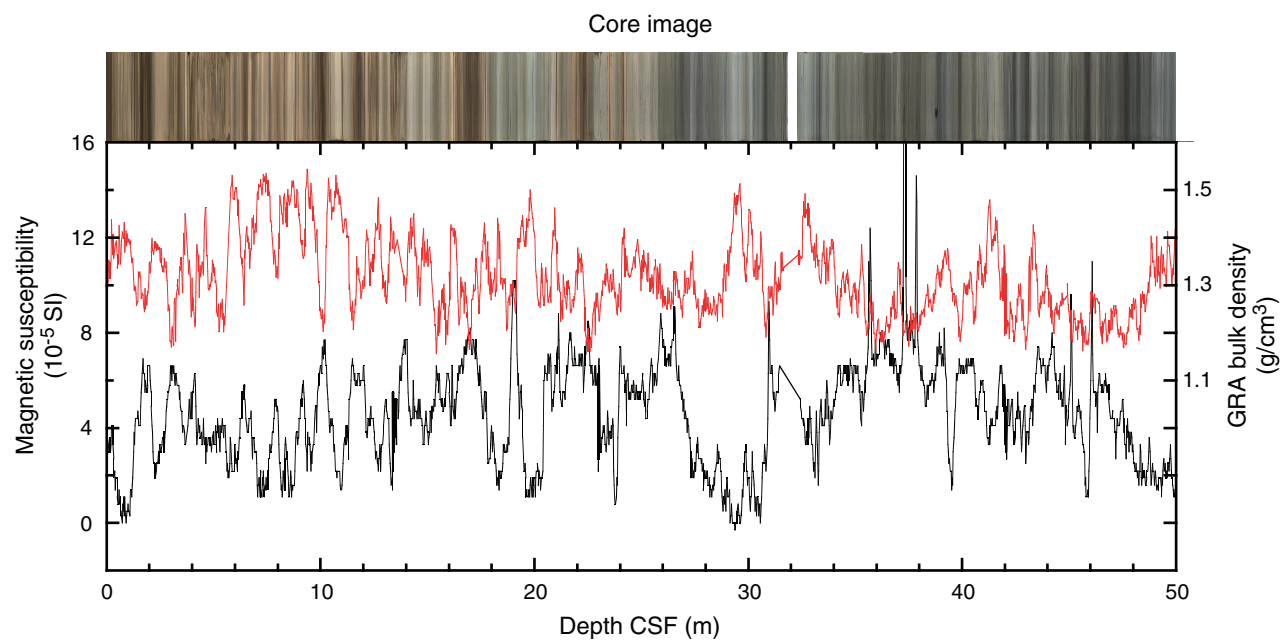


Figure F33. Compressional wave velocity from the PWL in Hole U1338B (gray lines) and discrete velocity measurements on split cores in Holes U1338A (black circles) and U1338B (red circles) using the contact probe for x -axis measurements and the insertion probe for y - and z -axis measurements.

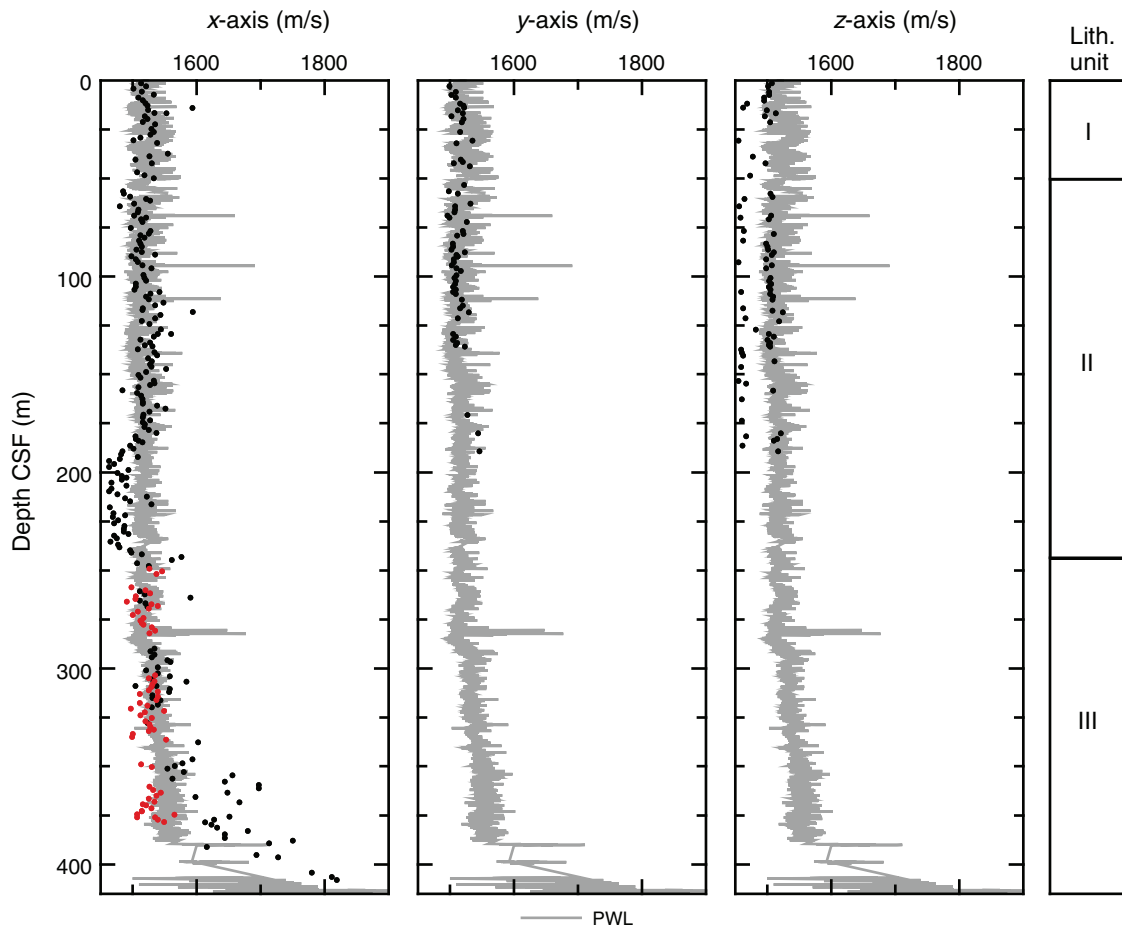


Figure F34. Gamma ray attenuation (GRA) bulk density vs. *P*-wave velocity. The relationship between bulk density and velocity varies among lithologic units. Unit I displays a strong negative correlation, Unit II shows low correlation, and Unit III displays a strong positive correlation.

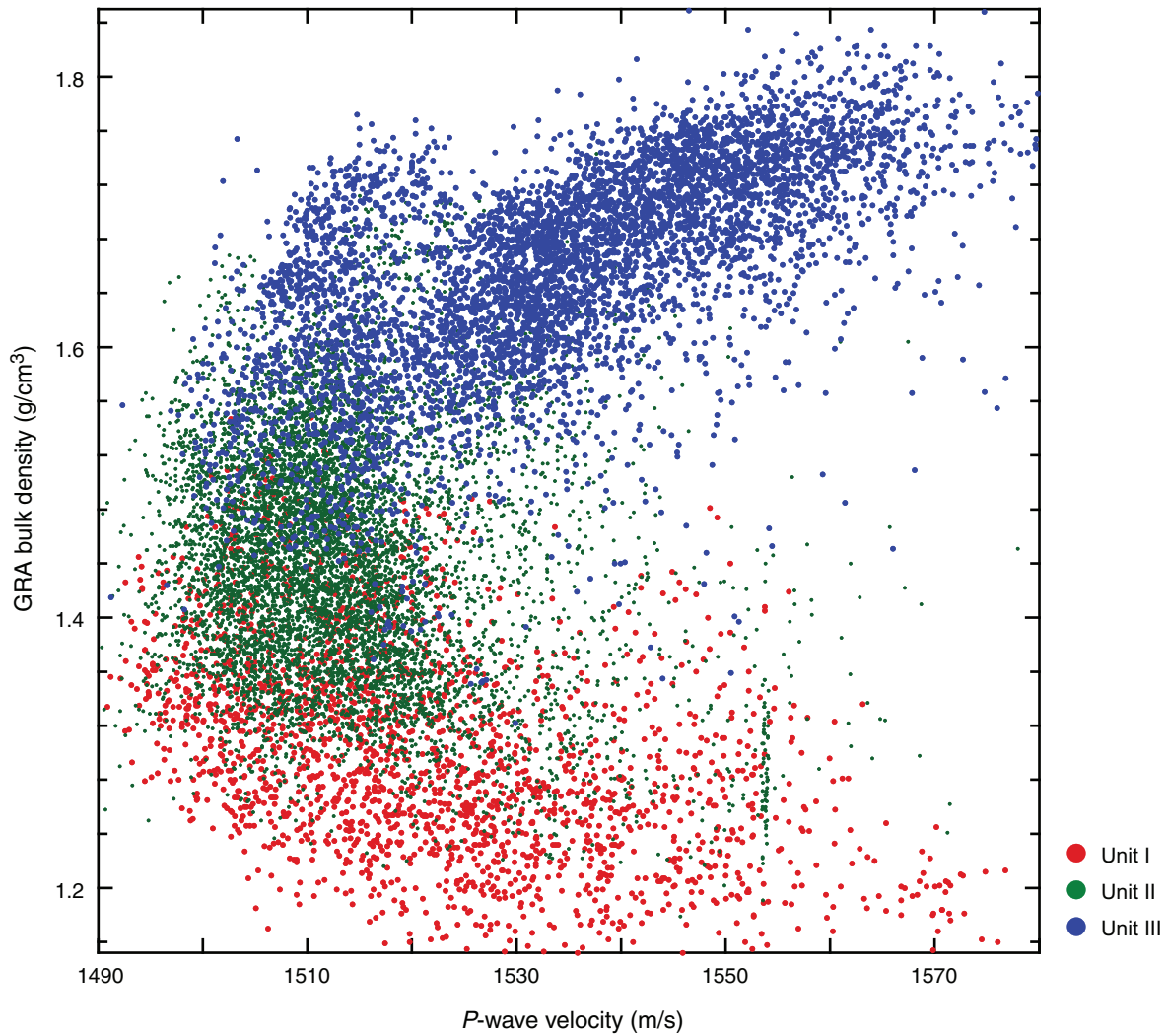


Figure F35. Comparison between the PWL (gray) and borehole log (red) P -wave velocities, Hole U1338B.

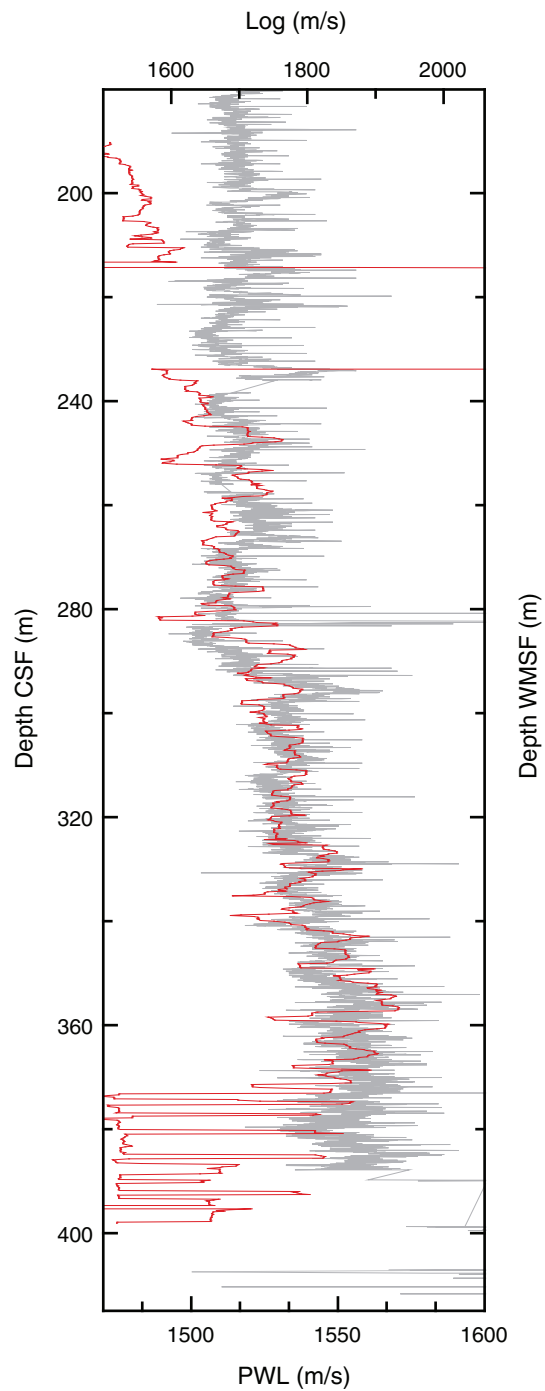


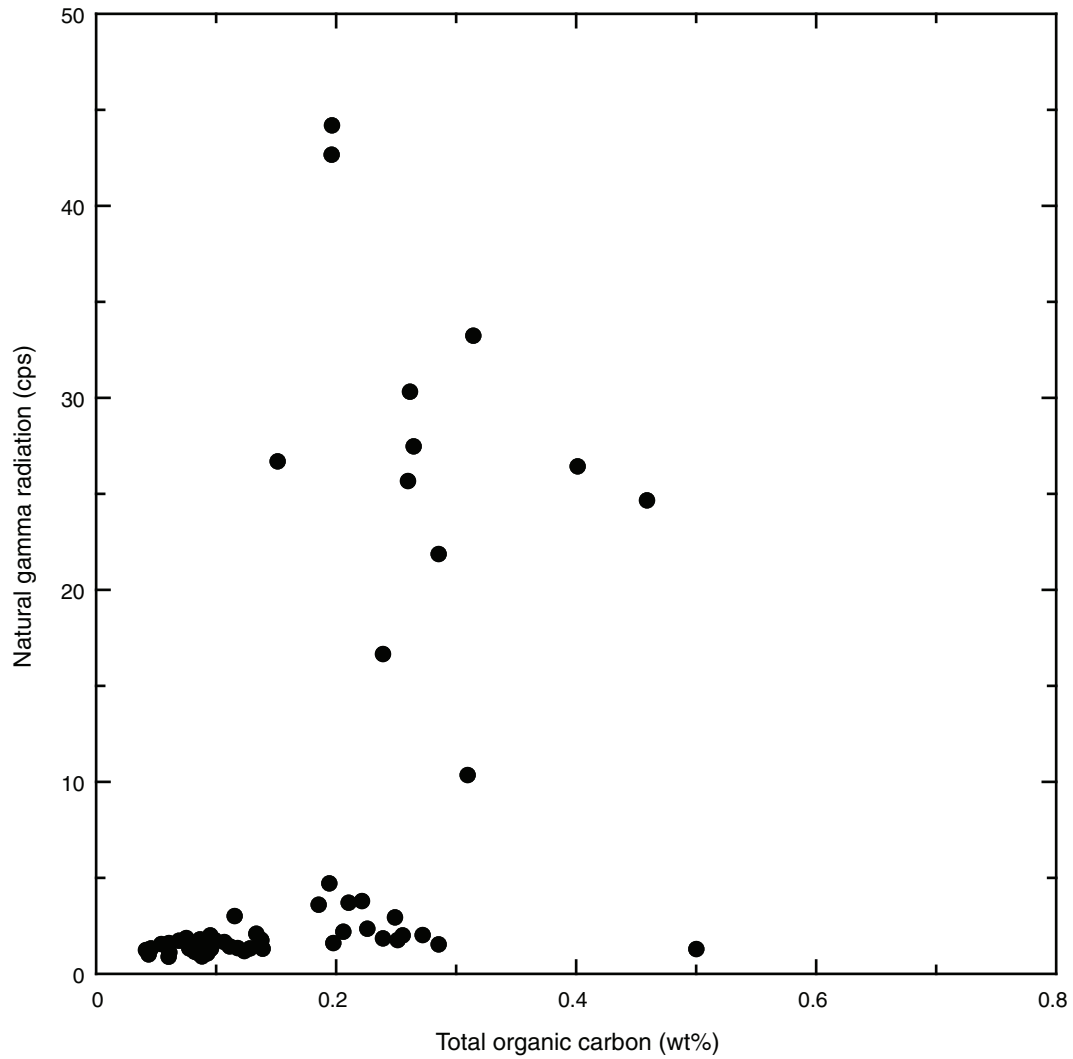
Figure F36. Natural gamma radiation vs. total organic carbon, Holes U1338A and U1338B.

Figure F37. Natural gamma radiation (NGR) plotted with gamma ray attenuation (GRA) bulk density, magnetic susceptibility, total organic carbon (TOC), and calcium carbonate (CaCO₃), Hole U1338A.

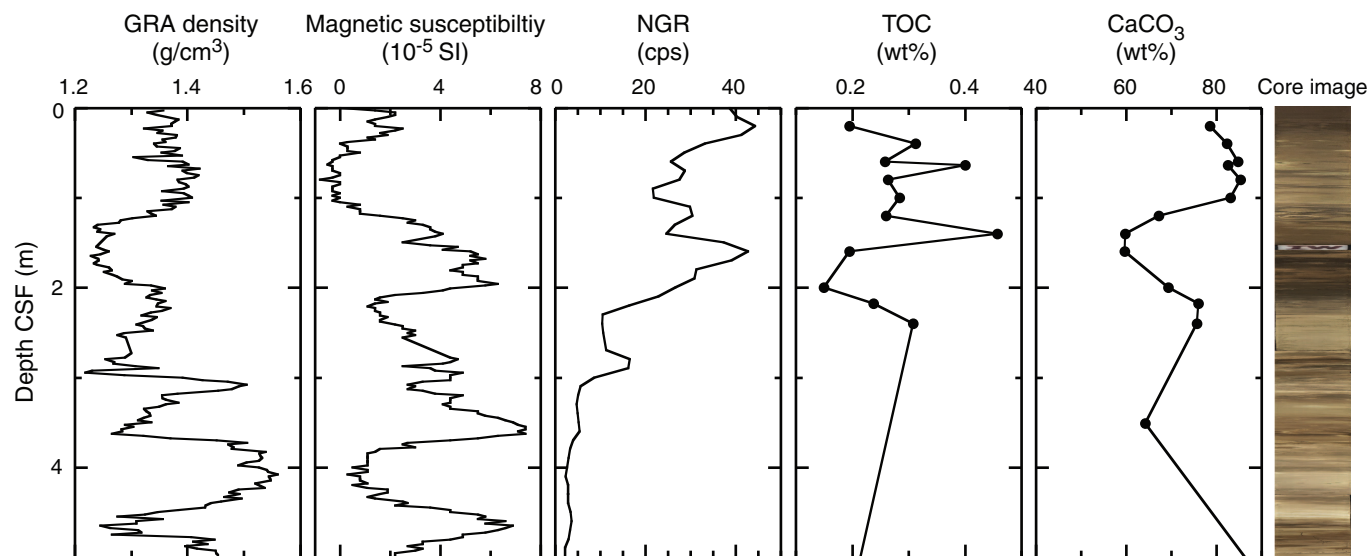


Figure F38. Thermal conductivity vs. depth, Hole U1338A.

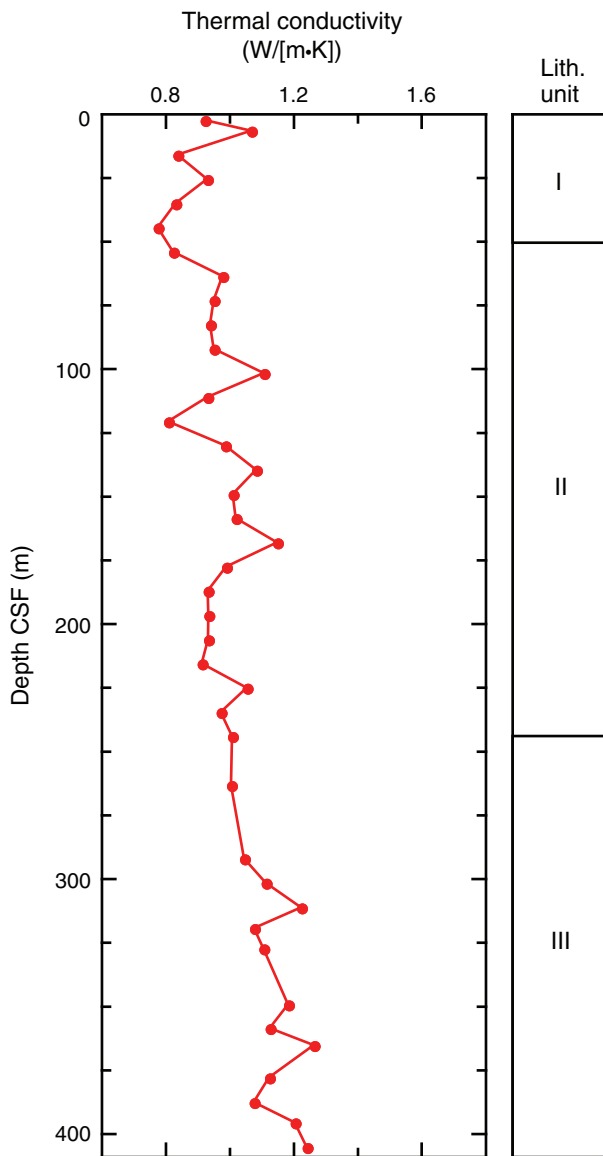


Figure F40. Reflectance spectroscopy, Hole U1338C. L^* = luminance, a^* = blue–yellow, b^* = green–red.

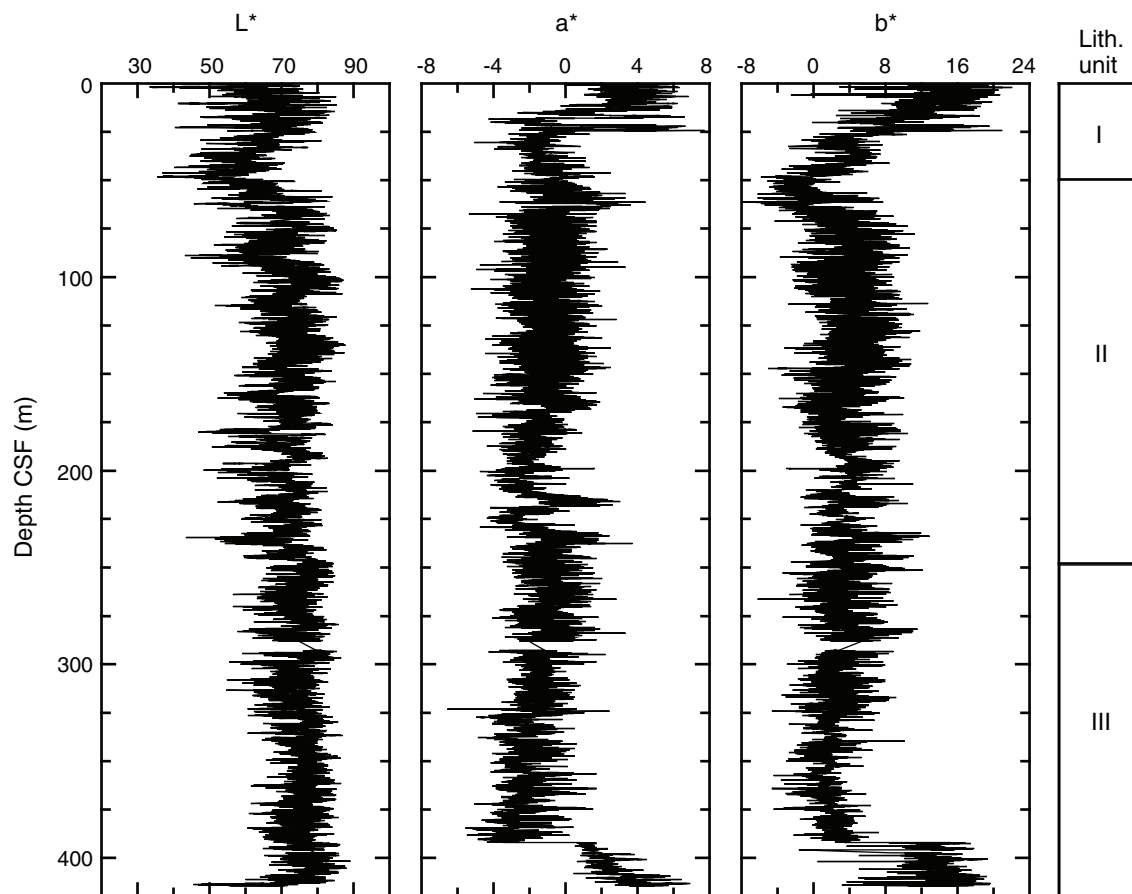


Figure F41. Magnetic susceptibility data, Site U1338. Upper panel: spliced section with core breaks (triangles) and hole designations. Lower panel: Holes U1338A–U1338C are offset from each other by a constant 10 SI units. A. 0–50 m CCSF-A. (**Continued on next eight pages.**)

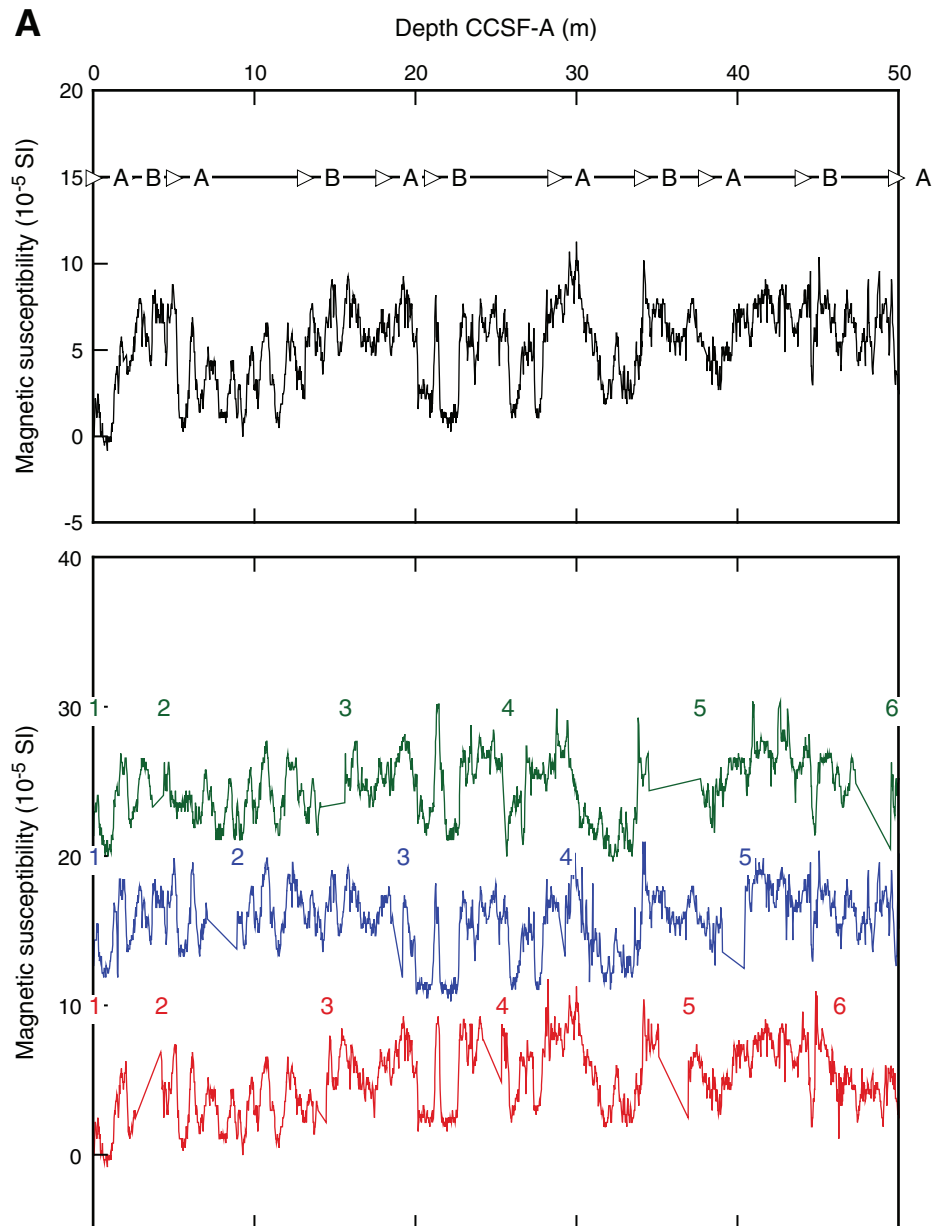


Figure F41 (continued). B. 50–100 m CCSF-A. (Continued on next page.)

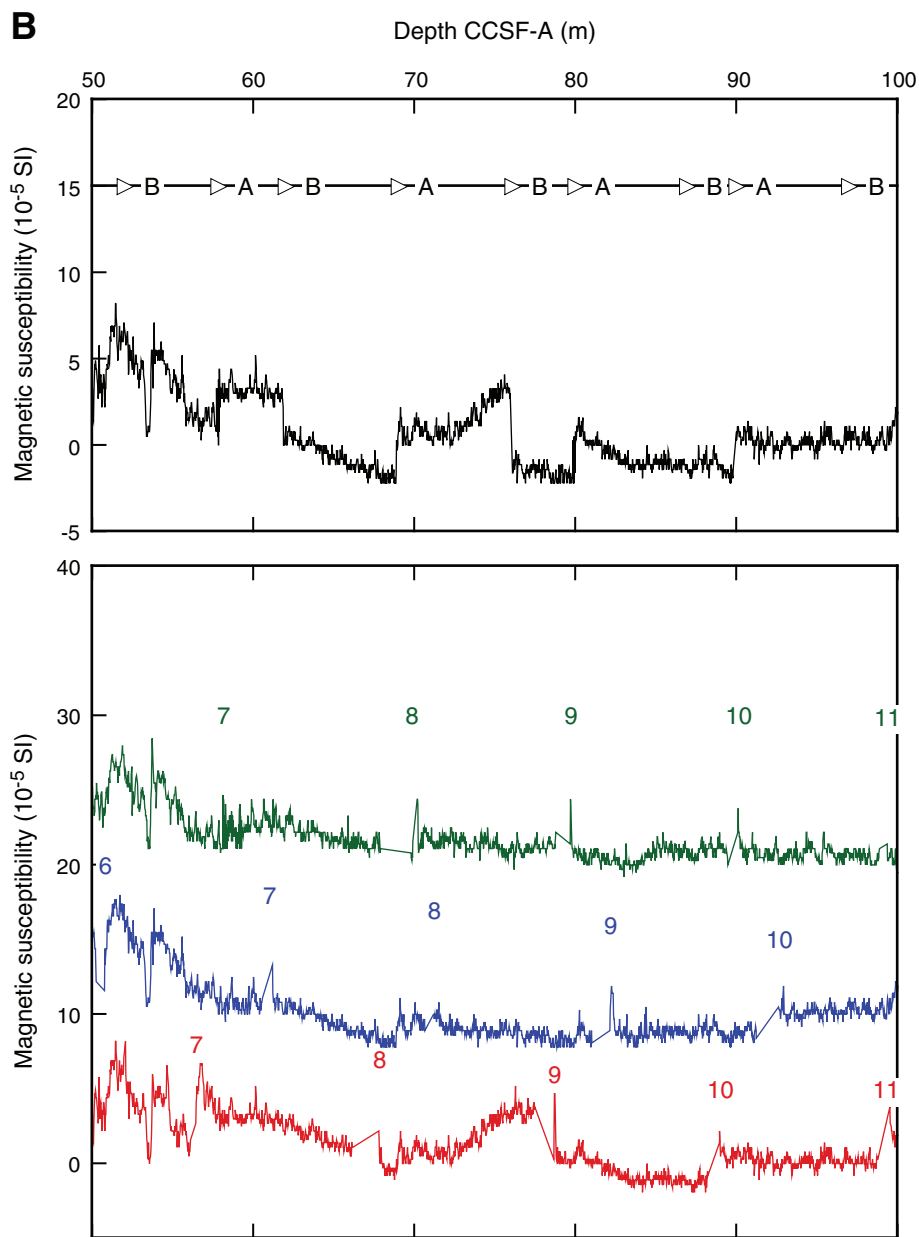


Figure F41 (continued). C. 100–150 m CCSF-A. (Continued on next page.)

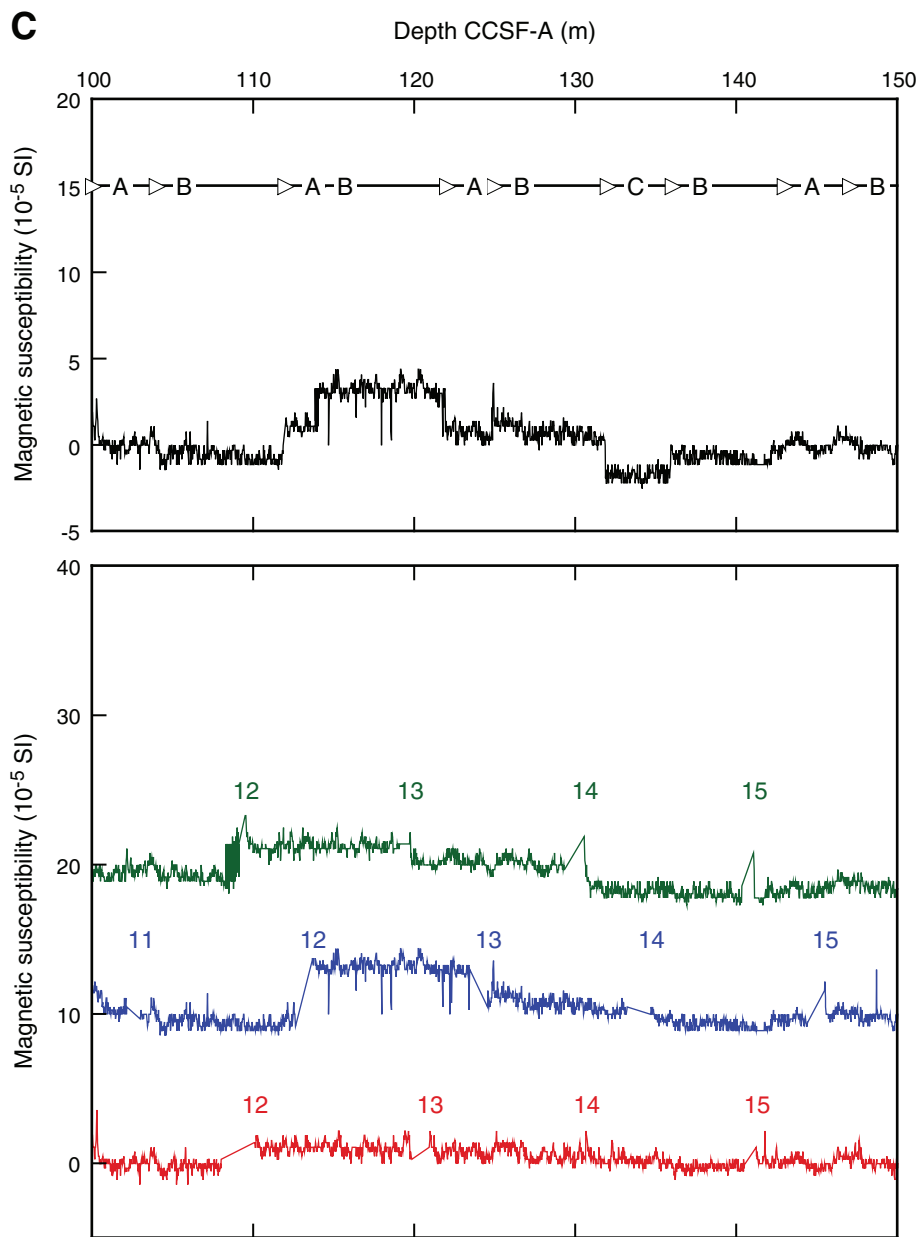


Figure F41 (continued). E. 200–250 CCSF-A. (Continued on next page.)

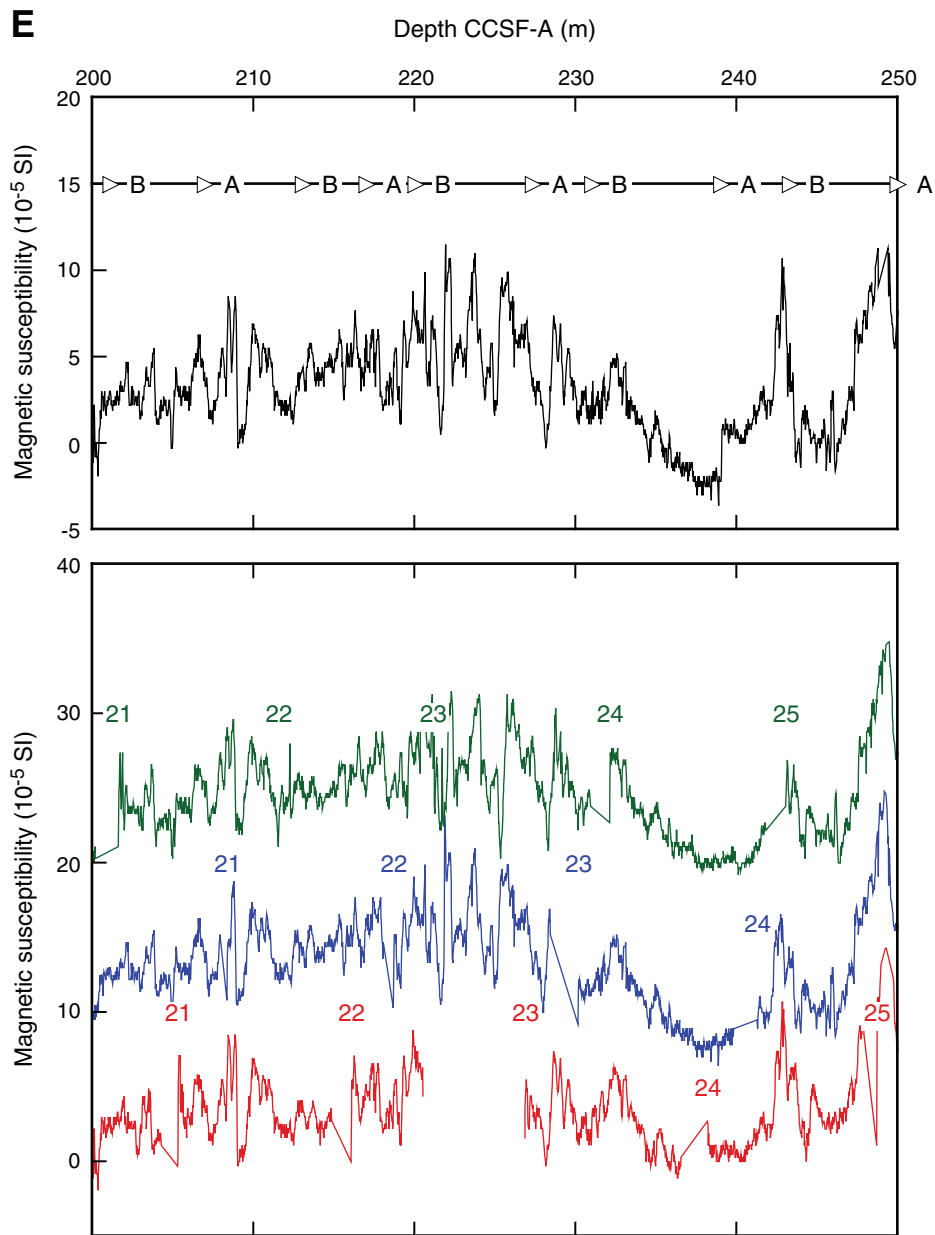


Figure F41 (continued). F. 250–300 CCSF-A. (Continued on next page.)

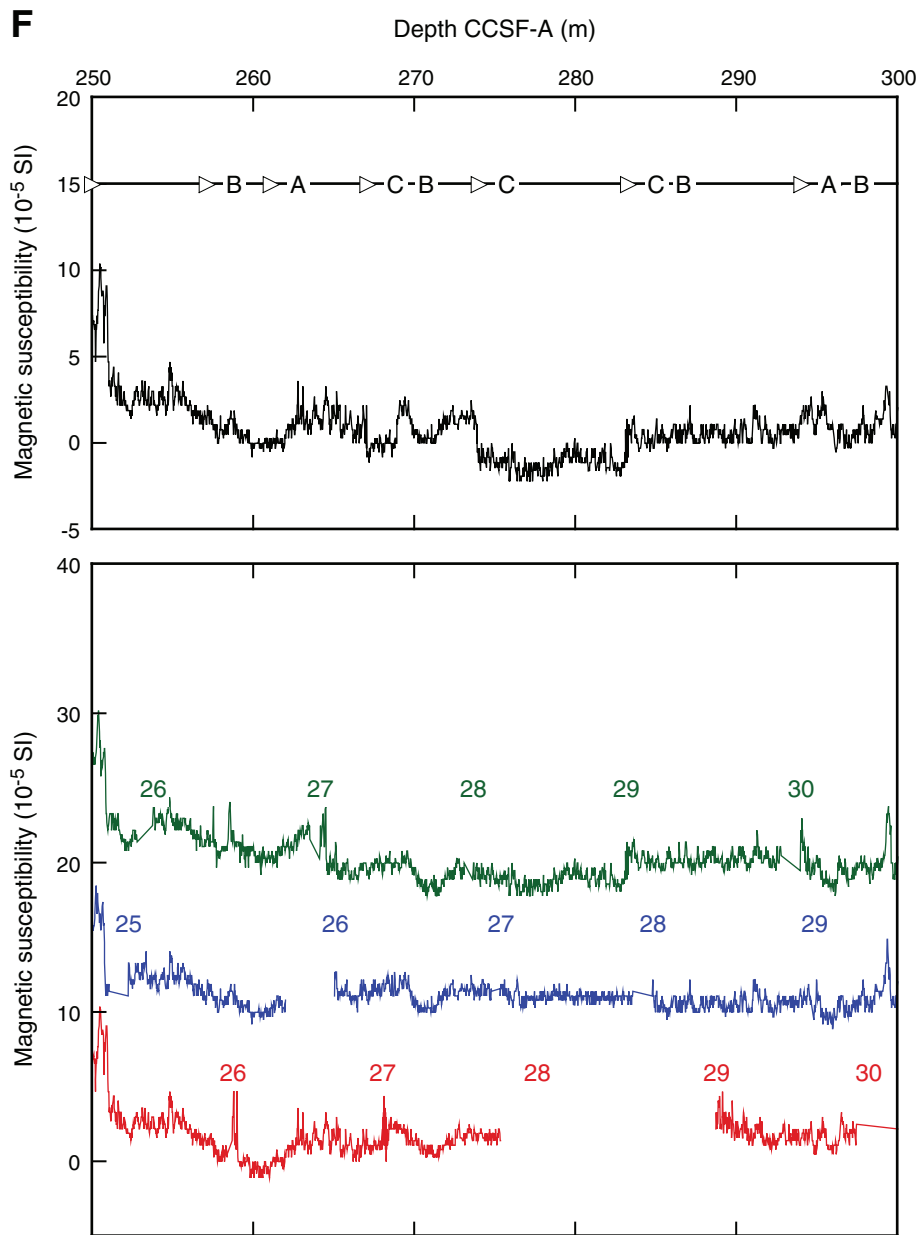


Figure F41 (continued). G. 300–350 CCSF-A. (Continued on next page.)

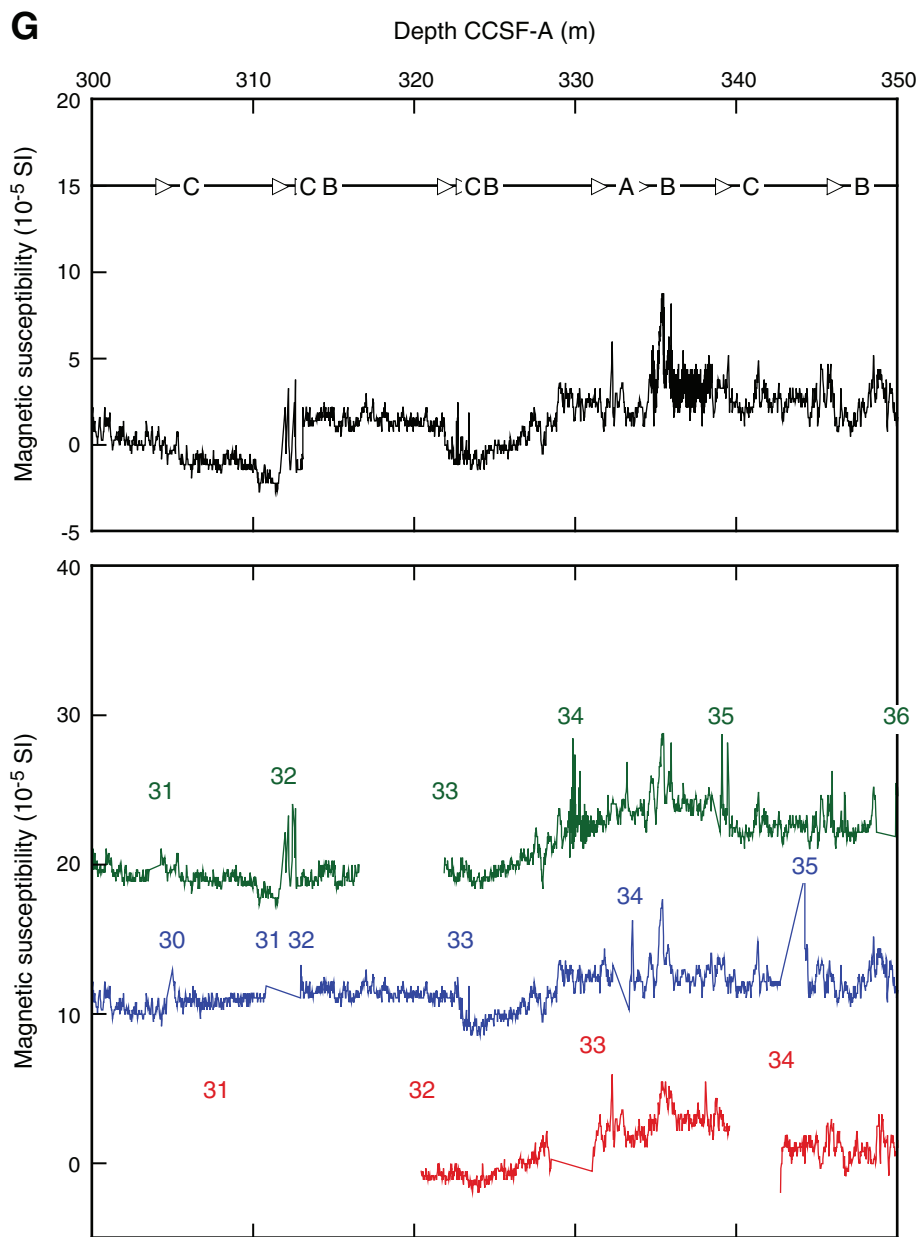


Figure F41 (continued). H. 350–400 CCSF-A. (Continued on next page.)

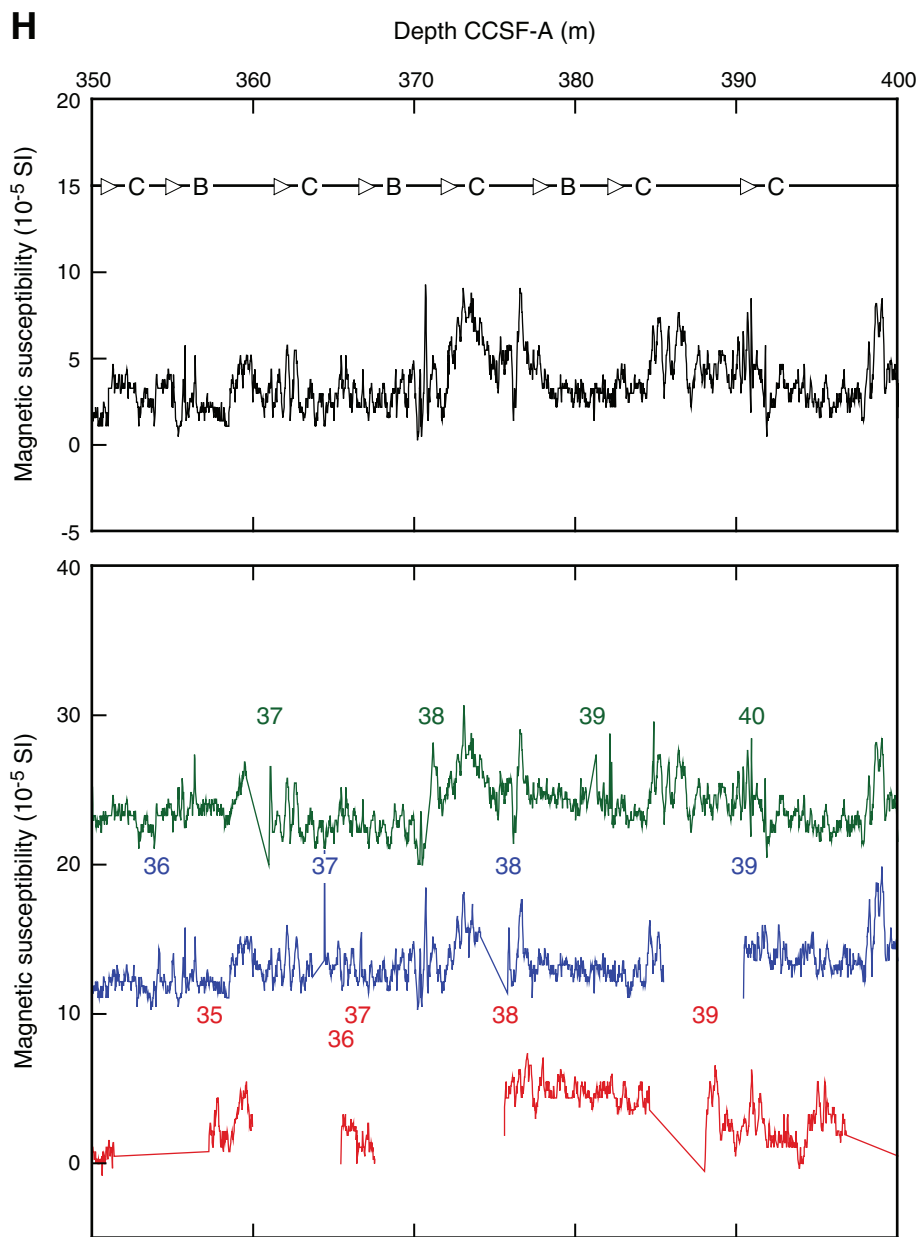


Figure F41 (continued). I. 400–450 CCSF-A.

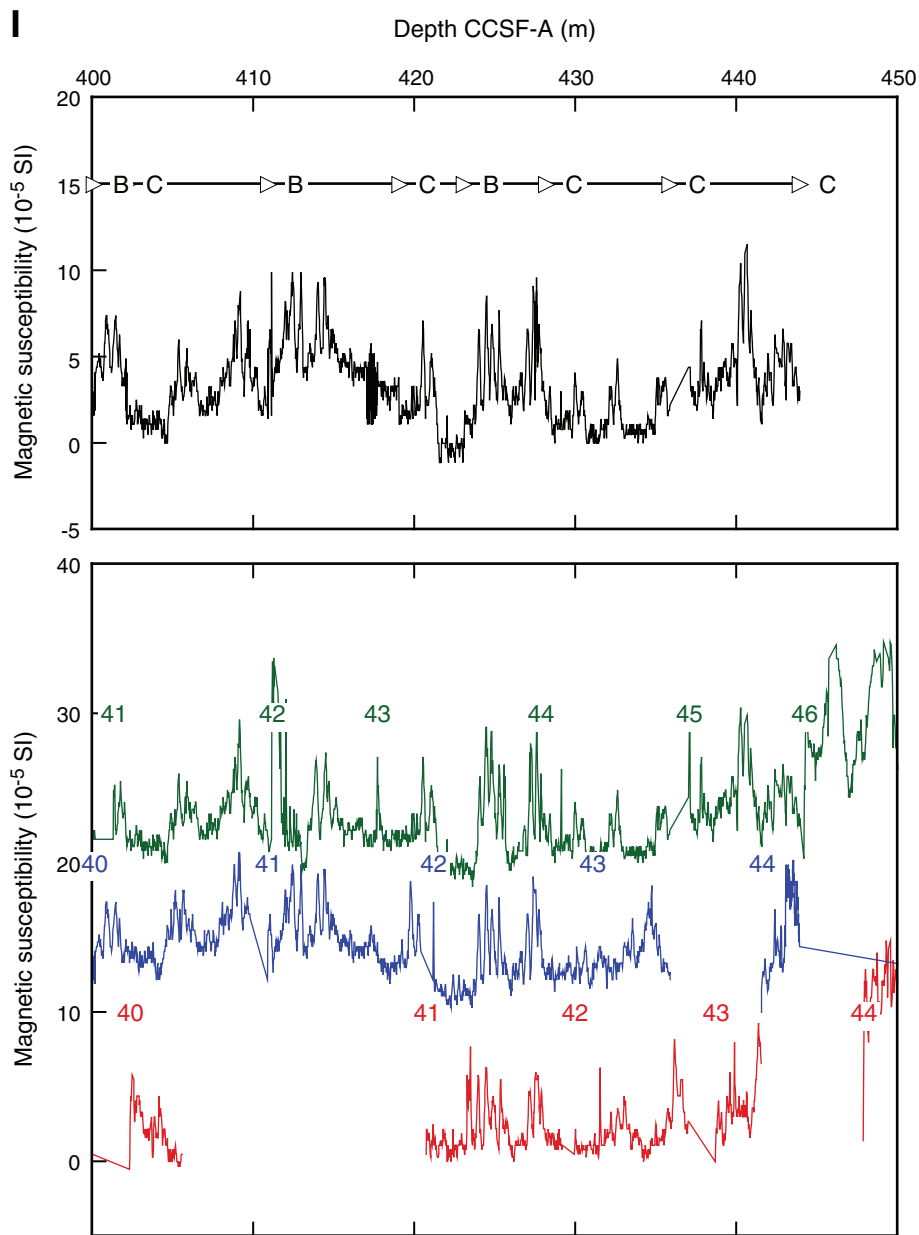


Figure F42. Gamma ray attenuation (GRA) density data, Site U1338. Upper panel: spliced section with core breaks (triangles) and hole designations. Lower panel: Holes U1338A–U1338C are offset from each other by a constant 0.05 g/cm³. A. 0–50 m CCSF-A. (**Continued on next eight pages.**)

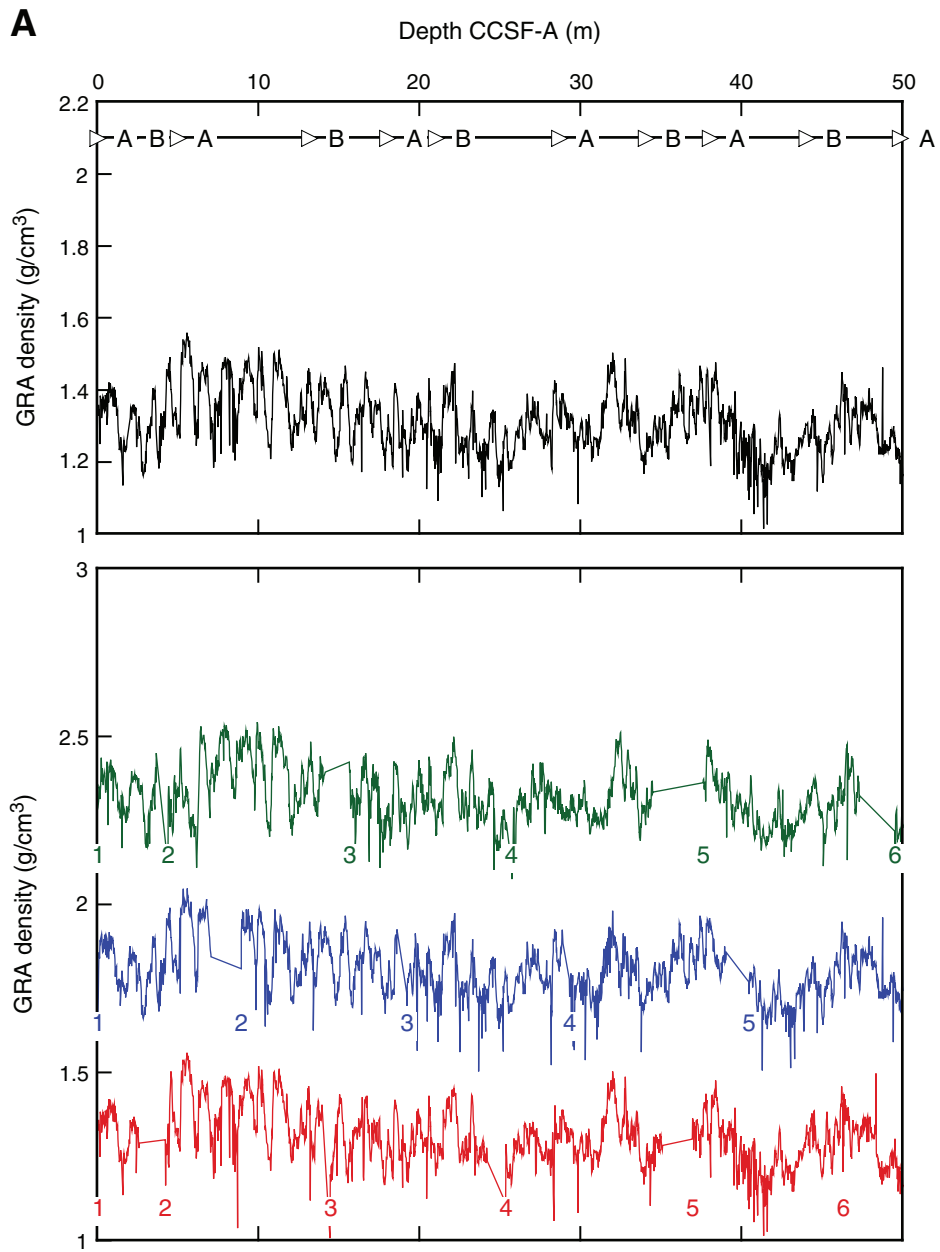


Figure F42 (continued). C. 100–150 m CCSF-A. (Continued on next page.)

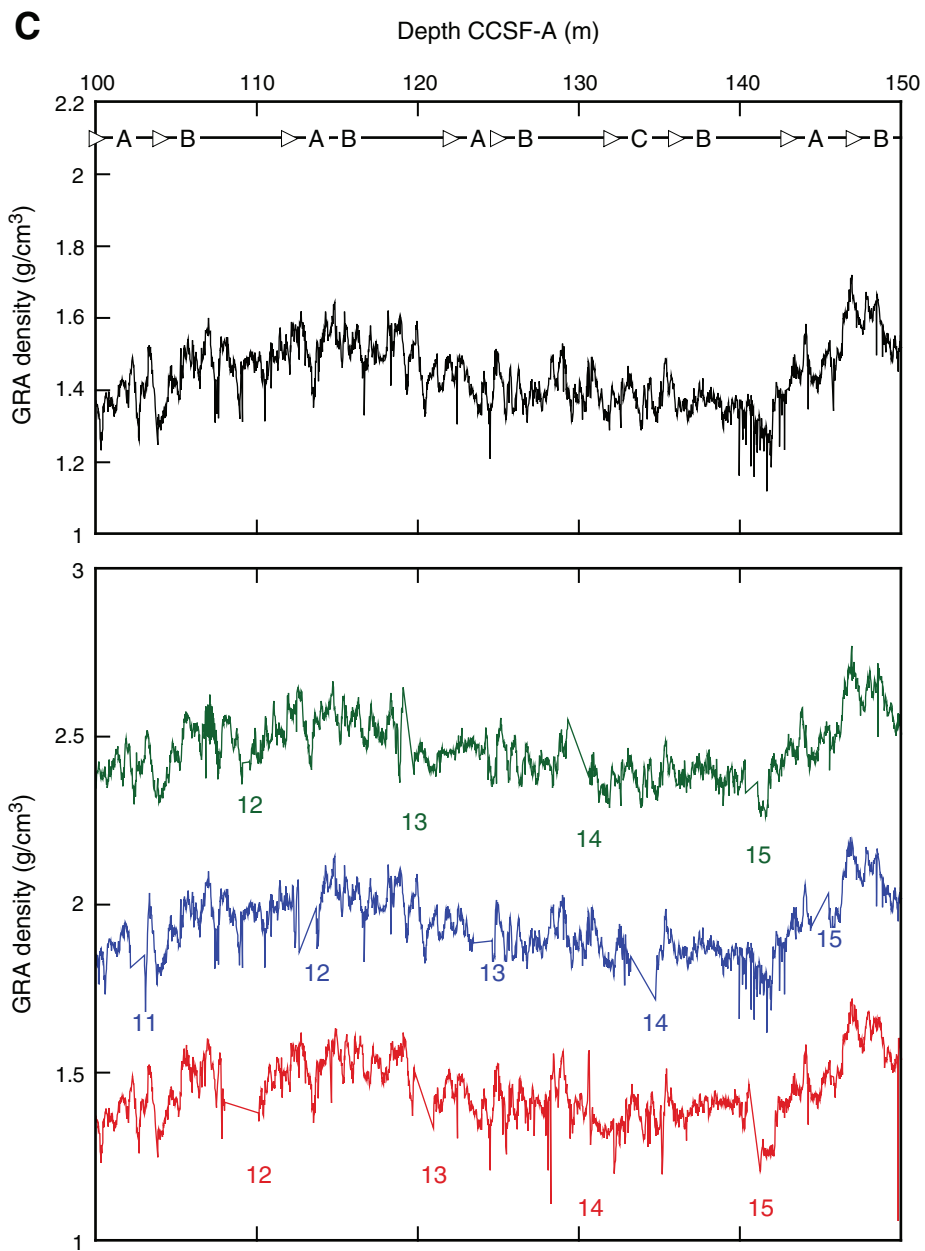


Figure F42 (continued). D. 150–200 CCSF-A. (Continued on next page.)

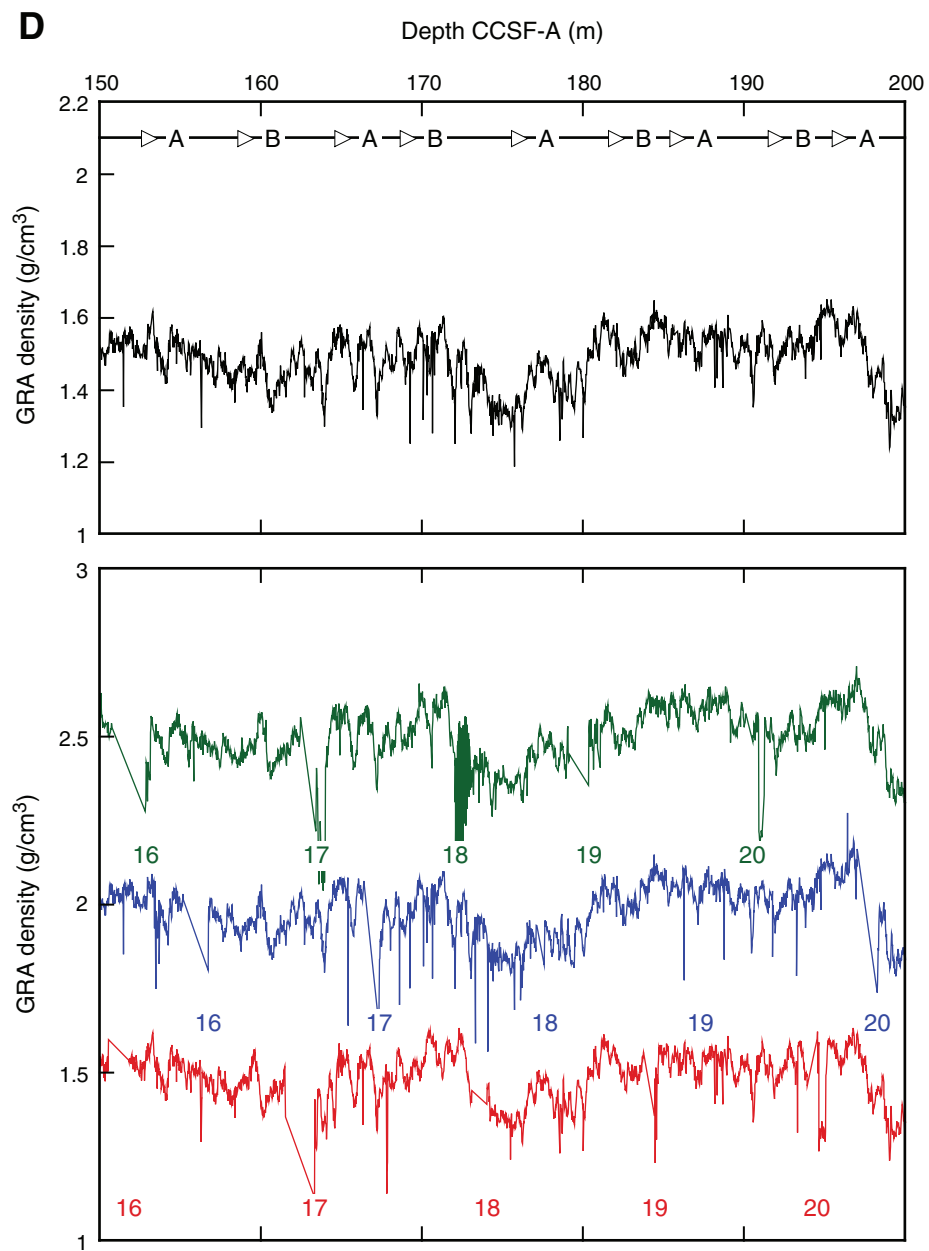


Figure F42 (continued). E. 200–250 CCSF-A. (Continued on next page.)

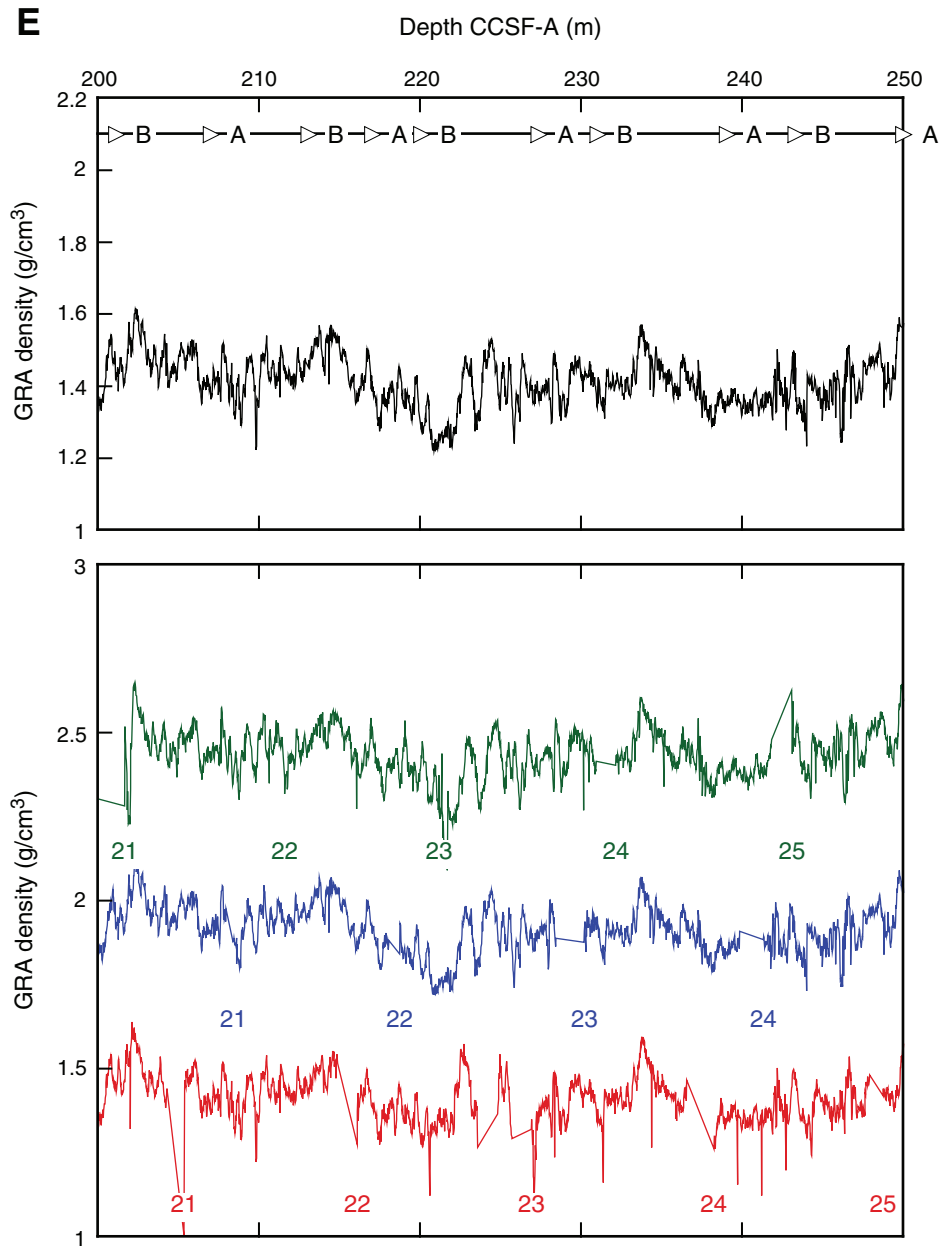


Figure F42 (continued). F. 250–300 CCSF-A. (Continued on next page.)

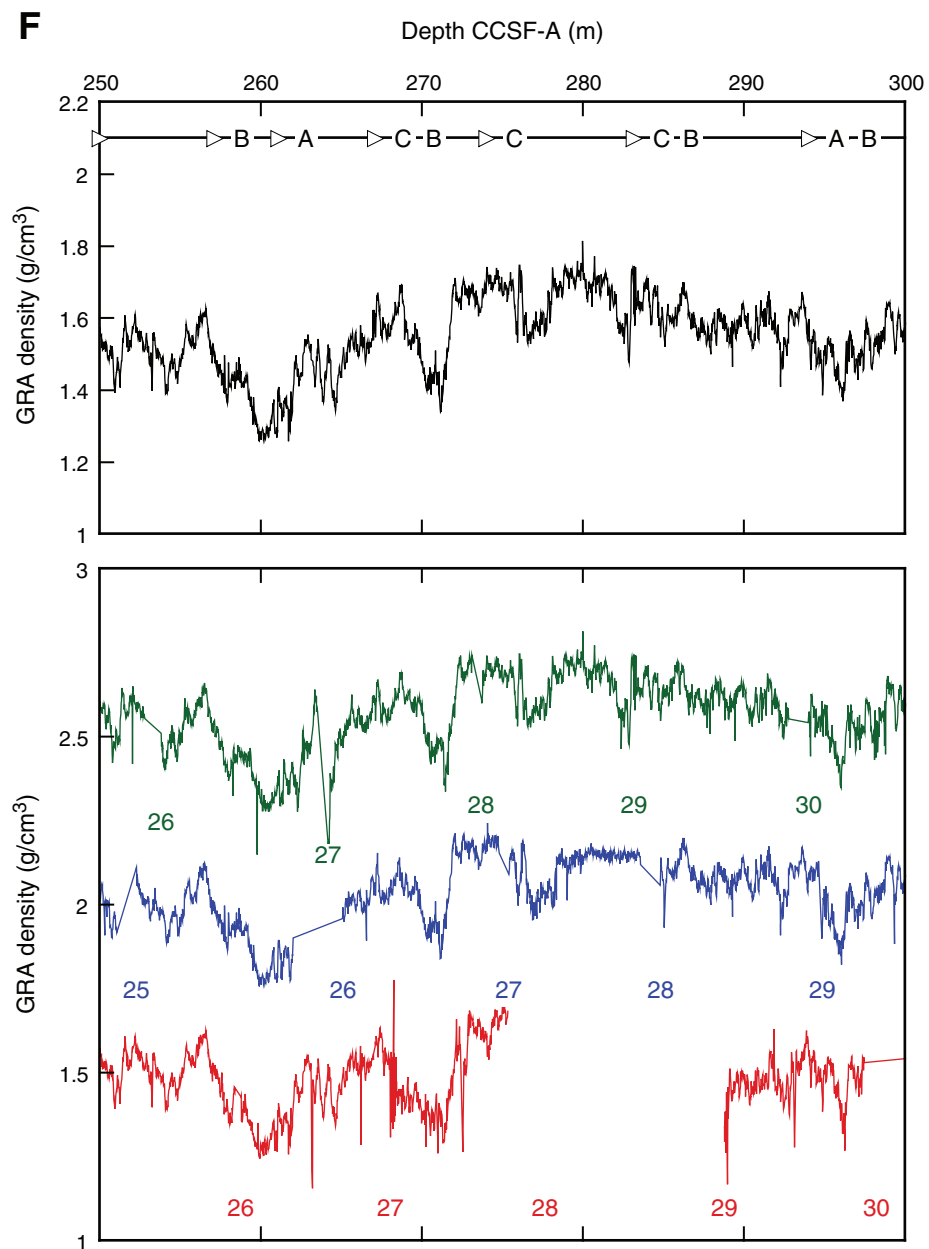


Figure F42 (continued). G. 300–350 CCSF-A. (Continued on next page.)

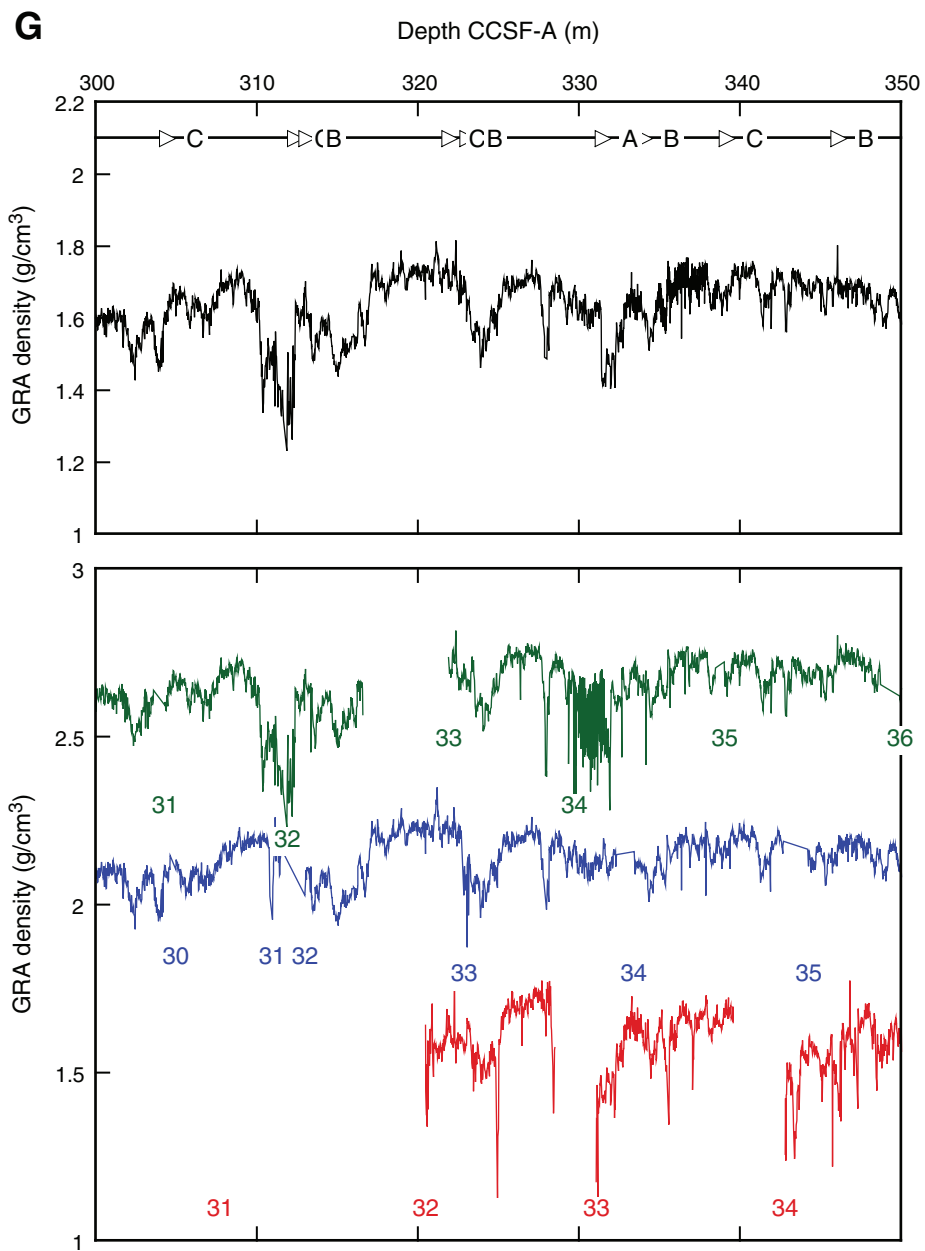


Figure F42 (continued). H. 350–400 CCSF-A. (Continued on next page.)

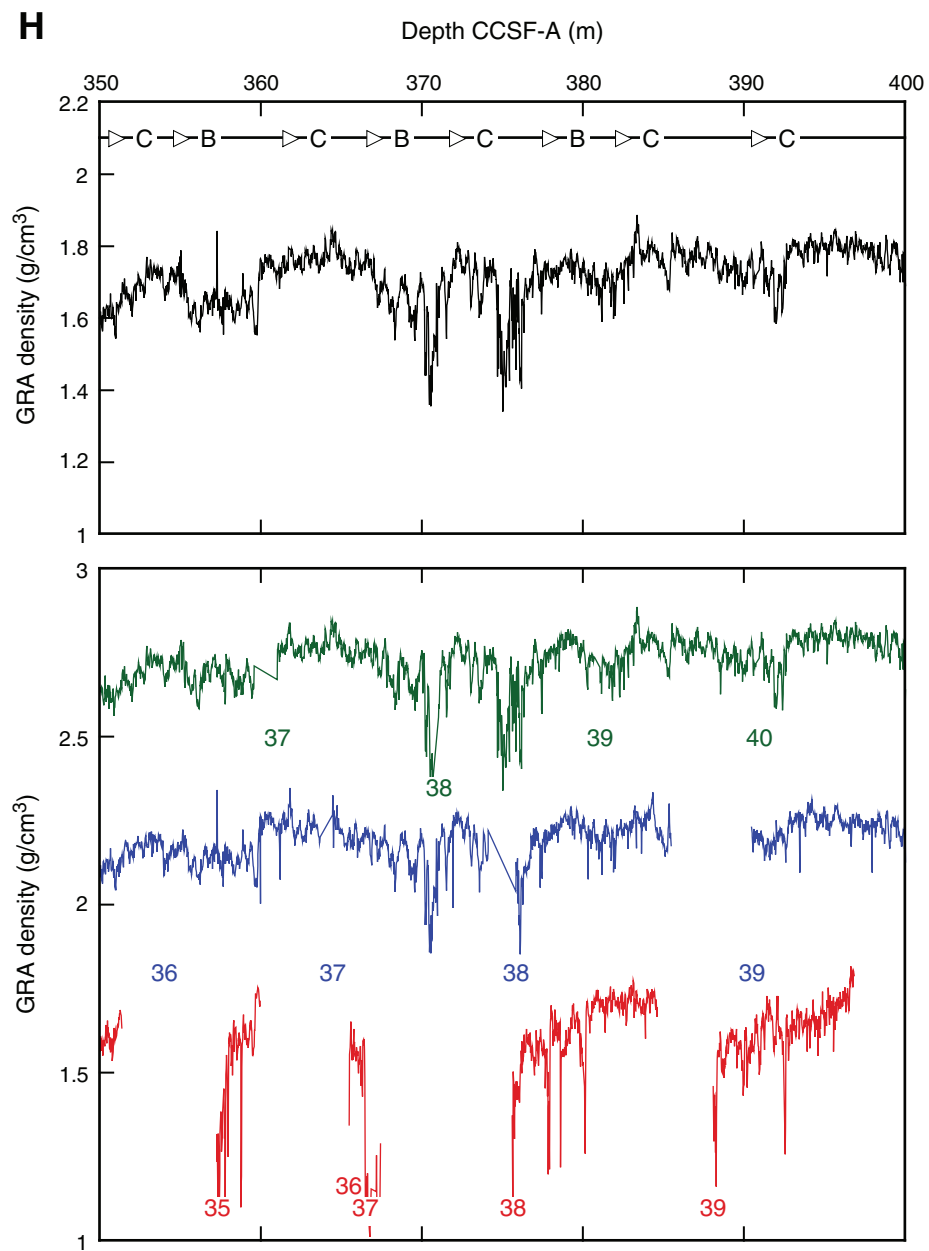


Figure F42 (continued). I. 400–450 CCSF-A.

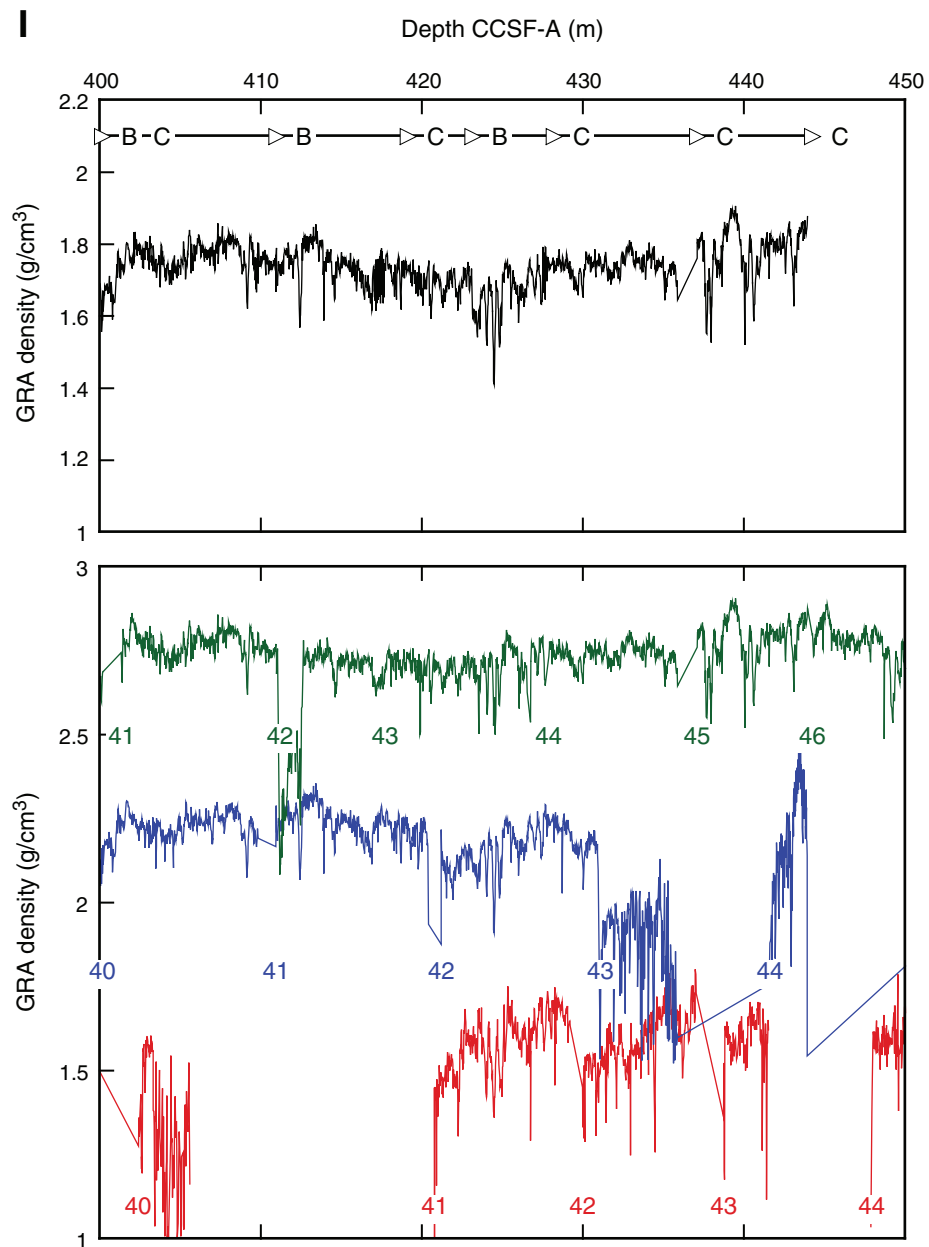




Figure F43. Core images, Holes U1338A–U1338C. Yellow lines = top of spliced interval, red lines = bottom of spliced interval, purple bars = disturbed core intervals. **A.** 0–50 m CCSF-A. **B.** 50–100 m CCSF-A. (Continued on next four pages.)

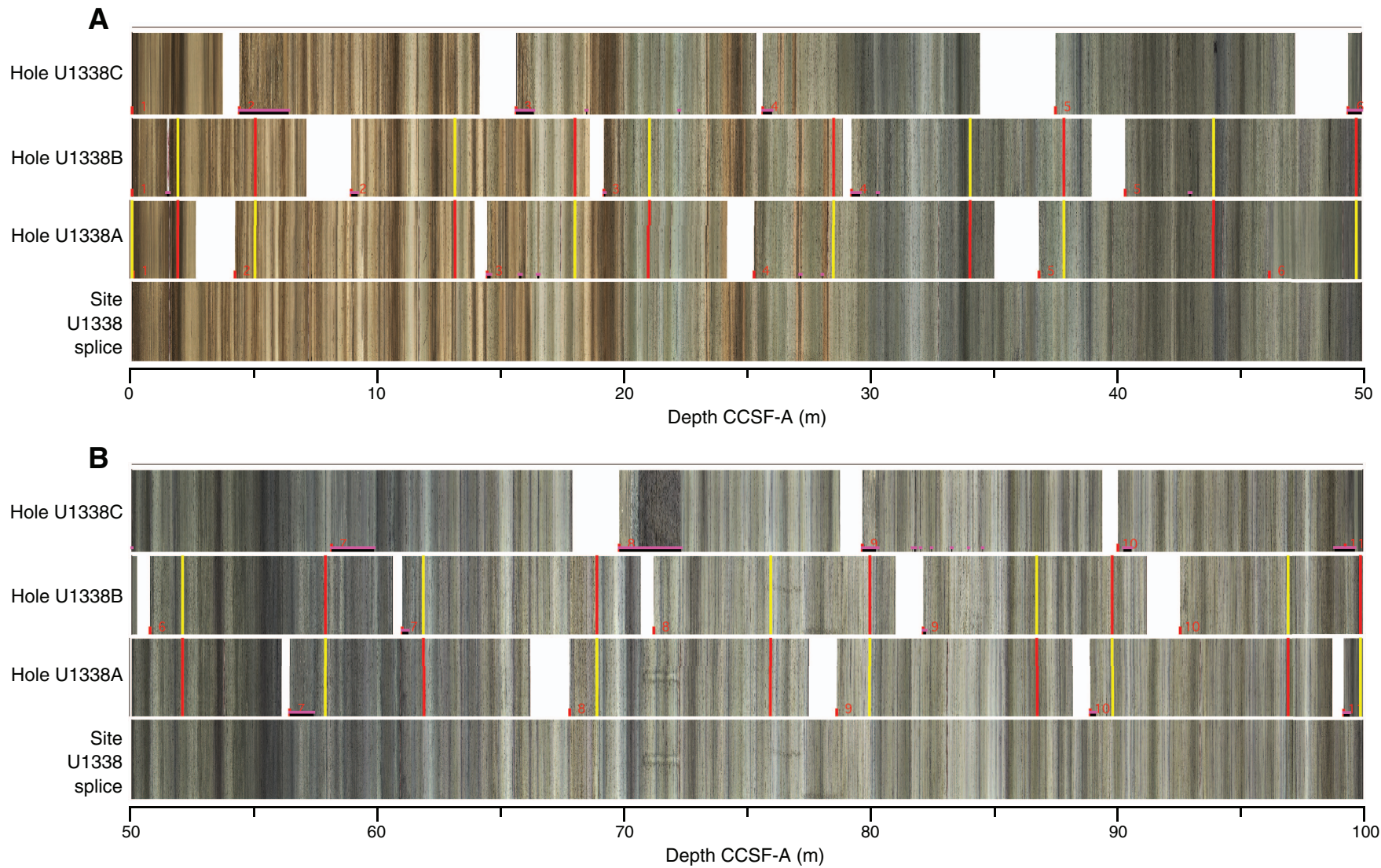




Figure F43 (continued). C. 100–150 m CCSF-A. D. 150–200 m CCSF-A. (Continued on next page.)

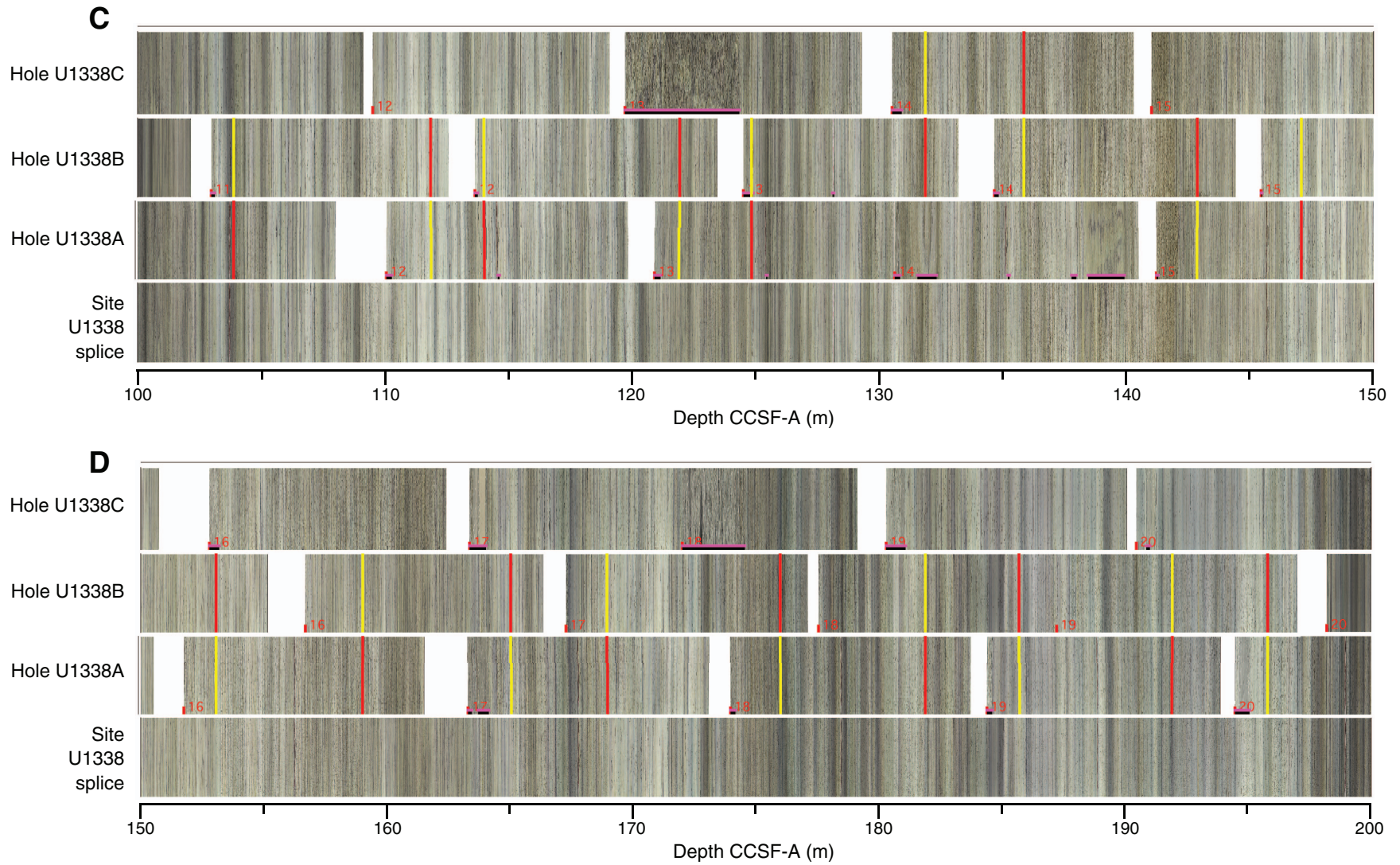




Figure F43 (continued). E. 200–250 m CCSF-A. F. 250–300 m CCSF-A. (Continued on next page.)

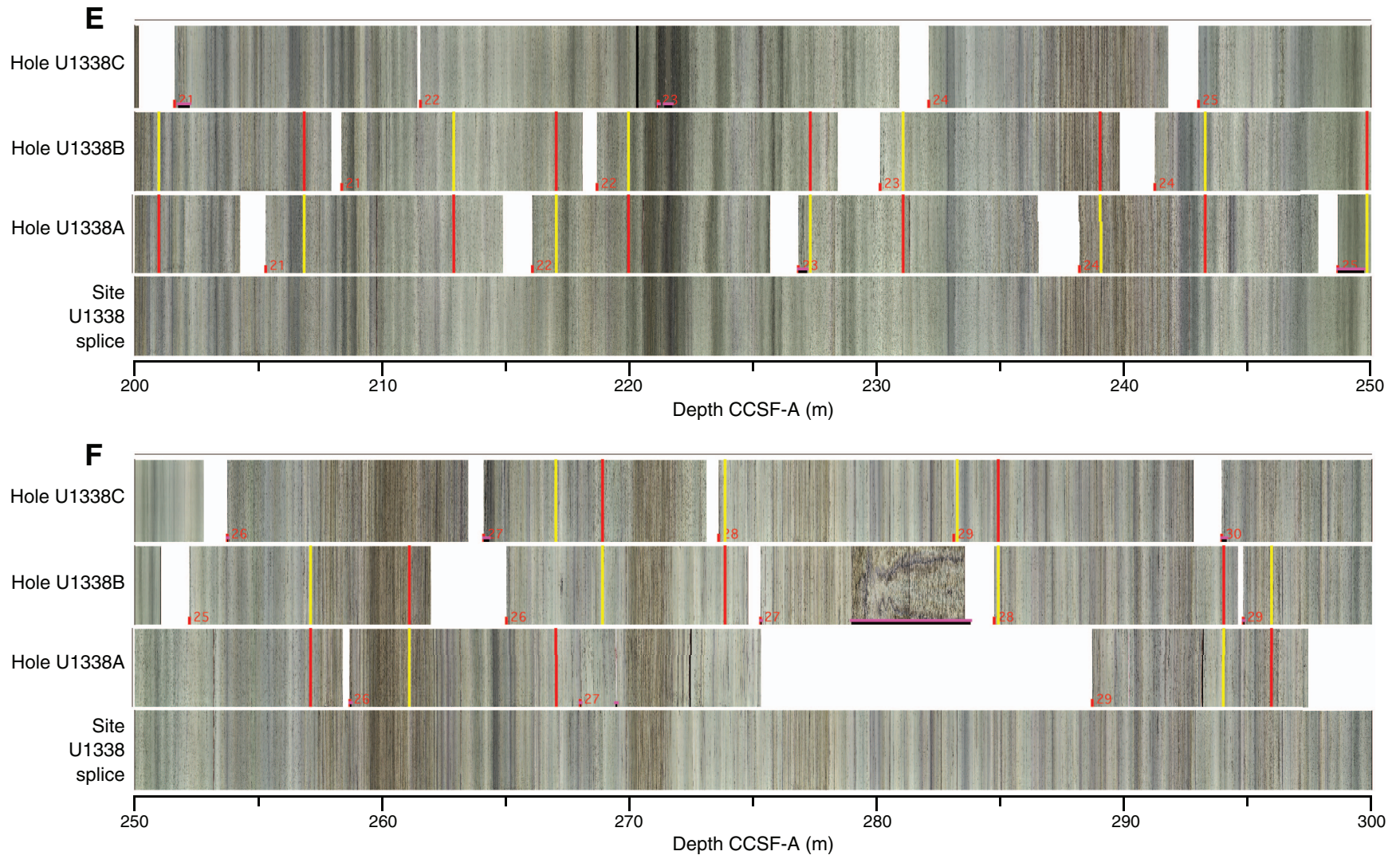




Figure F43 (continued). G. 300–350 m CCSF-A. H. 350–400 m CCSF-A. (Continued on next page.)

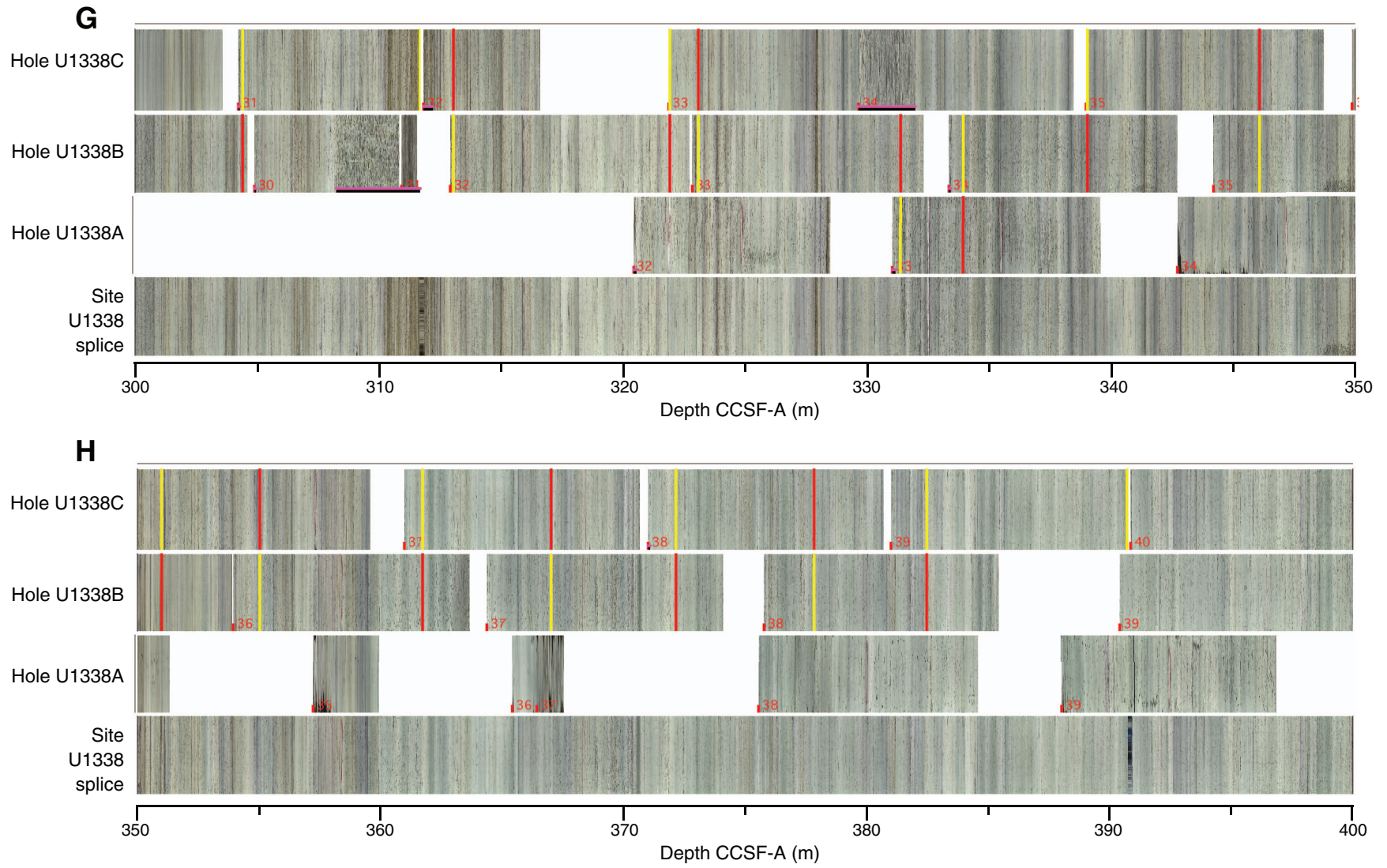


Figure F43 (continued). I. 400–460 m CCSF-A.

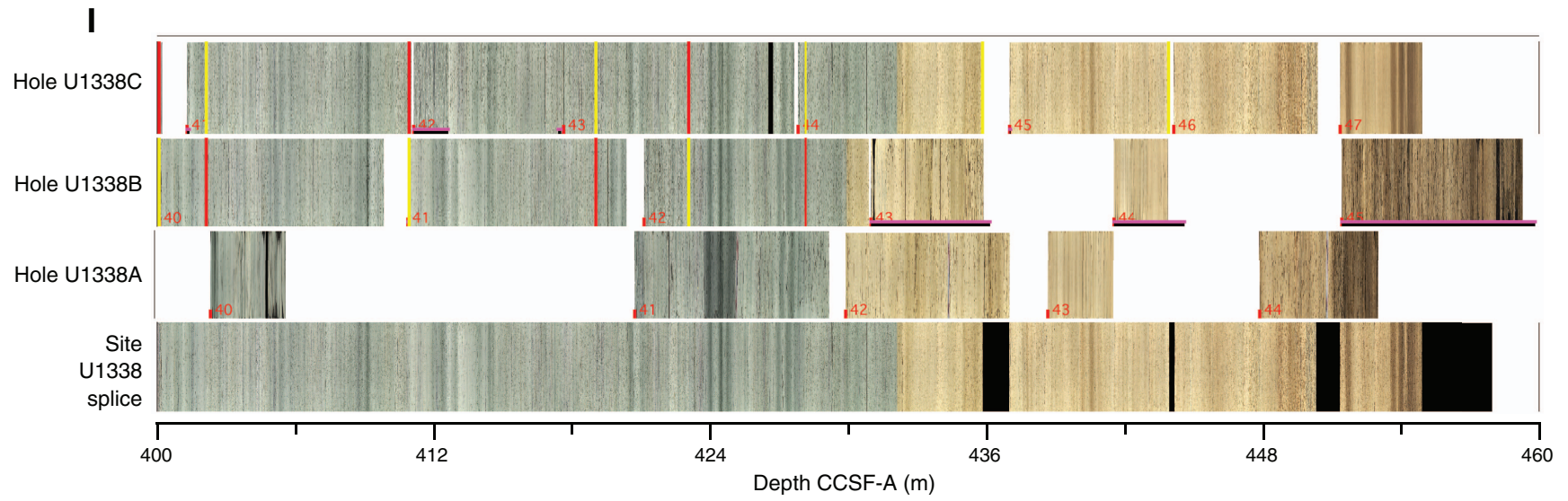


Figure F44. CSF depth vs. CCSF-A depth for tops of cores, Site U1338. Growth factor is the slope of the regression line. On average, CCSF-A depth of spliced section is 12% greater than CSF depth.

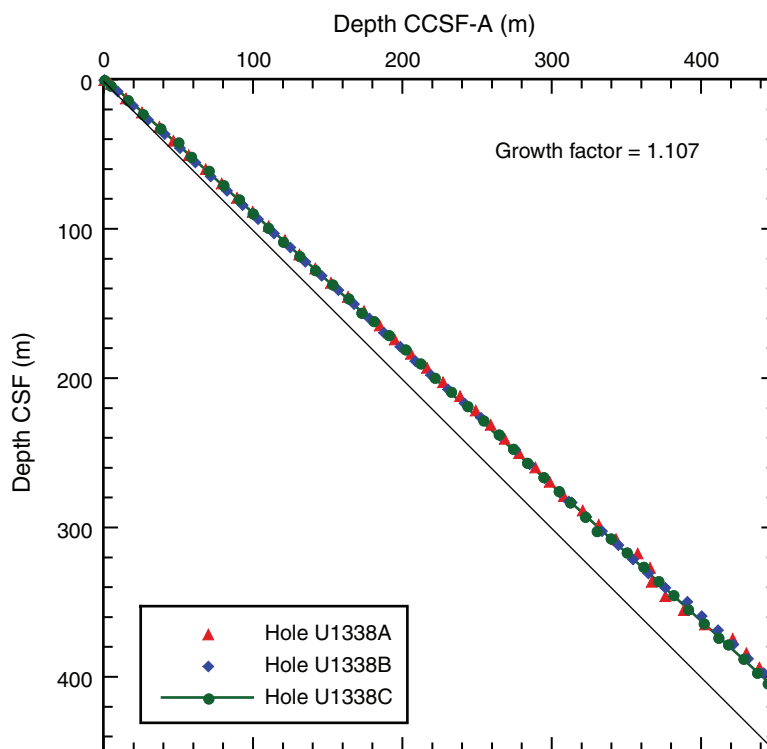


Figure F45. A. Modified triple combination tool string. HNGS = Hostile Environment Natural Gamma Ray Sonde, HLDS = Hostile Environment Litho-Density Sonde, GPIT = General Purpose Inclinomater Tool, DIT = Dual Induction Tool, SFLU = spherically focused resistivity. **B.** Logging pass schematic, Hole U1338B. In the main uplog pass, a borehole restriction was encountered near the base of the drill pipe (hatched interval).

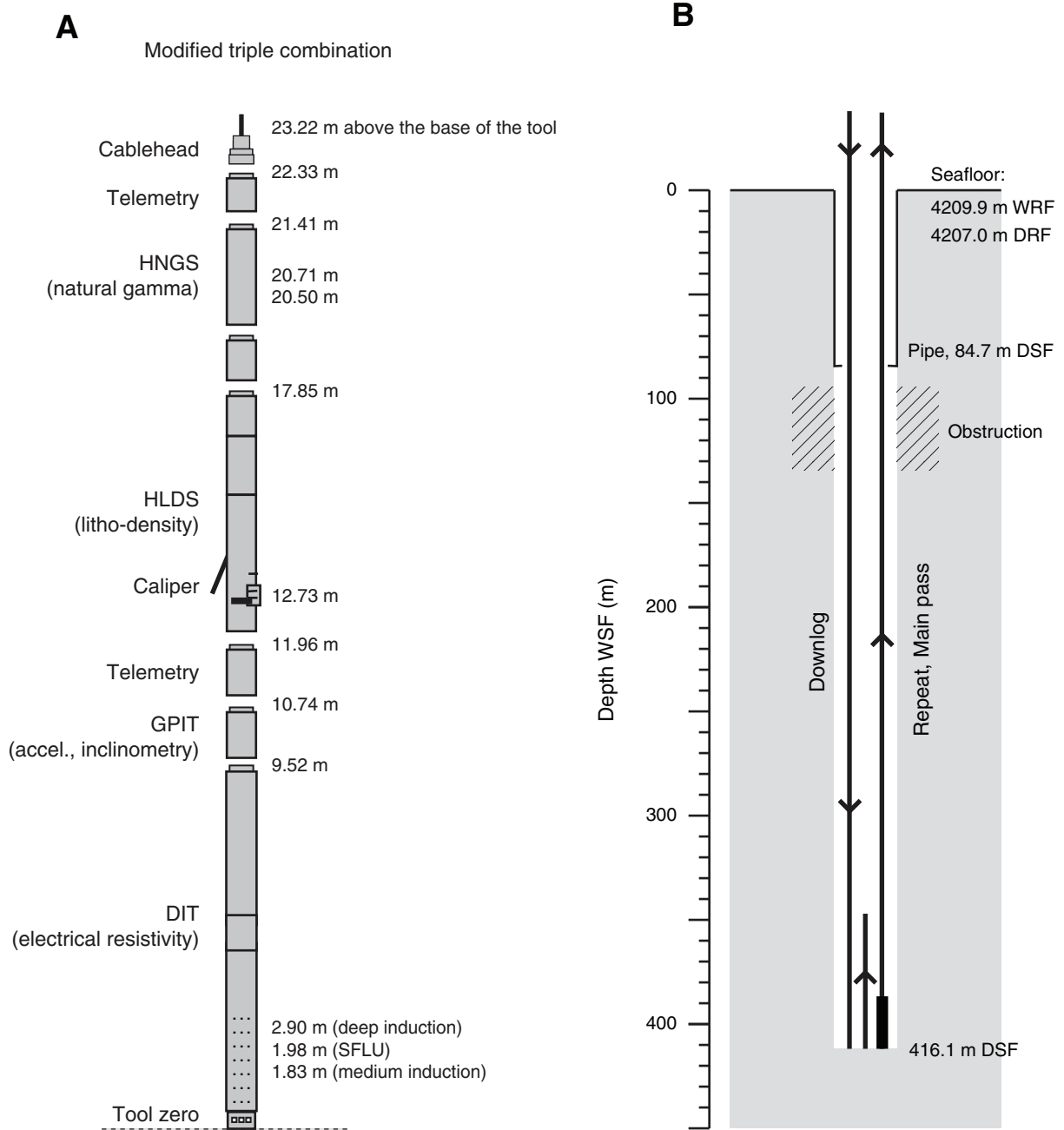


Figure F46. A. Formation MicroScanner (FMS)-sonic tool string. HNGS = Hostile Environment Natural Gamma Ray Sonde, DSI = Dipole Sonic Imager, GPIT = General Purpose Inclinerometer Tool. B. Logging pass schematic, Hole U1338B. Before the FMS-sonic logging run, the base of the drill pipe was lowered below the borehole restriction encountered during the triple combination run (Fig. F45).

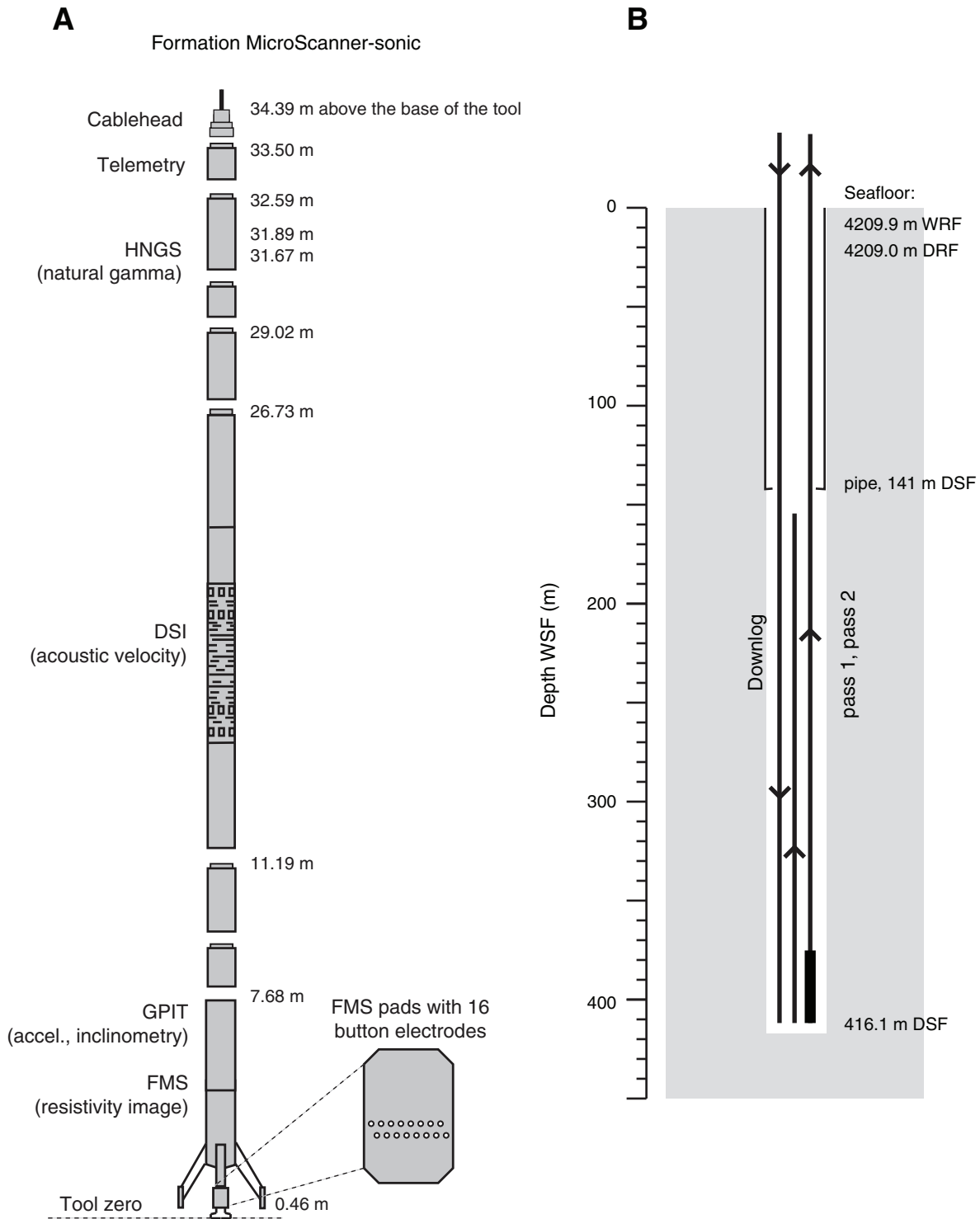


Figure F47. Downhole log measurement summary, Hole U1338B. TC = triple combination, MAD = moisture and density, IMPH = medium induction phasor-processed resistivity, SFLU = spherically focused resistivity, VSP = vertical seismic profile, FMS = Formation MicroScanner.

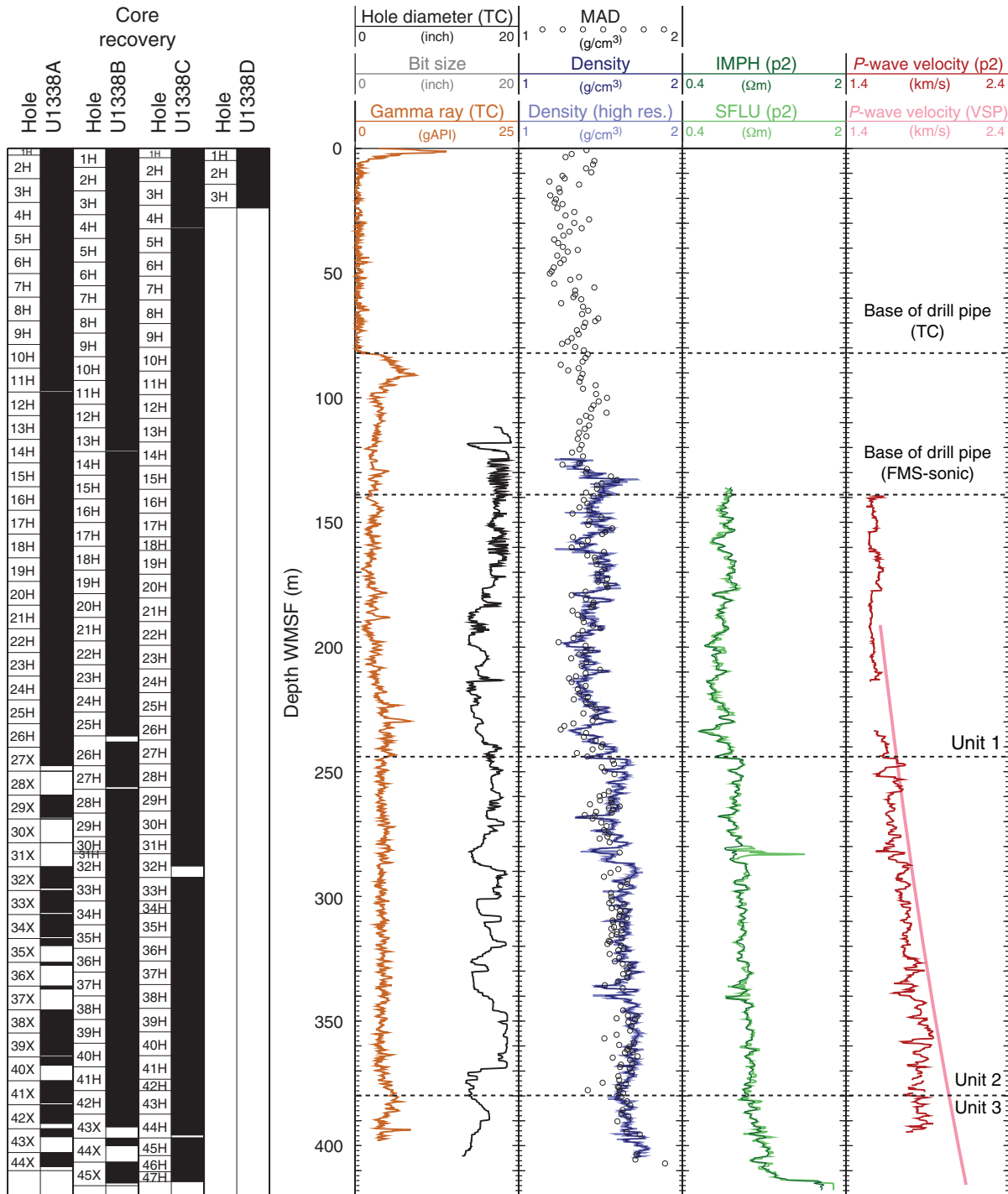


Figure F48. Natural gamma ray log measurement summary, Hole U1338B. FMS = Formation MicroScanner, TC = triple combination.

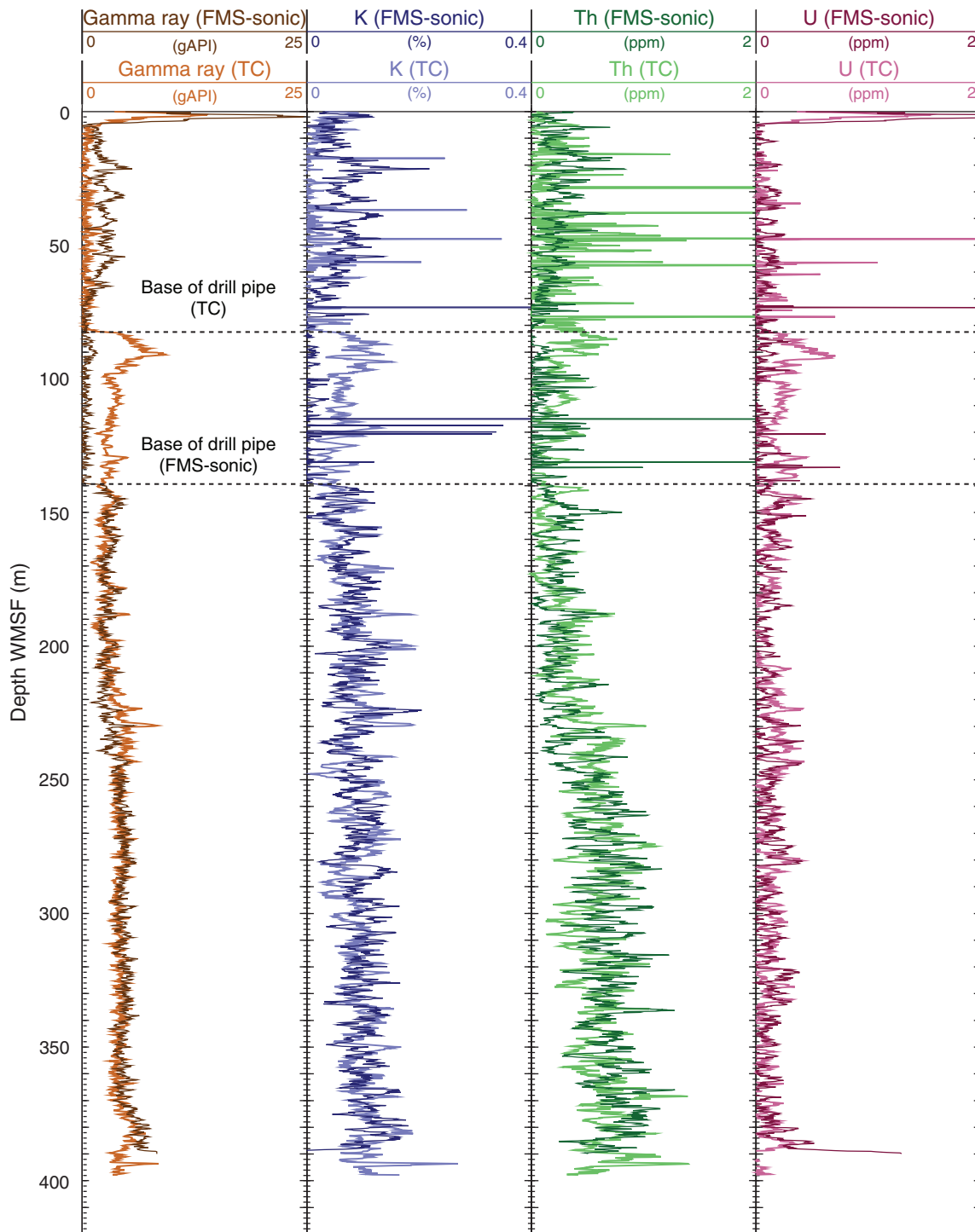




Figure F49. Downhole log curves in Hole U1338B from 230 to 252 m WSF showing Formation MicroScanner (FMS) four-pad downhole resistivity images from (A) Pass 1 and (B) Pass 2 with (C) DIT-measured SFLU resistivity, (D) HLDS-measured bulk density (red = high resolution, pink = standard resolution), (E) HNGS-measured total gamma radiation (dark green = triple combination, light green = FMS-sonic), (F) Site U1338 spliced core image (CCSF-B depth scale), and (G) Hole U1338C core description.

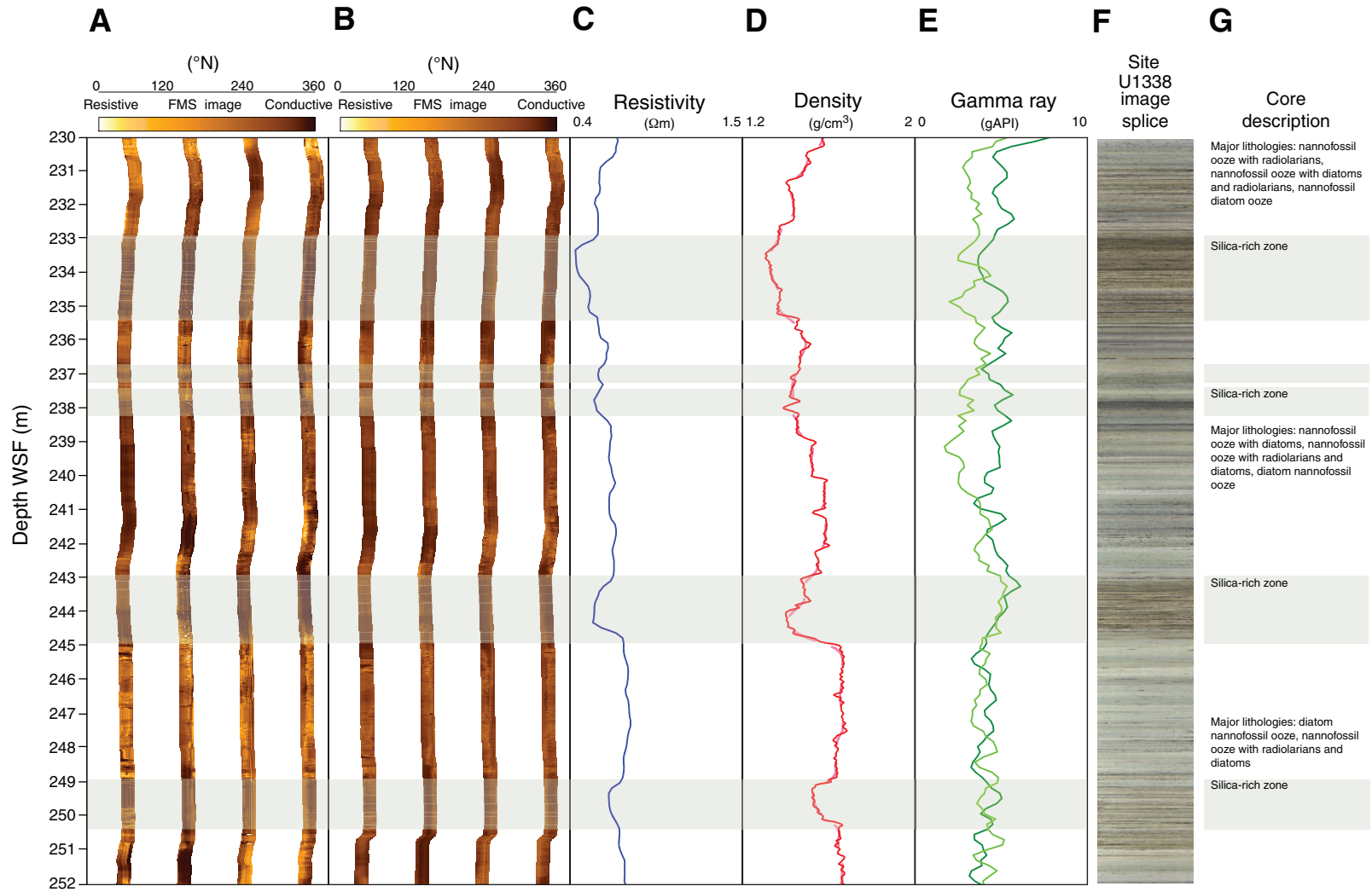




Figure F50. Downhole log curves in Hole U1338B from 270 to 288 m WSF showing Formation MicroScanner (FMS) four-pad downhole resistivity images from (A) Pass 1 and (B) Pass 2 with (C) DIT-measured SFLU resistivity, (D) HLDS-measured bulk density (red = high resolution, pink = standard resolution), (E) HNGS-measured total gamma radiation (dark green = triple combination, light green = FMS-sonic, and (F) Site U1338 spliced core images (CCSF-B depth scale).

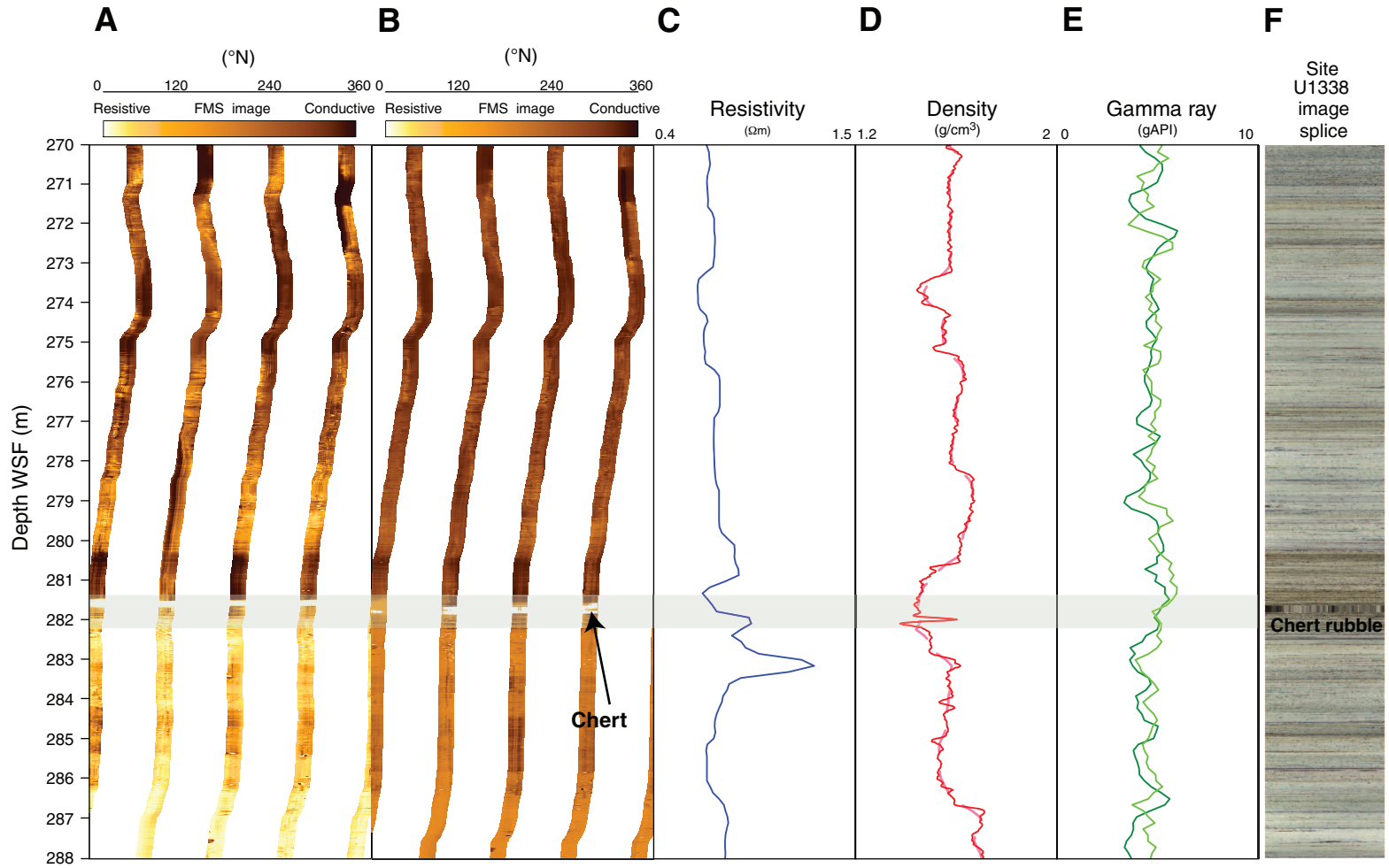


Figure F51. A. Vertical seismic profile (VSP) waveforms and direct arrival times (red circles), Hole U1338B. B. Interpolation of the VSP direct arrival times defines a relationship between two-way traveltime (TWT) in seismic records and depth at Site U1338.

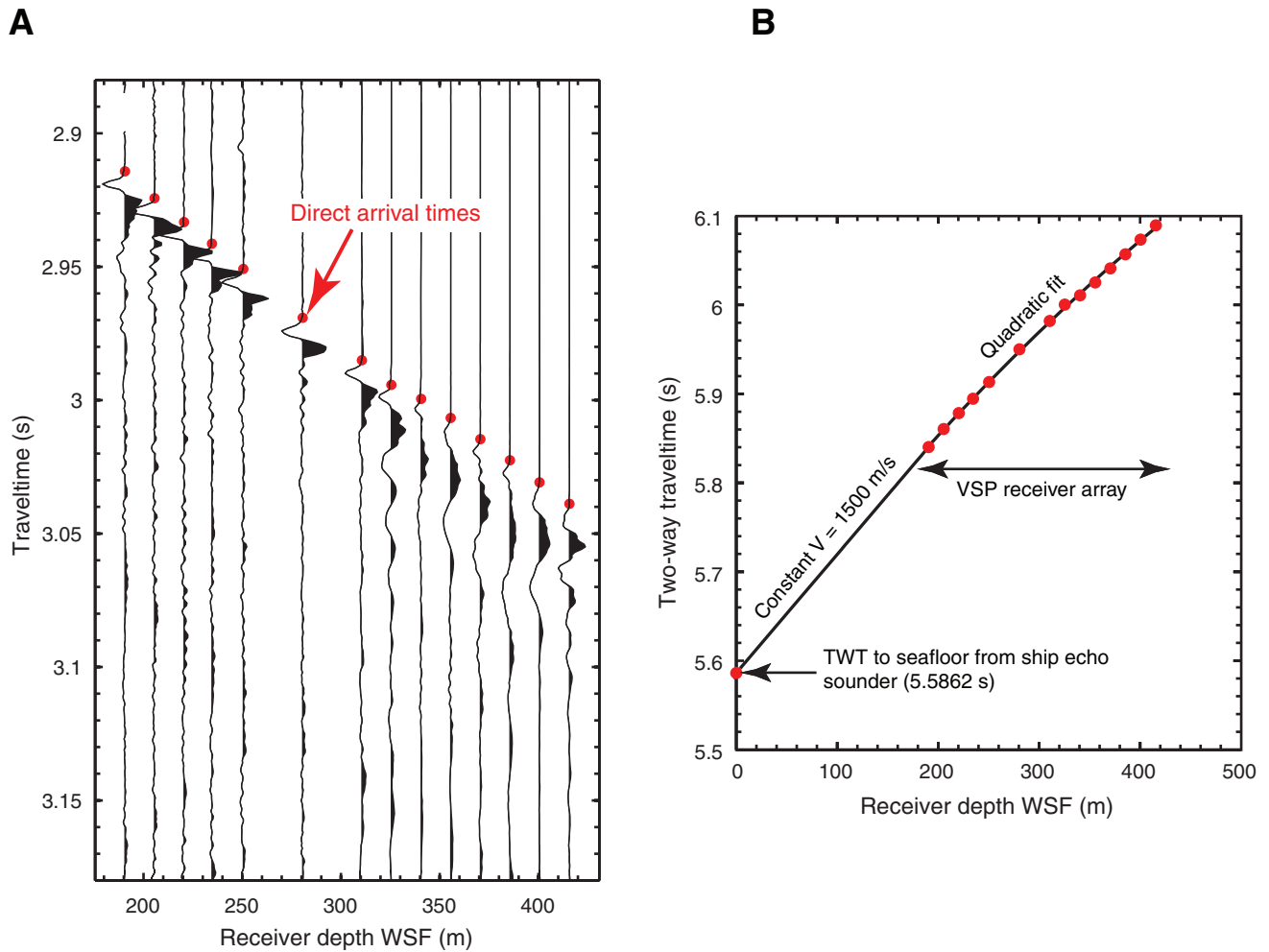


Figure F52. Correlation between seismic reflection record at Site U1338 (AMAT-03 site survey) and depth, Hole U1338B. TC = triple combination, IMPH = medium induction phasor-processed resistivity, SFLU = spherically focused resistivity, VSP = vertical seismic profile.

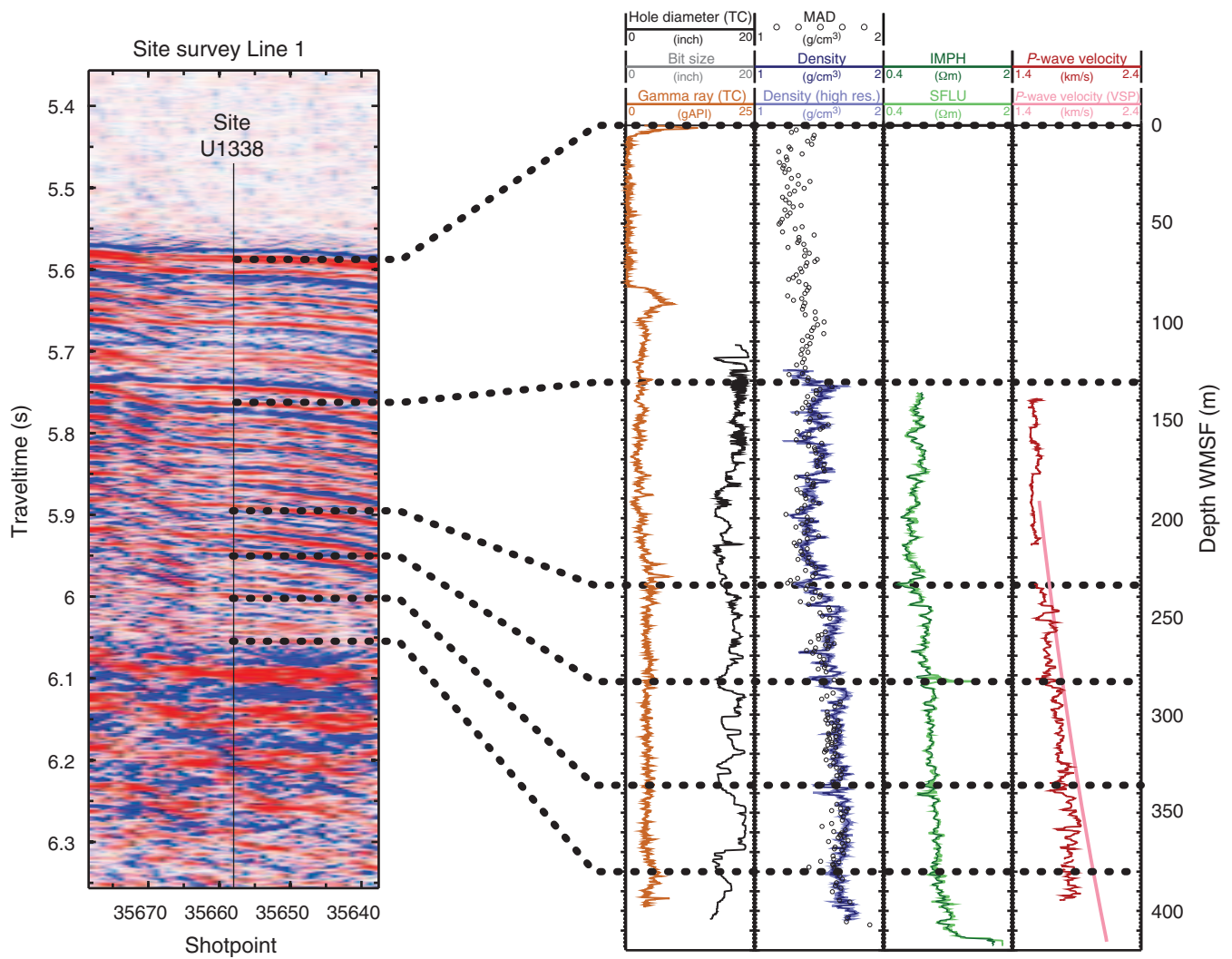


Figure F53. Geothermal gradient, in situ thermal conductivities, and temperature vs. thermal resistance, Site U1338. Heat flow determined from the slope of a line fitted to the relationship between temperature and thermal resistance.

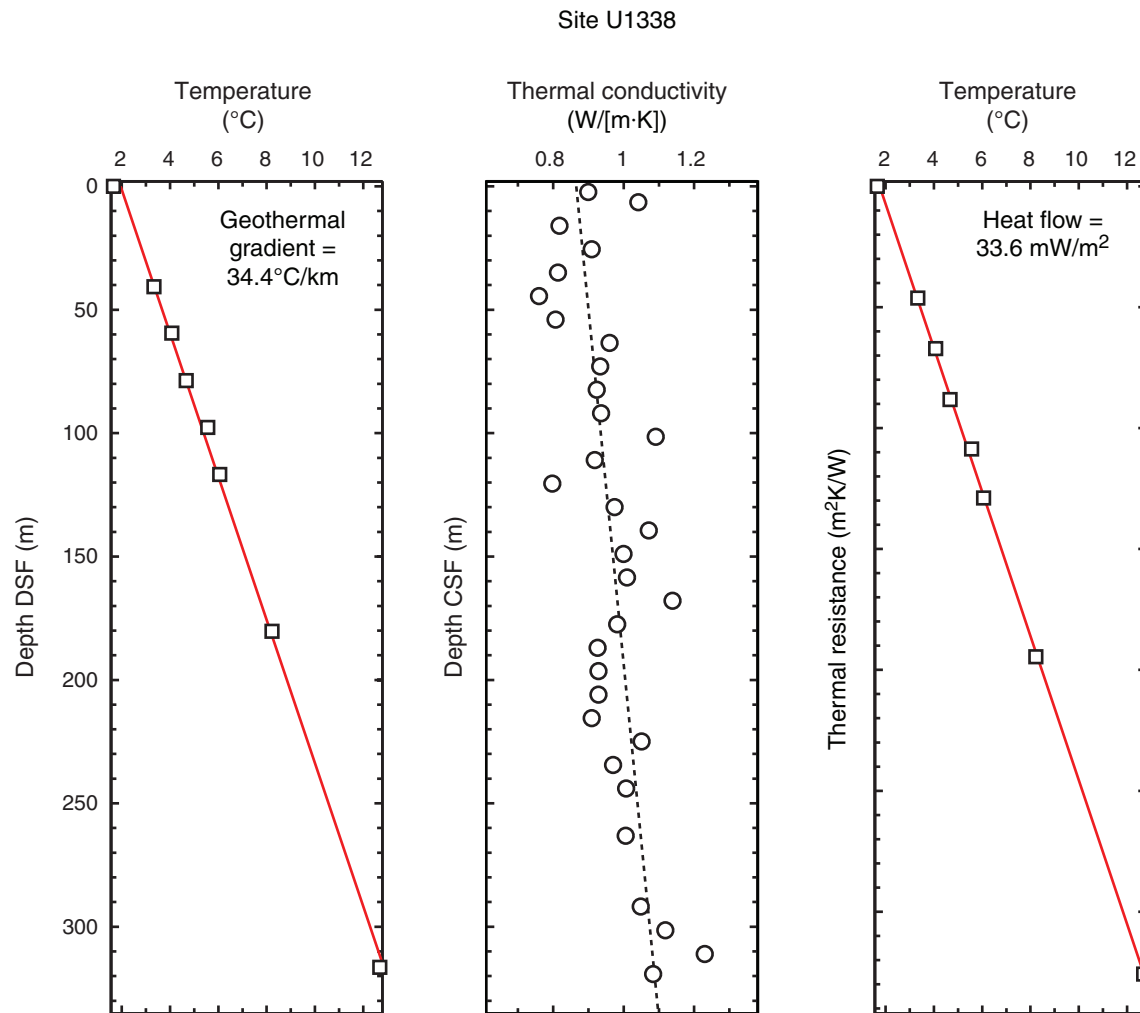


Table T1. Coring summary, Site U1338. (See table notes.) (Continued on next three pages.)

Site U1338

Time on site (h): 275.25 (2315 h, 3 June–1030 h, 15 June 2009)

Hole U1338A

Latitude: 2°30.469'N

Longitude: 117°58.162'W

Time on hole (h): 67.75 (2315 h, 3 June–1900 h, 6 June 2009)

Seafloor (drill pipe measurement below rig floor, m DRF): 4210.8

Distance between rig floor and sea level (m): 11.2

Water depth (drill pipe measurement from sea level, mbsl): 4199.6

Total depth (drill pipe measurement from rig floor, m DRF): 4620.8

Total penetration (drilling depth below seafloor, m DSF): 410.0

Total length of cored section (m): 410.0

Total core recovered (m): 345.96

Core recovery (%): 84

Total number of cores: 44

Hole U1338B

Latitude: 2°30.469'N

Longitude: 117°58.174'W

Time on hole (h): 118.0 (1900 h, 6 June–1700 h, 11 June 2009)

Seafloor (drill pipe measurement below rig floor, m DRF): 4209.9

Distance between rig floor and sea level (m): 11.3

Water depth (drill pipe measurement from sea level, mbsl): 4198.6

Total depth (drill pipe measurement from rig floor, m DRF): 4626.0

Total penetration (drilling depth below seafloor, m DSF): 416.1

Total length of cored section (m): 413.6

Total core recovered (m): 417.18

Core recovery (%): 101

Total number of cores: 45

Hole U1338C

Latitude: 2°30.469'N

Longitude: 117°58.184'W

Time on hole (h): 75.25 (1700 h, 11 June–2015 h, 14 June 2009)

Seafloor (drill pipe measurement below rig floor, m DRF): 4212.7

Distance between rig floor and sea level (m): 11.3

Water depth (drill pipe measurement from sea level, mbsl): 4201.4

Total depth (drill pipe measurement from rig floor, m DRF): 4627.1

Total penetration (drilling depth below seafloor, m DSF): 414.4

Total length of cored section (m): 414.4

Total core recovered (m): 423.48

Core recovery (%): 104

Total number of cores: 47

Hole U1338D

Latitude: 2°30.469'N

Longitude: 117°58.195'W

Time on hole (h): 14.25 (2015 h, 14 June–1030 h, 15 June 2009)

Seafloor (drill pipe measurement below rig floor, m DRF): 4212.6

Distance between rig floor and sea level (m): 11.3

Water depth (drill pipe measurement from sea level, mbsl): 4201.3

Total depth (drill pipe measurement from rig floor, m DRF): 4236.5

Total penetration (drilling depth below seafloor, m DSF): 23.9

Total length of cored section (m): 23.9

Total core recovered (m): 24.79

Core recovery (%): 104

Total number of cores: 3

Core	Date (2009)	Local time (h)	Depth DSF (m)			Depth CSF (m)		Length of core recovered (m)	Recovery (%)
			Top of cored interval	Bottom of cored interval	Interval advanced (m)	Top of cored interval	Bottom of cored interval		
321-U1338A-									
1H	4 Jun	1220	0.00	2.70	2.7	0.00	2.73	2.73	101
2H	4 Jun	1320	2.70	12.20	9.5	2.70	12.65	9.95	105
3H	4 Jun	1420	12.20	21.70	9.5	12.20	22.17	9.97	105
4H	4 Jun	1515	21.70	31.20	9.5	21.70	31.70	10.00	105
5H	4 Jun	1630	31.20	40.70	9.5	31.20	41.30	10.10	106
6H	5 Jun	1730	40.70	50.20	9.5	40.70	50.75	10.05	106
7H	5 Jun	1850	50.20	59.70	9.5	50.20	60.19	9.99	105
8H	5 Jun	1950	59.70	69.20	9.5	59.70	69.70	10.00	105

Table T1 (continued). (Continued on next page.)

Core	Date (2009)	Local time (h)	Depth DSF (m)		Interval advanced (m)	Depth CSF (m)		Length of core recovered (m)	Recovery (%)
			Top of cored interval	Bottom of cored interval		Top of cored interval	Bottom of cored interval		
9H	5 Jun	2100	69.20	78.70	9.5	69.20	79.36	10.16	107
10H	5 Jun	2205	78.70	88.20	9.5	78.70	88.78	10.08	106
11H	5 Jun	2315	88.20	97.70	9.5	88.20	97.10	8.90	94
12H	5 Jun	0020	97.70	107.20	9.5	97.70	107.69	9.99	105
13H	5 Jun	0145	107.20	116.70	9.5	107.20	117.14	9.94	105
14H	5 Jun	0240	116.70	126.20	9.5	116.70	126.85	10.15	107
15H	5 Jun	0335	126.20	135.70	9.5	126.20	135.73	9.53	100
16H	5 Jun	0435	135.70	145.20	9.5	135.70	145.74	10.04	106
17H	5 Jun	0530	145.20	154.70	9.5	145.20	155.31	10.11	106
18H	5 Jun	0635	154.70	164.20	9.5	154.70	164.65	9.95	105
19H	5 Jun	0735	164.20	173.70	9.5	164.20	173.84	9.64	101
20H	5 Jun	0830	173.70	183.20	9.5	173.70	183.76	10.06	106
21H	5 Jun	0930	183.20	192.70	9.5	183.20	193.00	9.80	103
22H	5 Jun	1030	192.70	202.20	9.5	192.70	202.63	9.93	105
23H	5 Jun	1155	202.20	211.70	9.5	202.20	212.21	10.01	105
24H	5 Jun	1335	211.70	221.20	9.5	211.70	221.69	9.99	105
25H	5 Jun	1530	221.20	230.70	9.5	221.20	231.17	9.97	105
26H	6 Jun	1800	230.70	240.20	9.5	230.70	240.69	9.99	105
27X	6 Jun	1915	240.20	249.80	9.6	240.20	247.65	7.45	78
28X	6 Jun	2025	249.80	259.40	9.6	249.80	249.82	0.02	0
29X	6 Jun	2135	259.40	269.00	9.6	259.40	268.38	8.98	94
30X	6 Jun	2230	269.00	278.50	9.5	269.00	269.01	0.01	0
31X	6 Jun	2345	278.50	288.10	9.6	278.50	278.55	0.05	1
32X	6 Jun	0130	288.10	297.70	9.6	288.10	296.62	8.52	89
33X	6 Jun	0245	297.70	307.30	9.6	297.70	306.50	8.80	92
34X	6 Jun	0350	307.30	316.90	9.6	307.30	316.15	8.85	92
35X	6 Jun	0510	316.90	326.50	9.6	316.90	319.84	2.94	31
36X	6 Jun	0610	326.50	336.00	9.5	326.50	327.73	1.23	13
37X	6 Jun	0720	336.00	345.50	9.5	336.00	337.23	1.23	13
38X	6 Jun	0825	345.50	354.80	9.3	345.50	354.75	9.25	99
39X	6 Jun	0930	354.80	364.40	9.6	354.80	363.81	9.01	94
40X	6 Jun	1035	364.40	374.00	9.6	364.40	367.79	3.39	35
41X	6 Jun	1145	374.00	383.60	9.6	374.00	382.77	8.77	91
42X	6 Jun	1305	383.60	393.20	9.6	383.60	391.12	7.52	78
43X	6 Jun	1450	393.20	402.80	9.6	393.20	396.46	3.26	34
44X	6 Jun	1640	402.80	410.00	7.2	402.80	408.45	5.65	78
Advanced total:					410.0			345.96	84
Total interval cored:					410.0				
321-U1338B-									
1H	7 Jun	2355	0.00	7.60	7.6	0.00	7.60	7.60	100
2H	7 Jun	0120	7.60	17.10	9.5	7.60	17.54	9.94	105
3H	7 Jun	0220	17.10	26.60	9.5	17.10	27.03	9.93	105
4H	7 Jun	0310	26.60	36.10	9.5	26.60	36.60	10.00	105
5H	7 Jun	0410	36.10	45.60	9.5	36.10	46.20	10.10	106
6H	7 Jun	0505	45.60	55.10	9.5	45.60	55.68	10.08	106
7H	7 Jun	0610	55.10	64.60	9.5	55.10	65.06	9.96	105
8H	7 Jun	0710	64.60	74.10	9.5	64.60	74.70	10.10	106
9H	7 Jun	0805	74.10	83.60	9.5	74.10	83.42	9.32	98
10H	7 Jun	0905	83.60	93.10	9.5	83.60	93.38	9.78	103
11H	7 Jun	1000	93.10	102.60	9.5	93.10	102.93	9.83	103
12H	7 Jun	1055	102.60	112.10	9.5	102.60	112.69	10.09	106
13H	7 Jun	1155	112.10	121.60	9.5	112.10	121.00	8.90	94
14H	7 Jun	1300	121.60	131.10	9.5	121.60	131.64	10.04	106
15H	7 Jun	1425	131.10	140.60	9.5	131.10	141.02	9.92	104
16H	7 Jun	1525	140.60	150.10	9.5	140.60	150.52	9.92	104
17H	7 Jun	1630	150.10	159.60	9.5	150.10	160.18	10.08	106
18H	8 Jun	1735	159.60	169.10	9.5	159.60	169.53	9.93	105
19H	8 Jun	1840	169.10	178.60	9.5	169.10	179.17	10.07	106
20H	8 Jun	1940	178.60	188.10	9.5	178.60	188.59	9.99	105
21H	8 Jun	2045	188.10	197.60	9.5	188.10	198.08	9.98	105
22H	8 Jun	2235	197.60	207.10	9.5	197.60	207.64	10.04	106
23H	8 Jun	0030	207.10	216.60	9.5	207.10	217.10	10.00	105
24H	8 Jun	0135	216.60	226.10	9.5	216.60	226.62	10.02	105
25H	8 Jun	0230	226.10	235.60	9.5	226.10	236.13	10.03	106
*****Drilled from 235.60 to 238.10 m DSF*****									
26H	8 Jun	0340	238.10	247.60	9.5	238.10	248.14	10.04	106
27H	8 Jun	0435	247.60	257.10	9.5	247.60	256.08	8.48	89

Table T1 (continued). (Continued on next page.)

Core	Date (2009)	Local time (h)	Depth DSF (m)		Interval advanced (m)	Depth CSF (m)		Length of core recovered (m)	Recovery (%)
			Top of cored interval	Bottom of cored interval		Top of cored interval	Bottom of cored interval		
28H	8 Jun	0600	257.10	266.60	9.5	257.10	267.24	10.14	107
29H	8 Jun	0735	266.60	276.10	9.5	266.60	276.65	10.05	106
30H	8 Jun	0835	276.10	282.10	6.0	276.10	282.25	6.15	102
31H	8 Jun	1010	282.10	282.90	0.8	282.10	282.91	0.81	101
32H	8 Jun	1135	282.90	292.40	9.5	282.90	292.95	10.05	106
33H	8 Jun	1335	292.40	301.90	9.5	292.40	302.17	9.77	103
34H	8 Jun	1540	301.90	311.40	9.5	301.90	311.57	9.67	102
35H	9 Jun	1820	311.40	320.90	9.5	311.40	321.37	9.97	105
36H	9 Jun	2110	320.90	330.40	9.5	320.90	330.91	10.01	105
37H	9 Jun	2305	330.40	339.90	9.5	330.40	340.38	9.98	105
38H	9 Jun	0050	339.90	349.40	9.5	339.90	349.86	9.96	105
39H	9 Jun	0255	349.40	358.90	9.5	349.40	359.36	9.96	105
40H	9 Jun	0450	358.90	368.40	9.5	358.90	368.91	10.01	105
41H	9 Jun	0620	368.40	377.90	9.5	368.40	378.21	9.81	103
42H	9 Jun	0830	377.90	387.40	9.5	377.90	387.95	10.05	106
43X	9 Jun	1005	387.40	397.00	9.6	387.40	392.55	5.15	54
44X	9 Jun	1155	397.00	406.60	9.6	397.00	400.08	3.08	32
45X	9 Jun	1345	406.60	416.10	9.5	406.60	414.99	8.39	88
Advanced total:					416.1			417.18	101
Total interval cored:					413.6				
321-U1338C-									
1H	12 Jun	2205	0.00	3.80	3.8	0.00	3.84	3.84	101
2H	12 Jun	2320	3.80	13.30	9.5	3.80	13.75	9.95	105
3H	12 Jun	0020	13.30	22.80	9.5	13.30	23.31	10.01	105
4H	12 Jun	0130	22.80	32.30	9.5	22.80	31.79	8.99	95
5H	12 Jun	0230	32.30	41.80	9.5	32.30	42.33	10.03	106
6H	12 Jun	0325	41.80	51.30	9.5	41.80	51.82	10.02	105
7H	12 Jun	0425	51.30	60.80	9.5	51.30	61.34	10.04	106
8H	12 Jun	0530	60.80	70.30	9.5	60.80	69.98	9.18	97
9H	12 Jun	0635	70.30	79.80	9.5	70.30	80.23	9.93	105
10H	12 Jun	0735	79.80	89.30	9.5	79.80	89.73	9.93	105
11H	12 Jun	0830	89.30	98.80	9.5	89.30	99.34	10.04	106
12H	12 Jun	0930	98.80	108.30	9.5	98.80	108.60	9.80	103
13H	12 Jun	1030	108.30	117.80	9.5	108.30	118.20	9.90	104
14H	12 Jun	1125	117.80	127.30	9.5	117.80	127.85	10.05	106
15H	12 Jun	1225	127.30	136.80	9.5	127.30	137.24	9.94	105
16H	12 Jun	1325	136.80	146.30	9.5	136.80	146.75	9.95	105
17H	12 Jun	1425	146.30	155.80	9.5	146.30	156.38	10.08	106
18H	12 Jun	1525	155.80	161.30	5.5	155.80	163.18	7.38	134
19H	12 Jun	1630	161.30	170.80	9.5	161.30	171.39	10.09	106
20H	13 Jun	1800	170.80	180.30	9.5	170.80	180.84	10.04	106
21H	13 Jun	1900	180.30	189.80	9.5	180.30	190.37	10.07	106
22H	13 Jun	2025	189.80	199.30	9.5	189.80	199.70	9.90	104
23H	13 Jun	2145	199.30	208.80	9.5	199.30	209.38	10.08	106
24H	13 Jun	2305	208.80	218.30	9.5	208.80	218.72	9.92	104
25H	13 Jun	0020	218.30	227.80	9.5	218.30	228.34	10.04	106
26H	13 Jun	0220	227.80	237.30	9.5	227.80	237.78	9.98	105
27H	13 Jun	0315	237.30	246.80	9.5	237.30	246.45	9.15	96
28H	13 Jun	0425	246.80	256.30	9.5	246.80	256.63	9.83	103
29H	13 Jun	0525	256.30	265.80	9.5	256.30	266.22	9.92	104
30H	13 Jun	0645	265.80	275.30	9.5	265.80	275.71	9.91	104
31H	13 Jun	0815	275.30	282.90	7.6	275.30	282.89	7.59	100
32H	13 Jun	0940	282.90	292.40	9.5	282.90	287.90	5.00	53
33H	13 Jun	1055	292.40	301.90	9.5	292.40	302.37	9.97	105
34H	13 Jun	1305	301.90	306.90	5.0	301.90	311.00	9.10	182
35H	13 Jun	1500	306.90	316.40	9.5	306.90	317.11	10.21	107
36H	13 Jun	1630	316.40	325.90	9.5	316.40	326.40	10.00	105
37H	14 Jun	1810	325.90	335.40	9.5	325.90	335.82	9.92	104
38H	14 Jun	2020	335.40	344.90	9.5	335.40	345.38	9.98	105
39H	14 Jun	2340	344.90	354.40	9.5	344.90	354.97	10.07	106
40H	14 Jun	0125	354.40	363.90	9.5	354.40	363.98	9.58	101
41H	14 Jun	0205	363.90	373.40	9.5	363.90	373.93	10.03	106
42H	14 Jun	0540	373.40	377.90	4.5	373.40	380.09	6.69	149
43H	14 Jun	0730	377.90	387.40	9.5	377.90	388.03	10.13	107
44H	14 Jun	1056	387.40	396.90	9.5	387.40	395.73	8.33	88
45H	14 Jun	1445	396.90	404.00	7.1	396.90	404.12	7.22	102
46H	14 Jun	1625	404.00	410.50	6.5	404.00	410.56	6.56	101

Table T1 (continued).

Core	Date (2009)	Local time (h)	Depth DSF (m)			Depth CSF (m)		Length of core recovered (m)	Recovery (%)
			Top of cored interval	Bottom of cored interval	Interval advanced (m)	Top of cored interval	Bottom of cored interval		
47H	15 Jun	1815	410.50	414.40	3.9	410.50	414.41	3.91	100
			Advanced total:		414.4			432.28	104
			Total interval cored:		414.4				
321-U1338D-									
1H	15 Jun	2215	0.00	4.90	4.9	0.00	4.89	4.89	100
2H	15 Jun	2325	4.90	14.40	9.5	4.90	14.79	9.89	104
3H	15 Jun	0010	14.40	23.90	9.5	14.40	24.41	10.01	105
			Advanced total:		23.9			24.79	104
			Total interval cored:		23.9				

Notes: DRF = drilling depth below rig floor, DSF = drilling depth below seafloor, CSF = core depth below seafloor. H = APC core, X = XCB core.
Local time = UTC - 7 h.



Table T2. Coring disturbance summary, Site U1338. (Continued on next two pages.)

Core, section	Depth in section (cm)	Core, section	Depth in core (cm)	Depth CSF (m)		Character	State	Comments
				Top	Bottom			
321-U1338A-		321-U1338A-						
3H-1	0-15	3H-1		12.20	12.35	Drilling disturbance	Soupy	
3H-1	130-139	3H-1		13.50	13.59	Drilling disturbance	Soupy	
3H-2	54-62	3H-2		14.24	14.32	Drilling disturbance	Soupy	
4H-2	35-42	4H-2		23.55	23.62	Drilling disturbance	Very disturbed	Filled with drill mud
4H-2	126-128	4H-2		24.46	24.48	Drilling disturbance	Very disturbed	Filled with drill mud
7H-1	0-97	7H-1		50.20	51.17	Fall in	Soupy	
10H-1	0-23	10H-1		78.70	78.93	Drilling disturbance	Soupy	
11H-1	0-24	11H-1		88.20	88.44	Drilling disturbance	Soupy	
12H-1	0-23	12H-1		97.70	97.93	Drilling disturbance	Soupy	
12H-4	0-7	12H-4		102.20	102.27	Puncture		
13H-1	0-25	13H-1		107.20	107.45	Flow-in		
13H-4	0-5	13H-4		111.71	111.76	Puncture		
14H-1	0-23	14H-1		116.70	116.93	Drilling disturbance	Very disturbed	
14H-1	92-19	14H-2		117.62	118.39	Flow-in		
14H-5	115-135	14H-5		123.85	124.05	Flow-in		
14H-6	32-29	14H-7		124.52	125.99	Flow-in		
14H-4	0-8	14H-4		121.27	121.35	Puncture		
15H-1	0-12	15H-1		126.20	126.32	Fall in		
17H-1	0-23	17H-1		145.20	145.35	Drilling disturbance	Soupy	
17H-1	41-85	17H-1		145.61	146.05	Drilling disturbance	Soupy	
18H-1	0-20	18H-1		154.70	154.90	Fall in		
19H-1	0-21	19H-1		164.20	164.41	Flow-in	Soupy	
20H-1	0-58	20H-1		173.70	174.28	Drilling disturbance	Soupy	
23H-1	0-35	23H-1		202.20	202.55	Drilling disturbance	Soupy	
25H-1	0-4	25H-1		221.20	222.24	Fall in	Disturbed	
26H-1	0-6	26H-1		230.70	230.76	Fall in	Very disturbed	
27X-1	0-4	27X-1		240.20	240.24	Drilling disturbance	Soupy	
27X-1	142-150	27X-1		241.62	241.70	Void	Void	
32X-1	0-15	32X-1		288.10	288.25	Fall in		
33X-1	0-14	33X-1		297.70	297.84	Drilling disturbance	Disturbed	
34X	0		885	307.30	316.15	Drilling disturbance	Biscuit	Fractured biscuits
35X	0		294	316.90	319.84	Drilling disturbance	Biscuit	Fractured biscuit
36X	0		123	326.50	327.73	Drilling disturbance		Slight disturbance
37X	0		123	336.00	337.23	Drilling disturbance	Brecciated	
38X	0		925	345.50	354.75	Drilling disturbance	Biscuit	Fractured biscuits
39X	0		901	354.80	363.81	Drilling disturbance	Biscuit	Fractured drilling biscuits
40X	0		339	364.40	367.79	Drilling disturbance	Biscuit	Highly fractured drilling biscuits
41X	0		877	374.00	382.77	Drilling disturbance	Biscuit	Fractured drilling biscuit
42X	0		752	383.60	391.12	Drilling disturbance	Biscuit	
43X-1	0-42	43X-CC		393.20	396.46	Drilling disturbance	Biscuit	Fractured drilling biscuits
44X	0		565	402.80	408.45	Drilling disturbance	Biscuit	Highly fractured biscuits
321-U1338B-		321-U1338B-						
1H-1	140-150	1H-1		1.40	1.50	Void	Void	
2H-1	0-26	2H-1		7.60	7.86	Drilling disturbance	Very disturbed	
3H-1	0-6	3H-1		17.10	17.16	Fall in		
4H-1	0-36	4H-1		26.60	26.96	Drilling disturbance	Disturbed	
4H-1	104-109	4H-1		27.64	27.69	Drilling disturbance	Slurry	
5H-2	110-118	5H-2		38.70	38.78	Drilling disturbance	Disturbed	



Table T2 (continued). (Continued on next page.)

Core, section	Depth in section (cm)	Core, section	Depth in core (cm)	Depth CSF (m)		Character	State	Comments
				Top	Bottom			
7H-1	0-25	7H-1		55.10	55.35	Drilling disturbance	Very disturbed	
9H-1	0-12	9H-1		74.10	74.22	Fall in		
11H-1	0-14	11H-1		93.10	93.24	Drilling disturbance	Slightly disturbed	
12H-1	0-12	12H-1		102.60	102.72	Drilling disturbance	Slightly disturbed	
13H-1	0-40	13H-1		112.10	112.50	Drilling disturbance	Slightly disturbed	
13H-3	59-65	13H-3		115.69	115.75	Void	Void	
14H-1	0-17	14H-1		121.60	121.77	Drilling disturbance	Slightly disturbed	
15H-1	0-4	15H-1		131.10	131.14		Slightly disturbed	
27H-1	0-5	27H-1		247.60	247.65	Drilling disturbance	Soupy	
27H-3	67-23	27H-CC		251.27	256.08	Flow-in		
29H-1	0-5	29H-1		266.60	266.65		Soupy	
30H-1	0-6	30H-1		276.10	276.16	Fall in		
30H-3	34-24	30H-CC		279.44	282.25	Flow-in		
31H	0		80	282.10	282.90	Fall in		
34H-1	0-7	34H-1		301.90	301.97	Drilling disturbance	Disturbed	
41H-1	0-3	41H-1		368.40	368.43	Fall in		
43X-1	0-71	43X-1		387.40	388.11	Drilling disturbance	Slurry	
43X-1	71-28	43X-CC		388.11	392.55	Drilling disturbance	Biscuit	Fractured drilling biscuits
44X	0		310	397.00	400.10	Drilling disturbance	Biscuit	Fractured biscuits
45X	0		839	406.60	414.99	Drilling disturbance	Biscuit	Fractured biscuits
321-U1338C-		321-U1338C-						
2H-1	0-50	2H-2		3.80	5.80	Flow-in	Very disturbed	
2H-2	29-46	2H-2		5.60	5.76	Void	Void	
3H-1	0-72	3H-1		13.30	14.02	Fall in	Very disturbed	
3H-2	133-138	3H-2		16.13	16.18	Void	Soupy	Filled with drill mud
3H-5	59-63	3H-5		19.89	19.93	Puncture		Small hole filled with drill mud; ~4 cm long × 2 wide, rest is intact around it
4H-1	0-38	4H-1		22.80	23.18	Fall in	Very disturbed	
6H-1	0-55	6H-1		41.80	42.35	Flow-in		
7H-1	0-23	7H-2		51.30	53.03	Flow-in	Very disturbed	
8H-1	0-101	8H-2		60.80	63.31	Flow-in	Very disturbed	Flow-in, some intervals less distorted but unsure of stratigraphic position
9H-1	0-55	9H-1		70.30	70.85	Drilling disturbance	Soupy	
9H-1	64-64	9H-1		70.94	70.94	Gas expansion	Void	
9H-2	52-54	9H-2		72.32	72.34	Gas expansion	Void	
9H-2	61-66	9H-2		72.41	72.46	Gas expansion	Void	
9H-2	85-87	9H-2		72.65	72.67	Gas expansion	Void	
9H-2	130-132	9H-2		73.10	73.12	Gas expansion	Void	
9H-3	61-64	9H-3		73.91	73.94	Gas expansion	Void	
9H-3	130-132	9H-3		74.60	74.62	Gas expansion	Void	
9H-4	37-39	9H-4		75.17	75.19	Gas expansion	Void	
10H-1	22-55	10H-1		80.02	80.35	Drilling disturbance	Disturbed	Appears to be flow-in
10H-7	0-81	10H-7		88.60	89.41	Drilling disturbance	Disturbed	Deformed liner
11H-1	0-36	11H-1		89.30	89.66	Flow-in	Very disturbed	
13H-1	0-15	13H-4		108.30	112.95	Flow-in	Very disturbed	
14H-1	0-38	14H-1		117.80	118.18	Drilling disturbance	Disturbed	
16H-1	0-40	16H-1		136.80	137.20	Drilling disturbance	Very disturbed	
17H-1	0-67	17H-1		146.30	146.97	Drilling disturbance	Soupy	
18H-1	0-107	18H-2		155.80	158.37	Flow-in	Very disturbed	
19H-1	0-79	19H-1		161.30	162.09	Flow-in	Very disturbed	
20H-1	41-56	20H-1		171.21	171.36	Drilling disturbance	Soupy	
21H-1	14-47	21H-1		180.44	180.91	Drilling disturbance	Soupy	



Table T2 (continued).

Core, section	Depth in section (cm)	Core, section	Depth in core (cm)	Depth CSF (m)		Character	State	Comments
				Top	Bottom			
23H-1	25–57	23H-1		199.55	199.87	Drilling disturbance	Soupy	
23H-1	0–5	23H-1		199.30	199.35	Fall in	Very disturbed	
26H-1	0–4	26H-1		227.80	227.84	Fall in	Very disturbed	
27H-1	0–23	27H-1		237.30	237.53	Fall in	Very disturbed	
30H-1	0–20	30H-1		265.80	266.00	Drilling disturbance	Disturbed	
31H-1	0–6	31H-1		275.30	275.36	Fall in	Very disturbed	
32H-1	0–39	32H-1		282.90	283.29	Drilling disturbance	Disturbed	
34H-1	0–82	34H-2		301.90	304.22	Drilling disturbance	Slurry	
38H-1	0–8	38H-1		335.40	335.48	Drilling disturbance	Slightly disturbed	
41H-1	0–11	41H-1		363.90	364.01	Fall in	Very disturbed	
42H-1	0–150	42H-1		373.40	374.90	Fall in	Very disturbed	Many small pieces of chert in fall-in
42H-5	56–69	42H-5		379.71	379.84	Drilling disturbance	Liner deformation	Minor liner deformation, stratigraphy intact
45H-1	0–4	45H-1		396.90	396.94	Fall in	Very disturbed	Many pieces of chert in fall-in

Table T3. Lithologic unit boundaries, Site U1338.

Unit	Core, section, interval (cm)	Depth (m)		
		CSF	CCSF-A	CCSF-B
321-U1338A-				
I/II	6H-7, 65	50.35	55.91	50.37
II/III	27X-3, 74	243.94	271.72	244.79
III/IV	44X-CC, 40	408.37	453.43	408.50
321-U1338B-				
I/II	6H-4, 51	50.61	55.76	50.23
II/III	26H-5, 44	244.54	271.47	244.57
III/IV	45X-CC, 48	414.94	459.78	414.22
321-U1338C-				
I/II	6H-5, 55	48.35	55.96	50.42
II/III	27H-6, 12	244.92	271.73	244.80

Table T4. Calcareous nannofossil datums, Site U1338. (See table notes.) (Continued on next page.)

Core, section, interval (cm)		Marker species (base zone)	Age (Ma)	Depth CSF (m)				Depth (m)	
Top	Bottom			Top	Bottom	Midpoint	±	CCSF-A	CCSF-B
321-U1338A-									
2H-1, 130	2H-2, 24	T <i>Pseudoemiliana lacunosa</i> (NN20)	0.44	4.00	4.44	4.22	0.22	7.53	6.80
2H-4, 90	2H-5, 120	Tc <i>Reticulofenestra asanoi</i>	0.91	8.10	9.90	9.00	0.90	12.13	10.96
3H-1, 90	3H-2, 70	T <i>Gephyrocapsa</i> (>5.5 µm)	1.26	13.10	14.40	13.75	0.65	17.38	15.70
3H-4, 80	3H-5, 80	T <i>Calcidiscus macintyreii</i>	1.61	17.50	19.00	18.25	0.75	19.88	17.95
		Pliocene/Pleistocene boundary	1.81						
4H-2, 50	4H-3, 50	T <i>Discoaster brouweri</i> (NN19)	1.93	23.70	25.20	24.45	0.75	26.50	23.93
4H-CC	5H-1, 60	T <i>Discoaster pentaradiatus</i> (NN18)	2.39	31.65	31.80	31.73	0.07	38.51	34.79
5H-1, 60	5H-2, 85	T <i>Discoaster surculus</i> (NN17)	2.49	31.80	33.55	32.68	0.88	41.28	37.29
6H-2, 40	6H-3, 120	T <i>Sphenolithus</i> spp.	3.54	42.60	44.72	43.66	1.06	48.91	44.18
6H-4, 30	6H-5, 40	T <i>Reticulofenestra pseudoumbilicus</i> (NN16)	3.70	45.50	47.10	46.30	0.80	52.61	47.52
8H-5, 110	8H-6, 83	T <i>Ceratolithus acutus</i>	5.04	66.80	68.03	67.42	0.62	77.13	69.67
		Miocene/Pliocene boundary	5.33						
9H-4, 70	9H-5, 70	B <i>Ceratolithus acutus</i>	5.35	74.40	75.90	75.15	0.75	86.65	78.27
10H-3, 70	10H-4, 70	T <i>Discoaster quinqueramus</i> (NN12)	5.58	82.40	83.90	83.15	0.75	94.14	85.04
11H-5, 120	11H-6, 120	T <i>Nicklithus amplifucus</i>	5.98	95.40	96.77	96.09	0.68	107.94	97.51
14H-2, 80	14H-3, 80	B <i>Nicklithus amplifucus</i>	6.91	119.00	120.50	119.75	0.75	132.08	119.31
16H-3, 50	16H-4, 50	TP <i>Reticulofenestra pseudoumbilicus</i>	7.07	139.20	140.70	139.95	0.75	157.25	142.05
17H-1, 95	17H-2, 50	B <i>Amaurolithus</i> spp.	7.36	146.15	147.20	146.68	0.52	159.18	143.79
18H-2, 90	18H-3, 65	B <i>Discoaster berggrenii</i> (NN11)	8.29	157.10	158.35	157.73	0.63	181.83	164.25
20H-3, 80	20H-4, 80	BP <i>Reticulofenestra pseudoumbilicus</i>	9.10	177.50	179.00	178.25	0.75	202.34	182.78
22H-4, 80	22H-5, 80	T <i>Discoaster hamatus</i> (NN10)	9.69	198.00	199.50	198.75	0.75	220.52	199.20
24H-CC	25H-1, 80	B <i>Discoaster hamatus</i> (NN9)	10.55	221.69	222.00	221.85	0.16	253.24	228.76
25H-1, 80	25H-2, 80	T <i>Coccolithus miopelagicus</i>	10.60	222.00	223.51	222.76	0.75	253.24	228.76
25H-3, 80	25H-4, 80	B <i>Catinaster coalitus</i> (NN8)	10.89	225.02	226.53	225.78	0.75	281.38	254.18
29X-5, 80	29X-6, 80	Bc <i>Discoaster kugleri</i> (NN7)	11.86	266.20	267.70	266.95	0.75	298.96	270.06
34X-5, 80	34X-6, 80	Tc <i>Cyclicargolithus floridanus</i>	13.33	314.10	315.60	314.85	0.75	350.28	316.42
35X-2, 80	35X-CC	T <i>Sphenolithus heteromorphus</i> (NN6)	13.53	319.20	319.79	319.50	0.30	359.83	325.05
39X-CC	40X-2, 80	Tc <i>Discoaster deflandrei</i>	15.66	363.81	366.68	365.25	1.44	400.81	362.06
39X-CC	40X-1, 80	B <i>Discoaster petaliformis</i>	15.70	363.76	365.20	364.48	0.72	400.04	361.37
44X-1, 2	44X-1, 80	Bc <i>Sphenolithus heteromorphus</i>	17.71	402.82	403.60	403.21	0.39	448.27	404.94
321-U1338B-									
1H-4, 80	1H-5, 80	T <i>Pseudoemiliana lacunosa</i> (NN20)	0.44	5.30	6.80	6.05	0.75	6.05	5.47
2H-2, 80	2H-3, 80	Tc <i>Reticulofenestra asanoi</i>	0.91	9.90	11.40	10.65	0.75	11.94	10.79
2H-5, 80	2H-6, 80	T <i>Gephyrocapsa</i> (>5.5 µm)	1.26	14.40	15.90	15.15	0.75	16.44	14.85
2H-CC	3H-1, 70	T <i>Calcidiscus macintyreii</i>	1.61	17.49	17.80	17.65	0.16	19.33	17.46
		Pliocene/Pleistocene boundary	1.81						
3H-4, 20	3H-5, 85	T <i>Discoaster brouweri</i> (NN19)	1.93	21.80	23.95	22.88	1.08	24.95	22.53
4H-5, 50	4H-6, 50	T <i>Discoaster pentaradiatus</i> (NN18)	2.39	33.10	34.60	33.85	0.75	36.51	32.98
4H-6, 50	4H-CC	T <i>Discoaster surculus</i> (NN17)	2.49	34.60	36.55	35.58	0.97	38.24	34.54
5H-5, 50	5H-6, 50	T <i>Sphenolithus</i> spp.	3.54	42.60	44.10	43.35	0.75	57.65	52.08
6H-1, 70	6H-2, 70	T <i>Reticulofenestra pseudoumbilicus</i> (NN16)	3.70	46.30	47.80	47.05	0.75	52.19	47.15
8H-3, 70	8H-4, 70	T <i>Ceratolithus acutus</i>	5.04	68.30	69.80	69.05	0.75	75.63	68.32
		Miocene/Pliocene boundary	5.33						

Table T4 (continued).

Core, section, interval (cm)		Marker species (base zone)	Age (Ma)	Depth CSF (m)				Depth (m)	
Top	Bottom			Top	Bottom	Midpoint	±	CCSF-A	CCSF-B
9H-2, 70	9H-3, 100	B <i>Ceratolithus acutus</i>	5.35	76.30	78.10	77.20	0.90	85.23	76.99
9H-CC	10H-1, 80	T <i>Discoaster quinqueramus</i> (NN12)	5.58	83.42	84.40	83.91	0.49	92.43	83.49
11H-3, 6	11H-4, 6	T <i>Nicklithus amplifucus</i>	5.98	96.16	97.66	96.91	0.75	106.78	96.46
13H-4, 80	13H-5, 80	B <i>Nicklithus amplifucus</i>	6.91	117.40	118.90	118.15	0.75	130.57	117.95
15H-CC	16H-1, 80	TP <i>Reticulofenestra pseudombilicus</i>	7.07	140.97	141.40	141.19	0.22	156.40	141.28
16H-5, 80	16H-6, 80	B <i>Amaurolithus</i> spp.	7.36	147.40	148.90	148.15	0.75	164.23	148.36
18H-2, 70	18H-3, 70	B <i>Discoaster berggrenii</i> (NN11)	8.29	161.80	163.30	162.55	0.75	180.51	163.06
20H-2, 70	20H-3, 70	BP <i>Reticulofenestra pseudombilicus</i>	9.10	180.80	182.30	181.55	0.75	201.18	181.73
21H-6, 70	21H-CC	T <i>Discoaster hamatus</i> (NN10)	9.69	196.30	198.03	197.17	0.86	217.42	196.40
24H-6, 80	24H-CC	B <i>Discoaster hamatus</i> (NN9)	10.55	224.90	226.62	225.76	0.86	250.42	226.21
24H-6, 80	24H-CC	T <i>Coccolithus miopelagicus</i>	10.60	224.90	226.62	225.76	0.86	250.42	226.21
27H-2, 80	28H-1, 80	Tc <i>Discoaster kugleri</i>	11.58	249.90	257.90	253.90	4.00	281.58	254.36
29H-1, 80	29H-2, 80	Bc <i>Discoaster kugleri</i> (NN7)	11.86	267.40	268.90	268.15	0.75	296.35	267.71
29H-2, 80	29H-3, 80	T <i>Cyclicargolithus floridanus</i>	12.03	268.90	270.40	269.65	0.75	297.85	269.06
29H-2, 80	29H-3, 80	T <i>Coronocyclus nitescens</i>	12.12	268.90	270.40	269.65	0.75	297.85	269.06
29H-4, 80	29H-5, 80	T <i>Calcidiscus premacintyreii</i>	12.45	271.90	273.40	272.65	0.75	300.85	271.77
35H-CC	36H-1, 70	Tc <i>Cyclicargolithus floridanus</i>	13.33	321.32	321.60	321.46	0.14	354.37	320.12
36H-6, 70	36H-7, 40	T <i>Sphenolithus heteromorphus</i> (NN6)	13.53	329.10	330.30	329.70	0.60	362.74	327.68
40H-5, 80	40H-6, 80	Tc <i>Discoaster deflandrei</i>	15.66	365.70	367.20	366.45	0.75	407.65	368.25
40H-CC	41H-1, 80	B <i>Discoaster petaliformis</i>	15.70	368.62	369.20	368.91	0.29	410.75	371.04
45X-1, 125	45X-2, 70	Bc <i>Sphenolithus heteromorphus</i>	17.71	407.85	408.71	408.28	0.43	453.12	409.32
321-U1338C-	321-U1338C-								
1H-CC	2H-1, 80	T <i>Pseudoemiliana lacunosa</i> (NN20)	0.44	3.79	4.60	4.20	0.40	4.47	4.04
2H-5, 80	2H-6, 80	Tc <i>Reticulofenestra asanoi</i>	0.91	10.60	12.10	11.35	0.75	11.90	10.75
2H-CC	3H-1, 80	T <i>Gephyrocapsa</i> (>5.5 µm)	1.26	13.70	14.10	13.90	0.20	15.33	13.85
3H-2, 80	3H-3, 120	T <i>Calcidiscus macintyreii</i>	1.61	15.60	17.50	16.55	0.95	18.86	17.04
		Pliocene/Pleistocene boundary	1.81						
4H-1, 50	4H-1, 100	T <i>Discoaster brouweri</i> (NN19)	1.93	23.30	23.80	23.55	0.25	26.41	23.86
4H-1, 100	4H-1, 150	Bc <i>Discoaster triradiatus</i>	2.14	23.80	24.30	24.05	0.25	26.91	24.31
4H-5, 70	4H-6, 70	T <i>Discoaster pentaradiatus</i> (NN18)	2.39	29.50	31.00	30.25	0.75	33.11	29.91
5H-1, 80	5H-2, 80	T <i>Discoaster surculus</i> (NN17)	2.49	33.10	34.60	33.85	0.75	39.11	35.33
6H-1, 80	6H-2, 80	T <i>Sphenolithus</i> spp.	3.54	42.60	44.10	43.35	0.75	51.01	46.08
6H-2, 80	6H-3, 80	T <i>Reticulofenestra pseudombilicus</i> (NN16)	3.70	44.10	45.60	44.85	0.75	52.51	47.43
8H-4, 120	8H-5, 120	T <i>Ceratolithus acutus</i>	5.04	66.50	68.00	67.25	0.75	76.23	68.86
		Miocene/Pliocene boundary	5.33						
9H-3, 80	9H-4, 80	B <i>Ceratolithus acutus</i>	5.35	74.10	75.60	74.85	0.75	84.22	76.08
10H-2, 80	10H-3, 20	T <i>Discoaster quinqueramus</i> (NN12)	5.58	82.10	83.00	82.55	0.45	92.82	83.85
11H-3, 80	11H-5, 80	T <i>Nicklithus amplifucus</i>	5.98	94.60	96.10	95.35	0.75	105.35	95.17
13H-4, 80*	13H-5, 80*	B <i>Nicklithus amplifucus</i>	6.91	113.60	115.10	114.35	0.75	125.75	113.60
16H-1, 80	16H-2, 80	TP <i>Reticulofenestra pseudombilicus</i>	7.07	137.60	139.10	138.35	0.75	154.34	139.42
16H-CC	17H-1, 70	B <i>Amaurolithus</i> spp.	7.36	146.75	147.00	146.88	0.13	163.41	147.62
19H-2, 90	19H-3, 90	B <i>Discoaster berggrenii</i> (NN11)	8.29	163.70	165.20	164.45	0.75	183.45	165.72
20H-6, 110	20H-CC	BP <i>Reticulofenestra pseudombilicus</i>	9.10	179.40	181.18	180.29	0.89	199.96	180.63
22H-CC	23H-1, 100	T <i>Discoaster hamatus</i> (NN10)	9.69	199.70	200.30	200.00	0.30	221.78	200.34
25H-4, 80	25H-5, 80	B <i>Discoaster hamatus</i> (NN9)	10.55	223.60	225.10	224.35	0.75	249.08	225.00
25H-3, 80	25H-4, 80	T <i>Coccolithus miopelagicus</i>	10.60	222.10	223.60	222.85	0.75	247.58	223.65
28H-CC	29H-1, 80	Tc <i>Discoaster kugleri</i>	11.58	256.58	257.10	256.84	0.26	283.65	256.23
30H-3, 80	30H-4, 80	Bc <i>Discoaster kugleri</i> (NN7)	11.86	269.60	271.10	270.35	0.75	298.49	269.64
30H-5, 80	30H-6, 80	T <i>Cyclicargolithus floridanus</i>	12.03	272.60	274.10	273.35	0.75	301.49	272.35
30H-5, 80	30H-6, 80	T <i>Coronocyclus nitescens</i>	12.12	272.60	274.10	273.35	0.75	301.49	272.35
30H-6, 80	30H-CC	T <i>Calcidiscus premacintyreii</i>	12.45	274.10	275.66	274.88	0.78	303.02	273.73
36H-2, 80	36H-4, 80	Tc <i>Cyclicargolithus floridanus</i>	13.33	318.70	321.70	320.20	1.50	353.67	319.49
37H-1, 80	37H-2, 80	T <i>Sphenolithus heteromorphus</i> (NN6)	13.53	326.70	328.20	327.45	0.75	362.52	327.48
41H-4, 80	41H-5, 80	Tc <i>Discoaster deflandrei</i>	15.66	369.20	370.70	369.95	0.75	407.34	367.97
41H-6, 80	41H-CC	B <i>Discoaster petaliformis</i>	15.70	372.21	373.88	373.05	0.84	410.44	370.76

Notes: * = flow-in, upper three sections in Core 321-U1338C-13H. T = top, Tc = top common, B = bottom, TP = top paracme, BP = bottom paracme, Bc = bottom common.

Table T5. Preservation and estimated abundances of calcareous nannofossils, Site U1338. This table is available in an [oversized format](#).

Table T6. Radiolarian datums, Site U1338. (See table note.)

Core, section, interval (cm)		Marker species	Age (Ma)	Depth CSF (m)			
Top	Bottom			Top	Bottom	Midpoint	±
321-U1338A-	321-U1338A-						
1H-CC	2H-2, 67–69	T <i>Stylatractus univervus</i>	0.44	2.73	4.87	3.80	1.07
1H-CC	2H-2, 67–69	B <i>Collosphaera tuberosa</i>	0.59	2.73	4.87	3.80	1.07
2H-5, 110–112	2H-CC	T <i>Anthocytidium angulare</i>	1.21	9.82	12.60	11.21	1.39
2H-5, 110–112	2H-CC	T <i>Theocorythium vetulum</i>	1.21	9.82	12.60	11.21	1.39
3H-2, 67–69	3H-5, 110–112	T <i>Lamprocyrtis heteroporos</i>	1.76	14.39	19.30	16.85	2.46
3H-2, 67–69	3H-5, 110–112	B <i>Theocorythium trachelium</i>	1.76	14.39	19.30	16.85	2.46
3H-2, 67–69	3H-5, 110–112	B <i>Anthocytidium angulare</i>	1.97	14.39	19.30	16.85	2.46
3H-5, 110–112	3H-CC	T <i>Pterocanium prismatium</i>	2.08	19.32	22.12	20.72	1.40
4H-4, 34–36	4H-CC	T <i>Didymocyrtis avita</i>	2.60	26.56	31.65	29.11	2.55
4H-CC	5H-2, 123–124	T <i>Stichocorys pergrina</i>	2.90	31.70	33.93	32.82	1.12
5H-2, 123–124	5H-4, 50–51	B <i>Lamprocyrtis heteroporos</i>	3.23	33.94	36.20	35.07	1.13
5H-4, 50–51	5H-CC	T <i>Phormostichoartus fistula</i>	3.52	36.21	41.25	38.73	2.52
6H-3, 131–133	6H-5, 131–133	T <i>Spongaster pentas</i>	3.96	45.03	48.01	46.52	1.49
6H-3, 131–133	6H-5, 131–133	T <i>Phormostichoartus doliolum</i>	3.96	45.03	48.01	46.52	1.49
6H-5, 131–133	6H-CC	B <i>Amphirhopalum ypsilon</i>	4.03	48.03	50.70	49.37	1.34
6H-CC	7H-2, 47–49	B <i>Spongaster tetras tetras</i>	4.26	50.75	52.17	51.46	0.71
6H-CC	7H-2, 47–49	T <i>Didymocyrtis penultima</i>	4.26	50.75	52.17	51.46	0.71
7H-2, 47–49	7H-4, 52–54	B <i>Pterocanium prismatium</i>	4.73	52.19	55.22	53.71	1.52
8H-CC	9H-3, 14–16	T <i>Spongaster berminghami</i>	5.57	69.70	72.34	71.02	1.32
10H-6, 118–120	10H-CC	B <i>Didymocyrtis avita</i>	6.15	87.40	88.73	88.07	0.66
10H-6, 118–120	10H-CC	B <i>Spongaster pentas</i>	6.17	87.40	88.73	88.07	0.66
10H-6, 118–120	10H-CC	T <i>Didymocyrtis antepenultima</i>	6.17	87.40	88.73	88.07	0.66
10H-CC	11H-3, 110–112	B <i>Didymocyrtis tetrathalamus</i>	6.60	88.78	92.30	90.54	1.76
11H-3, 110–112	11H-5, 73–75	T <i>Stichocorys delmontensis</i>	6.89	92.32	94.93	93.63	1.31
14H-CC	15H-2, 48–50	<i>S. delmontensis</i> > <i>S. pergrina</i>	7.84	126.85	128.18	127.52	0.67
15H-2, 48–50	15H-4, 97–99	B <i>Theocorythium vetulum</i>	7.98	128.20	131.99	130.10	1.90
17H-CC	18H-2, 68–70	T <i>Diartus hughesi</i>	8.39	155.31	156.88	156.10	0.78
17H-CC	18H-2, 68–70	T <i>Didymocyrtis laticonus</i>	8.43	155.31	156.88	156.10	0.78
20H-3, 13–15	20H-5, 11–13	B <i>Didymocyrtis penultima</i>	8.51	176.85	179.81	178.33	1.48
20H-3, 13–15	20H-5, 11–13	T <i>Botryostrobos miralestensis</i>	8.59	176.85	179.81	178.33	1.48
20H-5, 11–13	20H-CC	B <i>Spongaster berminghami</i>	8.76	179.83	183.71	181.77	1.94
20H-5, 11–13	20H-CC	<i>D. pettersoni</i> > <i>D. hughesi</i>	8.76	179.83	183.71	181.77	1.94
20H-CC	21H-2, 42–44	B <i>Diartus hughesi</i>	8.63	183.76	185.12	184.44	0.68
22H-5, 53–55	22H-CC	B <i>Didymocyrtis antepenultima</i>	10.01	199.25	202.58	200.92	1.67
23H-5, 108–110	23H-CC	T <i>Cyrtocapsella japonica</i>	10.31	209.30	212.16	210.73	1.43
24H-2, 42–44	24H-5, 133–135	T <i>Carpocanopsis cristata</i>	10.88	213.64	219.03	216.34	2.69
24H-2, 42–44	24H-5, 133–135	T <i>Lithopera neotera</i>	11.16	213.64	219.03	216.34	2.69
29X-4, 24–26	29X-CC	T <i>Cyrtocapsella cornuta</i>	11.88	264.16	268.33	266.25	2.08
29X-4, 24–26	29X-CC	T <i>Lithopera renzae</i>	11.91	264.16	268.33	266.25	2.08
29X-4, 24–26	29X-CC	T <i>Cyrtocapsella tetrapera</i>	11.91	264.16	268.33	266.25	2.08
31X-CC	32X-2, 83–85	B <i>Diartus pettersoni</i>	12.11	278.55	290.43	284.49	5.94
34X-2, 67–69	34X-4, 81–83	B <i>Lithopera neotera</i>	12.95	309.49	312.61	311.05	1.56
35X-CC	36X-1, 29–31	T <i>Calocyclus robusta</i>	13.35	319.84	326.79	323.32	3.48
36X-CC	37X-1, 37–39	T <i>Acrocubus octopyle</i>	13.88	327.73	336.37	332.05	4.32
36X-CC	37X-1, 37–39	T <i>Liriospyris parkerae</i>	13.88	327.73	336.37	332.05	4.32
36X-CC	37X-1, 37–39	T <i>Didymocyrtis mammifera</i>	13.89	327.73	336.37	332.05	4.32
37X-CC	38X-2, 35–37	T <i>Didymocyrtis violina</i>	14.20	337.23	347.35	342.29	5.06
37X-CC	38X-2, 35–37	T <i>Calocyclus virginis</i>	14.23	337.23	347.35	342.29	5.06
37X-CC	38X-2, 35–37	T <i>Calocyclus costata</i>	14.23	337.23	347.35	342.29	5.06
39X-2, 75–78	39X-5, 87–89	T <i>Carpocanopsis bramlettei</i>	14.33	357.08	361.67	359.38	2.30
39X-2, 75–78	39X-5, 87–89	T <i>Didymocyrtis tubaria</i>	14.35	357.08	361.67	359.38	2.30
39X-CC	40X-1, 103–105	<i>D. dentata</i> > <i>D. alata</i>	14.77	363.81	365.43	364.62	0.81
40X-1, 103–105	40X-3, 27–29	T <i>Liriospyris stauropora</i>	14.78–14.83	365.45	367.16	366.31	0.86
41X-4, 22–24	41X-CC	B <i>Liriospyris parkerae</i>	14.79–15.03	378.74	382.72	380.73	1.99
41X-CC	42X-2, 46–48	T <i>Carpocanopsis cingulata</i>	15.13	382.77	385.56	384.17	1.39
42X-4, 100–102	42X-CC	B <i>Acrocubus octopylus</i>	15.75	389.12	391.07	390.10	0.98
43X-2, 63–64	43X-CC	B <i>Calocyclus costata</i>	17.19	395.34	396.41	395.88	0.54
321-U1338B-	321-U1338B-						
29H-2, 29–31	29H-5, 110–112	T <i>Cyrtocapsella cornuta</i>	11.88	268.41	273.70	271.06	2.64
29H-2, 29–31	29H-5, 110–112	T <i>Cyrtocapsella tetrapera</i>	11.91	268.41	273.70	271.06	2.64
29H-5, 110–112	30H-2, 141–143	B <i>Diartus pettersoni</i>	12.11	273.72	279.01	276.37	2.64

Note: T = top, B = bottom.

Table T7. Preservation and relative abundance of radiolarians, Holes U1337A and U1338A. This table is available in an [oversized format](#).**Table T8.** Preservation and relative abundance of radiolarians, Hole U1338B. ([See table notes.](#))

Core, section, interval (cm)	Radiolarian zone		Abundance	Preservation	<i>Anthocyrtidium plicocnica</i>	<i>Botryostrobus miralestensis</i>	<i>Calocyclus caepta</i>	<i>Carpocanopsis cristata</i>	<i>Cyrtocapsella cornuta</i>	<i>Cyrtocapsella japonica</i>	<i>Cyrtocapsella tetrapera</i>	<i>Diartus petterssoni</i>	<i>Didymocyrtilis laticonus</i>	<i>Lithopera neotera</i>	<i>Stichocorys delmontensis</i>	<i>Stichocorys wolffii</i>
	Abundance	Preservation														
321-U1338B- 27H-2, 34–36	RN6	A	G		R	R	R		F	F	R		F	R		
28H-2, 130–132		A	G		R	R			F	F	R	R	F	R		
28H-6, 118–120		A	G	R	R	R	R		F	F	R	R	F	R		
29H-2, 29–31		A	G		R	R	R		F		R	R	F			
29H-5, 110–112		A	G	R	R	R	R	R		R	R	R	R	F	R	
30H-2, 141–143		A	G	R	R	R	R	R		R		R	R	F	R	
		A	G	R	R	R	R	R		R		R	R	F	R	

Notes: Abundance: A = abundant. Preservation: G = good, F = few, R = rare. No mixing of older specimens detected.

Table T9. Diatom datums, Site U1338. ([See table note.](#))

Core, section, interval (cm)		Marker species	Age (Ma)	Depth CSF (m)		
Top	Base			Top	Bottom	Mean
321-U1338A- 1H-1, 98–100	321-U1338A- 1H-CC	<i>T Nitzschia fossilis</i>	0.92	0.98	2.55	1.77
2H-CC	3H-1, 90	<i>B Azpeitia barronii</i>	1.62	9.89	12.45	11.17
3H-1, 90	3H-2, 65–66	<i>B Fragilariopsis doliolus</i>	1.88	12.45	13.10	12.78
3H-CC	4H-1, 50	<i>T Rhizosolenia praebergonii</i>	1.92	21.98	22.50	22.24
4H-4, 30–31	4H-CC	<i>T Nitzschia jouseae</i>	2.71	26.50	31.45	28.98
5H-CC	6H-1, 40	<i>B Rhizosolenia praebergonii</i>	3.13	41.25	44.95	43.10
7H-2, 50–51	7H-3, 55	<i>T Actinocyclus ellipticus</i> f. <i>lanceolata</i>	3.35	52.20	53.75	52.98
9H-5, 70	9H-6, 110–111	<i>T Fragilariopsis cylindrica</i>	4.69	75.90	77.80	76.85
9H-6, 110–111	9H-CC	<i>B Nitzschia jouseae</i>	4.92	77.80	78.78	78.29
10H-6, 129–130	10H-3, 58–59	<i>B Thalassiosira oestrupii</i>	5.70	82.28	87.49	84.89
11H-5, 57–58	11-CC	<i>T Thalassiosira praeconvexa</i>	6.56	94.77	96.96	95.87
14H-2, 40–41	14H-4, 38–39	<i>B Thalassiosira convexa</i>	6.86	118.50	121.58	120.04
14H-4, 38–39	14H-CC	<i>B Thalassiosira praeconvexa</i>	7.07	121.58	126.57	124.08
16H-CC	17H-1, 95	<i>B Nitzschia miocena</i>	7.58	145.45	146.15	145.80
17H-4, 26–27	17H-4, 55	<i>T Rossiella paleacea</i>	7.64	149.96	150.20	150.08
18H-3, 65	18H-4, 72–73	<i>T Thalassiosira burckliana</i>	7.86	157.98	159.92	158.95
19H-5, 70	19H-6, 70	<i>T Thalassiosira yabei</i>	8.44	170.90	172.40	171.65
20H-6, 80	20H-CC	<i>B Nitzschia cylindrica</i>	8.44	181.80	183.47	182.64
21H-2, 36–37	21H-5, 56–57	<i>B Azpeitia nodulifera</i> var. <i>cylopa</i>	8.58	185.10	189.80	187.45
23H-5, 126–127	23H-CC	<i>B Actinocyclus ellipticus</i> f. <i>lanceolata</i>	9.90	209.46	211.90	210.68
26H-6, 117	27X-2, 5–6	<i>B Hemidiscus cuneiformis</i>	11.24	239.37	241.75	240.56
27X-CC	28X-CC	<i>B Thalassiosira brunii</i>	11.50	247.54	249.80	248.67
29X-CC	30X-CC	<i>T Cestodiscus pulchellus</i>	12.05	268.15	269.00	268.58
30X-CC	31X-CC	<i>B Nitzschia porteri</i>	12.11	269.00	278.50	273.75
31X-CC	32X-CC	<i>T Crucidentacula nicobarica</i>	12.50	278.50	288.90	283.70
32X-CC	32X-2, 86–87	<i>T Coscinodiscus lewisianus</i>	12.99	288.90	290.46	289.68
33X-4, 80	33X-5, 72–73	<i>B Triceratium cinnamomeum</i>	13.52	303.00	304.42	303.71
35X-2, 80	35X-CC	<i>B Actinocyclus ellipticus</i>	14.37	317.81	319.79	318.80
37X-1, 43–44	37X-CC	<i>B Thalassiosira tapanae</i>	14.55	336.43	337.18	336.81
40X-1, 122–123	40X-3, 27–28	<i>B Actinocyclus ingens</i>	15.25	365.55	367.16	366.36
42X-CC	43X-2, 70–71	<i>T Thalassiosira fraga</i>	15.96	391.07	395.40	393.24

Note: T = top, B = bottom.

Table T10. Preservation and estimated abundances of diatoms, Site U1338. This table is available in an [oversized format](#).**Table T11.** Planktonic foraminifer datums, Site U1338. (See table note.)

Core, section, interval (cm)		Marker species	Age (Ma)	Depth CSF (m)				Depth CCSF (m)			
Top	Bottom			Top	Bottom	Midpoint	±	Top	Bottom	Midpoint	±
321-U1338A- 2H-2, 70–72	321-U1338A- 2H-5, 115–117	T <i>Globorotalia (Truncorotalia) tosaensis</i>	0.61	4.92	9.85	7.39	2.47	6.40	11.33	8.87	2.47
3H-2, 70–72	3H-CC	T <i>Globigerinoides fistulosus</i>	1.77	14.42	22.12	18.27	3.85	16.65	24.35	20.50	3.85
Pleistocene/Pliocene boundary											
4H-5, 56–58	4H-CC	T <i>Globigerinoides extremus</i>	1.98	28.28	31.65	29.97	1.69	31.90	35.27	33.59	1.69
4H-3, 56–58	4H-5, 56–58	T <i>Globorotalia pseudomiocenica</i>	2.30	25.28	28.26	26.77	1.49	28.90	31.88	30.39	1.49
4H-5, 56–58	4H-CC	T <i>Globorotalia (Menardella) multicamerata</i>	2.98	28.28	31.65	29.97	1.69	31.90	35.27	33.59	1.69
5H-2, 117–118	5H-CC	T <i>Dentoglobigerina altispira</i>	3.47	33.88	41.25	37.57	3.69	39.58	46.95	43.27	3.69
5H-2, 117–118	5H-CC	T <i>Sphaeroidinellopsis seminulina</i>	3.59	33.88	41.25	37.57	3.69	39.58	46.95	43.27	3.69
6H-5, 118–120	6H-CC	T <i>Globorotalia (Hirsutella) margaritae</i>	3.85	47.90	50.70	49.30	1.40	53.46	56.26	54.86	1.40
6H-5, 118–120	6H-CC	X <i>Pulleniatina</i> spp. sinistral → dextral	4.08	47.90	50.70	49.30	1.40	53.46	56.26	54.86	1.40
7H-2, 52–54	7H-4, 58–60	T <i>Globoturborotalita nepenthes</i>	4.37	52.24	55.28	53.76	1.52	58.45	61.49	59.97	1.52
7H-4, 58–60	7H-CC	B <i>Globorotalia (Menardella) exilis</i>	4.45	55.30	60.14	57.72	2.42	61.51	66.35	63.93	2.42
Pliocene/Miocene boundary											
8H-2, 43–45	8H-5, 106–108	B <i>Sphaeroidinella dehiscentis</i> s.l.	5.54	61.65	66.76	64.21	2.56	69.73	74.84	72.29	2.55
10H-3, 47–49	10H-6, 108–110	B <i>Globorotalia tumida</i>	5.57	82.19	87.28	84.74	2.55	92.42	97.51	94.97	2.55
12H-CC	13H-2, 105–107	B <i>Globorotalia (Hirsutella) margaritae</i>	6.08	107.69	109.75	108.72	1.03	120.04	123.47	121.76	1.72
13H-5, 44–46	13H-CC	T <i>Globorotalia languaensis</i>	6.13	113.66	117.09	115.38	1.72	127.38	130.81	129.10	1.72
21H-2, 39–41	21H-5, 50–52	B <i>Globorotalia plesiotumida</i>	8.58	185.11	189.70	187.41	2.29	207.20	211.79	209.50	2.29
25H-3, 9–11	25H-6, 5–7	B <i>Neogloboquadrina acostaensis</i>	9.83	224.33	228.79	226.56	2.23	251.81	256.27	254.04	2.23
24H-CC	25H-3, 9–11	T <i>Paragloborotalia mayeri</i>	10.46	221.69	224.31	223.00	1.31	248.17	251.79	249.98	1.81
27X-CC	29X-2, 136–138	B <i>Globoturborotalita decoraperta</i>	11.49	247.65	262.26	254.96	7.30	275.43	291.57	283.50	8.07
26H-2, 50–52	26H-6, 130–132	B <i>Globoturborotalita nepenthes</i>	11.63	232.72	239.50	236.11	3.39	260.70	267.48	264.09	3.39
29X-2, 136–138	29X-4, 32–34	T <i>Globorotalia (Fohsella) fohsi</i> s.l.	11.79	262.28	264.22	263.25	0.97	291.59	293.53	292.56	0.97
34X-2, 78–80	34X-4, 91–93	B <i>Globorotalia (Fohsella) fohsi robusta</i>	13.13	309.60	312.71	311.16	1.55	345.03	348.14	346.59	1.56
35X-2, 9–11	35X-CC	T <i>Globorotalia (Fohsella) fohsi</i> s.l.	13.41	318.51	319.79	319.15	0.64	358.84	360.12	359.48	0.64
33X-5, 47–49	33X-CC	T <i>Globorotalia praescitula</i>	13.73	304.19	306.45	305.32	1.13	337.51	339.77	338.64	1.13
36X-1, 36–38	36X-CC	B <i>Globorotalia (Fohsella) "praefohsi"</i>	13.77	326.88	327.68	327.28	0.40	365.80	366.60	366.20	0.40
36X-CC	37X-1, 43–45	B <i>Globorotalia (Fohsella) peripheroacuta</i>	14.24	327.73	336.43	332.08	4.35	366.65	366.86	366.76	0.10
38X-5, 109–111	38X-CC	T <i>Globigerinatella insueta</i>	14.66	352.61	354.70	353.66	1.04	382.69	384.78	383.74	1.05
35X-2, 9–11	35X-CC	B <i>Orbulina</i> spp.	14.74	318.51	319.79	319.15	0.64	358.84	360.12	359.48	0.64
37X-CC	38X-2, 35–37	B <i>Clavatorella bermudezi</i>	14.89	337.23	347.35	342.29	5.06	367.66	377.43	372.55	4.88
40X-CC	41X-2, 66–68	B <i>Praeorbulina glomerosa</i>	16.27	367.79	376.16	371.98	4.19	405.70	422.88	414.29	8.59
42X-4, 114–116	42X-CC	B <i>Praeorbulina sicana</i>	16.97	389.26	391.07	390.17	0.90	435.58	437.39	436.49	0.91
43X-CC	44X-2, 55–57	B <i>Globigerinatella insueta</i>	17.59	396.46	404.85	400.66	4.19	441.93	449.91	445.92	3.99
42X-CC	43X-2, 18–20	T <i>Globoquadrina binaiensis</i>	19.09	391.12	394.88	393.00	1.88	437.44	440.35	438.90	1.45
321-U1338B- 27H-2, 57–59	321-U1338B- 28H-2, 120–122	B <i>Globoturborotalita decoraperta</i>	11.49	249.69	259.80	254.75	5.06	277.40	287.45	282.42	5.03
27H-2, 57–59	28H-2, 120–122	B <i>Globoturborotalita nepenthes</i>	11.63	249.69	259.80	254.75	5.06	277.40	287.45	282.42	5.03
28H-2, 120–122	28H-6, 107–109	T <i>Globorotalia (Fohsella) fohsi</i> s.l.	11.79	259.82	265.67	262.75	2.93	287.47	293.32	290.39	2.93

Note: T = top, X = abundance crossover, B = bottom.

Table T12. Preservation and estimated abundances of planktonic foraminifers, Site U1338. This table is available in an [oversized format](#).**Table T13.** Distribution of benthic foraminifers, Hole U1338A. This table is available in an [oversized format](#).

Table T14. FlexIt tool core orientation summary, Site U1338. (See table note.) (Continued on next page.)

Core	Orientation angle (°)	Standard deviation	Tool number	Remarks
321-U1338A-				
1H	0.3	4.79	936	
2H	73.3	4.19	936	
3H	153.4	4.35	936	
4H	40.7	4.60	936	
5H	189.6	4.23	936	
6H	336.7	4.89	936	
7H	52.1	1.80	936	
8H	21.4	4.01	936	
9H	132.2	5.73	937	
10H	229.3	12.73	937	
11H	259.0	4.71	937	
12H	328.6	6.11	937	Suspect; very short usable orientations
13H	325.1	1.72	937	
14H	176.2	2.36	937	Suspect; very short usable orientations
15H	177.8	5.52	937	
16H	314.5	5.96	937	Suspect; very short usable orientations
17H	338.7	6.36	937	
18H	275.1	6.96	937	
19H	340.2	9.79	937	
20H	226.6	3.70	937	
21H	28.8	5.40	937	
22H	175.4	1.33	937	
23H	154.1	4.25	937	
24H	50.8	0.78	937	
25H	304.1	4.84	937	
26H	27.7	6.01	936	
321-U1338B-				
1H	114.8	2.85	936	
2H	134.1	2.09	936	
3H	119.6	4.28	936	
4H	270.4	5.24	936	
5H	86.3	3.79	936	
6H	341.5	6.31	936	
7H	32.9	5.64	936	
8H	133.1	5.16	936	
9H	301.1	3.18	936	
10H	225.4	10.73	936	Suspect; slow rotation
11H	23.1	4.99	936	
12H	237.9	4.09	936	Suspect; slow rotation
13H	126.2	9.33	936	Suspect; poor quality noisy data
14H	314.9	1.91	936	
15H	47.2	5.01	936	
16H	308.3	4.16	937	
17H	4.4	5.79	937	
18H	15.6	2.92	937	
19H	316.6	3.78	937	
20H	81.6	11.42	936	Suspect; slow rotation
21H	187.1	1.63	936	
22H	49.7	0.50	936	
23H	329.7	1.12	936	
24H	29.8	1.58	936	
25H	209.0	0.73	936	
26H	81.5	1.62	936	
27H	112.3	1.82	936	
28H	338.2	2.31	936	
29H	347.6	5.97	936	
30H	142.9	2.31	936	
31H	198.8	1.59	936	
32H	302.9	1.39	936	
33H	330.2	3.86	937	
34H	87.5	0.62	937	
35H	276.3	3.29	937	
36H	NA	NA	936	Data lost
37H	NA	NA	936	Data lost
38H	NA	NA	936	Data lost
39H	NA	NA	936	Data lost
40H	NA	NA	936	Data lost

Table T14 (continued).

Core	Orientation angle (°)	Standard deviation	Tool number	Remarks
41H	NA	NA	936	Data lost
42H	NA	NA	936	Data lost
321-U1338C-				
1H	272.8	4.15	936	
2H	52.5	6.74	936	
3H	354.1	5.66	936	
4H	224.7	3.83	936	
5H	38.8	5.24	937	Suspect; very short usable orientations
6H	276.2	6.64	937	
7H	86.1	5.66	937	
8H	32.3	9.40	937	Suspect; poor quality noisy data
9H	253.8	6.11	936	
10H	151.0	10.05	936	
11H	291.7	10.98	936	
12H	235.4	9.74	936	
13H	249.1	2.83	937	
14H	111.1	10.89	937	Suspect; poor quality noisy data
15H	29.1	3.13	937	
16H	160.8	9.64	937	
17H	104.5	4.30	936	
18H	193.6	3.80	936	
19H	89.7	2.60	936	
20H	303.0	4.09	936	
21H	302.3	2.98	936	
22H	91.6	2.29	937	
23H	268.5	2.51	937	
24H	85.0	0.61	937	
25H	219.2	1.38	937	
26H	198.4	2.07	936	
27H	21.8	2.14	936	
28H	250.9	3.46	936	
29H	85.3	4.52	936	
30H	32.7	2.99	936	
31H	160.6	2.31	937	
32H	346.1	3.27	937	
33H	176.1	2.77	937	
34H	22.8	1.47	937	
35H	340.0	1.76	936	
36H	318.9	1.79	936	
37H	338.4	2.04	936	
38H	17.9	0.91	936	
39H	257.7	1.29	937	
40H	195.4	1.38	937	
41H	111.6	1.55	937	
42H	210.5	2.51	936	
43H	240.6	2.28	936	
44H	214.7	1.30	936	

Note: NA = not available.

Table T15. Interpretation of polarity stratigraphy, Site U1338. (See table note.)

Chron	Age (Ma)	Hole U1338A		Hole U1338B		Hole U1338C	
		Core, section, interval (cm)	Depth CCSF-A (m)	Core, section, interval (cm)	Depth CCSF-A (m)	Core, section, interval (cm)	Depth CCSF-A (m)
C1n/C1r.1r	0.781	2H-4, 122	9.91	2H-1, 115	9.92	2H-4, 105	9.92
C1r.1r/C1r.1n	0.988	2H-6, 92	12.61	2H-3, 85	12.62	2H-6, 87	12.75
C1r.1n/C1r.2r	1.072	2H-7, 42	13.61	2H-4, 27	13.54	2H-7, 40	13.75
C1r/C2n	1.778	3H-7, 0	23.56	3H-3, 120	23.50	3H-6, 40	23.50
C2n/C2r.1r	1.945			3H-5, 37	25.66	3H-7, 67	25.30
C2r/C2An.1n	2.581	4H-7, 48	35.05	4H-4, 112	35.15		
C2An.1n/C2An.1r	3.032	5H-3, 130	41.20	5H-1, 75	41.16	5H-3, 47	41.40
C2An.1r/C2An.2n	3.116	5H-5, 0	42.89	5H-2, 40	42.30	5H-4, 17	42.60
C2An.2n/C2An.2r	3.207			5H-3, 18	43.58	5H-5, 10	44.02
C2An.2r/C2An.3	3.330	5H-6, 140	45.80	5H-4, 32	45.21	5H-6, 30	45.72
C2An.3/C2Ar	3.596	6H-2, 140	49.20	5H-6, 120	49.13		
C4An/C4Ar.1r	9.098					21H-6, 15	209.35
C4Ar.1r/C4Ar.1n	9.312	21H-6, 10	212.37	21H-4, 0	212.70	22H-1, 140	212.94
C4Ar.1n/C4Ar.2r	9.409	22H-1, 10	216.08	21H-5, 110	215.30	22H-3, 112	215.66
C4Ar.2r/C4Ar.2n	9.656	22H-3, 122	220.21	22H-2, 22	220.40	22H-7, 50	220.85
C4Ar.2n/C4Ar.3r	9.717	22H-5, 10	222.08	22H-3, 60	222.27	23H-1, 125	222.38
C4Ar.3r/C5n.1n	9.779			22H-4, 22	223.40	23H-2, 105	223.71
C5n.1n/C5n.1r	9.934	23H-1, 15	226.75				
C5n.1r/C5n.2n	9.987			22H-6, 117	227.35	23H-5, 57	227.72
C5Ar.1r/C5Ar.1n	12.730			33H-6, 87	331.17	34H-2, 95	332.05
C5Ar.2n/C5Ar.3r	12.878			34H-3, 67	337.00	34H-6, 17	337.32
C5Ar.3r/C5AAn	13.015			34H-6, 90	341.77	35H-2, 125	341.73
C5AAn/C5AAr	13.183			35H-3, 117	348.36	35H-7, 35	348.17
C5AAr/C5ABn	13.369			35H-6, 110	352.78	36H-2, 140	352.77
C5ABn/C5ABr	13.605			36H-6, 15	361.60		
C5ABr/C5ACn	13.734			36H-7, 65	363.80		
C5ACn/C5ACr	14.095					38H-4, 0	375.50
C5ACr/C5ADn	14.194					38H-6, 0	378.50
C5ADn/C5ADr	14.581					40H-1, 0	390.88
C5ADr/C5Bn.1n	14.784			39H-2, 87	392.80	40H-2, 72	393.10
C5Bn.1n/C5Bn.1r	14.877			39H-3, 77	394.20	40H-3, 37	394.26
C5Bn.1r/C5Bn.2n	15.032					41H-3, 40	404.69
C5Bn.2n/C5Br	15.160			40H-6, 0	407.70	41H-5, 80	408.09

Note: See Figure F4.

Table T16. Interstitial water data from squeezed whole-round and Rhizon samples, Site U1338. This table is available in an [oversized format](#).

Table T17. Inorganic geochemistry of solid samples, Site U1338. (See table notes.)

Hole, core, section, interval (cm)	Top depth (m)		Major element oxide (wt%)										Trace element (ppm)				
	CSF	CCSF-A	SiO ₂	Al ₂ O ₃	Fe ₂ O ₃ T	MnO	MgO	CaO	Na ₂ O	K ₂ O	TiO ₂	P ₂ O ₅	Ba	Sr	V	Zr	
321-																	
U1338A-1H-2, 68–69	2.18	2.22	13.6	0.746	0.622	0.190	0.532	43.0	2.29	0.196	BDL	0.094	1860	1313	BDL	21.3	
U1338A-2H-4, 82–83	8.02	9.50	9.9	0.712	0.957	0.354	0.510	45.5	1.90	0.182	BDL	0.086	1319	1516	BDL	11.8	
U1338A-3H-4, 77–78	17.47	19.70	22.4	1.625	1.925	0.989	1.064	35.4	3.59	0.446	BDL	0.085	4376	1198	BDL	42.9	
U1338A-4H-4, 66–67	26.86	30.48	18.6	1.210	2.543	0.404	1.285	37.7	3.01	0.428	BDL	0.089	4198	1300	BDL	33.0	
U1338A-5H-4, 77–78	36.47	42.17	30.5	2.041	3.228	0.401	1.895	27.7	3.91	0.652	BDL	0.133	6980	1043	BDL	57.3	
U1338A-6H-4, 78–79	45.98	51.54	19.2	1.537	2.414	0.410	1.280	37.2	2.69	0.462	BDL	0.092	3865	1304	14.0	39.7	
U1338A-7H-4, 107–108	55.77	61.98	9.1	0.674	1.325	0.351	0.651	46.0	1.51	0.192	BDL	0.092	2249	1710	BDL	21.6	
U1338A-8H-4, 87–88	65.07	73.15	15.3	0.531	0.415	0.234	0.482	43.5	1.59	0.156	BDL	0.137	2058	1590	BDL	13.7	
U1338A-9H-4, 77–78	74.47	83.92	22.2	0.276	0.194	0.251	0.495	39.5	1.91	0.111	BDL	0.080	1396	1349	BDL	12.2	
U1338A-10H-4, 82–83	84.02	94.25	19.1	0.502	0.838	0.211	0.652	39.9	1.81	0.163	BDL	0.062	2308	1451	BDL	15.8	
U1338A-11H-4, 82–83	93.52	104.55	26.4	0.368	0.232	0.163	0.463	37.7	1.71	0.117	BDL	0.066	2075	1369	BDL	9.0	
U1338A-12H-4, 82–83	103.02	115.37	18.5	0.667	1.179	0.122	0.646	41.3	1.66	0.193	BDL	0.139	4099	1540	BDL	22.2	
U1338A-13H-4, 82–83	112.52	126.24	17.8	0.418	0.558	0.153	0.523	40.3	1.67	0.135	BDL	0.064	1607	1483	BDL	12.9	
U1338A-14H-4, 78–79	121.98	135.91	33.3	0.372	0.476	0.086	0.525	33.6	2.06	0.140	BDL	0.064	2040	1267	BDL	15.2	
U1338A-15H-4, 83–84	131.53	146.53	8.3	0.283	1.507	0.138	0.394	47.3	1.22	0.093	BDL	0.076	1738	1676	BDL	13.2	
U1338A-16H-4, 77–78	140.97	157.03	27.2	0.281	0.125	0.115	0.391	37.8	1.55	0.101	BDL	0.069	1952	1382	BDL	10.8	
U1338A-17H-4, 126–127	150.96	169.04	22.9	0.352	0.865	0.196	0.554	39.5	1.75	0.139	BDL	0.075	2491	1434	BDL	10.7	
U1338A-18H-4, 85–86	160.05	179.33	36.1	0.752	1.600	0.175	0.889	29.4	2.43	0.273	BDL	0.075	5105	1165	BDL	29.4	
U1338A-19H-4, 97–98	169.67	189.87	14.9	0.295	0.907	0.255	0.478	43.5	1.36	0.114	BDL	0.063	1824	1521	BDL	9.7	
U1338A-20H-4, 96–97	179.16	199.95	39.9	0.504	1.036	0.144	0.572	28.0	2.33	0.182	BDL	0.051	3067	1112	BDL	15.9	
U1338A-21H-4, 76–77	188.46	210.55	24.9	0.876	2.463	0.256	0.953	34.7	1.86	0.312	BDL	0.171	5904	1490	BDL	30.9	
U1338A-22H-4, 87–88	198.07	221.42	53.0	0.892	1.696	0.126	0.953	14.7	2.85	0.311	BDL	0.011	3497	707	36.3	28.4	
U1338A-23H-4, 77–78	207.47	232.11	22.0	1.002	2.143	0.218	0.929	37.2	1.96	0.332	BDL	0.125	4150	1587	BDL	28.7	
U1338A-24H-4, 75–76	216.95	243.43	29.6	0.808	1.775	0.284	0.817	33.5	1.91	0.277	BDL	0.096	3212	1414	BDL	20.3	
U1338A-25H-4, 86–87	226.59	254.07	33.1	0.703	1.401	0.184	0.754	32.0	2.08	0.234	BDL	0.076	3840	1381	BDL	22.8	
U1338A-26H-4, 81–82	236.01	263.99	31.2	0.526	1.394	0.209	0.662	33.6	1.81	0.204	BDL	0.086	2814	1391	BDL	9.2	
U1338A-27X-4, 83–84	245.53	273.31	8.0	0.221	1.049	0.256	0.443	48.9	1.03	0.084	BDL	0.051	1292	1853	BDL	6.6	
U1338B-27H-1, 62–63	248.22	275.93	17.6	0.200	1.036	0.188	0.472	42.1	1.31	0.087	BDL	0.087	1276	1641	BDL	11.1	
U1338B-28H-4, 81–82	262.41	290.06	15.3	0.327	0.287	0.200	0.315	44.5	0.82	0.079	BDL	0.078	2510	1572	BDL	7.9	
U1338A-29X-4, 68–69	264.58	293.89	12.1	0.236	0.329	0.164	0.358	45.3	1.20	0.095	BDL	0.048	1564	1600	BDL	10.8	
U1338B-29H-4, 80–81	271.90	300.10	17.8	0.376	0.942	0.149	0.507	42.7	1.22	0.123	BDL	0.054	2468	1528	BDL	19.1	
U1338A-32X-4, 98–99	293.58	325.90	4.6	0.192	0.049	0.191	0.289	50.9	0.81	0.045	BDL	0.086	1317	1692	BDL	16.8	
U1338A-33X-4, 103–104	303.25	333.57	8.8	0.316	0.925	0.182	0.433	47.7	1.01	0.093	BDL	0.091	2134	1660	BDL	BDL	
U1338B-34H-4, 86–87	307.30	338.73	11.0	0.312	0.838	0.174	0.389	46.2	0.92	0.093	BDL	0.064	2219	1669	BDL	7.6	
U1338A-34X-4, 120–121	313.00	348.43	13.5	0.334	1.104	0.193	0.451	44.7	0.95	0.104	BDL	0.121	3085	1612	BDL	16.4	
U1338B-35H-4, 87–88	316.77	349.55	13.1	0.329	0.944	0.184	0.444	45.7	0.99	0.104	BDL	0.048	2256	1665	BDL	18.3	
U1338A-35X-2, 67–68	319.07	359.40	13.7	0.473	1.412	0.178	0.554	44.4	1.06	0.168	BDL	0.108	3526	1584	BDL	16.5	
U1338B-36H-4, 72–73	326.12	359.16	15.5	0.445	1.577	0.156	0.604	42.2	1.08	0.163	BDL	0.059	3077	1563	BDL	12.3	
U1338A-36X-1, 60–61	327.10	366.02	8.5	0.269	1.089	0.206	0.504	47.6	0.97	0.096	BDL	0.070	1797	1542	BDL	6.4	
U1338A-37X-1, 97–98	336.97	367.40	11.4	0.346	1.148	0.216	0.543	46.0	0.95	0.122	BDL	0.073	2327	1456	BDL	18.1	
U1338A-38X-4, 46–47	350.46	380.54	8.9	0.315	1.119	0.174	0.526	47.1	0.88	0.098	BDL	0.063	2227	1496	BDL	12.6	
U1338A-39X-4, 102–103	360.31	393.52	9.4	0.193	0.425	0.168	0.401	47.7	0.81	0.065	BDL	0.077	1367	1304	BDL	7.4	
U1338A-40X-2, 58–59	366.46	404.37	13.2	0.333	0.897	0.169	0.598	44.8	1.20	0.119	BDL	0.054	2407	1247	BDL	13.0	
U1338A-41X-4, 47–48	378.97	425.69	13.5	0.358	1.316	0.159	0.677	44.4	0.92	0.121	BDL	0.064	2322	1219	BDL	6.1	
U1338A-42X-4, 40–41	388.50	434.82	11.7	0.281	1.164	0.163	0.582	45.3	0.73	0.065	BDL	0.082	2504	1273	BDL	16.7	
U1338A-43X-2, 83–84	395.53	441.00	17.9	0.375	1.612	0.156	0.696	42.2	0.81	0.090	BDL	0.094	2622	1266	BDL	12.2	
U1338A-44X-3, 131–132	407.11	452.17	6.7	0.408	2.223	0.402	1.640	46.8	0.41	0.112	BDL	0.136	2895	1214	BDL	16.2	

Notes: BDL = below detection limit (TiO₂ = 0.00293 wt%, V = 7.76 ppm, Zr = 5.25 ppm). Values for Sr and Ba are well above calibration range (Sr < 700 ppm, Ba < 570 ppm). See "Geochemistry" in the "Methods" chapter for uncertainty estimates and assessment of accuracy.

Table T18. Element/Ca ratios of bulk carbonate leachates, Sites U1336–U1338. (See table notes.)

Core, section, interval (cm)	Depth (m)		CaCO ₃ (wt%)	Ratios (mM/M)				
	CSF	CCSF-A		Mg/Ca	Si/Ca	Mn/Ca	Fe/Ca	Sr/Ca
320-U1336B-								
2H-2, 72–73	4.02	4.55	94.4	3.94	BDL	0.44	BDL	1.65
7H-2, 72–73	51.52	60.21	85.4	3.89	BDL	0.53	BDL	1.71
8H-2, 72–73	61.02	69.90	77.7	3.90	BDL	0.57	BDL	2.05
9H-2, 72–73	70.52	79.33	86.7	3.46	BDL	1.01	BDL	1.92
11H-2, 71–72	89.51	100.20	91.9	3.03	BDL	1.50	BDL	1.65
12H-2, 71–72	99.01	111.52	88.0	3.01	BDL	1.09	BDL	2.09
13H-2, 71–72	108.51	122.77	94.0	2.81	BDL	1.42	0.247	1.51
14H-2, 72–73	118.02	135.00	87.1	2.43	BDL	0.93	0.043	2.04
14H-4, 70–71	121.00	137.98	95.9	2.70	BDL	1.16	0.301	1.08
15H-2, 72–73	127.52	145.31	92.9	1.90	BDL	1.03	0.082	1.89
16H-1, 42–43	135.22	153.01	94.1	2.21	BDL	1.15	0.197	1.29
17H-2, 72–73	139.02	156.81	92.0	2.15	BDL	0.86	0.232	1.49
18H-2, 71–72	147.61	165.40	90.4	2.42	BDL	0.93	0.151	1.65
19H-2, 71–72	157.11	174.90	84.9	2.32	BDL	0.83	0.058	1.78
20H-2, 71–72	166.61	184.40	89.5	2.77	BDL	1.08	0.133	1.74
321-U1337A-								
2H-6, 70–71	13.70	8.49	87.6	3.45	BDL	3.00	BDL	2.33
13H-1, 89–90	110.89	118.93	72.2	5.55	0.02	9.91	BDL	2.69
14H-4, 65–66	124.7	134.91	62.0	4.94	1.89	4.58	BDL	2.85
16H-4, 71–72	143.71	155.93	32.3	31.83	11.24	87.23	BDL	2.78
26X-4, 70–71	238.2	259.30	74.9	4.17	BDL	1.73	BDL	2.45
25H-4, 108–109	231.98	253.99	84.6	3.21	BDL	2.29	BDL	2.40
28X-4, 36–37	256.06	276.65	89.9	2.80	BDL	1.42	BDL	2.33
30X-4, 72–73	276.02	305.30	83.6	3.98	BDL	1.92	BDL	2.39
32X-2, 90–91	292.6	321.87	87.8	3.80	BDL	2.12	0.074	1.91
34X-4, 71–72	314.51	344.25	79.0	3.79	BDL	1.11	BDL	2.25
36X-3, 72–73	332.22	362.16	85.2	3.97	BDL	2.78	BDL	1.85
37X-4, 81–82	343.31	373.85	60.1	5.88	BDL	2.40	BDL	2.68
38X-4, 29–30	351.89	382.99	82.6	3.57	BDL	3.26	BDL	2.32
40X-4, 128–129	372.58	405.31	79.2	4.01	BDL	2.36	BDL	2.18
44X-4, 114–115	410.54	445.67	90.4	3.67	BDL	1.51	BDL	2.37
48X-4, 109–110	448.79	493.78	76.9	6.91	BDL	0.00	BDL	1.78
321-U1338A-								
4H-5, 71–72	28.46		85.8	3.46	BDL	4.91	BDL	2.35
5H-1, 77–78	31.97		76.6	5.63	BDL	4.18	BDL	2.56
5H-3, 81–82	35.01		71.7	6.05	BDL	4.02	BDL	2.57
13H-6, 82–83	115.52		68.8	3.59	BDL	2.51	BDL	2.56
14H-7, 69–80	126.39		60.4	3.26	BDL	2.15	BDL	2.66
15H-5, 83–84	133.03		88.1	2.58	BDL	1.84	BDL	2.43
16H-1, 78–79	136.48		75.6	2.98	BDL	2.16	BDL	2.42
20H-1, 96–97	174.66		85.3	3.32	BDL	4.63	BDL	2.28
21H-1, 76–77	183.96		76.0	3.55	BDL	4.44	BDL	2.50
21H-7, 56–57	192.46		78.5	3.28	BDL	3.08	BDL	2.91
22H-6, 77–78	200.97		71.8	3.97	BDL	3.82	BDL	2.97
23H-5, 77–78	208.97		78.2	3.92	BDL	3.25	BDL	3.06
32X-2, 100–101	290.6		81.8	3.67	BDL	2.08	0.039	2.45
32X-6, 32–33	295.92		83.2	3.26	BDL	2.77	0.131	2.43
41X-4, 47–48	378.97		79.9	4.87	BDL	2.41	0.049	1.78
42X-2, 57–58	385.67		73.2	4.46	BDL	2.22	BDL	1.90

Notes: BDL = below detection limit (Si/Ca = 0.189 mM/M, Fe/Ca = 0.002 mM/M). See “Geochemistry” in the “Methods” chapter for uncertainty estimates and assessment of accuracy.

Table T19. Carbon concentrations, Site U1338. (See table notes.) (Continued on next two pages.)

Core, section, interval (cm)	Depth (m)		Carbon (wt%)				Core, section, interval (cm)	Depth (m)		Carbon (wt%)			
	CSF	CCSF-A	CaCO ₃	IC	TC	TOC		CSF	CCSF-A	CaCO ₃	IC	TC	TOC
321-U1338A-							10H-1, 82-83	79.52	89.75	66.2	7.9	ND	ND
1H-1, 20-21	0.20	0.24	78.6	9.4	9.64	0.20	10H-2, 82-83	81.02	91.25	67.3	8.1	ND	ND
1H-1, 40-41	0.40	0.44	82.4	9.9	10.22	0.31	10H-3, 82-83	82.52	92.75	77.8	9.3	ND	ND
1H-1, 60-61	0.60	0.64	84.8	10.2	10.39	0.26	10H-4, 82-83	84.02	94.25	72.7	8.7	8.76	0.22
1H-1, 64-65	0.64	0.68	82.7	9.9	10.25	0.40	10H-5, 80-81	85.50	95.73	69.6	8.4	ND	ND
1H-1, 80-81	0.80	0.84	85.4	10.2	10.47	0.26	10H-6, 62-63	86.82	97.05	35.7	4.3	ND	ND
1H-1, 100-101	1.00	1.04	83.1	10.0	10.20	0.28	10H-7, 47-48	88.17	98.40	67.3	8.1	ND	ND
1H-1, 120-121	1.20	1.24	67.2	8.1	8.28	0.26	11H-1, 82-83	89.02	100.05	58.1	7.0	ND	ND
1H-1, 140-141	1.40	1.44	59.8	7.2	7.50	0.46	11H-2, 82-83	90.52	101.55	71.7	8.6	ND	ND
1H-2, 10-11	1.60	1.64	59.7	7.2	7.31	0.20	11H-3, 82-83	92.02	103.05	67.7	8.1	ND	ND
1H-2, 50-51	2.00	2.04	69.3	8.3	8.45	0.15	11H-4, 82-83	93.52	104.55	65.5	7.9	8.04	0.18
1H-2, 68-69	2.18	2.22	76.0	9.1	9.31	0.24	11H-5, 82-83	95.02	106.05	78.8	9.5	ND	ND
1H-2, 90-91	2.40	2.44	75.8	9.1	9.15	0.31	11H-6, 82-83	96.39	107.42	68.4	8.2	ND	ND
2H-1, 81-82	3.51	4.99	64.3	7.7	ND	ND	12H-1, 82-83	98.52	110.87	76.9	9.2	ND	ND
2H-2, 82-83	5.02	6.50	86.7	10.4	ND	ND	12H-2, 82-83	100.02	112.37	83.4	10.0	ND	ND
2H-3, 82-83	6.52	8.00	88.0	10.6	ND	ND	12H-3, 82-83	101.52	113.87	77.5	9.3	ND	ND
2H-4, 82-83	8.02	9.50	81.1	9.7	9.81	0.11	12H-4, 82-83	103.02	115.37	73.0	8.8	8.88	0.22
2H-5, 82-83	9.52	11.00	84.2	10.1	ND	ND	12H-5, 77-78	104.47	116.82	77.2	9.3	ND	ND
2H-6, 80-81	11.00	12.48	62.7	7.5	ND	ND	12H-6, 82-83	106.02	118.37	84.2	10.1	ND	ND
2H-7, 32-33	12.02	13.50	67.0	8.0	ND	ND	12H-7, 52-53	107.22	119.57	67.7	8.1	ND	ND
3H-1, 104-105	13.24	15.47	47.8	5.7	ND	ND	13H-1, 83-84	108.03	121.75	74.2	8.9	ND	ND
3H-2, 78-79	14.48	16.71	77.1	9.3	ND	ND	13H-2, 83-84	109.53	123.25	62.7	7.5	ND	ND
3H-3, 74-75	15.94	18.17	60.0	7.2	ND	ND	13H-3, 83-84	111.03	124.75	75.0	9.0	ND	ND
3H-4, 77-78	17.47	19.70	59.7	7.2	7.34	0.14	13H-4, 82-83	112.52	126.24	73.5	8.8	9.06	0.21
3H-5, 71-72	18.91	21.14	63.4	7.6	ND	ND	13H-5, 83-84	114.03	127.75	57.3	6.9	ND	ND
3H-6, 82-83	20.52	22.75	55.0	6.6	ND	ND	13H-6, 82-83	115.52	129.24	68.8	8.3	ND	ND
3H-7, 39-40	21.59	23.82	51.5	6.2	ND	ND	13H-7, 32-33	116.52	130.24	60.5	7.3	ND	ND
4H-1, 72-73	22.42	26.04	66.5	8.0	ND	ND	14H-2, 71-72	118.91	132.84	43.5	5.2	ND	ND
4H-2, 76-77	23.96	27.58	58.4	7.0	ND	ND	14H-3, 101-102	120.71	134.64	57.4	6.9	ND	ND
4H-3, 77-78	25.47	29.09	75.0	9.0	ND	ND	14H-4, 78-79	121.98	135.91	58.3	7.0	7.14	0.24
4H-4, 66-67	26.86	30.48	66.2	7.9	8.01	0.14	14H-7, 69-80	126.39	140.32	60.4	7.3	ND	ND
4H-5, 76-77	28.46	32.08	85.8	10.3	ND	ND	15H-1, 74-75	126.94	141.94	36.9	4.4	ND	ND
4H-6, 71-72	29.91	33.53	76.6	9.2	ND	ND	15H-2, 78-79	128.48	143.48	72.9	8.8	ND	ND
4H-7, 54-55	31.24	34.86	63.6	7.6	ND	ND	15H-3, 81-83	130.01	145.01	69.2	8.3	ND	ND
5H-1, 77-78	31.97	37.67	76.6	9.2	ND	ND	15H-4, 83-84	131.53	146.53	85.7	10.3	10.33	0.13
5H-2, 77-78	33.47	39.17	67.5	8.1	ND	ND	15H-5, 83-84	133.03	148.03	88.1	10.6	ND	ND
5H-3, 81-82	35.01	40.71	71.7	8.6	ND	ND	15H-6, 67-68	134.37	149.37	74.0	8.9	ND	ND
5H-4, 77-78	36.47	42.17	47.1	5.7	5.86	0.25	15H-7, 26-27	135.06	150.06	76.0	9.1	ND	ND
5H-5, 77-78	37.97	43.67	53.0	6.4	ND	ND	16H-1, 78-79	136.48	152.54	75.6	9.1	ND	ND
5H-6, 83-84	39.53	45.23	58.7	7.0	ND	ND	16H-2, 77-78	137.97	154.03	66.9	8.0	ND	ND
5H-7, 34-35	40.54	46.24	75.8	9.1	ND	ND	16H-3, 83-84	139.53	155.59	70.4	8.5	ND	ND
6H-1, 78-79	41.48	47.04	65.3	7.8	ND	ND	16H-4, 77-78	140.97	157.03	65.6	7.9	8.05	0.20
6H-2, 78-79	42.98	48.54	34.1	4.1	ND	ND	16H-5, 81-82	142.51	158.57	70.3	8.4	ND	ND
6H-3, 92-93	44.62	50.18	44.7	5.4	ND	ND	16H-6, 77-78	143.97	160.03	62.9	7.6	ND	ND
6H-4, 78-79	45.98	51.54	65.6	7.9	8.02	0.25	16H-7, 59-60	145.29	161.35	72.6	8.7	ND	ND
6H-5, 91-92	47.61	53.17	32.9	3.9	ND	ND	17H-1, 128-129	146.48	164.56	49.8	6.0	ND	ND
6H-6, 106-107	49.26	54.82	39.2	4.7	ND	ND	17H-2, 127-128	147.97	166.05	78.5	9.4	ND	ND
6H-7, 41-42	50.11	55.67	30.2	3.6	ND	ND	17H-3, 126-127	149.46	167.54	53.2	6.4	ND	ND
7H-1, 126-127	51.46	57.67	72.0	8.6	ND	ND	17H-4, 126-127	150.96	169.04	69.5	8.3	8.43	0.14
7H-2, 81-82	52.51	58.72	65.6	7.9	ND	ND	17H-5, 123-124	152.43	170.51	85.9	10.3	ND	ND
7H-3, 91-92	54.11	60.32	38.2	4.6	ND	ND	17H-6, 104-105	153.74	171.82	79.7	9.6	ND	ND
7H-4, 107-108	55.77	61.98	82.2	9.9	9.92	0.11	17H-7, 40-41	154.60	172.68	80.7	9.7	ND	ND
7H-5, 76-77	56.96	63.17	53.2	6.4	ND	ND	18H-1, 117-118	155.87	175.15	51.5	6.2	ND	ND
7H-6, 85-86	58.55	64.76	66.7	8.0	ND	ND	18H-2, 116-117	157.36	176.64	66.7	8.0	ND	ND
7H-7, 43-44	59.63	65.84	56.9	6.8	ND	ND	18H-3, 111-112	158.81	178.09	59.0	7.1	ND	ND
8H-1, 81-82	60.51	68.59	67.6	8.1	ND	ND	18H-4, 85-86	160.05	179.33	50.6	6.1	6.31	0.25
8H-2, 87-88	62.07	70.15	65.9	7.9	ND	ND	18H-5, 112-113	161.82	181.10	84.1	10.1	ND	ND
8H-3, 76-77	63.46	71.54	74.5	8.9	ND	ND	18H-6, 111-112	163.31	182.59	68.0	8.2	ND	ND
8H-4, 87-88	65.07	73.15	77.8	9.3	9.37	0.19	18H-7, 48-49	164.18	183.46	73.4	8.8	ND	ND
8H-5, 82-83	66.52	74.60	72.2	8.7	ND	ND	19H-1, 97-98	165.17	185.37	75.7	9.1	ND	ND
8H-6, 104-105	68.24	76.32	80.5	9.7	ND	ND	19H-2, 97-98	166.67	186.87	77.4	9.3	ND	ND
9H-1, 76-77	69.96	79.41	74.6	9.0	ND	ND	19H-3, 97-98	168.17	188.37	80.9	9.7	ND	ND
9H-2, 76-77	71.46	80.91	74.2	8.9	ND	ND	19H-4, 97-98	169.67	189.87	78.1	9.4	9.50	0.09
9H-3, 71-72	72.91	82.36	70.3	8.4	ND	ND	19H-5, 92-93	171.12	191.32	78.4	9.4	ND	ND
9H-4, 77-78	74.47	83.92	70.2	8.4	8.42	0.12	19H-6, 97-98	172.67	192.87	79.3	9.5	ND	ND
9H-5, 76-77	75.96	85.41	65.0	7.8	ND	ND	19H-7, 52-53	173.62	193.82	67.7	8.1	ND	ND
9H-6, 77-78	77.47	86.92	52.8	6.3	ND	ND	20H-1, 96-97	174.66	195.45	85.3	10.2	ND	ND
9H-7, 17-18	78.37	87.82	50.6	6.1	ND	ND	20H-2, 86-87	176.06	196.85	85.7	10.3	ND	ND

Table T19 (continued). (Continued on next page.)

Core, section, interval (cm)	Depth (m)		Carbon (wt%)				Core, section, interval (cm)	Depth (m)		Carbon (wt%)			
	CSF	CCSF-A	CaCO ₃	IC	TC	TOC		CSF	CCSF-A	CaCO ₃	IC	TC	TOC
20H-3, 101–102	177.71	198.50	66.3	8.0	ND	ND	34X-1, 89–90	308.19	343.62	85.2	10.2	ND	ND
20H-4, 96–97	179.16	199.95	48.7	5.8	6.09	0.27	34X-2, 91–92	309.71	345.14	77.1	9.3	ND	ND
20H-5, 111–112	180.81	201.60	67.4	8.1	ND	ND	34X-3, 95–96	311.25	346.68	84.4	10.1	ND	ND
20H-6, 91–92	182.11	202.90	68.5	8.2	ND	ND	34X-4, 120–121	313.00	348.43	81.5	9.8	9.72	0.09
21H-1, 76–77	183.96	206.05	76.0	9.1	ND	ND	34X-5, 98–99	314.28	349.71	78.8	9.5	ND	ND
21H-2, 76–77	185.46	207.55	54.1	6.5	ND	ND	34X-6, 74–75	315.54	350.97	77.8	9.3	ND	ND
21H-3, 77–78	186.97	209.06	59.1	7.1	ND	ND	35X-1, 93–94	317.83	358.16	76.0	9.1	9.20	0.08
21H-4, 76–77	188.46	210.55	62.3	7.5	7.50	0.09	35X-2, 67–68	319.07	359.40	79.4	9.5	ND	ND
21H-5, 77–78	189.97	212.06	62.4	7.5	ND	ND	36X-1, 60–61	327.10	366.02	84.9	10.2	10.31	0.06
21H-6, 72–73	191.42	213.51	71.6	8.6	ND	ND	37X-1, 97–98	336.97	367.40	83.5	10.0	10.04	0.06
21H-7, 56–57	192.46	214.55	78.5	9.4	ND	ND	38X-1, 22–23	345.72	375.80	85.7	10.3	ND	ND
22H-1, 76–77	193.46	216.81	61.4	7.4	ND	ND	38X-2, 81–82	347.81	377.89	84.5	10.1	ND	ND
22H-2, 76–77	194.96	218.31	56.3	6.8	ND	ND	38X-3, 41–42	348.91	378.99	78.9	9.5	ND	ND
22H-3, 76–77	196.46	219.81	48.8	5.9	ND	ND	38X-4, 46–47	350.46	380.54	84.6	10.2	10.27	0.07
22H-4, 87–88	198.07	221.42	26.2	3.2	2.49	0.28	38X-5, 52–53	352.02	382.10	83.7	10.0	ND	ND
22H-5, 77–78	199.47	222.82	66.1	7.9	ND	ND	38X-6, 81–82	353.81	383.89	86.1	10.3	ND	ND
22H-6, 77–78	200.97	224.32	71.8	8.6	ND	ND	39X-1, 71–73	355.51	388.72	76.8	9.2	ND	ND
22H-7, 52–53	201.93	225.28	57.2	6.9	ND	ND	39X-2, 64–66	356.94	390.15	59.5	7.1	ND	ND
23H-1, 77–78	202.97	227.61	61.7	7.4	ND	ND	39X-3, 91–93	358.71	391.92	89.6	10.8	ND	ND
23H-2, 77–78	204.47	229.11	48.1	5.8	ND	ND	39X-4, 101–103	360.31	393.52	84.7	10.2	10.37	0.05
23H-3, 77–78	205.97	230.61	67.9	8.1	ND	ND	39X-5, 77–79	361.57	394.78	81.6	9.8	ND	ND
23H-4, 77–78	207.47	232.11	66.4	8.0	7.96	0.09	39X-6, 23–25	362.53	395.74	83.2	10.0	ND	ND
23H-5, 77–78	208.97	233.61	78.2	9.4	ND	ND	40X-1, 58–59	364.98	402.89	78.2	9.4	9.46	0.09
23H-6, 77–78	210.47	235.11	66.9	8.0	ND	ND	40X-2, 58–59	366.46	404.37	79.3	9.5	ND	ND
23H-7, 47–48	211.67	236.31	52.3	6.3	ND	ND	40X-3, 58–59	367.47	405.38	78.2	9.4	ND	ND
24H-1, 75–76	212.45	238.93	43.3	5.2	ND	ND	41X-1, 73–74	374.73	421.45	78.0	9.4	ND	ND
24H-2, 75–76	213.95	240.43	48.7	5.8	ND	ND	41X-2, 86–87	376.36	423.08	69.9	8.4	ND	ND
24H-3, 75–76	215.45	241.93	52.2	6.3	ND	ND	41X-3, 70–71	377.70	424.42	40.1	4.8	ND	ND
24H-4, 75–76	216.95	243.43	58.1	7.0	6.72	0.07	41X-4, 47–48	378.97	425.69	79.9	9.6	9.66	0.08
24H-5, 75–76	218.45	244.93	59.6	7.2	ND	ND	41X-5, 48–49	380.48	427.20	73.6	8.8	ND	ND
24H-6, 75–76	219.95	246.43	66.2	7.9	ND	ND	41X-6, 78–79	382.28	429.00	79.3	9.5	ND	ND
24H-7, 40–41	221.10	247.58	55.6	6.7	ND	ND	42X-1, 20–21	383.80	430.12	80.7	9.7	ND	ND
25H-1, 86–87	222.06	249.54	61.5	7.4	ND	ND	42X-2, 57–58	385.67	431.99	73.2	8.8	ND	ND
25H-2, 86–87	223.57	251.05	66.2	7.9	ND	ND	42X-3, 59–60	387.19	433.51	74.7	9.0	ND	ND
25H-3, 86–87	225.08	252.56	77.0	9.2	ND	ND	42X-4, 40–41	388.50	434.82	82.2	9.9	9.69	0.04
25H-4, 86–87	226.59	254.07	55.6	6.7	6.78	0.11	42X-5, 61–62	390.21	436.53	68.7	8.3	ND	ND
25H-5, 85–86	228.08	255.56	68.2	8.2	ND	ND	43X-1, 141–142	394.61	440.08	66.0	7.9	7.94	0.04
25H-6, 85–86	229.59	257.07	71.9	8.6	ND	ND	43X-2, 83–84	395.53	441.00	75.6	9.1	ND	ND
25H-7, 46–47	230.51	257.99	44.4	5.3	ND	ND	44X-1, 72–73	403.52	448.58	72.6	8.7	8.74	0.04
26H-1, 92–93	231.62	259.60	27.1	3.3	ND	ND	44X-2, 131–132	405.61	450.67	73.3	8.8	ND	ND
26H-2, 81–82	233.01	260.99	30.4	3.7	ND	ND	44X-3, 131–132	407.11	452.17	84.6	10.2	9.26	ND
26H-3, 82–83	234.52	262.50	63.0	7.6	ND	ND	321-U1338B-						
26H-4, 81–82	236.01	263.99	59.3	7.1	7.14	0.08	27H-1, 62–63	248.22	275.93	76.9	9.2	ND	0.12
26H-5, 82–83	237.52	265.50	71.4	8.6	ND	ND	27H-2, 66–67	249.76	277.47	80.3	9.6	ND	ND
26H-6, 81–82	239.01	266.99	78.3	9.4	ND	ND	27H-3, 36–37	250.96	278.67	85.3	10.2	ND	ND
26H-7, 40–41	240.10	268.08	71.1	8.5	ND	ND	28H-1, 81–82	257.91	285.56	79.6	9.6	ND	ND
27X-1, 90–91	241.10	268.88	76.2	9.1	ND	ND	28H-2, 83–84	259.43	287.08	73.2	8.8	ND	ND
27X-2, 90–91	242.60	270.38	62.0	7.4	ND	ND	28H-3, 83–84	260.93	288.58	79.5	9.5	ND	ND
27X-3, 83–84	244.03	271.81	72.6	8.7	ND	ND	28H-4, 81–82	262.41	290.06	80.0	9.6	9.49	0.08
27X-4, 83–84	245.53	273.31	86.6	10.4	10.45	0.08	28H-5, 78–79	263.88	291.53	76.9	9.2	ND	ND
27X-5, 75–76	246.95	274.73	87.0	10.4	ND	ND	28H-6, 61–62	265.21	292.86	80.1	9.6	ND	ND
29X-1, 49–50	259.89	289.20	74.8	9.0	ND	ND	28H-7, 53–54	266.43	294.08	80.9	9.7	ND	ND
29X-2, 63–64	261.53	290.84	78.8	9.5	ND	ND	29H-1, 86–87	267.46	295.66	57.5	6.9	ND	ND
29X-3, 68–69	263.08	292.39	71.5	8.6	ND	ND	29H-2, 70–71	268.80	297.00	63.6	7.6	ND	ND
29X-4, 68–69	264.58	293.89	82.6	9.9	9.86	0.09	29H-3, 79–80	270.39	298.59	75.3	9.0	ND	ND
29X-5, 71–72	266.11	295.42	70.6	8.5	ND	ND	29H-4, 80–81	271.90	300.10	76.3	9.2	9.05	0.13
29X-6, 80–81	267.70	297.01	71.2	8.5	ND	ND	29H-5, 80–81	273.40	301.60	79.2	9.5	ND	ND
32X-1, 100–101	289.10	321.42	87.1	10.5	ND	ND	29H-6, 76–77	274.86	303.06	74.0	8.9	ND	ND
32X-2, 100–101	290.60	322.92	81.8	9.8	ND	ND	29H-7, 56–57	276.06	304.26	79.2	9.5	ND	ND
32X-3, 105–106	292.15	324.47	77.8	9.3	ND	ND	30H-1, 75–76	276.85	305.63	76.2	9.2	ND	ND
32X-4, 98–99	293.58	325.90	91.0	10.9	10.97	0.09	30H-2, 71–72	278.31	307.09	77.7	9.3	ND	ND
32X-5, 100–101	295.10	327.42	90.7	10.9	ND	ND	33H-4, 65–66	297.55	327.95	30.5	3.7	4.06	0.50
32X-6, 32–33	295.92	328.24	83.2	10.0	ND	ND	34H-1, 86–87	302.76	334.19	76.3	9.2	ND	ND
33X-1, 99–100	298.69	332.01	79.3	9.5	ND	ND	34H-2, 86–87	304.27	335.70	77.5	9.3	ND	ND
33X-2, 105–106	300.25	333.57	84.5	10.1	ND	ND	34H-3, 86–87	305.78	337.21	84.1	10.1	ND	ND
33X-3, 101–102	301.71	335.03	83.4	10.0	ND	ND	34H-4, 86–87	307.30	338.73	83.9	10.1	9.98	0.06
33X-4, 103–104	303.23	336.55	85.7	10.3	10.27	0.09	34H-5, 87–88	308.79	340.22	86.3	10.4	ND	ND
33X-5, 106–107	304.76	338.08	79.3	9.5	ND	ND	34H-6, 86–87	310.32	341.75	75.8	9.1	ND	ND
33X-6, 76–77	305.96	339.28	88.1	10.6	ND	ND							

Table T19 (continued).

Core, section, interval (cm)	Depth (m)		Carbon (wt%)			
	CSF	CCSF-A	CaCO ₃	IC	TC	TOC
34H-7, 73–74	311.16	342.59	83.7	10.1	ND	ND
35H-1, 87–88	312.27	345.05	82.2	9.9	ND	ND
35H-2, 87–88	313.77	346.55	86.2	10.3	ND	ND
35H-3, 87–88	315.27	348.05	83.6	10.0	ND	ND
35H-4, 87–88	316.77	349.55	81.9	9.8	9.84	0.09
35H-5, 78–79	318.18	350.96	57.9	7.0	7.11	0.20
35H-5, 83–84	318.23	351.01	74.1	8.9	ND	ND
35H-6, 87–88	319.77	352.55	83.1	10.0	ND	ND
35H-7, 57–58	320.97	353.75	85.3	10.2	ND	ND
36H-1, 72–73	321.62	354.66	83.7	10.0	ND	ND
36H-2, 72–73	323.12	356.16	73.2	8.8	ND	ND
36H-3, 72–73	324.62	357.66	77.9	9.4	ND	ND
36H-4, 72–73	326.12	359.16	77.5	9.3	9.27	0.10
36H-5, 72–73	327.62	360.66	77.1	9.3	ND	ND
36H-6, 72–73	329.12	362.16	83.1	10.0	ND	ND
36H-7, 57–58	330.47	363.51	87.5	10.5	ND	ND
37H-1, 72–73	331.12	365.10	85.6	10.3	ND	ND
37H-2, 72–73	332.62	366.60	86.2	10.3	ND	ND
37H-3, 72–73	334.12	368.10	78.4	9.4	ND	ND
37H-4, 72–73	335.62	369.60	74.9	9.0	ND	ND
38H-6, 72–73	348.12	384.00	89.0	10.7	ND	ND
38H-7, 47–48	349.37	385.25	85.8	10.3	ND	ND
40H-1, 72–73	359.62	400.82	77.1	9.3	ND	ND
40H-2, 72–73	361.12	402.32	82.7	9.9	ND	ND
40H-3, 72–73	362.62	403.82	78.3	9.4	ND	ND
40H-4, 72–73	364.12	405.32	84.1	10.1	ND	ND
40H-5, 72–73	365.62	406.82	84.0	10.1	ND	ND
40H-6, 72–73	367.12	408.32	83.9	10.1	ND	ND
40H-7, 72–73	368.62	409.82	78.2	9.4	ND	ND
41H-1, 72–73	369.12	411.59	81.5	9.8	ND	ND
41H-2, 72–73	370.62	413.09	82.0	9.8	ND	ND
41H-3, 72–73	372.12	414.59	70.3	8.4	ND	ND
41H-4, 73–74	373.63	416.10	78.0	9.4	ND	ND
41H-5, 72–73	375.12	417.59	82.9	10.0	ND	ND
41H-6, 72–73	376.62	419.09	72.8	8.7	ND	ND
41H-7, 62–63	377.74	420.21	73.1	8.8	ND	ND

Notes: IC = inorganic carbon, TC = total carbon, TOC = total organic carbon determined by acidification method. ND = not determined. Bold = averaged values of replicated measurements.

Table T20. Moisture and density measurements, Site U1338. (Continued on next two pages.)

Core, section, interval (cm)	Depth CSF (m)	Water content (wt%)	Density (g/cm ³)				Porosity (%)	Core, section, interval (cm)	Depth CSF (m)	Water content (wt%)	Density (g/cm ³)				Porosity (%)
			Wet bulk	Dry bulk	Grain						Wet bulk	Dry bulk	Grain		
321-U1338A-							11H-3, 79-81	92.00	57.1	1.38	0.59	2.57	77.0		
1H-1, 66-68	0.67	54.9	1.41	0.64	2.64	75.8	11H-4, 79-81	93.50	57.5	1.37	0.58	2.53	77.0		
1H-2, 72-74	2.23	63.0	1.32	0.49	2.63	81.4	11H-5, 79-81	95.00	50.0	1.47	0.73	2.60	71.7		
2H-1, 78-80	3.49	66.3	1.29	0.43	2.58	83.2	11H-6, 79-81	96.37	56.2	1.39	0.61	2.59	76.4		
2H-2, 78-80	4.99	51.6	1.46	0.71	2.68	73.6	12H-1, 79-81	98.50	50.1	1.47	0.74	2.63	72.1		
2H-3, 78-80	6.49	51.9	1.46	0.70	2.67	73.8	12H-2, 79-81	100.00	45.5	1.54	0.84	2.65	68.4		
2H-4, 79-81	8.00	55.4	1.41	0.63	2.67	76.4	12H-3, 79-81	101.50	49.0	1.49	0.76	2.64	71.2		
2H-5, 79-81	9.50	53.1	1.44	0.68	2.69	74.9	12H-4, 79-81	103.00	51.1	1.46	0.71	2.62	72.7		
2H-6, 77-79	10.98	68.0	1.27	0.41	2.56	84.2	12H-5, 74-76	104.45	52.3	1.44	0.69	2.62	73.7		
2H-7, 29-31	12.00	67.3	1.28	0.42	2.65	84.2	12H-6, 79-81	106.00	46.0	1.54	0.83	2.68	69.1		
3H-1, 102-104	13.23	77.4	1.19	0.27	2.60	89.7	12H-7, 49-51	107.20	54.7	1.41	0.64	2.60	75.4		
3H-2, 75-77	14.46	59.0	1.37	0.56	2.65	78.8	13H-1, 79-81	108.00	52.2	1.44	0.69	2.60	73.5		
3H-3, 76-78	15.97	70.8	1.24	0.36	2.62	86.1	13H-2, 79-81	109.50	57.6	1.37	0.58	2.54	77.1		
3H-4, 79-81	17.50	70.2	1.25	0.37	2.61	85.7	13H-3, 79-81	111.00	53.4	1.43	0.67	2.62	74.5		
3H-5, 68-70	18.89	76.3	1.19	0.28	2.55	88.9	13H-4, 79-81	112.50	55.1	1.40	0.63	2.57	75.4		
3H-6, 79-81	20.50	72.1	1.23	0.34	2.53	86.5	13H-5, 80-82	114.01	57.8	1.37	0.58	2.53	77.2		
3H-7, 40-42	21.61	73.2	1.22	0.33	2.55	87.2	13H-6, 79-81	115.50	54.2	1.41	0.65	2.56	74.7		
4H-1, 71-73	22.42	68.4	1.27	0.40	2.62	84.7	13H-7, 29-31	116.50	57.9	1.36	0.57	2.49	77.0		
4H-2, 74-76	23.95	72.1	1.23	0.34	2.62	86.9	14H-2, 74-76	118.95	56.7	1.39	0.60	2.58	76.7		
4H-3, 74-76	25.45	61.5	1.34	0.52	2.63	80.4	14H-3, 98-100	120.69	57.5	1.37	0.58	2.54	77.0		
4H-4, 63-65	26.84	66.8	1.29	0.43	2.64	83.9	14H-4, 80-82	122.01	61.2	1.33	0.51	2.49	79.3		
4H-5, 74-76	28.45	53.8	1.43	0.66	2.67	75.2	14H-5, 80-82	123.51	56.0	1.39	0.61	2.57	76.2		
4H-6, 69-71	29.90	61.8	1.34	0.51	2.67	80.8	14H-7, 67-69	126.38	57.1	1.37	0.59	2.51	76.5		
4H-7, 52-54	31.23	70.1	1.25	0.38	2.66	85.9	15H-1, 70-72	126.91	66.5	1.27	0.42	2.39	82.2		
5H-1, 74-76	31.95	57.7	1.38	0.59	2.66	78.0	15H-2, 80-82	128.51	54.1	1.42	0.65	2.59	74.8		
5H-2, 74-76	33.45	64.5	1.31	0.47	2.67	82.6	15H-3, 80-82	130.01	54.3	1.41	0.64	2.58	75.0		
5H-3, 76-78	34.97	68.5	1.27	0.40	2.70	85.2	15H-4, 80-82	131.51	43.9	1.56	0.88	2.66	67.1		
5H-4, 74-76	36.45	73.8	1.22	0.32	2.60	87.7	15H-5, 80-82	133.01	41.6	1.60	0.93	2.66	64.9		
5H-5, 74-76	37.95	71.5	1.24	0.35	2.62	86.5	15H-6, 64-66	134.35	47.5	1.51	0.79	2.64	69.9		
5H-6, 80-82	39.51	68.1	1.27	0.41	2.61	84.5	15H-7, 23-25	135.04	49.4	1.48	0.75	2.61	71.3		
5H-7, 51-53	40.72	59.7	1.36	0.55	2.65	79.4	16H-1, 74-76	136.45	49.5	1.48	0.75	2.61	71.5		
6H-1, 74-76	41.45	65.0	1.30	0.45	2.60	82.5	16H-2, 74-76	137.95	54.0	1.41	0.65	2.55	74.5		
6H-2, 74-76	42.95	71.4	1.24	0.35	2.57	86.3	16H-3, 79-81	139.50	51.1	1.46	0.71	2.61	72.6		
6H-3, 94-96	44.65	67.7	1.27	0.41	2.62	84.3	16H-4, 74-76	140.95	55.5	1.40	0.62	2.56	75.8		
6H-4, 74-76	45.95	69.7	1.25	0.38	2.59	85.4	16H-5, 78-80	142.49	53.8	1.42	0.66	2.58	74.5		
6H-5, 94-96	47.65	73.7	1.21	0.32	2.50	87.2	16H-6, 74-76	143.95	56.9	1.37	0.59	2.47	76.1		
6H-6, 109-111	49.30	75.3	1.20	0.30	2.53	88.2	16H-7, 55-57	145.26	52.9	1.43	0.67	2.59	74.0		
6H-7, 44-46	50.15	76.5	1.19	0.28	2.52	88.9	17H-1, 122-124	146.43	61.3	1.33	0.51	2.50	79.5		
7H-1, 129-131	51.50	59.0	1.37	0.56	2.65	78.8	17H-2, 129-131	148.00	47.9	1.51	0.78	2.65	70.5		
7H-2, 84-86	52.55	63.5	1.32	0.48	2.60	81.6	17H-3, 122-124	149.43	52.8	1.43	0.68	2.60	74.0		
7H-3, 94-96	54.15	72.9	1.22	0.33	2.48	86.7	17H-4, 122-124	150.93	53.5	1.42	0.66	2.59	74.4		
7H-4, 109-111	55.80	51.3	1.46	0.71	2.66	73.2	17H-5, 119-121	152.40	43.1	1.57	0.89	2.64	66.2		
7H-5, 79-81	57.00	60.9	1.34	0.53	2.62	79.9	17H-6, 112-114	153.83	46.1	1.53	0.82	2.64	68.9		
7H-6, 89-91	58.60	60.4	1.34	0.53	2.57	79.2	17H-7, 44-46	154.65	47.3	1.51	0.79	2.63	69.8		
7H-7, 46-48	59.67	61.3	1.33	0.52	2.56	79.8	18H-1, 114-116	155.85	60.9	1.33	0.52	2.50	79.2		
8H-1, 79-81	60.50	57.3	1.38	0.59	2.60	77.3	18H-2, 114-116	157.35	53.8	1.42	0.66	2.61	74.8		
8H-2, 89-91	62.10	68.2	1.26	0.40	2.49	83.9	18H-3, 109-111	158.80	56.6	1.39	0.60	2.58	76.7		
8H-3, 74-76	63.45	56.5	1.39	0.61	2.62	76.8	18H-4, 86-88	160.07	61.4	1.32	0.51	2.46	79.2		
8H-4, 89-91	65.10	54.0	1.42	0.66	2.62	75.0	18H-5, 109-111	161.80	46.9	1.52	0.81	2.65	69.6		
8H-5, 79-81	66.50	56.7	1.39	0.60	2.59	76.8	18H-6, 109-111	163.30	53.6	1.42	0.66	2.57	74.3		
8H-6, 101-103	68.22	49.4	1.49	0.75	2.66	71.7	18H-7, 46-48	164.17	50.1	1.47	0.73	2.59	71.8		
8H-7, 46-48	69.17	51.0	1.47	0.72	2.66	73.0	19H-1, 99-101	165.20	50.3	1.47	0.73	2.63	72.2		
9H-1, 79-81	70.00	55.1	1.41	0.63	2.59	75.6	19H-2, 99-101	166.70	49.7	1.48	0.74	2.61	71.6		
9H-2, 78-80	71.49	55.8	1.40	0.62	2.60	76.3	19H-3, 99-101	168.20	46.3	1.52	0.82	2.63	68.9		
9H-3, 74-76	72.95	59.2	1.36	0.55	2.56	78.4	19H-4, 99-101	169.70	47.7	1.51	0.79	2.64	70.2		
9H-4, 79-81	74.50	58.4	1.37	0.57	2.57	77.9	19H-5, 94-96	171.15	49.5	1.48	0.75	2.65	71.7		
9H-5, 79-81	76.00	62.1	1.32	0.50	2.53	80.3	19H-6, 99-101	172.70	45.4	1.54	0.84	2.65	68.3		
9H-6, 80-82	77.51	64.1	1.30	0.47	2.49	81.3	19H-7, 54-56	173.65	49.5	1.49	0.75	2.66	71.8		
9H-7, 19-21	78.40	67.0	1.27	0.42	2.43	82.9	20H-1, 94-96	174.65	46.1	1.53	0.83	2.67	69.1		
10H-1, 79-81	79.50	60.2	1.35	0.54	2.57	79.2	20H-2, 84-86	176.05	45.5	1.54	0.84	2.67	68.5		
10H-2, 79-81	81.00	55.9	1.40	0.62	2.61	76.4	20H-3, 99-101	177.70	54.9	1.41	0.64	2.58	75.4		
10H-3, 79-81	82.50	53.5	1.42	0.66	2.57	74.3	20H-4, 94-96	179.15	61.3	1.32	0.51	2.48	79.3		
10H-4, 79-81	84.00	55.0	1.41	0.63	2.61	75.7	20H-5, 109-111	180.80	54.1	1.41	0.65	2.54	74.5		
10H-5, 77-79	85.48	56.6	1.39	0.60	2.60	76.8	20H-6, 89-91	182.10	51.4	1.46	0.71	2.63	73.1		
10H-6, 59-61	86.80	68.2	1.26	0.40	2.46	83.7	20H-7, 31-33	183.02	51.1	1.45	0.71	2.60	72.7		
10H-7, 44-46	88.15	58.5	1.36	0.57	2.57	78.0	21H-1, 79-81	184.00	51.9	1.45	0.70	2.61	73.3		
11H-1, 79-81	89.00	64.0	1.30	0.47	2.51	81.3	21H-2, 79-81	185.50	61.4	1.33	0.51	2.52	79.7		
11H-2, 79-81	90.50	56.7	1.39	0.60	2.60	76.9	21H-3, 79-81	187.00	58.5	1.36	0.57	2.53	77.7		

Table T20 (continued). (Continued on next page.)

Core, section, interval (cm)	Depth CSF (m)	Water content (wt%)	Density (g/cm ³)			Porosity (%)	Core, section, interval (cm)	Depth CSF (m)	Water content (wt%)	Density (g/cm ³)			Porosity (%)
			Wet bulk	Dry bulk	Grain					Wet bulk	Dry bulk	Grain	
21H-4, 79-81	188.50	56.4	1.39	0.61	2.61	76.8	35X-1, 94-96	317.85	44.7	1.55	0.86	2.65	67.6
21H-5, 79-81	190.00	55.5	1.40	0.62	2.56	75.8	35X-2, 68-70	319.09	44.8	1.54	0.85	2.61	67.4
21H-6, 69-71	191.40	51.7	1.45	0.70	2.63	73.3	36X-1, 60-62	327.11	39.6	1.63	0.99	2.68	63.1
21H-7, 54-56	192.45	48.4	1.50	0.77	2.65	70.8	37X-1, 95-97	336.96	39.5	1.64	0.99	2.68	63.1
22H-1, 79-81	193.50	56.1	1.39	0.61	2.56	76.1	38X-1, 19-21	345.70	38.8	1.64	1.00	2.64	62.1
22H-2, 79-81	195.00	58.2	1.36	0.57	2.53	77.5	38X-2, 78-80	347.79	37.6	1.67	1.04	2.68	61.2
22H-3, 79-81	196.50	61.2	1.33	0.52	2.56	79.8	38X-3, 40-42	348.91	41.7	1.60	0.93	2.67	65.1
22H-4, 89-91	198.10	68.4	1.24	0.39	2.33	83.2	38X-4, 45-47	350.46	37.5	1.67	1.04	2.68	61.1
22H-5, 79-81	199.50	54.9	1.41	0.64	2.60	75.6	38X-5, 50-52	352.01	36.3	1.69	1.08	2.67	59.8
22H-6, 79-81	201.00	52.7	1.44	0.68	2.64	74.1	38X-6, 81-83	353.82	36.8	1.68	1.06	2.68	60.4
22H-7, 54-56	201.96	55.5	1.41	0.63	2.63	76.2	39X-1, 73-75	355.54	40.8	1.60	0.95	2.61	63.7
23H-1, 79-81	203.00	58.1	1.37	0.57	2.56	77.6	39X-2, 67-69	356.98	45.4	1.52	0.83	2.57	67.6
23H-2, 79-81	204.50	62.2	1.32	0.50	2.53	80.3	39X-3, 90-92	358.71	36.0	1.71	1.09	2.73	59.9
23H-3, 79-81	206.00	54.5	1.41	0.64	2.60	75.3	39X-4, 102-104	360.33	37.0	1.67	1.05	2.67	60.5
23H-4, 79-81	207.50	56.9	1.38	0.60	2.58	76.9	39X-5, 75-77	361.56	37.8	1.66	1.03	2.68	61.4
23H-5, 79-81	209.00	48.4	1.50	0.77	2.64	70.7	39X-6, 23-25	362.54	35.6	1.70	1.09	2.67	59.0
23H-6, 79-81	210.50	54.6	1.41	0.64	2.57	75.1	40X-1, 33-35	364.74	41.8	1.57	0.92	2.56	64.3
23H-7, 44-46	211.65	58.7	1.35	0.56	2.46	77.3	40X-3, 57-59	367.47	40.1	1.62	0.97	2.67	63.5
24H-1, 79-81	212.50	62.0	1.31	0.50	2.38	79.1	41X-1, 76-78	374.77	46.0	1.51	0.82	2.55	68.0
24H-2, 79-81	214.00	61.3	1.32	0.51	2.46	79.1	41X-2, 91-93	376.42	40.6	1.61	0.95	2.62	63.6
24H-3, 79-81	215.50	54.4	1.41	0.64	2.55	74.8	41X-3, 77-79	377.78	52.5	1.42	0.68	2.49	72.9
24H-4, 79-81	217.00	58.6	1.36	0.56	2.53	77.8	41X-4, 38-40	378.89	38.9	1.64	1.00	2.66	62.3
24H-5, 79-81	218.50	57.5	1.37	0.58	2.53	77.0	41X-5, 42-44	380.43	39.6	1.63	0.98	2.65	63.0
24H-6, 79-81	220.00	53.2	1.42	0.66	2.55	73.9	41X-6, 72-74	382.23	37.5	1.66	1.04	2.65	60.9
24H-7, 34-36	221.05	60.5	1.34	0.53	2.51	78.9	42X-1, 19-21	383.80	37.2	1.68	1.06	2.71	61.0
25H-1, 88-90	222.09	55.3	1.41	0.63	2.66	76.3	42X-2, 57-59	385.68	38.4	1.64	1.01	2.60	61.3
25H-2, 89-91	223.61	52.6	1.44	0.68	2.65	74.2	42X-3, 59-61	387.20	39.5	1.63	0.98	2.65	62.9
25H-3, 89-91	225.12	49.4	1.48	0.75	2.59	71.2	42X-4, 40-42	388.51	37.2	1.67	1.05	2.66	60.7
25H-4, 89-91	226.63	55.5	1.40	0.62	2.55	75.7	42X-5, 61-63	390.22	40.6	1.60	0.95	2.61	63.5
25H-5, 89-91	228.13	49.4	1.47	0.74	2.57	71.0	43X-1, 140-142	394.61	36.9	1.66	1.05	2.61	59.8
25H-6, 89-91	229.64	50.8	1.45	0.71	2.55	72.0	43X-2, 83-85	395.54	32.8	1.74	1.17	2.64	55.8
25H-7, 49-51	230.55	60.2	1.33	0.53	2.46	78.4	44X-1, 72-74	403.53	33.7	1.72	1.14	2.64	56.7
26H-1, 89-91	231.60	64.9	1.28	0.45	2.36	81.0	44X-2, 129-131	405.60	33.7	1.71	1.13	2.60	56.3
26H-2, 79-81	233.00	66.5	1.26	0.42	2.29	81.6	44X-3, 129-131	407.10	26.8	1.89	1.39	2.75	49.6
26H-3, 79-81	234.50	54.1	1.41	0.65	2.55	74.6							
26H-4, 79-81	236.00	55.2	1.40	0.63	2.55	75.4	321-U1338B-						
26H-5, 78-80	237.49	49.4	1.47	0.74	2.56	71.0	27H-1, 64-66	248.25	47.3	1.51	0.79	2.62	69.7
26H-6, 79-81	239.00	47.2	1.51	0.80	2.63	69.7	27H-2, 69-71	249.80	46.4	1.53	0.82	2.64	69.1
26H-7, 36-38	240.07	47.8	1.51	0.79	2.64	70.2	27H-3, 39-41	251.00	42.7	1.59	0.91	2.68	66.1
27X-1, 86-88	241.07	51.5	1.45	0.70	2.61	73.0	28H-1, 78-80	257.89	44.6	1.55	0.86	2.64	67.4
27X-2, 86-88	242.57	58.7	1.35	0.56	2.50	77.6	28H-2, 78-80	259.39	46.1	1.52	0.82	2.60	68.5
27X-3, 78-80	243.99	54.0	1.42	0.65	2.60	74.9	28H-3, 79-81	260.90	43.5	1.57	0.89	2.65	66.5
27X-4, 79-81	245.50	43.6	1.57	0.89	2.69	67.1	28H-4, 78-80	262.39	43.1	1.57	0.89	2.61	65.9
27X-5, 70-72	246.91	43.0	1.58	0.90	2.69	66.4	28H-5, 75-77	263.86	39.9	1.62	0.97	2.62	62.9
29X-1, 46-48	259.87	48.1	1.49	0.78	2.60	70.2	28H-6, 57-59	265.18	42.7	1.58	0.90	2.64	65.8
29X-2, 61-63	261.52	47.6	1.50	0.78	2.58	69.6	28H-7, 50-52	266.41	43.4	1.57	0.89	2.65	66.5
29X-3, 66-68	263.07	52.5	1.44	0.68	2.58	73.6	29H-1, 81-83	267.42	54.2	1.40	0.64	2.50	74.2
29X-4, 66-68	264.57	44.8	1.55	0.86	2.65	67.7	29H-2, 66-68	268.77	50.9	1.45	0.71	2.57	72.2
29X-5, 68-70	266.09	50.0	1.47	0.74	2.62	71.9	29H-3, 75-77	270.36	47.2	1.50	0.79	2.59	69.3
29X-6, 78-80	267.69	50.4	1.46	0.73	2.59	72.0	29H-4, 76-78	271.87	44.8	1.54	0.85	2.58	67.2
32X-1, 98-100	289.09	41.5	1.61	0.94	2.70	65.1	29H-5, 83-85	273.44	46.4	1.52	0.82	2.63	69.0
32X-2, 97-99	290.58	43.6	1.56	0.88	2.62	66.4	29H-6, 79-81	274.90	44.0	1.55	0.87	2.61	66.7
32X-3, 103-105	292.14	46.3	1.52	0.82	2.62	68.8	29H-7, 52-54	276.03	44.2	1.54	0.86	2.57	66.5
32X-4, 99-101	293.60	37.6	1.66	1.04	2.67	61.1	30H-1, 78-80	276.89	48.1	1.49	0.78	2.60	70.2
32X-5, 98-100	295.09	37.6	1.66	1.04	2.66	61.0	30H-2, 73-75	278.34	43.7	1.56	0.88	2.61	66.5
32X-6, 29-31	295.90	40.2	1.62	0.97	2.67	63.7	31H-1, 33-35	282.44	33.3	1.62	1.08	2.28	52.6
33X-1, 96-98	298.67	43.8	1.56	0.88	2.65	66.9	34H-1, 88-90	302.79	44.0	1.55	0.87	2.62	66.7
33X-2, 103-105	300.24	43.5	1.57	0.89	2.65	66.5	34H-2, 88-90	304.30	41.7	1.60	0.93	2.67	65.0
33X-3, 99-101	301.70	43.5	1.57	0.89	2.66	66.6	34H-3, 88-90	305.80	40.3	1.62	0.97	2.67	63.7
33X-4, 101-103	303.22	39.2	1.65	1.00	2.71	63.0	34H-4, 88-90	307.31	40.7	1.62	0.96	2.68	64.3
33X-5, 104-106	304.75	43.3	1.57	0.89	2.64	66.3	34H-5, 84-86	308.77	37.8	1.66	1.03	2.66	61.2
33X-6, 73-75	305.94	38.4	1.65	1.02	2.69	62.1	34H-6, 88-90	310.32	42.8	1.58	0.90	2.64	65.8
34X-1, 89-91	308.20	40.2	1.61	0.96	2.64	63.4	34H-7, 69-71	311.13	39.4	1.63	0.99	2.66	62.8
34X-2, 89-91	309.70	42.1	1.57	0.91	2.58	64.7	35H-1, 89-91	312.30	42.3	1.58	0.91	2.64	65.4
34X-3, 92-94	311.23	39.7	1.63	0.98	2.67	63.2	35H-2, 79-81	313.70	39.9	1.63	0.98	2.67	63.4
34X-4, 118-120	312.99	43.5	1.57	0.88	2.64	66.5	35H-3, 89-91	315.30	41.3	1.60	0.94	2.64	64.5
34X-5, 96-98	314.27	41.0	1.60	0.94	2.63	64.0	35H-4, 89-91	316.80	39.7	1.63	0.98	2.67	63.2
34X-6, 76-78	315.57	43.2	1.57	0.89	2.63	66.1	35H-5, 85-87	318.26	43.6	1.56	0.88	2.61	66.3
							35H-6, 89-91	319.80	39.7	1.62	0.98	2.64	63.0

Table T20 (continued).

Core, section, interval (cm)	Depth CSF (m)	Water content (wt%)	Density (g/cm ³)			Porosity (%)
			Wet bulk	Dry bulk	Grain	
35H-7, 59-61	321.00	39.0	1.64	1.00	2.67	62.5
36H-1, 74-76	321.65	40.7	1.61	0.95	2.65	64.0
36H-2, 74-76	323.15	43.9	1.56	0.87	2.62	66.7
36H-3, 74-76	324.65	40.4	1.61	0.96	2.65	63.7
36H-4, 74-76	326.15	42.3	1.59	0.92	2.66	65.5
36H-5, 74-76	327.65	36.7	1.68	1.06	2.67	60.2
36H-6, 74-76	329.15	38.4	1.66	1.02	2.71	62.2
36H-7, 59-61	330.50	37.4	1.67	1.05	2.69	61.0
37H-1, 74-76	331.15	38.9	1.64	1.00	2.66	62.3
37H-2, 74-76	332.65	38.3	1.66	1.03	2.72	62.2
37H-3, 74-76	334.15	41.1	1.61	0.95	2.67	64.5
37H-4, 74-76	335.65	45.8	1.53	0.83	2.61	68.3
38H-6, 74-76	348.15	34.9	1.72	1.12	2.72	58.7
38H-7, 49-51	349.40	35.4	1.71	1.10	2.70	59.1
40H-1, 74-76	359.65	40.6	1.61	0.96	2.66	64.0
40H-2, 74-76	361.15	36.8	1.67	1.05	2.63	59.9
40H-3, 74-76	362.65	38.3	1.65	1.02	2.65	61.6
40H-4, 74-76	364.15	34.0	1.73	1.14	2.68	57.4
40H-5, 74-76	365.65	36.3	1.68	1.07	2.65	59.6
40H-6, 74-76	367.15	36.1	1.69	1.08	2.69	59.8
40H-7, 54-56	368.45	39.6	1.62	0.98	2.62	62.7
41H-1, 74-76	369.15	36.5	1.68	1.06	2.65	59.9
41H-2, 74-76	370.65	35.5	1.69	1.09	2.63	58.5
41H-3, 74-76	372.15	40.0	1.61	0.96	2.60	62.9
41H-4, 75-77	373.66	40.1	1.61	0.97	2.63	63.2
41H-5, 74-76	375.15	38.2	1.65	1.02	2.66	61.6
41H-6, 74-76	376.65	39.7	1.61	0.97	2.60	62.5
41H-7, 64-66	377.77	39.8	1.62	0.97	2.62	62.8

Table T21. Split-core *P*-wave velocity measurements, Site U1338. (Continued on next page.)

Core, section	Depth CSF (m)	Velocity (m/s)			Core, section	Depth CSF (m)	Velocity (m/s)			Core, section	Depth CSF (m)	Velocity (m/s)		
		x-axis	y-axis	z-axis			x-axis	y-axis	z-axis			x-axis	y-axis	z-axis
321-U1338A-														
1H-1	0.67	1514			7H-7	59.68	1521			13H-2	109.60		1507	
1H-1	0.76			1505	7H-7	59.76			1462	13H-3	111.01	1528		
1H-2	2.23	1521			8H-1	60.50	1527			13H-3	111.10		1516 1506	
1H-2	2.32		1497	1499	8H-2	62.10	1502			13H-4	112.61	1552		
2H-1	3.49	1501			8H-2	62.18		1530		13H-4	112.70		1416	
2H-1	3.60		1425	1432	8H-3	63.45	1481			13H-5	114.02	1540		
2H-2	5.00	1514			8H-3	63.56		1506	1454	13H-5	114.10		1518	
2H-2	5.10		1507	1501	8H-4	65.10	1509			13H-6	115.50	1521		
2H-3	6.50	1534			8H-4	65.21		1506		13H-6	115.60		1514 1460	
2H-3	6.60		1500	1501	8H-5	66.51	1509			13H-7	116.50	1519		
2H-4	8.00	1510			8H-5	66.60		1505		13H-7	116.63		1401 1506	
2H-4	8.09		1507	1493	8H-6	68.23	1503			14H-1	117.48	1600		
2H-5	9.50	1516			8H-6	68.32		1494	1504	14H-1	117.60		1527 1522	
2H-5	9.60			1493	8H-7	69.18	1521			14H-2	118.96	1547		
2H-6	10.97	1520			8H-7	69.26		1497	1456	14H-2	119.04			
2H-6	11.10		1514	1466	9H-1	70.01	1513			14H-3	120.62		1510 1464	
2H-7	12.00	1524			9H-1	70.10			1500	14H-3	120.70	1540		
2H-7	12.09		1519	1404	9H-2	71.49	1516			14H-4	122.01	1520		
3H-1	13.15		1520	1460	9H-2	71.60		1524		14H-4	122.10		1421 1516	
3H-1	13.28	1594			9H-4	74.50	1500			14H-5	123.52	1532		
3H-2	14.46	1524			9H-4	74.60			1410	14H-5	123.60		1419	
3H-2	14.57		1510	1497	9H-5	76.02	1527			14H-7	126.20	1549		
3H-3	15.87	1534			9H-5	76.10		1518	1461	14H-7	126.30		1480	
3H-3	15.97	1553			9H-6	77.51	1525			15H-2	128.51	1545		
3H-3	16.07		1518	1511	9H-6	77.60		1519	1508	15H-1	128.55	1567		
3H-4	17.51	1519			9H-7	78.41	1512			15H-2	128.60		1503 1500	
3H-4	17.60		1500	1494	9H-7	78.49		1509		15H-3	130.00	1540		
3H-5	18.89	1525			10H-1	79.52	1518			15H-3	130.10		1507 1508	
3H-5	19.00		1519		10H-2	81.01	1511			15H-4	131.51	1519		
3H-6	20.50	1517			10H-2	81.10			1460	15H-4	131.60		1503 1498	
3H-6	20.60		1516	1502	10H-3	82.51	1513			15H-5	133.01	1534		
3H-7	21.62	1535			10H-3	82.60		1502	1496	15H-5	133.11		1509 1502	
4H-1	22.52		1390	1445	10H-4	84.00	1515			15H-6	134.27		1507 1500	
4H-2	24.00	1529			10H-4	84.10		1503	1498	15H-6	134.35	1525		
4H-2	24.10		1419		10H-5	85.47	1507			15H-7	135.04	1538		
4H-3	25.50	1534			10H-5	85.61		1500	1499	15H-7	135.12		1521 1502	
4H-3	25.60		1514	1412	10H-6	86.81	1515			16H-1	136.48	1514		
4H-4	26.84	1528			10H-6	86.90		1521	1508	16H-1	136.60		1457	
4H-5	28.50	1512			10H-7	88.17	1535			16H-2	138.00	1539		
4H-6	29.90	1501			10H-7	88.27		1508	1505	16H-2	138.10		1458	
4H-6	29.99		1533	1453	11H-1	89.00	1498			16H-3	139.51	1543		
4H-7	31.24	1538			11H-1	89.10		1510		16H-3	139.64		1460	
4H-7	31.36		1508		11H-2	90.52	1506			16H-4	141.00	1529		
5H-4	36.52	1556			11H-2	90.60		1504	1496	16H-5	142.50	1536		
5H-4	36.62		1443		11H-3	92.01	1509			16H-5	142.60		1509	
5H-5	38.00	1526			11H-3	92.10		1504	1453	16H-6	144.00	1533		
5H-5	38.10			1475	11H-4	93.51	1517			16H-7	145.26	1534		
5H-6	39.59	1504			11H-4	93.60		1501	1505	16H-7	145.38		1457	
5H-6	39.68		1515		11H-5	95.00	1530			17H-1	146.44	1557		
5H-7	40.87		1518		11H-5	95.10		1508	1496	17H-2	148.01	1525		
6H-1	41.50	1529			11H-6	96.47		1515		17H-3	149.45	1514		
6H-1	41.60		1504	1495	12H-1	98.50	1519			17H-4	150.95	1517		
6H-2	43.10		1529		12H-1	98.60		1508		17H-5	152.41	1537		
6H-3	44.75		1428		12H-2	100.02	1520			17H-5	152.50		1453	
6H-4	46.01	1507			12H-2	100.10		1505	1503	17H-6	153.84	1539		
6H-4	46.10		1420		12H-3	101.52	1524			17H-6	153.92		1465	
6H-5	47.65	1518			12H-3	101.60		1507	1501	17H-7	154.65	1532		
6H-5	47.76			1471	12H-4	103.02	1507			18H-1	155.89	1513		
6H-6	49.31	1534			12H-4	103.11		1506	1504	18H-2	157.39	1488		
6H-6	49.40		1401		12H-5	104.48	1508			18H-2	157.47		1507	
7H-2	52.65		1520		12H-5	104.56		1503	1500	18H-3	158.79	1511		
7H-4	55.81	1486			12H-6	106.01	1507			18H-4	160.07	1517		
7H-4	55.90		1496	1444	12H-6	106.10		1507	1503	18H-5	161.81	1518		
7H-5	57.02	1487			12H-7	107.11		1503	1457	18H-5	161.90		1458	
7H-5	57.11		1510	1503	12H-7	107.19	1545			18H-6	163.32	1520		
7H-6	58.60	1497			13H-1	108.01	1531			18H-7	164.17	1519		
7H-6	58.70			1506	13H-1	108.10		1507	1502	19H-1	165.22	1541		
					13H-2	109.51	1524			19H-2	166.67	1555		

Table T21 (continued).

Core, section	Depth CSF (m)	Velocity (m/s)			Core, section	Depth CSF (m)	Velocity (m/s)			Core, section	Depth CSF (m)	Velocity (m/s)		
		x-axis	y-axis	z-axis			x-axis	y-axis	z-axis			x-axis	y-axis	z-axis
19H-3	168.22	1530			27X-3	243.99	1561			27H-3	251.00	1535		
19H-4	169.72	1520			27X-4	245.51	1508			28H-1	257.90	1496		
19H-4	169.82		1525		27X-5	246.92	1525			28H-2	259.40	1518		
19H-5	171.17	1519			29X-1	259.88	1511			28H-3	260.90	1525		
19H-6	172.71	1530			29X-2	261.53	1516			28H-4	262.40	1503		
19H-6	172.84			1458	29X-3	263.07	1589			28H-5	263.86	1502		
19H-7	173.65	1519			29X-4	264.57	1509			28H-6	265.19	1489		
20H-1	174.66	1522			29X-5	266.10	1517			28H-7	266.42	1527		
20H-2	176.05	1521			29X-6	267.69	1520			29H-1	267.43	1537		
20H-3	177.71	1527			32X-1	289.10	1536			29H-2	268.77	1523		
20H-4	179.18	1539			32X-2	290.58	1527			29H-3	270.36	1506		
20H-4	179.28		1542	1519	32X-3	292.14	1533			29H-4	271.88	1498		
20H-5	180.82	1506			32X-4	293.60	1530			29H-5	273.46	1515		
20H-5	180.94			1465	32X-5	295.10	1555			29H-6	274.92	1510		
20H-6	182.10	1507			32X-6	295.91	1560			29H-7	276.03	1512		
20H-6	182.21			1513	33X-1	298.67	1540			30H-1	276.90	1515		
20H-7	183.02	1511			33X-2	300.24	1523			30H-2	278.35	1528		
20H-7	183.10			1508	33X-3	301.70	1540			30H-3	279.97	1533		
21H-1	184.01	1518			33X-4	303.20	1560			30H-4	281.36	1524		
21H-2	185.52	1499			33X-5	304.76	1533			34H-1	302.80	1533		
21H-2	185.60			1459	33X-6	305.95	1586			34H-2	304.31	1523		
21H-3	187.02	1504			34X-1	308.15	1510			34H-3	305.81	1532		
21H-4	188.51	1486			34X-1	308.19	1542			34H-4	307.32	1529		
21H-4	188.60		1544	1515	34X-2	309.71	1563			34H-5	308.77	1527		
21H-5	190.00	1485			34X-3	311.23	1562			34H-6	310.33	1523		
21H-6	191.38	1510			34X-4	312.99	1537			34H-7	311.13	1537		
21H-7	192.44	1483			34X-5	314.27	1535			35H-1	312.30	1509		
22H-1	193.55	1466			34X-6	315.56	1547			35H-2	313.70	1537		
22H-2	194.99	1474			35X-1	317.84	1544			35H-3	315.26	1535		
22H-3	196.48	1466			35X-2	319.08	1537			35H-4	316.80	1509		
22H-4	198.11	1493			36X-1	327.11	1531			35H-5	318.26	1521		
22H-5	199.50	1478			37X-1	336.96	1600			35H-6	319.80	1495		
22H-6	201.00	1484			38X-1	345.66	1591			35H-7	321.00	1547		
22H-7	201.94	1492			38X-2	347.76	1576			36H-1	321.65	1517		
23H-1	203.01	1486			38X-3	348.90	1564			36H-2	323.15	1510		
23H-2	204.50	1471			38X-4	350.47	1552			36H-3	324.65	1528		
23H-3	206.00	1494			38X-5	352.02	1578			36H-4	326.15	1518		
23H-4	207.50	1470			38X-6	353.83	1654			36H-5	327.65	1524		
23H-5	209.00	1467			39X-1	355.55	1560			36H-6	329.15	1526		
23H-6	210.50	1479			39X-2	356.98	1642			36H-7	330.49	1531		
23H-7	211.65	1526			39X-3	358.73	1695			37H-1	331.13	1523		
24H-1	212.54	1490			39X-4	360.35	1695			37H-2	332.65	1498		
24H-2	214.00	1498			39X-6	362.56	1646			37H-3	334.23	1497		
24H-3	215.48	1531			40X-1	364.74	1596			37H-4	335.65	1550		
24H-4	217.03	1465			40X-3	367.46	1665			38H-6	348.15	1511		
24H-5	218.52	1454			41X-1	374.77	1649			38H-7	349.40	1528		
24H-6	220.03	1471			41X-2	376.43	1625			40H-1	359.65	1524		
24H-7	221.03	1489			41X-3	377.80	1611			40H-2	361.15	1530		
25H-1	222.10	1470			41X-4	378.91	1621			40H-3	362.65	1542		
25H-2	223.61	1477			41X-5	380.47	1630			40H-4	364.15	1535		
25H-3	225.12	1471			41X-6	382.21	1678			40H-5	365.65	1523		
25H-4	226.63	1486			42X-1	383.82	1642			40H-6	367.15	1532		
25H-5	228.13	1486			42X-2	385.69	1642			40H-7	368.45	1514		
25H-6	229.52	1485			42X-3	387.21	1748			41H-1	369.15	1519		
25H-7	230.55	1493			42X-4	388.54	1711			41H-2	370.65	1527		
26H-1	231.60	1471			42X-5	390.26	1614			41H-3	372.15	1512		
26H-2	233.00	1476			43X-1	394.31	1691			41H-3	372.02	1512		
26H-3	234.50	1465			43X-2	395.58	1725			41H-4	373.65	1505		
26H-4	236.00	1478			44X-1	403.56	1778			41H-4	373.81	1563		
26H-5	237.50	1480			44X-2	405.61	1809			41H-5	375.15	1505		
26H-6	239.00	1495			44X-3	407.17	1817			41H-5	375.15	1533		
26H-7	240.08	1498								41H-6	376.40	1537		
27X-1	241.07	1515			321-U1338B-					41H-7	377.55	1547		
27X-2	242.53	1577			27H-1	248.26	1524							
					27H-2	249.81	1544							

Table T22. Thermal conductivity, Hole U1338A.

Core, section, interval (cm)	Depth CSF (m)	Thermal conductivity (W/[m·K])
321-U1338A-		
1H-2, 75	2.25	0.921
2H-3, 75	6.45	1.066
3H-3, 75	15.95	0.836
4H-3, 75	25.45	0.929
5H-3, 75	34.95	0.830
6H-3, 75	44.45	0.775
7H-3, 75	53.95	0.822
8H-3, 75	63.45	0.977
9H-3, 75	72.95	0.949
10H-3, 75	82.45	0.938
11H-3, 75	91.95	0.950
12H-3, 80	101.50	1.106
13H-3, 75	110.95	0.930
14H-3, 75	120.45	0.807
15H-3, 75	129.95	0.985
16H-3, 75	139.45	1.082
17H-3, 75	148.95	1.009
18H-3, 75	158.45	1.018
19H-3, 75	167.95	1.147
20H-3, 75	177.45	0.988
21H-3, 75	186.95	0.931
22H-3, 75	196.45	0.933
23H-3, 75	205.95	0.932
24H-3, 75	215.45	0.912
25H-3, 75	224.97	1.053
26H-3, 75	234.45	0.971
27X-3, 75	243.95	1.007
29X-3, 75	263.15	1.004
32X-3, 75	291.85	1.044
33X-3, 75	301.45	1.112
34X-3, 75	311.05	1.222
35X-2, 75	319.15	1.076
36X-1, 63	327.13	1.105
38X-3, 70	349.20	1.182
39X-3, 65	358.45	1.125
40X-1, 63	365.03	1.262
41X-3, 80	377.80	1.122
42X-3, 80	387.40	1.074
43X-2, 70	395.40	1.203
44X-2, 80	405.10	1.240

Table T23. Shipboard composite and corrected composite depths, Site U1338.

Core	Depth CSF (m)	Offset (m)	Top depth (m)		Core	Depth CSF (m)	Offset (m)	Top depth (m)		Core	Depth CSF (m)	Offset (m)	Top depth (m)	
			CCSF-A	CCSF-B				CCSF-A	CCSF-B				CCSF-A	CCSF-B
321-U1338A-					2H	7.6	1.290	8.89	8.03	2H	3.8	0.546	4.35	3.93
1H	0	0.04	0.04	0.04	3H	17.1	2.068	19.17	17.32	3H	13.3	2.308	15.61	14.10
2H	2.7	1.48	4.18	3.78	4H	26.6	2.665	29.26	26.44	4H	22.8	2.859	25.66	23.18
3H	12.2	2.23	14.43	13.04	5H	36.1	4.296	40.40	36.49	5H	32.3	5.260	37.56	33.93
4H	21.7	3.62	25.32	22.87	6H	45.6	5.145	50.74	45.84	6H	41.8	7.661	49.46	44.68
5H	31.2	5.70	36.90	33.33	7H	55.1	5.862	60.96	55.07	7H	51.3	6.802	58.10	52.49
6H	40.7	5.56	46.26	41.79	8H	64.6	6.582	71.18	64.30	8H	60.8	8.979	69.78	63.03
7H	50.2	6.21	56.41	50.96	9H	74.1	8.029	82.13	74.19	9H	70.3	9.365	79.67	71.97
8H	59.7	8.08	67.78	61.23	10H	83.6	9.000	92.60	83.65	10H	79.8	10.270	90.07	81.36
9H	69.2	9.45	78.65	71.04	11H	93.1	9.874	102.97	93.02	11H	89.3	9.998	99.30	89.70
10H	78.7	10.23	88.93	80.33	12H	102.6	11.045	113.64	102.66	12H	98.8	10.687	109.49	98.90
11H	88.2	11.03	99.23	89.64	13H	112.1	12.421	124.52	112.49	13H	108.3	11.399	119.70	108.13
12H	97.7	12.35	110.05	99.41	14H	121.6	13.054	134.65	121.64	14H	117.8	12.728	130.53	117.91
13H	107.2	13.72	120.92	109.23	15H	131.1	14.347	145.45	131.39	15H	127.3	13.733	141.03	127.40
14H	116.7	13.93	130.63	118.00	16H	140.6	16.079	156.68	141.54	16H	136.8	15.989	152.79	138.02
15H	126.2	15.00	141.20	127.56	17H	150.1	17.187	167.29	151.12	17H	146.3	17.081	163.38	147.59
16H	135.7	16.06	151.76	137.09	18H	159.6	17.959	177.56	160.40	18H	155.8	16.206	172.01	155.38
17H	145.2	18.08	163.28	147.50	19H	169.1	18.148	187.25	169.15	19H	161.3	19.000	180.30	162.87
18H	154.7	19.28	173.98	157.17	20H	178.6	19.625	198.23	179.07	20H	170.8	19.675	190.47	172.06
19H	164.2	20.20	184.40	166.57	21H	188.1	20.251	208.35	188.21	21H	180.3	21.308	201.61	182.12
20H	173.7	20.79	194.49	175.69	22H	197.6	21.070	218.67	197.53	22H	189.8	21.735	211.53	191.09
21H	183.2	22.09	205.29	185.44	23H	207.1	23.041	230.14	207.90	23H	199.3	21.830	221.13	199.76
22H	192.7	23.35	216.05	195.17	24H	216.6	24.664	241.26	217.94	24H	208.8	23.301	232.10	209.67
23H	202.2	24.64	226.84	204.91	25H	226.1	26.114	252.21	227.84	25H	218.3	24.725	243.03	219.54
24H	211.7	26.48	238.18	215.16	26H	238.1	26.933	265.03	239.42	26H	227.8	25.939	253.74	229.21
25H	221.2	27.48	248.68	224.64	27H	247.6	27.706	275.31	248.70	27H	237.3	26.811	264.11	238.58
26H	230.7	27.98	258.68	233.68	28H	257.1	27.647	284.75	257.22	28H	246.8	26.811	273.61	247.16
27X	240.2	27.78	267.98	242.08	29H	266.6	28.200	294.80	266.31	29H	256.3	26.811	283.11	255.75
28X	249.8	27.78	277.58	250.75	30H	276.1	28.783	304.88	275.41	30H	265.8	28.135	293.94	265.52
29X	259.4	29.31	288.71	260.80	31H	282.1	28.783	310.88	280.83	31H	275.3	28.923	304.22	274.82
30X	269.0	29.14	298.14	269.32	32H	282.9	30.022	312.92	282.68	32H	282.9	28.923	311.82	281.68
31X	278.5	29.14	307.64	277.90	33H	292.4	30.402	322.80	291.60	33H	292.4	29.442	321.84	290.73
32X	288.1	32.32	320.42	289.45	34H	301.9	31.431	333.33	301.11	34H	301.9	27.736	329.64	297.77
33X	297.7	33.32	331.02	299.03	35H	311.4	32.776	344.18	310.91	35H	306.9	32.080	338.98	306.21
34X	307.3	35.43	342.73	309.60	36H	320.9	33.037	353.94	319.73	36H	316.4	33.468	349.87	316.05
35X	316.9	40.33	357.23	322.70	37H	330.4	33.981	364.38	329.16	37H	325.9	35.067	360.97	326.08
36X	326.5	38.92	365.42	330.10	38H	339.9	35.883	375.78	339.46	38H	335.4	35.589	370.99	335.13
37X	336.0	30.43	366.43	331.01	39H	349.4	41.028	390.43	352.69	39H	344.9	36.102	381.00	344.18
38X	345.5	30.08	375.58	339.28	40H	358.9	41.196	400.10	361.42	40H	354.4	36.482	390.88	353.10
39X	354.8	33.21	388.01	350.51	41H	368.4	42.467	410.87	371.15	41H	363.9	37.392	401.29	362.50
40X	364.4	37.91	402.31	363.42	42H	377.9	43.240	421.14	380.43	42H	373.4	37.712	411.11	371.38
41X	374.0	46.72	420.72	380.06	43X	387.4	43.615	431.01	389.35	43H	377.9	39.752	417.65	377.28
42X	383.6	46.32	429.92	388.36	44X	397.0	44.526	441.53	398.85	44H	387.4	40.411	427.81	386.46
43X	393.2	45.47	438.67	396.27	45X	406.6	44.841	451.44	407.81	45H	396.9	40.111	437.01	394.77
44X	402.8	45.06	447.86	404.57	321-U1338C-					46H	404	40.166	444.17	401.23
321-U1338B-					1H	0	0.000	0.00	0.00	47H	410.5	40.867	451.37	407.74
1H	0.0	0.000	0.00	0.00										

Table T24. Splice tie points, Site U1338. (Continued on next page.)

Hole, core, section, interval (cm)	Depth (m)			Hole, core, section, interval (cm)	Depth (m)	
	CSF	CCSF-A			CSF	CCSF-A
321-				321-		
U1338A-1H-2, 47	1.98	2.02	Tie to	U1338B-1H-2, 52	2.02	2.02
U1338B-1H-4, 51	5.01	5.01	Tie to	U1338A-2H-1, 83	3.53	5.01
U1338A-2H-6, 145	11.66	13.14	Tie to	U1338B-2H-3, 125	11.85	13.14
U1338B-2H-7, 10	16.70	17.99	Tie to	U1338A-3H-3, 56	15.76	17.99
U1338A-3H-5, 58	18.79	21.02	Tie to	U1338B-3H-2, 35	18.95	21.02
U1338B-3H-7, 50	26.60	28.67	Tie to	U1338A-4H-3, 35	25.05	28.67
U1338A-4H-6, 124	30.44	34.06	Tie to	U1338B-4H-4, 29	31.39	34.06
U1338B-4H-6, 127	35.36	38.03	Tie to	U1338A-5H-1, 113	32.33	38.03
U1338A-5H-5, 112	38.32	44.02	Tie to	U1338B-5H-3, 62	39.72	44.02
U1338B-5H-7, 40	45.51	49.81	Tie to	U1338A-6H-3, 55	44.24	49.81
U1338A-6H-4, 127	46.46	52.02	Tie to	U1338B-6H-1, 128	46.88	52.02
U1338B-6H-5, 110	52.70	57.84	Tie to	U1338A-7H-1, 143	51.63	57.84
U1338A-7H-4, 110	55.80	62.01	Tie to	U1338B-7H-1, 105	56.15	62.01
U1338B-7H-6, 56	63.17	69.03	Tie to	U1338A-8H-1, 125	60.95	69.03
U1338A-8H-6, 82	68.02	76.10	Tie to	U1338B-8H-4, 41	69.51	76.10
U1338B-8H-6, 131	73.41	79.99	Tie to	U1338A-9H-1, 134	70.54	79.99
U1338A-9H-6, 78	77.48	86.93	Tie to	U1338B-9H-4, 30	78.90	86.93
U1338B-9H-6, 35	81.95	89.98	Tie to	U1338A-10H-1, 105	79.75	89.98
U1338A-10H-6, 55	86.75	96.98	Tie to	U1338B-10H-3, 138	87.98	96.98
U1338B-10H-5, 145	91.05	100.05	Tie to	U1338A-11H-1, 82	89.02	100.05
U1338A-11H-4, 27	92.97	104.00	Tie to	U1338B-11H-1, 103	94.13	104.00
U1338B-11H-7, 22	102.11	111.99	Tie to	U1338A-12H-2, 44	99.64	111.99
U1338A-12H-3, 95	101.65	113.99	Tie to	U1338B-12H-1, 34	102.95	113.99
U1338B-12H-6, 88	110.98	122.02	Tie to	U1338A-13H-1, 110	108.30	122.02
U1338A-13H-3, 104	111.24	124.96	Tie to	U1338B-13H-1, 44	112.54	124.96
U1338B-13H-5, 149	119.59	132.01	Tie to	U1338C-14H-1, 148	119.28	132.01
U1338C-14H-4, 101	123.31	136.03	Tie to	U1338B-14H-1, 138	122.98	136.03
U1338B-14H-6, 84	129.94	142.99	Tie to	U1338A-15H-2, 29	127.99	142.99
U1338A-15H-4, 135	132.05	147.06	Tie to	U1338B-15H-2, 11	132.71	147.06
U1338B-15H-6, 10	138.71	153.05	Tie to	U1338A-16H-1, 129	137.00	153.05
U1338A-16H-5, 128	142.98	159.04	Tie to	U1338B-16H-2, 86	142.96	159.04
U1338B-16H-6, 87	148.98	165.05	Tie to	U1338A-17H-2, 27	146.97	165.05
U1338A-17H-4, 132	151.02	169.10	Tie to	U1338B-17H-2, 31	151.91	169.10
U1338B-17H-6, 122	158.82	176.01	Tie to	U1338A-18H-2, 52	156.73	176.01
U1338A-18H-6, 56	162.76	182.04	Tie to	U1338B-18H-3, 148	164.08	182.04
U1338B-18H-6, 79	167.89	185.85	Tie to	U1338A-19H-1, 145	165.65	185.85
U1338A-19H-6, 6	171.76	191.96	Tie to	U1338B-19H-4, 21	173.81	191.96
U1338B-19H-6, 118	177.78	195.93	Tie to	U1338A-20H-1, 143	175.14	195.93
U1338A-20H-5, 63	180.32	201.12	Tie to	U1338B-20H-2, 139	181.49	201.12
U1338B-20H-6, 127	187.37	207.00	Tie to	U1338A-21H-2, 20	184.91	207.00
U1338A-21H-6, 26	190.96	213.05	Tie to	U1338B-21H-4, 20	192.80	213.05
U1338B-21H-6, 117	196.77	217.02	Tie to	U1338A-22H-1, 97	193.67	217.02
U1338A-22H-3, 101	196.71	220.07	Tie to	U1338B-22H-1, 139	199.00	220.07
U1338B-22H-6, 117	206.27	227.34	Tie to	U1338A-23H-1, 50	202.70	227.34
U1338A-23H-3, 119	206.38	231.02	Tie to	U1338B-23H-1, 88	207.98	231.02
U1338B-23H-6, 140	216.00	239.04	Tie to	U1338A-24H-1, 86	212.56	239.04
U1338A-24H-4, 62	216.82	243.30	Tie to	U1338B-24H-2, 53	218.64	243.30
U1338B-24H-6, 122	225.32	249.98	Tie to	U1338A-25H-1, 131	222.51	249.98
U1338A-25H-6, 89	229.63	257.11	Tie to	U1338B-25H-4, 39	230.99	257.11
U1338B-25H-6, 137	234.97	261.08	Tie to	U1338A-26H-2, 90	233.10	261.08
U1338A-26H-6, 90	239.11	267.09	Tie to	U1338C-27H-2, 148	240.28	267.09
U1338C-27H-4, 41	242.21	269.02	Tie to	U1338B-26H-3, 99	242.09	269.02
U1338B-26H-6, 146	247.06	273.99	Tie to	U1338C-28H-1, 38	247.18	273.99
U1338C-28H-7, 64	256.44	283.25	Append to	U1338C-29H-1, 3	256.33	283.14
U1338C-29H-2, 39	258.19	285.00	Tie to	U1338B-28H-1, 25	257.35	285.00
U1338B-28H-7, 47	266.37	294.02	Tie to	U1338A-29X-4, 82	264.71	294.02
U1338A-29X-5, 134	266.74	296.05	Tie to	U1338B-29H-1, 125	267.85	296.05
U1338B-29H-7, 73	276.22	304.42	Tie to	U1338C-31H-1, 19	275.50	304.42
U1338C-31H-5, 143	282.73	311.65	Append to	U1338C-32H-1, 55	283.45	312.37
U1338C-32H-1, 125	284.15	313.07	Tie to	U1338B-32H-1, 16	283.05	313.07
U1338B-32H-7, 18	291.88	321.90	Tie to	U1338C-33H-1, 10	292.50	321.94
U1338C-33H-1, 123	293.63	323.07	Tie to	U1338B-33H-1, 27	292.67	323.07
U1338B-33H-6, 116	301.06	331.46	Tie to	U1338A-33X-1, 43	298.14	331.46
U1338A-33X-2, 150	300.71	334.03	Tie to	U1338B-34H-1, 70	302.60	334.03
U1338B-34H-4, 131	307.72	339.15	Tie to	U1338C-35H-1, 17	307.07	339.15
U1338C-35H-5, 109	314.02	346.10	Tie to	U1338B-35H-2, 42	313.32	346.10
U1338B-35H-5, 84	318.24	351.02	Tie to	U1338C-36H-1, 115	317.55	351.02

Table T24 (continued).

Hole, core, section, interval (cm)	Depth (m)			Hole, core, section, interval (cm)	Depth (m)	
	CSF	CCSF-A			CSF	CCSF-A
U1338C-36H-4, 66	321.56	355.03	Tie to	U1338B-36H-1, 110	322.00	355.04
U1338B-36H-6, 39	328.72	361.76	Tie to	U1338C-37H-1, 86	326.76	361.83
U1338C-37H-5, 5	331.96	367.02	Tie to	U1338B-37H-2, 115	333.05	367.03
U1338B-37H-6, 27	338.15	372.13	Tie to	U1338C-38H-1, 118	336.58	372.17
U1338C-38H-5, 93	342.26	377.85	Tie to	U1338B-38H-2, 66	342.06	377.94
U1338B-38H-5, 71	346.59	382.47	Tie to	U1338C-39H-1, 149	346.39	382.49
U1338C-39H-7, 72	354.62	390.72	Append to	U1338C-40H-1, 5	354.45	390.93
U1338C-40H-7, 65	363.60	400.08	Tie to	U1338B-40H-1, 3	358.93	400.13
U1338B-40H-2, 53	360.93	402.13	Tie to	U1338C-41H-1, 83	364.73	402.12
U1338C-41H-7, 61	373.53	410.92	Tie to	U1338B-41H-1, 8	368.48	410.95
U1338B-41H-6, 74	376.59	419.06	Tie to	U1338C-43H-1, 145	379.35	419.10
U1338C-43H-4, 95	383.32	423.07	Tie to	U1338B-42H-2, 48	379.88	423.12
U1338B-42H-5, 100	384.93	428.17	Tie to	U1338C-44H-1, 36	387.76	428.17
U1338C-44H-6, 76	395.42	435.83	Append to	U1338C-45H-1, 5	396.95	437.06
U1338C-45H-5, 86	403.82	443.93	Append to	U1338C-46H-1, 5	404.05	444.22

Table T25. Magnetostratigraphic and biostratigraphic datums, Site U1338. (See table note.) (Continued on next three pages.)

Event	Age (Ma)	Depth (m)		Error (m)
		CCSF-A	CCSF-B	
Polarity chron				
C1n/C1r	0.781	9.92	8.96	
C1r.1r/C1r.1n	0.988	12.62	11.40	
C1r.1n/C1r	1.072	13.54	12.23	
C1r/C2n	1.778	23.5	21.23	
C2n/C2r	1.945	25.66	23.18	
C2r/C2An.1n	2.581	35.15	31.75	
C2An.1n/C2An.1r	3.032	41.16	37.18	
C2An.1r/C2An.2n	3.116	42.3	38.21	
C2An.2n/C2An.2r	3.207	43.58	39.37	
C2An.2r/C2An.3	3.33	45.21	40.84	
C2An.3/C2Ar	3.596	49.13	44.38	
C4An/C4Ar.1r	9.098	209.35	189.11	
C4Ar.1r/C4Ar.1n	9.312	212.7	192.14	
C4Ar.1n/C4Ar.2r	9.409	215.3	194.49	
C4Ar.2r/C4Ar.2n	9.656	220.4	199.10	
C4Ar.2n/C4Ar.3r	9.717	222.27	200.79	
C4Ar.3r/C5n.1n	9.779	223.4	201.81	
C5n.1n/C5n.1r	9.934	226.75	204.83	
C5n.1r/C5n.2n	9.987	227.35	205.37	
C5Ar.1r/C5Ar.1n	12.73	331.17	299.16	
C5Ar.2n/C5Ar.3r	12.878	337	304.43	
C5Ar.3r/C5AAn	13.015	341.77	308.74	
C5AAn/C5AAr	13.183	348.36	314.69	
C5AAr/C5ABn	13.369	352.78	318.68	
C5ABn/C5ABr	13.605	361.6	326.65	
C5ABr/C5ACn	13.734	363.8	328.64	
C5ACn/C5ACr	14.095	375.5	339.21	
C5ACr/C5ADn	14.194	378.5	341.92	
C5ADn/C5ADr	14.581	390.88	353.10	
C5ADr/C5Bn.1n	14.784	392.8	354.83	
C5Bn.1n/C5Bn.1r	14.877	394.2	356.10	
C5Bn.1r/C5Bn.2n	15.032	404.69	365.57	
C5Bn.2n/C5Br	15.16	407.7	368.29	
Nannofossils				
T <i>Pseudoemiliania lacunosa</i> (NN20)	0.44	5.70	5.15	0.22
Tc <i>Reticulofenestra asanoi</i>	0.91	10.48	9.47	0.9
T <i>Gephyrocapsa</i> (>5.5 µm)	1.26	15.98	14.44	0.65
T <i>Calcidiscus macintyreii</i>	1.61	20.48	18.50	0.75
T <i>Discoaster brouweri</i> (NN19)	1.93	28.07	25.36	0.75
T <i>Discoaster pentaradiatus</i> (NN18)	2.39	35.34	31.93	0.075
T <i>Discoaster surculus</i> (NN17)	2.49	38.37	34.66	0.875
T <i>Sphenolithus</i> spp.	3.54	49.22	44.46	1.06

Table T25 (continued). (Continued on next page.)

Event	Age (Ma)	Depth (m)		Error (m)
		CCSF-A	CCSF-B	
T <i>Reticulofenestra pseudumbilicus</i> (NN16)	3.70	51.86	46.85	0.8
T <i>Ceratolithus acutus</i> (NN13)	5.04	75.49	68.19	0.615
B <i>Ceratolithus acutus</i>	5.35	84.60	76.42	0.75
T <i>Discoaster quinqueramus</i> (NN12)	5.58	93.38	84.35	0.75
T <i>Nicklithus amplificus</i>	5.98	107.12	96.76	0.685
B <i>Nicklithus amplificus</i>	6.91	133.68	120.76	0.75
TP <i>Reticulofenestra pseudumbilicus</i>	7.07	156.01	140.93	0.75
B <i>Amaurolithus</i> spp.	7.36	164.76	148.83	0.525
B <i>Discoaster berggrenii</i> (NN11)	8.29	177.01	159.90	0.625
BP <i>Reticulofenestra pseudumbilicus</i>	9.10	199.04	179.80	0.75
T <i>Discoaster hamatus</i> (NN10)	9.69	222.10	200.64	0.75
B <i>Discoaster hamatus</i> (NN9)	10.55	248.33	224.33	0.155
T <i>Coccolithus miopelagicus</i>	10.60	250.23	226.04	0.755
B <i>Catinaster coalitus</i> (NN8)	10.89	253.25	228.77	0.755
Bc <i>Discoaster kugleri</i> (NN7)	11.86	296.26	267.62	0.75
Tc <i>Cyclicargolithus floridanus</i>	13.33	350.28	316.42	0.75
T <i>Sphenolithus heteromorphus</i> (NN6)	13.53	359.82	325.04	0.295
B <i>Discoaster petaliformis</i>	15.70	397.69	359.25	0.72
Tc <i>Discoaster deflandrei</i>	15.80	398.46	359.94	1.435
Bc <i>Sphenolithus heteromorphus</i>	17.71	448.27	404.94	0.39
Radiolarians				
T <i>Stylatractus universus</i>	0.44	3.84	3.47	1.07
B <i>Collosphaera tuberosa</i>	0.59	3.84	3.47	1.07
T <i>Anthocorythidium angulare</i>	1.21	12.69	11.47	1.39
T <i>Theocorythium vetulum</i>	1.21	12.69	11.47	1.39
T <i>Lamprocyrtis heteroporos</i>	1.76	19.07	17.23	2.46
B <i>Theocorythium trachelium</i>	1.76	19.07	17.23	2.46
B <i>Anthocorythidium angulare</i>	1.97	19.07	17.23	2.46
T <i>Pterocanium prismatium</i>	2.08	22.95	20.73	1.40
T <i>Didymocyrtis avita</i>	2.60	32.72	29.56	2.55
T <i>Stichocorys pergrina</i>	2.90	36.43	32.91	1.12
B <i>Lamprocyrtis neoheteroporos</i>	3.23	40.77	36.83	1.13
B <i>Lamprocyrtis heteroporos</i>	3.23	40.77	36.83	1.13
T <i>Phormostichoartus fistula</i>	3.52	44.43	40.13	2.52
T <i>Spongaster pentas</i>	3.96	52.08	47.05	1.49
T <i>Phormostichoartus doliolum</i>	3.96	52.08	47.05	1.49
B <i>Spongaster tetras teteras</i>	4.26	57.02	51.51	0.71
T <i>Didymocyrtis penultima</i>	4.26	57.02	51.51	0.71
B <i>Pterocanium prismatium</i>	4.73	59.92	54.12	1.52
T <i>Spongaster berminghami</i>	5.57	79.10	71.45	1.32
B <i>Didymocyrtis avita</i>	6.15	98.29	88.79	0.66
B <i>Spongaster pentas</i>	6.17	98.29	88.79	0.66
T <i>Didymocyrtis antepenultima</i>	6.17	98.29	88.79	0.66
B <i>Didymocyrtis tetrathalamus</i>	6.60	100.77	91.03	1.76
T <i>Stichocorys delmontensis</i>	6.89	104.66	94.54	1.31
<i>S. delmontensis</i> > <i>S. pergrina</i>	7.84	141.44	127.77	0.67
B <i>Theocorythium vetulum</i>	7.98	145.10	131.07	1.90
T <i>Diartus hughesi</i>	8.39	174.18	157.34	0.78
T <i>Didymocyrtis laticonus</i>	8.43	174.18	157.34	0.78
B <i>Didymocyrtis penultima</i>	8.51	199.12	179.87	1.48
T <i>Botryostrobos miralestensis</i>	8.59	199.12	179.87	1.48
B <i>Spongaster berminghami</i>	8.76	202.56	182.98	1.94
<i>D. pettersoni</i> > <i>D. hughesi</i>	8.76	202.56	182.98	1.94
B <i>Diartus hughesi</i>	8.63	205.23	185.39	0.68
B <i>Didymocyrtis antepenultima</i>	10.01	224.27	202.59	1.67
T <i>Cyrtocapsella japonica</i>	10.31	235.37	212.62	1.43
T <i>Carpocanopsis cristata</i>	10.88	242.82	219.35	2.69
T <i>Lithopera neotera</i>	11.16	242.82	219.35	2.69
T <i>Cyrtocapsella cornuta</i>	11.88	295.55	266.98	2.08
Bc <i>Cyrtocapsella japonica</i>	11.88	295.55	266.98	2.08
T <i>Lithopera renzae</i>	11.91	295.55	266.98	2.08
T <i>Cyrtocapsella tetrapera</i>	11.91	295.55	266.98	2.08
B <i>Diartus pettersoni</i>	12.11	313.63	283.31	5.94
B <i>Lithopera neotera</i>	12.95	346.48	312.99	1.56
T <i>Calocyclus robusta</i>	13.35	363.64	328.49	3.48
T <i>Acrocubus octopyle</i>	13.88	370.97	335.12	4.32
T <i>Liriospyris parkerae</i>	13.88	370.97	335.12	4.32
T <i>Didymocyrtis mammifera</i>	13.89	370.97	335.12	4.32

Table T25 (continued). (Continued on next page.)

Event	Age (Ma)	Depth (m)		Error (m)
		CCSF-A	CCSF-B	
T <i>Didymocyrtis violina</i>	14.20	372.72	336.70	5.06
T <i>Calocyctetta virginis</i>	14.23	372.72	336.70	5.06
T <i>Calocyctetta costata</i>	14.23	372.72	336.70	5.06
T <i>Carpocanopsis bramlettei</i>	14.33	392.59	354.64	2.30
T <i>Didymocyrtis tubaria</i>	14.35	392.59	354.64	2.295
<i>D. dentata</i> > <i>D. alata</i>	14.77	397.83	359.38	0.81
T <i>Liriospyris stauropora</i>	14.82	404.21	365.14	0.855
B <i>Liriospyris parkerae</i>	14.91	427.45	386.13	1.99
T <i>Carpocanopsos cingulata</i>	15.13	430.89	389.24	1.395
B <i>Acrocubus octopylus</i>	15.75	436.41	394.23	0.975
B <i>Calocyctetta costata</i>	17.19	441.35	398.69	0.535
Foraminifers				
T <i>Globigerinoides ruber</i> (pink)	0.12	1.84	1.66	0.885
T <i>Globorotalia (Truncorotalia) tosaensis</i>	0.61	8.87	8.01	2.465
T <i>Globigerinoides obliquus</i>	1.3	20.50	18.52	3.85
T <i>Globigerinoides fistulosus</i>	1.77	20.50	18.52	3.85
T <i>Globigerinoides extremus</i>	1.98	33.58	30.34	1.685
T <i>Globorotalia pseudomiocenica</i>	2.3	30.39	27.45	1.49
T <i>Globoturborotalita woodi</i>	2.3	129.10	116.62	1.715
T <i>Globorotalia (Menardella) multicamerata</i>	2.98	33.58	30.34	1.685
B <i>Globigerinoides fistulosus</i>	3.33	43.26	39.08	3.685
T <i>Dentoglobigerina altispira</i>	3.47	43.26	39.08	3.685
T <i>Sphaeroidinellopsis seminulina</i>	3.59	43.26	39.08	3.685
T <i>Globorotalia (Hirsutella) margaritae</i>	3.85	54.86	49.56	1.4
X <i>Pulleniatina</i> spp. sinistral → dextral	4.08	54.86	49.56	1.4
T <i>Globoturborotalita nepenthes</i>	4.37	59.97	54.17	1.52
B <i>Globorotalia (Menardella) exilis</i>	4.45	63.93	57.75	2.42
B <i>Sphaeroidinella dehiscens</i> s.l.	5.54	72.28	65.30	2.555
B <i>Globorotalia tumida</i>	5.57	94.96	85.78	2.545
T <i>Globoquadrina dehiscens</i>	5.92	98.24	88.75	0.715
B <i>Globorotalia (Hirsutella) margaritae</i>	5.99	121.07	109.36	1.03
T <i>Globorotalia linguaensis</i>	6.13	129.10	116.62	1.715
B <i>Pulleniatina primalis</i>	6.57	106.99	96.65	1.09
B <i>Globorotalia plesiotumida</i>	8.58	209.49	189.24	2.295
B <i>Neogloboquadrina acostaensis</i>	9.83	254.04	229.48	2.23
T <i>Paragloborotalia mayeri</i>	10.57	249.48	225.37	1.31
B <i>Globoturborotalita decoraperta</i>	11.49	282.74	255.41	7.305
T <i>Globigerinoides subquadratus</i>	11.54	282.74	255.41	7.305
B <i>Globoturborotalita nepenthes</i>	11.63	264.09	238.56	3.39
T <i>Globorotalia (Fohsella) fohsi</i> s.l.	11.79	292.56	264.28	0.97
B <i>Globorotalia (Fohsella) fohsi robusta</i>	13.13	346.58	313.08	1.555
B <i>Globorotalia (Fohsella) fohsi</i> s.l.	13.41	359.48	324.73	0.64
T <i>Globorotalia praescitula</i>	13.73	338.64	305.91	1.13
B <i>Globorotalia (Fohsella) "praefohsi"</i>	13.77	366.20	330.81	0.4
B <i>Globorotalia (Fohsella) peripheroacuta</i>	14.24	371.00	335.14	4.35
T <i>Globigerinatella insueta</i>	14.66	383.73	346.64	1.045
B <i>Orbulina</i> spp.	14.74	359.48	324.73	0.64
B <i>Clavatorella bermudezi</i>	14.89	372.72	336.70	5.06
B <i>Praeorbulina glomerosa</i>	16.27	409.88	370.27	4.185
X <i>Pargloborotalia</i> spp. random to sinistral	16.27	408.77	369.26	5.295
B <i>Praeorbulina sicana</i>	16.97	436.48	394.29	0.905
B <i>Globorotalia birnageae</i>	16.69	397.89	359.43	0.87
B <i>Globigerinatella insueta</i>	17.59	446.13	403.01	4.195
T <i>Globoquadrina binaiensis</i>	19.09	439.32	396.85	1.88
Diatoms				
T <i>Nitzschia fossilis</i>	0.92	1.81	1.63	0.79
T <i>Thalassiosira convexa</i>	2.18	15.01	13.52	0.33
T <i>Nitzschia jouseae</i>	2.71	22.86	20.59	1.36
B <i>Rhizosolenia praebergonii</i>	3.13	48.66	43.84	1.85
T <i>Actinocyclus ellipticus</i> f. <i>lanceolata</i>	3.35	59.19	53.32	0.77
T <i>Nitzschia cylindrica</i>	4.69	86.30	77.75	0.95
B <i>Nitzschia jouseae</i>	4.92	87.74	79.05	0.49
B <i>Thalassiosira oestrupii</i>	5.70	95.12	85.69	2.61
T <i>Thalassiosira praeconvexa</i>	6.56	106.90	96.30	1.10
B <i>Thalassiosira miocenica</i>	6.86	144.93	130.57	1.85
B <i>Nitzschia miocenica</i>	7.58	164.53	148.23	1.00
T <i>Rossiella paleacea</i>	7.64	168.16	151.50	0.12
T <i>Thalassiosira burckliana</i>	7.86	178.23	160.57	0.97

Table T25 (continued).

Event	Age (Ma)	Depth (m)		Error (m)
		CCSF-A	CCSF-B	
T <i>Thalassiosira yabei</i>	8.44	191.85	172.84	0.75
T <i>Actinocyclus moronensis</i>	9.77	237.38	213.86	0.80
B <i>Hemidiscus cuneiformis</i>	11.24	268.85	242.21	0.68
B <i>Thalassiosira brunii</i>	11.50	276.45	249.05	1.13
T <i>Cestodiscus pulchellus</i>	12.05	297.89	268.36	0.43
B <i>Nitzschia porteri</i>	12.11	302.89	272.87	4.75
T <i>Coscinodiscus lewisianus</i>	12.99	316.02	284.70	5.20
T <i>Thalassiosira tappanae</i>	13.37	343.42	309.38	1.66
B <i>Actinocyclus ellipticus</i>	14.37	359.13	323.54	0.99
B <i>Thalassiosira tappanae</i>	14.55	371.75	334.91	4.88
B <i>Actinocyclus ingens</i>	15.25	403.37	363.40	1.70
T <i>Thalassiosira fraga</i>	15.96	438.71	395.23	2.16

Note: T = top, Tc = Top common occurrence, B = bottom, TP = top paracme, BP = bottom paracme, Bc = bottom common occurrence, X = abundance crossover.

Table T26. Vertical seismic profile direct arrival times. (See table notes.)

Receiver depth (m)		One-way traveltime (s)	
WRF	WSF	Measured	Corrected
4398.1	190.6	2.9142	2.9202
4413.0	205.5	2.9243	2.9303
4428.1	220.6	2.9333	2.9392
4442.2	234.7	2.9413	2.9473
4458.1	250.6	2.9508	2.9567
4488.1	280.6	2.9691	2.9751
4518.1	310.6	2.9851	2.9910
4533.0	325.5	2.9943	3.0002
4548.1	340.6	2.9995	3.0054
4563.1	355.6	3.0067	3.0126
4578.1	370.6	3.0146	3.0206
4593.1	385.6	3.0225	3.0285
4608.1	400.6	3.0308	3.0367
4623.2	415.7	3.0389	3.0448

Notes: Measured traveltimes are times between arrival of the pulse at a hydrophone located 2 m below the air guns and at the receivers in the borehole. Corrected traveltimes are between sea level and the borehole receivers.

Table T27. Temperature data and thermal resistance, Site U1338. (See table notes.)

Core	Tool	Depth DSF (m)	Temperature (°C)		Thermal resistance (m ² K/W)
			At mudline	In situ	
321-U1338A-					
5H	APCT-3	40.7	1.57	3.33	46.3
7H		59.5	1.60	4.07	67.2
9H		78.7	1.70	4.67	88.2
11H		97.7	1.70	5.56	108.7
13H		116.7	1.65	6.06	128.9
321-U1338C-					
20H		180.3	1.56	8.22	194.6
35H		316.4	1.78	12.69	325.9
		Average:	1.651		

Notes: Thermal resistance determined from the trend of in situ thermal conductivities with depth (Fig. F53). APCT-3 = advanced piston corer temperature tool.